Parallel Finite Element Simulations of Localization Phenomena in Porous Media

Von der Fakultät Bau- und Umweltingenieurwissenschaften
der Universität Stuttgart zur Erlangung der Würde
eines Doktor-Ingenieurs (Dr.-Ing.)
genehmigte Abhandlung

Vorgelegt von

Dipl.-Ing. Martin Ammann

aus
Ellwangen/Jagst

Hauptberichter: Prof. Dr.-Ing. Wolfgang Ehlers
Mitberichter: Prof. Dr. rer. nat. Christian Wieners

Tag der mündlichen Prüfung: 22. April 2005

Institut für Mechanik (Bauwesen) der Universität Stuttgart
Lehrstuhl II, Prof. Dr.-Ing. W. Ehlers

Editor:

Prof. Dr.-Ing. W. Ehlers

Acknowledgments

The work presented in this thesis was carried out in the years between 1999 and 2005, when I was an assistant lecturer at the Institute of Applied Mechanics (Civil Engineering) at the University of Stuttgart. Numerous people contributed in many ways to the realization of this work - all their support is most gratefully acknowledged.

First of all, I want to thank my supervisor Professor Wolfgang Ehlers for giving me the opportunity to prepare my thesis at the institute, for his scientific support and for the many interesting discussions we had. His research in the field of Continuum Mechanics built the important foundation for the numerical results achieved in this work.

I am also very grateful to my co-supervisor Professor Christian Wieners. Without his valuable advice and support concerning the realization of the interface M++/PANDAS, the large scale parallel calculations could not have been carried out.

Next, I want to thank all my fellow workers at the institute for creating a pleasant and friendly working atmosphere. Especially, I would like to express my gratitude to my room mate Tobias Graf for the support he gave me and the many discussions on the design of boundary-value problems we had. Furthermore, I owe my special thanks to Peter Ellsiepen, as he introduced me very carefully into PANDAS, and to Holger Steeb, who had always time to discuss different aspects of the generalized variational calculus. Finally, I would like to thank Oliver Klar for being a very good friend.

Very important and time-consuming work was done by Professor Herbert Schneckenburger, Tobias Graf and Holger Steeb at the proof-reading stage. They not only corrected my Swabian English but also improved the quality of this thesis fundamentally. In this context, I also want to thank the people at `http://dict.leo.org`.

I would like to thank my girl-friend Alexandra, who has put up with my crazy PhD life style, especially in the last year, where my research was resulting in many late nights. She has always been there supporting me, understood the importance of my work and is a very important part of my life.

Finally, I would like to thank my parents for always taking care of me. It is through their support that I have made it through all the steps to reach this point in life.

Stuttgart, May 2005 Martin Ammann

Jetzt weiß ich, warum es so viele Leute gibt, die gern Holz spalten. Bei dieser Tätigkeit sieht man nämlich immer sofort den Erfolg.
(*Albert Einstein)*

Deutsche Zusammenfassung

In vielen Bereichen des Ingenieurwesens ist die Berücksichtigung mehrerer Phasen eines Materials und deren Interaktion untereinander für eine adequate kontinuumsmechanische Beschreibung unerläßlich. Betrachtet man etwa ein Beispiel aus dem Bereich des Bauingenieurwesens, das Versagen einer Böschung verursacht durch einen starken Regen, so muß für eine realitätsnahe Beschreibung dieses Vorgangs die poröse Struktur des Bodens in den Modellierungsprozeß mit einbezogen werden. Neben Geomaterialien, wie z. B. Böden oder Steinen, weisen weitere Materialien, die in unterschiedlichsten Bereichen ihre Anwendung finden, eine ausgezeichnete poröse Matrixstruktur auf. So finden etwa im Bereich der Automobilindustrie mehrphasige Materialien, wie z. B. hochporöse Kunststoffschäume, ihre Anwendung als Energieabsorber für den Insassenaufprallschutz. In der Medizin treten poröse Materialien beispielsweise in Form von blutdurchströmtem Muskelgewebe oder Knorpel- bzw. Knochenmaterialien auf.

In den oben genannten Fällen ist das charakteristische Verhalten des betrachteten Mehrphasenmaterials durch das gleichzeitige Wirken von unterschiedlichen Effekten gekennzeichnet, die aus den einzelnen Phasen des porösen Werkstoffs stammen. So müssen etwa für eine korrekte Modellierung des oben genannten Böschungsbruchs insgesamt drei unterschiedliche Phasen berücksichtigt werden: Festkörperskelett, Wasser und Luft. Auf Basis dieser Wahl kann ein kontinuumsmechanisches Modell entwickelt werden, mit dessen Hilfe teilgesättigte Zustände in Böden abgebildet werden können. Des weiteren kann somit der Regen als die Ursache des Versagens der Böschung über eine Randbedingung im Rahmen einer numerischen Berechnung direkt modelliert werden.

Die numerische Simulation mit Hilfe der Finite-Elemente-Methode (FEM) von Anfangs-Randwertproblemen mit den eben beschriebenen mehrphasigen Materialien wird aufgrund der rasanten Entwicklung in der Computertechnologie immer interessanter. Gleichzeitig wachsen allerdings auch die Ansprüche hinsichtlich der Genauigkeit der numerischen Simulationen im Vergleich mit der Realität. So kann etwa der oben beschriebene Böschungsbruch mit Hilfe einer 2-dimensionalen Simulation auf der Basis eines einfachen mechanischen Modells grob beschrieben werden. Ausgehend von diesem Ansatz sind beliebige Erweiterungen der Komplexität der numerischen Simulation und als Folge davon beliebige Verbesserungen der Qualität der Ergebnisse denkbar. Um etwa die Geometrie der Böschung und deren Versagen genauer abbilden zu können, wird eine 3-dimensionale Diskretisierung der Böschung unerläßlich sein, wobei die Zonen, in denen das Versagen stattfindet, räumlich sehr genau aufgelöst werden müssen, um die dort auftretenden hohen Gradienten in den Feldfunktionen abbilden zu können. Wenn zusätzlich noch das zugrundeliegende mechanische Modell zu dem oben genannten Mehrphasen-Materialmodell erweitert wird, können viele Effekte des wirklichen Böschungsbruchs numerisch simuliert werden. Gleichzeitig hat allerdings die Komplexität des Problems und der Aufwand der numerischen Simulation im Vergleich zu dem anfänglichen 2-d Modell enorm zugenommen.

Aus diesen Überlegungen kann gefolgert werden, daß selbst die schnelle Entwicklung in der Computertechnologie alleine den ständig wachsenden Anforderungen an die Qualität

der Ergebnisse nicht gerecht werden kann. Es müssen vielmehr gleichzeitig die Algorithmen und Strategien der numerischen Umsetzung weiterentwickelt werden. Im Hinblick auf effiziente numerische Lösungsmethoden sind in diesem Zusammenhang etwa orts- und zeitadaptive Ansätze, parallele Strategien und die Weiterentwicklung auf dem Gebiet der linearen Gleichungslöser zu nennen. Adaptive Verfahren passen die Orts- bzw. Zeitdiskretisierung automatisch an die Bedürfnisse des jeweiligen Anfangs-Randwertproblems an und können somit die Effizienz einer numerischen Simulation deutlich steigern. Ein großer Nachteil bei der alleinigen Anwendung von adaptiven Strategien liegt in der Beschränkung der realisierbaren Problemgröße. Die obere Grenze einer solchen Problemgröße ist dabei durch den auf einem Rechner vorhandenen Arbeitsspeicher bzw. dessen Prozessorgeschwindigkeit gegeben. Eine offensichtliche Lösung dieses Nachteils ist durch das gleichzeitige (parallele) Verwenden von mehreren Rechnern für die Ermittlung der Lösung einer numerischen Simulation gegeben. Im Rahmen einer solchen parallelen Rechnung müssen die einzelnen Rechenknoten über ein leistungsstarkes Netzwerk miteinander verbunden sein, um ein effizientes Verhalten zu erzielen.

Untersucht man den numerischen Aufwand für das Berechnen eines Zeitschritts in einer numerischen Simulation, so stellt man fest, daß der rechenzeitintensivste Teil durch das Lösen des linearen Gleichungssystems innerhalb des *Newton-Raphson*-Verfahrens gegeben ist. Neben relativ neuen Entwicklungen auf diesem Gebiet, wie etwa sogenannte Mehrgitterverfahren, die im Vergleich zu den klassischen Gleichungslösern eine enorme Zeitersparnis liefern, beinhaltet der parallele Ansatz auch für dieses Problem einen vielversprechenden Lösungsansatz. Durch die Zerlegung des gesamten Rechengebiets in viele Teilgebiete und die Verteilung dieser Teilgebiete auf die einzelnen Rechner können die Lösungen der daraus resultierenden kleinen Unterprobleme parallel auf genau den Rechnern durchgeführt werden, auf denen die jeweiligen Teilgebiete definiert sind.

Basierend auf den oben skizzierten Überlegungen motiviert sich der Inhalt der vorliegenden Arbeit. Es sollen alle wichtigen Punkte diskutiert werden, die notwendig sind, um realistische numerische Simulationen von Lokalisierungsphänomenen der Bodenmechanik mit Hilfe von kontinuumsmechanischen Modellen für Mehrphasenmaterialien effizient durchführen zu können.

Dabei wird zu Beginn der Arbeit in **Kapitel 2** ein kontinuumsmechanisches Modell präsentiert, das auf Basis einer makroskopischen Betrachtungsweise hergeleitet wird: der Theorie Poröser Medien (TPM) [20, 21, 53]. Wie allgemein üblich wird die Herleitung dieses Modells in drei Abschnitte unterteilt: kinematische Beziehungen, Bilanzrelationen und konstitutive Annahmen. Während die kinematischen Zusammenhänge und die axiomatischen Überlegungen aus den Bilanzgleichungen in einem allgemeinen Kontext betrachtet werden können, sind in den konstitutiven Annahmen die speziellen Eigenschaften der in dieser Arbeit betrachteten Klasse von Anfangs-Randwertproblemen, mit z. B. quasistatischen und isothermen Bedingungen, und der betrachteten Klasse von Geomaterialien, wie z. B. lehmiger Schluff, enthalten. Basierend auf Arbeiten von *Ehlers* [53] und *Ehlers et al.* [62] wird ein Dreiphasenmodell präsentiert, das in der Lage ist, teilgesättigte Zustände in Böden abzubilden. Die hierfür nötigen Konstituierenden des Dreiphasenmaterials bestehen aus einem porösen, elastoplastischen (elastoviskoplastischen), inkompressiblen Festkörperskelett, einem viskosen, inkompressiblen Porenliquid (Wasser) und einem

viskosen, kompressiblen Porengas (Luft).

In **Kapitel 3** wird die Orts- und Zeitdiskretisierung der Gleichungen diskutiert, die aus den kontinuumsmechanischen Überlegungen des vorherigen Kapitels stammen. Im Rahmen dieser Arbeit werden dabei die Diskretisierungen im Ort und in der Zeit nacheinander und mit Hilfe von zwei unterschiedlichen Methoden durchgeführt. Für die Ortsdiskretisierung wird die Finite-Elemente-Methode gewählt, wohingegen die Zeitdiskretisierung mit einem finiten Differenzenschema, dem impliziten *Euler*-Verfahren, realisiert wird. Speziell bei der Diskussion der FEM wird auf die besondere Struktur des resultierenden Gleichungssystems für das betrachtete Dreiphasenmodell eingegangen. So muß etwa die Tatsache berücksichtigt werden, daß durch die numerische Umsetzung des zugrundeliegenden Modells eine sogenannte gemischte Formulierung entsteht, d. h. eine Formulierung resultiert, die nicht nur aus den Freiheitsgraden für die (Festkörper-)Verschiebung besteht, sondern die sich auch noch zusätzlich aus den Porendrücken der beiden Porenfluide Wasser und Luft zusammensetzt. Für diese unterschiedlichen Freiheitsgrade können keine beliebigen FE Ansatzfunktionen gewählt werden, da ansonsten instabile und somit unphysikalische Ergebnisse aus den numerischen Berechnungen resultieren. Es müssen vielmehr sogenannte *Taylor-Hood*-Elemente gewählt werden, die z. B. quadratische Ansatzfunktionen für die Verschiebungen und lineare Ansatzfunktionen für die Druckterme vorsehen, vgl. z. B. *Brezzi & Fortin* [35] oder *Braess* [34]. Das vollständig diskretisierte System liefert für das gewählte Materialmodell ein nichtlineares Gleichungssystem, das mit dem *Newton-Raphson*-Verfahren gelöst werden muß. Die Struktur und die detaillierte Beschreibung des Verfahrens wird in Abschnitt 3.3 ausführlich und mit Hinblick auf die in Kapitel 5 folgende Abhandlung der parallelen FEM diskutiert. Dabei wird insbesondere eine lokale, d. h. eine auf der Ebene eines finiten Elements definierte Assemblierungsschnittstelle vorgestellt, die auf eine Arbeit von *Wieners et al.* [151] zurückgeht und in der Diskussion über die Parallelisierungsstrategie ein zentrale Rolle spielt.

Kapitel 4 behandelt die Probleme und deren Lösungsmöglichkeiten, die mit entfestigendem Materialverhalten einhergehen, d. h. mit einem Materialverhalten zusammenhängen, das sich in einem Spannungs-Dehnungs-Diagramm nach Überschreiten der kritischen Dehnung und dem damit verbundenen Erreichen der Fließspannung durch eine sinkende Spannungsantwort bei einer weiterhin steigenden Verzerrung äußert. Die direkte Implementierung der in den beiden vorangegangenen Kapiteln diskutierten Gleichungen resultiert in Kombination mit diesem Materialverhalten in einem sogenannten netzabhängigen Verhalten, d. h. die numerische Lösung zeigt eine starke Abhängigkeit von der gewählten Ortsdiskretisierung mit finiten Elementen. So wirkt sich etwa eine stetige Verfeinerung des FE Netzes immer auf die Rechenergebnisse einer numerischen Simulation aus. Betrachtet man z. B. ein Anfangs-Randwertproblem, bei dem sich eine Zone mit konzentrierten plastischen Verzerrungen, d. h. ein Scherband, ausbildet, so zeigt die Dicke des Scherbands eine starke Abhängigkeit zum verwendeten FE Netz. Dieses unphysikalische Verhalten wird in Abschnitt 4.1 an einem einfachen 1-dimensionalen Beispiel veranschaulicht. Um diese Problematik zu umgehen, muß das aus mathematischer Sicht schlecht gestellte Problem mit Hilfe eines Regularisierungsverfahrens in ein gut gestelltes Problem überführt werden. Die in der Literatur vorhandenen Regularisierungsverfahren können in drei Hauptgruppen unterteilt werden, die in Abschnitt 4.2 im Sinne eines Überblicks

ausführlich diskutiert werden.

Ein sehr weit verbreitetes Verfahren, um das schlecht gestellte Problem zu regularisieren, besteht darin, ein ratenabhängiges (viskoses) Materialverhalten gezielt in der Modellierung der plastischen Materialantwort zu berücksichtigen, vgl. *Perzyna* [118]. Auf diese Weise werden in Abhängigkeit eines zusätzlichen Materialparameters, der Viskosität, sogenannte Überspannungen zugelassen, d. h. Spannungen erlaubt, die über der eigentlichen Fließspannung liegen. Somit kann über die Viskosität als charakteristischen Parameter des betrachteten Materials die Breite eines Scherbands unabhängig von dem zugrundeliegenden FE Netz definiert werden [113]. Eine weitere Regularisierungsmethode ist durch die mikropolare Theorie gegeben, die auf die Gebrüder *Cosserat* [38] zurückgeht und die eine physikalisch motivierte Erweiterung des bekannten *Boltzmann* Kontinuums darstellt. Die Grundidee dieser Theorie besteht darin, neben den translatorischen Freiheitsgraden eines materiellen Punkts zusätzlich noch dessen rotatorische Freiheitsgrade zu berücksichtigen. Dadurch müssen in der mikropolaren Theorie neben Verschiebungen auch noch Verdrehungen als Freiwerte in numerischen Simulationen ermittelt werden. Der regularisierende Einfluß der *Cosserat*-Theorie kann über eine sogenannte interne Länge gesteuert werden, die in der konstitutiven Beziehung zwischen den Momentenspannungen und den elastischen Krümmungen als Materialparameter beinhaltet ist [24]. Schließlich werden als dritte Hauptgruppe der Regularisierungsverfahren nichtlokale Modelle diskutiert, die für die punktweise Ermittlung bestimmter Größen die Umgebung des jeweiligen Punkts mit berücksichtigen. So werden etwa die plastischen Verzerrungen, die innerhalb der FEM an den Integrationspunkten der numerischen Quadratur ermittelt werden, in ihrer nichtlokalen Darstellung unter Berücksichtigung der Werte der plastischen Verzerrungen an den umliegenden Integrationspunkten berechnet. Die Größe der zu betrachtenden Umgebung ist dabei, ähnlich zu der mikropolaren Theorie, durch eine interne Länge definiert. Für die Berücksichtigung der Umgebung findet man in der Literatur zwei unterschiedliche Strategien. Es existieren zum einen Ansätze, die für die punktweise Berechnung von Gradienten die Umgebung um diesen Punkt benötigen. Des weiteren findet man Arbeiten, die eine nichtlokale Größe an einem Punkt durch die Auswertung eines Integrals über ein begrenztes Gebiet um diesen Punkt ermitteln. Die Äquivalenz der beiden, auf den ersten Blick unterschiedlichen Ansätze wurde von *Mühlhaus & Aifantis* [110] hergestellt, indem sie eine integralbasierte in eine gradientenbasierte Formulierung überführten.

Abschließend werden in Abschnitt 4.6 anhand von zwei numerischen Beispielen die Leistungsfähigkeit und das Verhalten von insgesamt drei Regularisierungstechniken eingehend untersucht und diskutiert. Dabei wird je ein Vertreter aus den oben erläuterten drei Hauptgruppen gewählt: ein viskoplastischer, ein mikropolarer und ein integralbasierter nichtlokaler Ansatz.

Um große Anfangs-Randwertprobleme im Rahmen der FEM rechnen zu können, ist es, wie oben bereits erwähnt, zwingend notwendig, daß parallele Lösungsstrategien eingesetzt werden. Aus diesem Grund wird in **Kapitel 5** die Parallelisierung von FE Berechnungen ausführlich diskutiert. Nach einiger generellen Bemerkungen zur parallelen FEM, werden dabei in Abschnitt 5.2 die grundlegenden Ideen zur Parallelisierung des bislang nur sequentiell lauffähigen FE Programms PANDAS (Porous media Adaptive Nonlinear finite element solver based on Differential Algebraic Systems) [58, 117] vorgestellt. Dieses Programm

wurde am Institut für Mechanik (Bauwesen), Lehrstuhl 2, der Universität Stuttgart entwickelt und eignet sich in besonderer Weise, geometrisch oder materiell nichtlineare Mehrphasenprobleme numerisch umzusetzen. Durch die Kopplung von PANDAS mit einem FE Programm, das sowohl über parallele Datenstrukturen als auch über effiziente parallele lineare Löser verfügt, ist es gelungen, parallele Rechnungen basierend auf den in PANDAS implementierten Materialmodellen durchzuführen und somit das Spektrum der mit PANDAS numerisch realisierbaren Anfangs-Randwertprobleme enorm zu vergrößern. Das parallel lauffähige Programm M++ (Meshes, Multigrid and more), mit dem diese Kopplung realisiert wurde, geht auf *Wieners* [147] zurück und wurde dabei so konzipiert, daß die Kopplung mit PANDAS auf Basis der in Kapitel 3 beschriebenen lokalen Assemblierungsschnittstelle umgesetzt werden konnte. So sind etwa für den Aufbau des linearen Gleichungssystems innerhalb des *Newton-Raphson*-Verfahrens in M++ insgesamt drei Funktionen notwendig, um die hierfür erforderlichen Informationen von PANDAS zu erhalten. Eine Funktion liefert die *Dirichlet*-Randbedingungen des Anfangs-Randwertproblems, die zweite Funktion ermittelt das Residuum zusammen mit den *Neumann*-Randbedingungen und schließlich wird mit der dritten Funktion die algorithmisch konsistente Tangente berechnet. Dabei wird jede der drei Funktionen für jedes finite Element des FE Netzes aufgerufen. So wird etwa für die Ermittlung der *Dirichlet*-Randbedingungen in M++ eine Schleife über alle Elemente des FE Netzes durchgeführt, und die darin elementweise ermittelten Informationen in das globale Gleichungssystem assembliert.

Das besondere an der gewählten Vorgehensweise ist einerseits, daß durch diese Art der Parallelisierung in PANDAS keinerlei Änderungen mit Hinblick auf die Parallelisierung durchgeführt werden mußten. Des weitern ist diese Strategie natürlich nicht auf die Parallelisierung von PANDAS beschränkt, sondern kann auf weitere sequentiell implementierte FE Programme angewandt werden.

Neben der Schnittstelle M++/PANDAS werden in Abschnitt 5.2 zusätzlich noch die M++ zugrunde liegende parallele Datenstruktur, die sogenannten „Distributed Point Objects" (DPO), und die einzelnen Schritte bei dem parallelen Lösen eines linearen Gleichungssystems ausführlich erläutert.

In **Kapitel 6** wird schließlich anhand von drei numerischen Beispielen die Anwendbarkeit und Effizienz der in dieser Arbeit erläuterten theoretischen Ausführungen aufgezeigt. Dabei wird basierend auf einer Arbeit von *Ehlers et al.* [60] in einer 2-dimensionalen sequentiellen Simulation eines Biaxial-Versuchs das Entstehen von dilatanten und kontraktanten Scherbändern in einem mikropolaren Material diskutiert. Des weitern wird anhand von zwei 3-dimensionalen Anfangs-Randwertproblemen die Effizienz der Schnittstelle M++/PANDAS demonstriert. Diese beiden Beispiele gehen auf Arbeiten von *Ehlers et al.* [62] und *Wieners et al.* [153] zurück und behandeln Versagenszustände von Böschungen, wie sie z. B. durch ansteigende Grundwasserspiegel oder starke Regenfälle verursacht werden.

Contents

Chapter 1: Introduction and overview

1.1   Motivation

In many branches of engineering, one often has to deal with problems, in which it is inevitable to consider the multiphasic character of the underlying material for a proper modeling. For example, within a civil engineering context, one may be interested in the description of a failure mechanism of a natural slope, which is caused by an extreme rainfall event, cf. Figure 1.1. Furthermore, the interest may be directed towards the investigation of the deformation of foamed shock absorbers or automotive seat cushions as well as towards biomechanical problems like the investigation of bones, cartilage or intervertebral disks. In such cases, the characteristic behavior of the respective problem under study is governed by the simultaneous action of different effects coming from the single phases of the multiphasic material. In the above mentioned investigation of a slope failure problem, the necessary phases for a proper modeling are defined by a solid skeleton and two fluid phases representing air and water, namely, a materially compressible gaseous and a materially incompressible liquid phase. By this choice, partially saturated soil conditions can be adequately described, including the possibility to model the driving force, which actually leads to the failure mechanism, i. e., the possibility to describe a rainfall event due to a boundary condition corresponding to the liquid phase.

Figure 1.1: Slope failure initiated by an extreme rainfall event
(www.dot.ca.gov/hq/esc/geotech/photos/north/north.htm).

As a result of the rapid development in computer technologies in the last years, the numerical simulations of engineering problems, like, e. g., the above described multiphasic problems, become more and more interesting. However, at the same time, the requirements towards the complexity of the problems rapidly increase. For example, the numerical description of the slope failure problem shown in Figure 1.1 can be carried out

on different accuracy levels. Starting from a 2-dimensional modeling with a rather simple mechanical model, almost no limits are given for an expansion of the complexity and, thus, an increase of the accuracy of the numerical simulation. In order to model the given geometry of the slope and the failure mechanism more accurately, e. g., a 3-dimensional discretization of the slope under study has to be carried out, where the zones, in which the failure occurs, have to be discretized on a rather fine level in order to exactly describe the high gradients in the field functions coming from the failure of the slope. By furthermore expanding the mechanical model to the class of multiphasic material models mentioned above, many effects of the realistic problem are numerically represented but also the complexity of the numerical problem is significantly increased. Obviously, the rapid increase on the requirements of the quality of numerical simulations is not only restricted to geotechnical problems. Thinking about crash test simulations of the automotive industry, the accuracy, by which a car is numerically modeled, also strongly influences the quality of the solution. Nowadays, in order to improve the agreement with the expensive crash test experiments, the discretization of a car for the numerical simulation of such crash tests even includes a detailed description of, e. g., the frontal bumper including its foamed (multiphasic), shock absorbing inlay. Expanding this to many other small elements within a car, the discretization of a whole car leads to a very high number of degrees of freedom and, thus, to an enormous numerical effort, which can also be increased arbitrarily due to the demand for improved numerical simulations.

Following this, the rapid development of the semiconductor industry cannot satisfy all these requirements alone. In addition, new results and improvements coming from the research of numerical strategies have to be taken into account. Very important developments in this context are adaptive and parallel strategies as well as the improvements of efficient linear solvers. Therein, adaptive methods automatically adapt the spatial and/or temporal discretizations with respect to the requirements of the problem under study and, therefore, they can significantly improve the efficiency of a numerical solution procedure. However, only applying adaptive strategies, the overall size of a problem is restricted by the system memory and the processing speed of a single computer. A straightforward solution of this drawback is to simultaneously use more than one computer for the solution procedure, which directly leads to the term "parallel computing". Finally, within each nonlinear code, the solution for the respective linear systems occurring in the *Newton-Raphson* method is the most time-consuming step. Apart from rather new strategies, like, e. g., the multigrid methods, which strongly improve the efficiency of solving a linear system compared to the standard solution methods for linear systems, the parallel approach is also a promising strategy for this problem. By decomposing the overall problem into many subproblems, the solutions for the small linear systems of these subproblems can be determined in parallel on those different computers, where the respective subproblems are defined.

1.2   Scope, aims and state of the art

It is the aim of this contribution to describe the whole procedure of the numerical simulation of localization phenomena. Starting from the continuum mechanical modeling, the spatial and temporal discretization by the finite element (FE) method and a proper time integration method are discussed in detail. Furthermore, the numerical problems coming along with softening material behavior are illustrated and methods to solve these problems are shown. Finally, an efficient numerical realization of the proposed mechanical models is presented based on parallel solution strategies.

Within this thesis, the numerical simulation of localization phenomena is going to be exemplarily illustrated using the example of multiphasic materials, whose continuum mechanical description is based on the well-founded Theory of Porous Media (TPM). The TPM in its current understanding is based on the publications by *Bowen* [32, 33] and was improved and developed continuously in the last years by *de Boer & Ehlers* [21] and *Ehlers* [48, 49, 51, 53]. An excellent survey of the historical development of the Theory of Porous Media is given in the book of *de Boer* [20]. By choosing the TPM as the continuum mechanical basis, volumetrically coupled multifield problems are obtained, which cannot be uniquely classified within the well-known disciplines of either solid or fluid mechanics. Furthermore, the problems under study in this thesis are mostly related to geotechnical problems, like, e. g., biaxial experiments or slope failure problems, and, therefore, the observed materials are soils, which are modeled by a solid and a fluid phase. Therein, the description of the solid skeleton is carried out within a geometrically linear approach and the solid skeleton is assumed to behave as a porous, incompressible and elasto-plastic material. In addition, the fluid phase is subdivided into a viscous, materially incompressible pore-liquid and a viscous, materially compressible pore-gas. To be more precise, a biphasic and a triphasic model are presented for the continuum mechanical description of soils, whereby in the biphasic model, the materially compressible gaseous phase is omitted. Both the biphasic and the triphasic models presented in this thesis are taken from the literature. Important publications dealing with the biphasic model and its numerical realization are given, e. g., by *Diebels et al.* [44] or *Ehlers & Ellsiepen* [59]. The triphasic model is intensively discussed in the works by *Ehlers* [53], *Blome* [18] or *Ehlers et al.* [62].

The discussion of the spatial and temporal discretization of the underlying porous media models is mainly based on the works by *Ellsiepen* [66], *Ehlers & Ellsiepen* [59] and *Wieners et al.* [151, 152]. Therein, the numerical difficulties within the spatial discretization by the finite element method coming from the multiphasic character of the considered models are discussed in detail.

The main focus of this thesis is put on the discussions of the numerical problems coming along with the FE simulations of localization phenomena. Therein, a major problem is given by the proper numerical description of the softening material behavior, which occurs within such failure mechanisms. Generally speaking, localization phenomena are characterized by concentrations of plastic strains within narrow zones. As a consequence of these localizations, softening material behavior is obtained, which leads to a change of type of the underlying partial differential equations resulting from the numerical realization of the respective continuum mechanical model. In order to solve the numerical problem in

such cases, additional methods, so-called regularization techniques, have to be applied, which preserve the well-posedness of the respective problem under study. Therefore, in this thesis, three different regularization techniques are implemented in the FE code PANDAS (Porous media Adaptive Nonlinear finite element solver based on Differential Algebraic Systems) and compared with each other considering their effect on the shear band development.

The above mentioned regularization techniques are a viscoplastic ansatz, a micropolar continuum theory and a non-local model and are taken from the literature. In case of the viscoplastic ansatz, the main publication concerning the theoretical background is given by *Perzyna* [118]. The suitability of this ansatz as a regularization method is proved by *Needleman* [113], and this fact is confirmed by many researchers, who applied the viscoplastic ansatz within their numerical simulations, cf., e. g., [44, 121, 146]. The micropolar theory dates back to the work by *Cosserat & Cosserat* [38], who established the theoretical basis of this theory. The regularizing effect of this theory within the numerical simulation of strain-softening problems was discovered almost 20 years ago, thus leading to many publications with emphasis on this topic, cf., e. g., *Mühlhaus & Vardoulakis* [111], *de Borst* [24, 25, 26], *Steinmann & Willam* [133], *Ehlers & Volk* [64] or *Ehlers et al.* [60]. Finally, the first ideas of non-local formulations in the context of elasticity models date back to the works by *Kröner* [97] and *Eringen & Edelen* [70]. The first application of a non-local ansatz as a regularization technique for strain-softening problems is published by *Belytschko et al.* [10]. An excellent overview on different non-local models is given by *Jirásek* [95]. In this work, for a clear classification of the different models, the single approaches are divided into integral- and gradient-type models. Within this classification, the non-local model presented in this thesis is an integral-type model, which is mainly taken from *Brinkgreve* [36] and *Schanz* [123].

Due to the enormous computational expense of the numerical simulations of realistic problems based on advanced continuum mechanical models, the efficiency of the numerical realization is increased within this thesis by the application of parallel solution strategies. Therein, based on the works by *Wieners* [150] and *Wieners et al.* [152, 153], a novel strategy is presented for the parallelization of sequential FE programs. To be more precise, an interface is implemented and illustrated in detail, which couples the existing sequential FE code PANDAS with the solver M++ (Meshes, Multigrid and more), which contains parallel data structures and efficient parallel linear solvers.

1.3   Outline of the thesis

The thesis is divided into five main chapters with the respective topic and its state of the art being discussed in detail at the beginning of each chapter.

In **Chapter 2**, the continuum mechanical models are presented, which serve as the basis for the later numerical investigations. As usual, the set of governing equations is subdivided into kinematical equations, balance relations and constitutive assumptions, whereby the multiphasic character of the underlying material has to be considered in each part. Especially within the part concerning the constitutive relations, the assumptions for the

proper modeling of the considered geotechnical problems are motivated in detail.

Chapter 3 is concentrated on the spatial and temporal discretization of the equations coming from the continuum mechanical considerations of the previous chapter. Again, the correct treatment of the underlying equations, which have a special structure due to the application of the TPM, is emphasized. Starting with the transformation of the strong into the weak formulations, the finite element method together with the single steps within the nonlinear solution procedure are discussed in detail. In addition, a standard time integration method, namely the implicit *Euler* method, is introduced for the proper temporal discretization.

The problems related to the numerical simulation of softening material behavior together with the possible solution strategies for these problems are explicitly pointed out in **Chapter 4**. First, the ill-posed behavior of the standard numerical realization procedure is demonstrated at a simple 1-dimensional example. After this, a comprehensive overview of existing regularization techniques is presented, whereby three different regularization methods, namely a viscoplastic ansatz, a micropolar continuum theory and a non-local model, are discussed in detail with respect to their theoretical aspects and their numerical realization. The effects of the single approaches are shown at the example of a tensile bar, which is described both in one and in two dimensions.

In order to complete the discussions on the numerical realization, in **Chapter 5**, parallel solution strategies are presented. After some general remarks on parallel computing, the special character of the interface between the two programs PANDAS and M++ is explained, where, again, the particular structures of the equations coming from the multiphasic modeling have to be considered. In addition, the underlying parallel data structure of M++, the so-called Distributed Point Objects, is presented together with its effect on the parallel solution strategy.

In **Chapter 6**, it is shown that, when using the presented theoretical and numerical methods for the solution of typical geotechnical questions, the numerical simulations of large scale problems can be efficiently carried out. In particular, at the example of a 2-dimensional biaxial experiment, the developments of both dilatant and contractant shear bands within a micropolar continuum are shown. Furthermore, the efficiency of the interface M++/PANDAS is demonstrated by two 3-dimensional initial boundary-value problems, both dealing with failure mechanisms of natural slopes.

Finally, **Chapter 7** gives the summary of the thesis and presents an outlook on possible further developments based on this work.

Chapter 2:
Porous media models in soil mechanics

Geomaterials such as soil, sand stone, rock and rock salt consist of a porous solid skeleton matrix, whose pores are saturated with one or more pore-fluids. In order to describe the behavior of these materials, their multiphasic character has to be considered. Because the exact structure of the pores usually is not known, one has to proceed from homogenization methods, where the real microstructure is statistically smeared out through the considered domain on the basis of a real or virtual averaging process. One possibility to model such materials in the context of a macroscopic approach is given by the Theory of Porous Media (TPM), which is based on the classical Theory of Mixtures including superimposed continua. By introducing the volume fractions as scalar structural variables, the microscopic volumetric composition of the overall material can be incorporated for a proper macroscopic modeling process.

Looking at the historical evolution of the TPM and the included theories, the first considerations about the Concept of Volume Fractions date back to the 18th and 19th centuries, whereas these ideas were applied to geotechnical problems in the last century by *Biot* [16] and *Heinrich & Desoyer* [86, 87, 88]. The origins of the Theory of Mixtures trace back to the work of *Truesdell & Toupin* [143], *Bowen* [31] and *Truesdell* [142]. The TPM in its current understanding is based on the publications by *Bowen* [32, 33] and was improved and developed continuously in the last years by *de Boer & Ehlers* [21] and *Ehlers* [48, 49, 51, 53]. An excellent survey of the historical development of the Theory of Porous Media is given in the book of *de Boer* [20].

Obviously, the range of applications of the TPM is not limited to geotechnical problems. One can directly apply the concepts of the TPM to other fields, in which the porous structure of the considered materials has also to be taken into account for a suitable modeling. Possible further applications in this context are for example problems from mechanical engineering or biomechanics, cf. *Ehlers et al.* [57, 63].

Within this chapter, the governing equations of two porous media models, which are used as a basis for the numerical studies in this thesis, are introduced briefly. On the one hand, this will be a rather simple biphasic model, by which fully saturated soils can be described, and on the other hand, a more sophisticated triphasic model will be introduced, by which it is possible to model partially saturated conditions in soils.

2.1   Kinematical relations

2.1.1   Mixture and Concept of Volume Fractions

Within the Theory of Mixtures, a multiphasic aggregate (mixture) φ is defined via a combination of its components (constituents) φ^α:

$$\varphi = \bigcup_\alpha \varphi^\alpha \,. \tag{2.1}$$

Therein, $\alpha = 1, \ldots, k$ is an index defining the k constituents. In the framework of this thesis, α can take the following values: S (solid), F (fluid), L (liquid) and G (gas).

PSfrag replacements
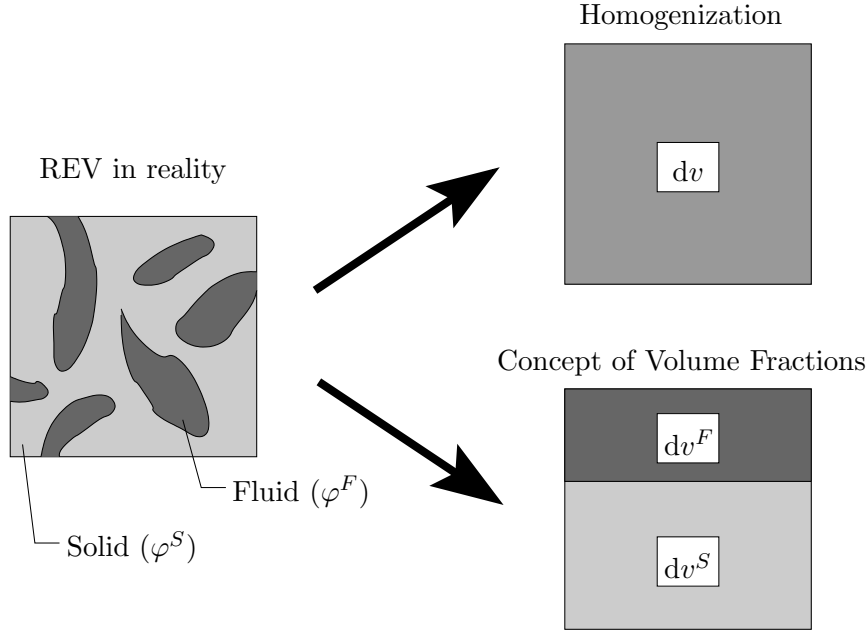
Figure 2.1: Homogenization and Concept of Volume Fractions.

All considerations concerning the behavior of the viewed material are based on a Representative Elementary Volume (REV), cf. Figure 2.1. In this context, one proceeds from the assumption that the constituents φ^α of a mixture φ are smeared out over the whole REV. Consequently, each spatial point $\mathbf{x}$ is occupied at the time t by parts of all constituents φ^α (superimposed continua) and each constituent follows its own motion function $\boldsymbol{\chi}_\alpha$. As a result of the homogenization process, the mathematical functions for the description of the geometrical and physical quantities are field functions defined over the whole mixture.

Remark: In the framework of this thesis, all necessary field quantities are assumed to be already given from proper averaging or homogenization techniques forming the local averages of the respective microscopic informations. The reader who is interested in more information on this topic is referred to the work by *Hassanizadeh & Gray* [85], *de Boer et al.* [22], *Miehe et al.* [105] and *Schröder* [126]. □

As the Theory of Mixtures does not provide a description of the inner structure of the considered multiphasic body $\mathcal{B}$, the volume fractions n^α are introduced as statistically averaged scalar variables. By doing this, one can, for example, define the fraction of the pore space in a fluid saturated solid, cf. Figure 2.1. Usually, the volume fractions n^α are

introduced via the partial volume V^α of the constituent α:

$$V^\alpha = \int_{\mathcal{B}} n^\alpha \, \mathrm{d}v \,. \tag{2.2}$$

The volume V of the whole multiphasic body $\mathcal{B}$ corresponds to the sum of the partial volumes of all constituents φ^α:

$$V = \int_{\mathcal{B}} \mathrm{d}v = \sum_{\alpha=1}^{k} V^\alpha = \sum_{\alpha=1}^{k} \int_{\mathcal{B}} n^\alpha \, \mathrm{d}v = \int_{\mathcal{B}} \sum_{\alpha=1}^{k} n^\alpha \, \mathrm{d}v = \int_{\mathcal{B}} \sum_{\alpha=1}^{k} \mathrm{d}v^\alpha \,. \tag{2.3}$$

From the above equation, it follows that n^α is defined as the ratio of the volume element $\mathrm{d}v^\alpha$ of a constituent φ^α with respect to the volume element $\mathrm{d}v$ of the mixture φ:

$$n^\alpha = \frac{\mathrm{d}v^\alpha}{\mathrm{d}v} \,. \tag{2.4}$$

Furthermore, as a result of Equation (2.3), the regarded mixture is saturated and contains no vacant space, which leads to the so-called saturation condition:

$$\sum_{\alpha=1}^{k} n^\alpha = 1 \,. \tag{2.5}$$

An analogous relation to (2.4) can be found for the incremental surface elements $\mathrm{d}a$ of the mixture φ and $\mathrm{d}a^\alpha$ for the constituent φ^α:

$$\mathrm{d}a^\alpha = n^\alpha \mathrm{d}a \,. \tag{2.6}$$

Assuming superimposed continua, one finds also

$$\begin{aligned} \mathrm{d}\mathbf{a}^\alpha &= \mathbf{n} \, \mathrm{d}a^\alpha \,, \\ \mathrm{d}\mathbf{a} &= \mathbf{n} \, \mathrm{d}a \,, \end{aligned} \tag{2.7}$$

with the outward oriented unit surface normal $\mathbf{n}$.

The Concept of Volume Fractions as defined in Equations (2.3) and (2.4) leads to two different density functions for a constituent φ^α:

$$\rho^{\alpha R} = \frac{\mathrm{d}m^\alpha}{\mathrm{d}v^\alpha} \,, \qquad \rho^\alpha = \frac{\mathrm{d}m^\alpha}{\mathrm{d}v} \,. \tag{2.8}$$

The material (realistic or effective) density $\rho^{\alpha R}$ represents the ratio of the local mass $\mathrm{d}m^\alpha$ to the local volume element $\mathrm{d}v^\alpha$, whereas the partial (global or bulk) density ρ^α represents the ratio of the local mass $\mathrm{d}m^\alpha$ to the volume element $\mathrm{d}v$.

When using Equations (2.4) and (2.8), the following relation between the two density functions can be established:

$$\rho^\alpha = n^\alpha \, \rho^{\alpha R} \,. \tag{2.9}$$

Corresponding to this, it is obvious that changes in the partial density can take place via a change in the volume fraction as well as via a change in the material density, which is an interesting fact in case of material incompressibility of a constituent ($\rho^{\alpha R} = $ const.). In such a case, Equation (2.9) shows that material incompressibility does not necessarily lead to bulk incompressibility, since the partial density ρ^α can still change due to a change in the volume fractions n^α.

The overall density ρ of the multiphasic body results from a sum of the partial densities ρ^α over all constituents φ^α:

$$\rho = \sum_{\alpha=1}^{k} \rho^\alpha = \sum_{\alpha=1}^{k} n^\alpha \rho^{\alpha R} \,. \tag{2.10}$$

Within the framework of this thesis, a biphasic and a triphasic model will be discussed. The biphasic model consists of a deformable, materially incompressible solid skeleton and a materially incompressible pore-fluid (*Diebels et al.* [44], *Ehlers & Ellsiepen* [59]), whereas in the case of the triphasic model, the overall fluid phase is split into a materially incompressible liquid phase and a materially compressible gaseous phase (*Ehlers* [53], *Blome* [18], *Ehlers et al.* [62]). For a suitable description of the triphasic model, the so-called saturation functions s^β have to be introduced for both the liquid constituent ($\beta = L$) and the gaseous constituent ($\beta = G$):

$$s^\beta = \frac{n^\beta}{n^F}\,, \qquad \text{where} \quad n^F = n^L + n^G \,. \tag{2.11}$$

From the above equation, it is evident that the saturation constraint

$$s^L + s^G = 1 \tag{2.12}$$

holds for the saturation functions s^β. Furthermore, one can recognize that (2.12) relates the saturation condition to the pore content, whereas (2.5) relates it to the overall medium.

2.1.2 Motion function

In the Theory of Porous Media, a multiphasic body $\mathcal{B}$ is defined as a coherent set of the material points X^α, whereas the set of all material points on the surface of $\mathcal{B}$ is called $\partial\mathcal{B}$. In order to describe the motion function of a constituent φ^α within the proper *Euclid*ian vector space $\mathcal{V}^3$, a fixed origin $\mathcal{O}$ and the reference position $\mathbf{X}_\alpha$ of the constituent has to be defined, cf. Figure 2.2. By doing this, the motion function of a constituent φ^α can be introduced via the following relation:

$$\mathbf{x} = \boldsymbol{\chi}_\alpha(\mathbf{X}_\alpha, t)\,. \tag{2.13}$$

From Equation (2.13) and Figure 2.2, the consequence of the assumption of superimposed continua can be recognized. Each spatial point $\mathbf{x}$ at time t is only occupied by one single material point X^α of each constituent φ^α. The independent motion functions $\boldsymbol{\chi}_\alpha(\mathbf{X}_\alpha, t)$

Current (actual) configuration (t)

PSfrag replacements

Reference configuration (t_0)
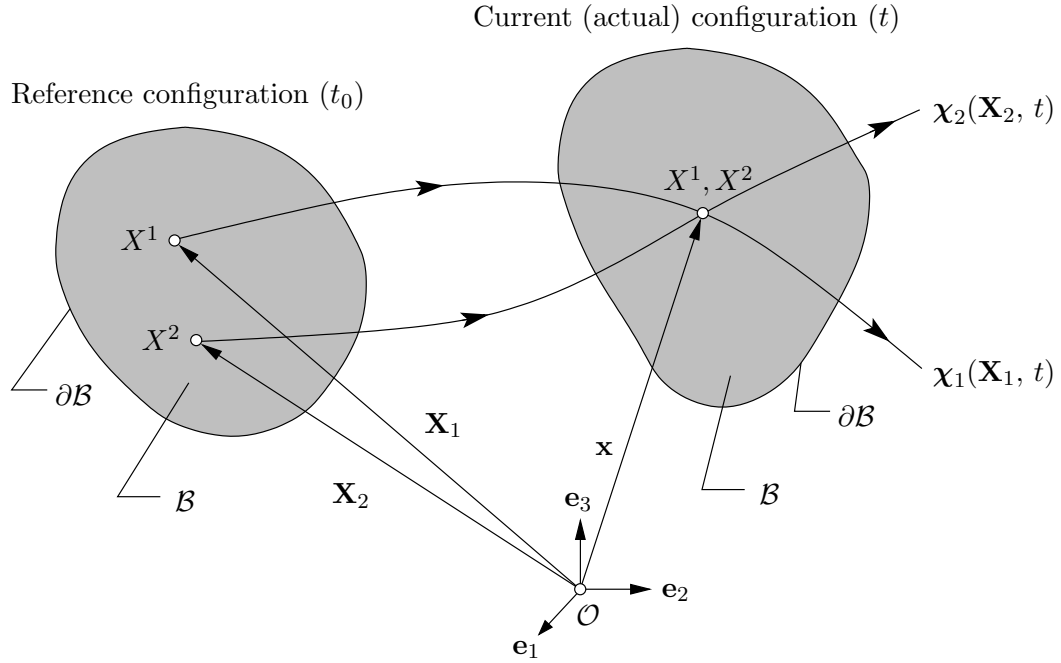
Figure 2.2: Motion of a biphasic mixture.

indicate that the same material points X^α at the position $\mathbf{x}$ originate from different referential positions $\mathbf{X}_\alpha$ at time $t = t_0$.

The requirement of a unique motion function causes the existence of a unique inverse motion function

$$\mathbf{X}_\alpha = \boldsymbol{\chi}_\alpha^{-1}(\mathbf{x},\,t)\,, \tag{2.14}$$

which is based on a non-singular *Jacobi*an determinant J_α:

$$J_\alpha = \det \frac{\partial \boldsymbol{\chi}_\alpha}{\partial \mathbf{X}_\alpha} \neq 0\,. \tag{2.15}$$

Remark: (2.13) and (2.14) show the two different possibilities to express geometrical and physical quantities within a continuum mechanical model. If a quantity is expressed with regard to the reference configuration, cf. (2.13), it is specified by the *Lagrange*an (or material) description, whereas, if a quantity is expressed with regard to the current configuration, cf. (2.14), it is specified by the *Euler*ian (or spatial) description. □

Since each constituent defines its own motion function, they consequently both have their own velocity field. The velocity of a material point X^α is defined via the material time derivate of the motion function $\boldsymbol{\chi}_\alpha$:

$$\overset{'}{\mathbf{x}}_\alpha = \frac{\mathrm{d}}{\mathrm{d}t}\,\boldsymbol{\chi}_\alpha(\mathbf{X}_\alpha,\,t)\,. \tag{2.16}$$

Using the inverse motion function (2.14), the *Euler*ian representation of the velocity field results in

$$\overset{'}{\mathbf{x}}_\alpha = \overset{'}{\mathbf{x}}_\alpha\,[\boldsymbol{\chi}_\alpha^{-1}(\mathbf{x},\,t),\,t] = \overset{'}{\mathbf{x}}_\alpha\,(\mathbf{x},\,t)\,. \tag{2.17}$$

Analogously, the acceleration field is defined via the material time derivative of the velocity field:

$$\overset{''}{\mathbf{x}}_\alpha = \frac{\mathrm{d}}{\mathrm{d}t}\,\overset{'}{\mathbf{x}}_\alpha\,(\mathbf{X}_\alpha,\,t) \qquad \text{or} \qquad \overset{''}{\mathbf{x}}_\alpha = \overset{''}{\mathbf{x}}_\alpha\,[\boldsymbol{\chi}_\alpha^{-1}(\mathbf{x},\,t),\,t] = \overset{''}{\mathbf{x}}_\alpha\,(\mathbf{x},\,t)\,. \tag{2.18}$$

The so-called mixture velocity

$$\dot{\mathbf{x}} = \frac{1}{\rho}\sum_{\alpha=1}^{k}\rho^\alpha\,\overset{'}{\mathbf{x}}_\alpha \tag{2.19}$$

indicates the barycentric velocity of φ, and the diffusion velocity

$$\mathbf{d}_\alpha = \overset{'}{\mathbf{x}}_\alpha - \dot{\mathbf{x}} \tag{2.20}$$

defines the relative velocity of a constituent φ^α with respect to the mixture velocity.

The definitions of the velocities $\overset{'}{\mathbf{x}}_\alpha$ and $\dot{\mathbf{x}}$ lead to the introduction of the so-called material time derivative. If Γ is an arbitrary, continuous and sufficiently often continuously differentiable scalar function of $(\mathbf{x},\,t)$, the material time derivative of Γ following the motion of φ^α is given by

$$(\Gamma)'_\alpha = \frac{\mathrm{d}_\alpha}{\mathrm{d}t}\,\Gamma = \frac{\partial\Gamma}{\partial t} + \operatorname{grad}\Gamma\cdot\overset{'}{\mathbf{x}}_\alpha\ . \tag{2.21}$$

Therein, the operator "$\operatorname{grad}(\,\cdot\,)$" denotes the partial derivative of $(\,\cdot\,)$ with respect to the actual position $\mathbf{x}$. For a vector-valued field function $\boldsymbol{\Gamma}(\mathbf{x},\,t)$, the material time derivative reads

$$(\boldsymbol{\Gamma})'_\alpha = \frac{\mathrm{d}_\alpha}{\mathrm{d}t}\,\boldsymbol{\Gamma} = \frac{\partial\boldsymbol{\Gamma}}{\partial t} + (\operatorname{grad}\boldsymbol{\Gamma})\,\overset{'}{\mathbf{x}}_\alpha\ . \tag{2.22}$$

Describing coupled solid-fluid problems, one usually starts from a *Lagrange*an description of the solid matrix by introducing the solid displacement vector $\mathbf{u}_S$ as the primary kinematic variable, whereas the pore-fluids are specified in a modified *Euler*ian setting by use of the seepage velocities $\mathbf{w}_\beta$ describing the fluid motions with respect to the deforming solid skeleton:

$$\mathbf{u}_S = \mathbf{x} - \mathbf{X}_S\,, \qquad \mathbf{w}_\beta = \overset{'}{\mathbf{x}}_\beta - \overset{'}{\mathbf{x}}_S\ . \tag{2.23}$$

From (2.13) and (2.14), one obtains the material deformation gradient $\mathbf{F}_\alpha$ and its inverse $(\mathbf{F}_\alpha)^{-1}$,

$$\mathbf{F}_\alpha = \frac{\partial\boldsymbol{\chi}_\alpha(\mathbf{X}_\alpha,\,t)}{\partial\mathbf{X}_\alpha} = \operatorname{Grad}_\alpha\mathbf{x}\,, \qquad (\mathbf{F}_\alpha)^{-1} = \frac{\partial\boldsymbol{\chi}_\alpha^{-1}(\mathbf{x},\,t)}{\partial\mathbf{x}} = \operatorname{grad}\mathbf{X}_\alpha\,, \tag{2.24}$$

with the operator "$\operatorname{Grad}_\alpha(\,\cdot\,)$" defining the partial derivative of $(\,\cdot\,)$ with respect to the reference position $\mathbf{X}_\alpha$. The inverse material deformation gradient exists, if the constraint (2.15) for the *Jacobi*an determinant holds. Furthermore, the range of $J_\alpha = \det\mathbf{F}_\alpha$ is limited to positive values, as the relation $\det\mathbf{F}_\alpha(t_0) = 1$ is valid.

Using the material deformation gradient $\mathbf{F}_\alpha$, differential line $\mathrm{d}\mathbf{X}_\alpha$, area $\mathrm{d}\mathbf{A}_\alpha$ and volume $\mathrm{d}V_\alpha$ elements of the reference configuration can be mapped to the respective quantities $\mathrm{d}\mathbf{x}$, $\mathrm{d}\mathbf{a}$ and $\mathrm{d}v$ of the actual configuration and vice versa. As the transport mechanism of

differential line elements is given by the definition of the material deformation gradient $(2.24)_1$ itself, the other transport theorems can be derived by using $\mathbf{F}_\alpha$, cf. *de Boer* [19]:

$$
\begin{aligned}
\mathrm{d}\mathbf{x} &= \mathbf{F}_\alpha\,\mathrm{d}\mathbf{X}_\alpha\,, \\
\mathrm{d}\mathbf{a} &= (\det \mathbf{F}_\alpha)\,\mathbf{F}_\alpha^{T-1}\,\mathrm{d}\mathbf{A}_\alpha\,, \\
\mathrm{d}v &= (\det \mathbf{F}_\alpha)\,\mathrm{d}V_\alpha\,.
\end{aligned}
\tag{2.25}
$$

Remark: Note that the material deformation gradient is a so-called two-field tensor, where, in the framework of a natural basis system, one basis system is located in the reference configuration and the other one in the current configuration. With this property, it is possible to transport geometrical and physical quantities from the reference to the actual configuration and vice versa. Very often, these transport mechanisms are called push-forward (reference to current configuration) and pull-back (current to reference configuration) operations. Within a natural basis system, even a further specification of the transport characteristics can be found. Therein, one recognizes immediately that one also has to differentiate between covariant or contravariant push-forward or pull-back operations. The reader who is interested in more information on this topic is referred to *de Boer* [19] or *Ehlers* [48]. □

2.1.3 Deformation and strain measures

After introducing the material deformation gradient, the deformation and strain measures can be defined in a next step. Within a continuum mechanical framework, a deformation measure defines how a body is deformed locally during the motion, whereas a strain measure compares the deformed state with the undeformed state of a body. Following this, starting from the reference configuration (undeformed state), a deformation measure is initially the identity tensor $\mathbf{I}$ and a strain measure is the zero tensor $\mathbf{0}$ at the beginning.

For the derivation of the deformation measures, it is helpful to apply the polar decomposition theorem to the material deformation gradient:

$$
\mathbf{F}_\alpha = \mathbf{R}_\alpha\,\mathbf{U}_\alpha = \mathbf{V}_\alpha\,\mathbf{R}_\alpha\,.
\tag{2.26}
$$

In this way, one obtains a unique decomposition of $\mathbf{F}_\alpha$ into a proper orthogonal rotation tensor $\mathbf{R}_\alpha$ and either a symmetric and positive definite right or left stretch tensor $\mathbf{U}_\alpha$ and $\mathbf{V}_\alpha$. Thus, a line element $\mathrm{d}\mathbf{x}$ of the actual configuration can be represented by a stretch of the referential line element $\mathrm{d}\mathbf{X}_\alpha$ with $\mathbf{U}_\alpha$ followed by a rotation through $\mathbf{R}_\alpha$ or, alternatively, by a rotation with $\mathbf{R}_\alpha$ followed by a stretch through $\mathbf{V}_\alpha$:

$$
\mathrm{d}\mathbf{x} = \mathbf{R}_\alpha\,(\mathbf{U}_\alpha\,\mathrm{d}\mathbf{X}_\alpha) = \mathbf{V}_\alpha\,(\mathbf{R}_\alpha\,\mathrm{d}\mathbf{X}_\alpha)\,.
\tag{2.27}
$$

Looking at the length variation of the line elements during the motion, either with respect to the reference configuration,

$$
\begin{aligned}
||\mathrm{d}\mathbf{x}||^2 &= \mathrm{d}\mathbf{x}\cdot\mathrm{d}\mathbf{x} \\
&= (\mathbf{F}_\alpha\,\mathrm{d}\mathbf{X}_\alpha)\cdot(\mathbf{F}_\alpha\,\mathrm{d}\mathbf{X}_\alpha) \\
&= \mathrm{d}\mathbf{X}_\alpha\cdot(\mathbf{F}_\alpha^T\,\mathbf{F}_\alpha)\,\mathrm{d}\mathbf{X}_\alpha\,,
\end{aligned}
\tag{2.28}
$$

or with respect to the actual configuration,

$$
\begin{aligned}
||\mathrm{d}\mathbf{X}_\alpha||^2 &= \mathrm{d}\mathbf{X}_\alpha \cdot \mathrm{d}\mathbf{X}_\alpha \\
&= (\mathbf{F}_\alpha^{-1}\,\mathrm{d}\mathbf{x}) \cdot (\mathbf{F}_\alpha^{-1}\,\mathrm{d}\mathbf{x}) \\
&= \mathrm{d}\mathbf{x} \cdot \underbrace{(\mathbf{F}_\alpha^{T-1}\,\mathbf{F}_\alpha^{-1})}_{(\mathbf{F}_\alpha\,\mathbf{F}_\alpha^T)^{-1}}\,\mathrm{d}\mathbf{x}\,,
\end{aligned}
\tag{2.29}
$$

one directly obtains the following definitions of the deformation tensors:

$$
\mathbf{C}_\alpha = \mathbf{F}_\alpha^T\,\mathbf{F}_\alpha = \mathbf{U}_\alpha\,\mathbf{U}_\alpha\,, \qquad \mathbf{B}_\alpha = \mathbf{F}_\alpha\,\mathbf{F}_\alpha^T = \mathbf{V}_\alpha\,\mathbf{V}_\alpha\,.
\tag{2.30}
$$

Therein, $\mathbf{C}_\alpha$ is the right *Cauchy-Green* deformation tensor and $\mathbf{B}_\alpha$ the left *Cauchy-Green* deformation tensor (or *Finger* tensor). The two deformation tensors are related to each other by the push-forward rotation:

$$
\mathbf{B}_\alpha = \mathbf{R}_\alpha\,\mathbf{C}_\alpha\,\mathbf{R}_\alpha^T\,.
\tag{2.31}
$$

For the derivation of two well-established strain measures, one proceeds from the differences of the squares of the current and referential line elements,

$$
\begin{aligned}
||\mathrm{d}\mathbf{x}||^2 - ||\mathrm{d}\mathbf{X}_\alpha||^2 &= \mathrm{d}\mathbf{X}_\alpha \cdot \mathbf{C}_\alpha\,\mathrm{d}\mathbf{X}_\alpha - \mathrm{d}\mathbf{X}_\alpha \cdot \mathrm{d}\mathbf{X}_\alpha &= \mathrm{d}\mathbf{X}_\alpha \cdot (\mathbf{C}_\alpha - \mathbf{I})\,\mathrm{d}\mathbf{X}_\alpha\,, \\
||\mathrm{d}\mathbf{x}||^2 - ||\mathrm{d}\mathbf{X}_\alpha||^2 &= \mathrm{d}\mathbf{x} \cdot \mathrm{d}\mathbf{x} - \mathrm{d}\mathbf{x} \cdot \mathbf{B}_\alpha^{-1}\,\mathrm{d}\mathbf{x} &= \mathrm{d}\mathbf{x} \cdot (\mathbf{I} - \mathbf{B}_\alpha^{-1})\,\mathrm{d}\mathbf{x}\,,
\end{aligned}
\tag{2.32}
$$

so that the definition of the *Green-Lagrange*an and the *Almansi*an strain tensors $\mathbf{E}_\alpha$ and $\mathbf{A}_\alpha$ is straightforward:

$$
\mathbf{E}_\alpha = \tfrac{1}{2}\,(\mathbf{C}_\alpha - \mathbf{I})\,, \qquad \mathbf{A}_\alpha = \tfrac{1}{2}\,(\mathbf{I} - \mathbf{B}_\alpha^{-1})\,.
\tag{2.33}
$$

Remark: The introduction of the factor $1/2$ is due to historical reasons, as the linearization of $\mathbf{E}$ or $\mathbf{A}$ (single-phase representation) for the one-dimensional case should result in the well-known *Hooke*an law $\sigma = E\,\varepsilon$, with the stress σ, *Young*'s modulus E and the (linearized) strain ε. $\qquad\square$

A relation between the *Almansi*an tensor $\mathbf{A}_\alpha$ and the *Green-Lagrange*an tensor $\mathbf{E}_\alpha$ can be established via a contravariant push-forward transport mechanism:

$$
\mathbf{A}_\alpha = \mathbf{F}_\alpha^{T-1}\,\mathbf{E}_\alpha\,\mathbf{F}_\alpha^{-1}\,.
\tag{2.34}
$$

Other strain tensors like the *Karni-Reiner* tensors will not be used within this thesis and can be taken from the literature, e. g., *Ehlers* [48].

2.1.4 Stress measures

In general, stress is defined as "force per unit area", i. e., stress is a physical quantity, which relates forces to area elements. This connection directly leads to the introduction

of various stress measures, since, obviously, several area elements can be defined, e. g., d$\mathbf{a}$ and d$\mathbf{A}_\alpha$ as the area elements of the current and reference configuration.

Stress tensors can be introduced with the application of *Cauchy*'s theorem:

$$\mathbf{t}^\alpha(\mathbf{x},\, t,\, \mathbf{n}) = \mathbf{T}^\alpha(\mathbf{x},\, t)\, \mathbf{n}\,. \tag{2.35}$$

Therein, $\mathbf{t}^\alpha$ is the surface traction vector including all effects, which result from contact forces acting on material points X^α on the surface $\partial\mathcal{B}$, and $\mathbf{n}$ is the outward oriented unit surface normal of the current configuration. With (2.35), the partial *Cauchy* stress tensor $\mathbf{T}^\alpha$ is defined, which is very often also named true stress tensor as it relates forces d$\mathbf{k}^\alpha$ acting on the constituent φ^α to the actual area element d$\mathbf{a}$. With this connection,

$$d\mathbf{k}^\alpha = \mathbf{T}^\alpha\, d\mathbf{a}\,(= \mathbf{t}^\alpha\, da)\,, \tag{2.36}$$

further stress tensors for a constituent φ^α can be defined. By relating the surface area force d$\mathbf{k}^\alpha$ to a weighted surface area element d$\bar{\mathbf{a}}_\alpha = (\det\mathbf{F}_\alpha)^{-1}\, d\mathbf{a}$, the *Kirchhoff* stress (or weighted *Cauchy* stress) $\boldsymbol{\tau}^\alpha$ can be introduced:

$$d\mathbf{k}^\alpha = \mathbf{T}^\alpha\,(\det\mathbf{F}_\alpha)\, d\bar{\mathbf{a}}_\alpha = \boldsymbol{\tau}^\alpha\, d\bar{\mathbf{a}}_\alpha\,. \tag{2.37}$$

Relating the true stress $\mathbf{T}^\alpha$ to a surface area element d$\mathbf{A}_\alpha$ of the reference configuration and using the transport theorem $(2.25)_2$, the first *Piola-Kirchhoff* stress tensor $\mathbf{P}^\alpha$ is obtained:

$$d\mathbf{k}^\alpha = \mathbf{T}^\alpha\,(\det\mathbf{F}_\alpha)\,\mathbf{F}_\alpha^{T-1}\, d\mathbf{A}_\alpha = \mathbf{P}^\alpha\, d\mathbf{A}_\alpha\,. \tag{2.38}$$

This stress tensor is, like the material deformation gradient, a two-field tensor, in which the first basis system is located in the actual configuration and the second one in the reference configuration. This fact is due to the incomplete covariant pull-back operation of the *Kirchhoff* stress:

$$\mathbf{P}^\alpha = \boldsymbol{\tau}_\alpha\,\mathbf{F}_\alpha^{T-1}\,. \tag{2.39}$$

By an additional transport of the first basis system of $\mathbf{P}^\alpha$ to the reference configuration, the second *Piola-Kirchhoff* stress tensor $\mathbf{S}^\alpha$ can be introduced:

$$\mathbf{S}^\alpha = \mathbf{F}_\alpha^{-1}\,\mathbf{P}^\alpha = \mathbf{F}_\alpha^{-1}\,\boldsymbol{\tau}_\alpha\,\mathbf{F}_\alpha^{T-1}\,. \tag{2.40}$$

2.2 Balance relations

Within a continuum mechanical framework, the balance relations are introduced based on axiomatic statements coming from physical observations. They combine the information given for a body $\mathcal{B}$ via, e. g., the motion or deformation with influences, which originate from outside the body like, e. g., contact or gravitational forces. In detail, the balance relations of the mechanical quantities mass, momentum and moment of momentum as well as the balance relations of the thermodynamical quantities energy and entropy are discussed in the following section. In this discussion, obviously, the multiphasic character of the regarded porous materials has to be considered particularly.

The structure of the balance relations for multiphasic materials is based on the so-called "metaphysical principles" by *Truesdell* [142]:

1. *All properties of the mixture must be mathematical consequences of properties of the constituents.*

2. *So as to describe the motion of a constituent, we may in imagination isolate it from the rest of the mixture, provided we allow properly for the actions of the other constituents upon it.*

3. *The motion of the mixture is governed by the same equations as is a single body.*

Following this, a balance relation of the mixture can be found via summation of the respective balance relations of the constituents φ^α. Furthermore, for the proper definition of the balance relations of the single phases, one has to introduce production terms, which allow for the consideration of the interaction between the single constituents, and, finally, the balance relations of the mixture must have the same structure as the balance relations known from the classical continuum mechanics.

2.2.1 General structure of the balance relations

For a compact formulation of the balance equations, it is useful in a first step to introduce the general structure of a balance equation at the example of an arbitrary physical quantity. In a second step, the generally introduced terms can be specified and discussed with respect to the individual mechanical and thermodynamical quantities. Essentially, this procedure follows the approach given by *Ehlers* [48, 53].

Following the above mentioned principles of *Truesdell*, the structure of the balance relations of the mixture has to be taken from the classical continuum mechanical description of single phase materials. Suppose that Ψ or $\boldsymbol{\Psi}$ are volume-specific scalar- or vector-valued mechanical quantities in $\mathcal{B}$. Thus, for the general structure of the balance relations of the mixture, it follows that

$$
\begin{aligned}
\frac{\mathrm{d}}{\mathrm{d}t} \int_{\mathcal{B}} \Psi \, \mathrm{d}v &= \int_{\partial\mathcal{B}} \boldsymbol{\phi} \cdot \mathbf{n} \, \mathrm{d}a \; + \; \int_{\mathcal{B}} \sigma \, \mathrm{d}v \; + \; \int_{\mathcal{B}} \hat{\Psi} \, \mathrm{d}v \,, \\
\frac{\mathrm{d}}{\mathrm{d}t} \int_{\mathcal{B}} \boldsymbol{\Psi} \, \mathrm{d}v &= \int_{\partial\mathcal{B}} \boldsymbol{\Phi} \, \mathbf{n} \, \mathrm{d}a \; + \; \int_{\mathcal{B}} \boldsymbol{\sigma} \, \mathrm{d}v \; + \; \int_{\mathcal{B}} \hat{\boldsymbol{\Psi}} \, \mathrm{d}v \,.
\end{aligned}
\tag{2.41}
$$

Therein, the temporal change of Ψ (or $\boldsymbol{\Psi}$) is balanced with the efflux $\boldsymbol{\phi}$ (or $\boldsymbol{\Phi}$) of the mechanical quantity through the surface $\partial\mathcal{B}$ resulting from the external vicinity, with the supply σ (or $\boldsymbol{\sigma}$) of the mechanical quantity into the body $\mathcal{B}$ resulting from the external distance and with the production terms $\hat{\Psi}$ (or $\hat{\boldsymbol{\Psi}}$) of the mechanical quantity resulting from possible couplings of $\mathcal{B}$ with its surrounding.

By differentiation of the left side of (2.41) and application of the *Gaussian* divergence theorem, in order to transform the surface integrals of (2.41) into volume integrals, one

finds with the usual assumptions of continuous and continuously differentiable integrands the local forms of the balance relations:

$$\dot{\Psi} \;+\; \Psi \operatorname{div} \dot{\mathbf{x}} \;=\; \operatorname{div} \boldsymbol{\phi} \;+\; \sigma \;+\; \hat{\Psi}\,,$$

$$\dot{\boldsymbol{\Psi}} \;+\; \boldsymbol{\Psi} \operatorname{div} \dot{\mathbf{x}} \;=\; \operatorname{div} \boldsymbol{\Phi} \;+\; \boldsymbol{\sigma} \;+\; \hat{\boldsymbol{\Psi}}\,. \tag{2.42}$$

Corresponding to *Truesdell*'s principles, the structure of the balance equations for the individual constituents φ^α is formulated in analogy to (2.41). All quantities are indicated as affiliated to φ^α by the superscripted index $(\cdot)^\alpha$. As a main difference to the balance relations of the mixture, the production terms $\hat{\Psi}^\alpha$ (or $\hat{\boldsymbol{\Psi}}^\alpha$) now additionally describe the coupling between the single constituents such that interchange processes between the single phases can be modeled. The global balance relations of a constituent φ^α yield

$$\frac{\mathrm{d}_\alpha}{\mathrm{d}t} \int_{\mathcal{B}} \Psi^\alpha \,\mathrm{d}v \;=\; \int_{\partial\mathcal{B}} \boldsymbol{\phi}^\alpha \cdot \mathbf{n} \,\mathrm{d}a \;+\; \int_{\mathcal{B}} \sigma^\alpha \,\mathrm{d}v \;+\; \int_{\mathcal{B}} \hat{\Psi}^\alpha \,\mathrm{d}v\,,$$

$$\frac{\mathrm{d}_\alpha}{\mathrm{d}t} \int_{\mathcal{B}} \boldsymbol{\Psi}^\alpha \,\mathrm{d}v \;=\; \int_{\partial\mathcal{B}} \boldsymbol{\Phi}^\alpha \,\mathbf{n} \,\mathrm{d}a \;+\; \int_{\mathcal{B}} \boldsymbol{\sigma}^\alpha \,\mathrm{d}v \;+\; \int_{\mathcal{B}} \hat{\boldsymbol{\Psi}}^\alpha \,\mathrm{d}v\,. \tag{2.43}$$

In analogy to (2.42), the local forms of the balance relations of the constituent φ^α are obtained:

$$(\Psi^\alpha)'_\alpha \;+\; \Psi^\alpha \operatorname{div} \overset{'}{\mathbf{x}}_\alpha \;=\; \operatorname{div} \boldsymbol{\phi}^\alpha \;+\; \sigma^\alpha \;+\; \hat{\Psi}^\alpha\,,$$

$$(\boldsymbol{\Psi}^\alpha)'_\alpha \;+\; \boldsymbol{\Psi}^\alpha \operatorname{div} \overset{'}{\mathbf{x}}_\alpha \;=\; \operatorname{div} \boldsymbol{\Phi}^\alpha \;+\; \boldsymbol{\sigma}^\alpha \;+\; \hat{\boldsymbol{\Psi}}^\alpha\,. \tag{2.44}$$

As already mentioned above in the discussion of *Truesdell*'s principles, the balance relations (2.42) of the overall medium φ have to be found via summation over the balance relations (2.44) of the single constituents φ^α. Therefore, the quantities occurring in (2.44) are not arbitrary but have to fulfill certain restrictions, e. g., for scalar-valued mechanical quantities, it follows that

$$
\begin{aligned}
\text{mechanical quantity} \;:\; \Psi \;&=\; \sum_{\alpha=1}^{k} \Psi^\alpha\,, \\[2mm]
\text{efflux} \;:\; \boldsymbol{\phi} \cdot \mathbf{n} \;&=\; \sum_{\alpha=1}^{k} (\boldsymbol{\phi}^\alpha - \Psi^\alpha \,\mathbf{d}_\alpha) \cdot \mathbf{n}\,, \\[2mm]
\text{supply} \;:\; \sigma \;&=\; \sum_{\alpha=1}^{k} \sigma^\alpha\,, \\[2mm]
\text{production} \;:\; \hat{\Psi} \;&=\; \sum_{\alpha=1}^{k} \hat{\Psi}^\alpha\,.
\end{aligned}
\tag{2.45}
$$

Analogously, one finds for vector-valued mechanical quantities the following restrictions:

$$
\begin{aligned}
\text{mechanical quantity} \quad &: \quad \boldsymbol{\Psi} \quad = \quad \sum_{\alpha=1}^{k} \boldsymbol{\Psi}^{\alpha}\,, \\[2mm]
\text{efflux} \quad &: \quad \boldsymbol{\Phi}\,\mathbf{n} \quad = \quad \sum_{\alpha=1}^{k} \left(\boldsymbol{\Phi}^{\alpha} - \boldsymbol{\Psi}^{\alpha} \otimes \mathbf{d}_{\alpha}\right) \mathbf{n}\,, \\[2mm]
\text{supply} \quad &: \quad \boldsymbol{\sigma} \quad = \quad \sum_{\alpha=1}^{k} \boldsymbol{\sigma}^{\alpha}\,, \\[2mm]
\text{production} \quad &: \quad \hat{\boldsymbol{\Psi}} \quad = \quad \sum_{\alpha=1}^{k} \hat{\boldsymbol{\Psi}}^{\alpha}\,.
\end{aligned}
\tag{2.46}
$$

Therein, $\mathbf{d}_{\alpha} = (\overset{\prime}{\mathbf{x}}_{\alpha} - \dot{\mathbf{x}})$ is the diffusion velocity introduced in (2.20).

2.2.2   Mass balances

Proceeding from the overall mixture, one axiomatically introduces that the mass of the body is conserved, i. e.,

$$
\int_{\mathcal{B}} \rho \, \mathrm{d}v = \text{const.} \qquad \rightsquigarrow \qquad \frac{\mathrm{d}}{\mathrm{d}t} \int_{\mathcal{B}} \rho \, \mathrm{d}v = 0\,.
\tag{2.47}
$$

Comparing (2.47) with the general structure of a balance relation $(2.41)_1$, the density ρ is identified as the mechanical quantity whereas the efflux, the supply and the production terms are zero:

$$
\Psi = \rho\,, \qquad \boldsymbol{\phi} = \mathbf{0}\,, \qquad \sigma = 0\,, \qquad \hat{\Psi} = 0\,.
\tag{2.48}
$$

With the above relation and $(2.42)_1$, one directly concludes to the local form of the mass balance of the mixture:

$$
\dot{\rho} + \rho \, \mathrm{div}\, \dot{\mathbf{x}} = 0\,.
\tag{2.49}
$$

For the mass balances of the constituents φ^{α}, one has to regard production terms $\hat{\rho}^{\alpha}$, which make it possible to model mass exchanges between the constituents, like, e. g., the transition of water (liquid phase) into steam (gaseous phase):

$$
\frac{\mathrm{d}_{\alpha}}{\mathrm{d}t} \int_{\mathcal{B}} \rho^{\alpha} \, \mathrm{d}v = \int_{\mathcal{B}} \hat{\rho}^{\alpha} \, \mathrm{d}v\,.
\tag{2.50}
$$

Referring to $(2.43)_1$, the following values for the mechanical quantity, the efflux, the supply and the production can be identified:

$$
\Psi^{\alpha} = \rho^{\alpha}\,, \qquad \boldsymbol{\phi}^{\alpha} = \mathbf{0}\,, \qquad \sigma^{\alpha} = 0\,, \qquad \hat{\Psi}^{\alpha} = \hat{\rho}^{\alpha}\,.
\tag{2.51}
$$

According to $(2.44)_1$, the local form of the mass balance for a constituent φ^α results in

$$(\rho^\alpha)'_\alpha + \rho^\alpha \operatorname{div} \overset{'}{\mathbf{x}}_\alpha = \hat{\rho}^\alpha \, . \tag{2.52}$$

Remark: In case of material incompressibility of a constituent ($\rho^{\alpha R} = \text{const.}$) and a simultaneous neglect of mass productions ($\hat{\rho}^\alpha = 0$), the mass balance (2.52) can be reduced to a volume balance by using relation (2.9): $(n^\alpha)'_\alpha + n^\alpha \operatorname{div} \overset{'}{\mathbf{x}}_\alpha = 0 \, .$ □

The evaluation of the restrictions (2.45) gives the relation for the partial densities (2.10) as already introduced, and evokes the disappearance of both the mass flow due to diffusion and the mass production:

$$\rho = \sum_{\alpha=1}^{k} \rho^\alpha \, , \qquad \mathbf{0} = \sum_{\alpha=1}^{k} \rho^\alpha \, \mathbf{d}_\alpha \, , \qquad 0 = \sum_{\alpha=1}^{k} \hat{\rho}^\alpha \, . \tag{2.53}$$

Note that $(2.53)_2$ can also be derived via a combination of the Equations (2.10), (2.19) and (2.20).

2.2.3 Momentum balances

The physical quantity momentum $\mathbf{p}$ is a central quantity for the description of the kinematical state of a body $\mathcal{B}$ and is defined by

$$\mathbf{p} = \int_{\mathcal{B}} \rho \, \dot{\mathbf{x}} \, dv. \tag{2.54}$$

For the formulation of the momentum balance, one axiomatically introduces that the temporal change of $\mathbf{p}$ corresponds to the sum of all surface and body forces acting on the body $\mathcal{B}$ during a deformation process:

$$\frac{d}{dt} \int_{\mathcal{B}} \rho \, \dot{\mathbf{x}} \, dv = \int_{\partial\mathcal{B}} \mathbf{T} \, \mathbf{n} \, da + \int_{\mathcal{B}} \rho \, \mathbf{b} \, dv \, . \tag{2.55}$$

Therein, $\mathbf{T}$ is the *Cauchy* stress tensor containing the overall stress state of the mixture and $\rho \, \mathbf{b}$ is the supply term, which is usually interpreted in the sense of an *a priori* constitutive assumption as the overall gravitation. After a comparison with $(2.41)_2$, one finds the following relations for the mechanical quantity (momentum density), the efflux (*Cauchy* stress tensor) and the supply term (body force density):

$$\mathbf{\Psi} = \rho \, \dot{\mathbf{x}} \, , \qquad \mathbf{\Phi} = \mathbf{T} \, , \qquad \boldsymbol{\sigma} = \rho \, \mathbf{b} \, , \qquad \hat{\mathbf{\Psi}} = \mathbf{0} \, . \tag{2.56}$$

When using the local mass balance (2.49), one directly concludes to the local form of the momentum balance for the mixture:

$$\rho \, \ddot{\mathbf{x}} = \operatorname{div} \mathbf{T} + \rho \, \mathbf{b} \, . \tag{2.57}$$

Looking at the momentum balances of the constituents φ^α, again, one has to introduce a production term $\hat{\mathbf{s}}^\alpha$, which is interpreted as an interaction force between the single constituents:

$$\frac{\mathrm{d}_\alpha}{\mathrm{d}t} \int_{\mathcal{B}} \rho^\alpha \, \overset{\prime}{\mathbf{x}}_\alpha \, \mathrm{d}v = \int_{\partial\mathcal{B}} \mathbf{T}^\alpha \, \mathbf{n} \, \mathrm{d}a + \int_{\mathcal{B}} \rho^\alpha \, \mathbf{b}^\alpha \, \mathrm{d}v + \int_{\mathcal{B}} \hat{\mathbf{s}}^\alpha \, \mathrm{d}v \, . \tag{2.58}$$

With the straightforward identification of the quantities from the general balance relations,

$$\boldsymbol{\Psi}^\alpha = \rho^\alpha \, \overset{\prime}{\mathbf{x}}_\alpha \, , \qquad \boldsymbol{\Phi}^\alpha = \mathbf{T}^\alpha \, , \qquad \boldsymbol{\sigma}^\alpha = \rho^\alpha \, \mathbf{b}^\alpha \, , \qquad \hat{\boldsymbol{\Psi}}^\alpha = \hat{\mathbf{s}}^\alpha \, , \tag{2.59}$$

and the consideration of the local form of the mass balance (2.52), the momentum balance for a constituent φ^α gives:

$$\rho^\alpha \, \overset{\prime\prime}{\mathbf{x}}_\alpha = \mathrm{div} \, \mathbf{T}^\alpha + \rho^\alpha \, \mathbf{b}^\alpha + \hat{\mathbf{p}}^\alpha \, . \tag{2.60}$$

Therein, the overall momentum production $\hat{\mathbf{s}}^\alpha = \hat{\mathbf{p}}^\alpha + \hat{\rho}^\alpha \, \overset{\prime}{\mathbf{x}}_\alpha$ is split into a direct term $\hat{\mathbf{p}}^\alpha$ and a term $\hat{\rho}^\alpha \, \overset{\prime}{\mathbf{x}}_\alpha$ resulting from the mass balance (density production). By insertion of the relations (2.56) and (2.59) into (2.46), the following vector-valued constraints can be found:

$$\rho \, \dot{\mathbf{x}} = \sum_{\alpha=1}^{k} \rho^\alpha \, \overset{\prime}{\mathbf{x}}_\alpha \, , \quad \mathbf{T} = \sum_{\alpha=1}^{k} \mathbf{T}^\alpha - \rho^\alpha \, \mathbf{d}_\alpha \otimes \mathbf{d}_\alpha \, , \quad \rho \, \mathbf{b} = \sum_{\alpha=1}^{k} \rho^\alpha \, \mathbf{b}^\alpha \, , \quad \mathbf{0} = \sum_{\alpha=1}^{k} \hat{\mathbf{s}}^\alpha \, . \tag{2.61}$$

2.2.4   Moment of momentum balances

Within the balance of moment of momentum (or angular momentum), it is axiomatically claimed that the temporal change of the moment of momentum corresponds to the moments, which are caused by all surface and body forces acting on the body $\mathcal{B}$:

$$\frac{\mathrm{d}}{\mathrm{d}t} \int_{\mathcal{B}} (\mathbf{x} \times \rho \, \dot{\mathbf{x}}) \, \mathrm{d}v = \int_{\partial\mathcal{B}} (\mathbf{x} \times \mathbf{T}) \, \mathbf{n} \, \mathrm{d}a + \int_{\mathcal{B}} (\mathbf{x} \times \rho \, \mathbf{b}) \, \mathrm{d}v \, . \tag{2.62}$$

Therein, the outer tensor product of a first order tensor (vector) and a second order tensor $\mathbf{x} \times \mathbf{T}$ is introduced, cf. Appendix A.1.6.

With the identification of the quantities from the general balance relation $(2.41)_2$,

$$\boldsymbol{\Psi} = \mathbf{x} \times \rho \, \dot{\mathbf{x}} \, , \qquad \boldsymbol{\Phi} = \mathbf{x} \times \mathbf{T} \, , \qquad \boldsymbol{\sigma} = \mathbf{x} \times \rho \, \mathbf{b} \, , \qquad \hat{\boldsymbol{\Psi}} = \mathbf{0} \, , \tag{2.63}$$

and the use of the local mass and momentum balances (2.49) and (2.57), one finds the well-known result of the angular momentum balance of single phase materials:

$$\mathbf{0} = \mathbf{I} \times \mathbf{T} \qquad \rightsquigarrow \qquad \mathbf{T}^T = \mathbf{T}. \tag{2.64}$$

For the definition of the moment of momentum balance of the constituents φ^α, one has to introduce a term $\hat{\mathbf{h}}^\alpha$, which represents the production of angular momentum:

$$\frac{\mathrm{d}_\alpha}{\mathrm{d}t} \int_{\mathcal{B}} (\mathbf{x} \times \rho^\alpha \, \overset{\prime}{\mathbf{x}}_\alpha) \, \mathrm{d}v = \int_{\partial\mathcal{B}} (\mathbf{x} \times \mathbf{T}^\alpha) \, \mathbf{n} \, \mathrm{d}a + \int_{\mathcal{B}} (\mathbf{x} \times \rho^\alpha \, \mathbf{b}^\alpha) \, \mathrm{d}v + \int_{\mathcal{B}} \hat{\mathbf{h}}^\alpha \, \mathrm{d}v \, . \tag{2.65}$$

Referring to $(2.43)_2$, the following relations for the quantities of the general balance equation can be found:

$$\boldsymbol{\Psi}^\alpha = \mathbf{x} \times \rho^\alpha\, \mathbf{x}'_\alpha\,, \qquad \boldsymbol{\Phi}^\alpha = \mathbf{x} \times \mathbf{T}^\alpha\,, \qquad \boldsymbol{\sigma}^\alpha = \mathbf{x} \times \rho^\alpha\, \mathbf{b}^\alpha\,, \qquad \hat{\boldsymbol{\Psi}}^\alpha = \hat{\mathbf{h}}^\alpha\,. \qquad (2.66)$$

Considering the local mass and momentum balances (2.52) and (2.60), the local form of the angular momentum for a constituent φ^α gives

$$\mathbf{0} = \mathbf{I} \times \mathbf{T}^\alpha + \hat{\mathbf{m}}^\alpha \qquad \rightsquigarrow \qquad (\mathbf{T}^\alpha)^T = \mathbf{T}^\alpha + \hat{\mathbf{M}}^\alpha. \qquad (2.67)$$

Therein, the overall production term of the angular momentum $\hat{\mathbf{h}}^\alpha$ is split into a direct term $\hat{\mathbf{m}}^\alpha$ and a term resulting from the mass and momentum balances:

$$\hat{\mathbf{h}}^\alpha = \mathbf{x} \times (\hat{\rho}^\alpha\, \mathbf{x}'_\alpha + \hat{\mathbf{p}}^\alpha) + \hat{\mathbf{m}}^\alpha\,. \qquad (2.68)$$

Furthermore, the relation $(2.67)_2$ can be found via the definition of a skew symmetric tensor $\hat{\mathbf{M}}^\alpha$, which represents the coupling of angular momentum between the single constituents φ^α:

$$\hat{\mathbf{m}}^\alpha = \tfrac{1}{2}\,(\,\mathbf{I} \times \hat{\mathbf{M}}^\alpha)\,. \qquad (2.69)$$

Note that this coupling tensor $\hat{\mathbf{M}}^\alpha$ vanishes for non-polar materials, since the symmetry of the partial stress tensors $\mathbf{T}^\alpha$ for such materials can be motivated via an analysis of the homogenization procedure, cf. *Hassanizadeh & Gray* [85]:

$$\mathbf{T}^\alpha = \frac{1}{V_{REV}} \int\limits_{\mathcal{B}_{REV}} \mathbf{T}^\alpha_{micro}\, \mathrm{d}v \quad \text{with} \quad V_{REV} = \int\limits_{\mathcal{B}_{REV}} \mathrm{d}v \quad \text{and} \quad \mathbf{T}^\alpha_{micro} = (\mathbf{T}^\alpha_{micro})^T. \qquad (2.70)$$

From the above equation, it follows that if the stress tensor $\mathbf{T}^\alpha_{micro}$ from the micro scale is symmetric, the homogenization procedure gives a symmetric macroscopic partial stress tensor:

$$(\mathbf{T}^\alpha)^T = \mathbf{T}^\alpha \qquad \rightsquigarrow \qquad \hat{\mathbf{M}}^\alpha = \mathbf{0}\,. \qquad (2.71)$$

Remark: Within the context of standard (non-polar) materials, the balance of angular momentum simply gives the symmetry of the stress tensors $\mathbf{T}$ and $\mathbf{T}^\alpha$ and is, therefore, usually not further investigated. In the case of micropolar materials, the balance of angular momentum is an equation for the determination of the total average grain rotation, cf. Section 4.4. □

2.2.5 Energy balances

The energy conservation equation balances the temporal change of the internal and kinetic energy with the power of all surface and body forces as well as with the heat influx and the heat supply:

$$\frac{\mathrm{d}}{\mathrm{d}t} \int\limits_{\mathcal{B}} \rho\,(\varepsilon + \tfrac{1}{2}\,\dot{\mathbf{x}} \cdot \dot{\mathbf{x}})\, \mathrm{d}v = \int\limits_{\partial\mathcal{B}} (\mathbf{T}^T \dot{\mathbf{x}} - \mathbf{q}) \cdot \mathbf{n}\, \mathrm{d}a + \int\limits_{\mathcal{B}} \rho\,(\mathbf{b} \cdot \dot{\mathbf{x}} + r)\, \mathrm{d}v\,. \qquad (2.72)$$

Therein, ε is the specific internal energy, $\mathbf{q}$ the heat influx vector (heat influx via the surface) and r is the heat supply resulting from the external distance (e. g., heat supply in a microwave).

After comparison with $(2.41)_1$,

$$\Psi = \rho \left(\varepsilon + \tfrac{1}{2} \, \dot{\mathbf{x}} \cdot \dot{\mathbf{x}} \right), \qquad \boldsymbol{\phi} = \mathbf{T}^T \dot{\mathbf{x}} - \mathbf{q} \,, \qquad \sigma = \rho \left(\mathbf{b} \cdot \dot{\mathbf{x}} + r \right), \qquad \hat{\Psi} = 0 \,, \qquad (2.73)$$

and consideration of the "lower" balance relations, i. e., the mass, momentum and angular momentum balances, the local form of the energy balance for the mixture reads

$$\rho \, \dot{\varepsilon} = \mathbf{T} \cdot \mathbf{L} - \operatorname{div} \mathbf{q} + \rho \, r \,. \qquad (2.74)$$

Therein, $\mathbf{L} = \operatorname{grad} \dot{\mathbf{x}}$ is the spatial velocity gradient of the mixture.

When introducing a term $\hat{e}^\alpha$ describing the energy exchange between the single constituents φ^α, the global form of the energy balance for each φ^α yields

$$\frac{\mathrm{d}_\alpha}{\mathrm{d}t} \int_{\mathcal{B}} \rho^\alpha \left(\varepsilon^\alpha + \tfrac{1}{2} \, \overset{\prime}{\mathbf{x}}_\alpha \cdot \overset{\prime}{\mathbf{x}}_\alpha \right) \mathrm{d}v =$$
$$= \int_{\partial \mathcal{B}} \left[(\mathbf{T}^\alpha)^T \overset{\prime}{\mathbf{x}}_\alpha - \mathbf{q}^\alpha \right] \cdot \mathbf{n} \, \mathrm{d}a + \int_{\mathcal{B}} \rho^\alpha \left(\mathbf{b}^\alpha \cdot \overset{\prime}{\mathbf{x}}_\alpha + r^\alpha \right) \mathrm{d}v + \int_{\mathcal{B}} \hat{e}^\alpha \, \mathrm{d}v \,. \qquad (2.75)$$

An analogous procedure as above leads to the following relations for the quantities of the global balance equation:

$$\begin{aligned} \Psi^\alpha &= \rho^\alpha \left(\varepsilon^\alpha + \tfrac{1}{2} \, \overset{\prime}{\mathbf{x}}_\alpha \cdot \overset{\prime}{\mathbf{x}}_\alpha \right), & \boldsymbol{\phi}^\alpha &= (\mathbf{T}^\alpha)^T \overset{\prime}{\mathbf{x}}_\alpha - \mathbf{q}^\alpha \,, \\ \sigma^\alpha &= \rho^\alpha \left(\mathbf{b}^\alpha \cdot \overset{\prime}{\mathbf{x}}_\alpha + r^\alpha \right), & \hat{\Psi}^\alpha &= \hat{e}^\alpha \,. \end{aligned} \qquad (2.76)$$

The total energy production $\hat{e}^\alpha = \hat{\mathbf{p}}^\alpha \cdot \overset{\prime}{\mathbf{x}}_\alpha + \hat{\rho}^\alpha (\varepsilon^\alpha + \tfrac{1}{2} \, \overset{\prime}{\mathbf{x}}_\alpha \cdot \overset{\prime}{\mathbf{x}}_\alpha) + \hat{\varepsilon}^\alpha$ is again split into a term coming from the "lower" balance relations and a direct term $\hat{\varepsilon}^\alpha$. After a comparison of the relations (2.76) and $(2.44)_1$, the local form for the energy balance of the constituents φ^α gives

$$\rho^\alpha \, (\varepsilon^\alpha)'_\alpha = \mathbf{T}^\alpha \cdot \mathbf{L}_\alpha - \operatorname{div} \mathbf{q}^\alpha + \rho^\alpha \, r^\alpha + \hat{\varepsilon}^\alpha \,. \qquad (2.77)$$

Therein, $\mathbf{L}_\alpha = \operatorname{grad} \overset{\prime}{\mathbf{x}}_\alpha$ is the spatial velocity gradient of a constituent φ^α.

Remark: Within the framework of this thesis, isothermal conditions are assumed and, therefore, the energy balances are only used for the proper formulation of the entropy inequality, cf. next section. If a change of the temperature of the whole mixture or of one constituent has to be regarded for a correct modeling, the energy balances serve as equations for the determination of the mixture or constituent temperatures, cf. *Ghadiani* [78]. □

2.2.6   Entropy balances

In the sixties of the last century, there was an intensive discussion among researchers about the correct formulation of the entropy balance for multiphasic materials, cf., e. g., for a historical overview *Ehlers* [48] or *Truesdell* [141]. The requirement that the entropy production for each constituent has to be positive was found to be too restrictive for the evaluation process of the entropy inequality. Consequently, the second law of thermodynamics, i. e., positive entropy production ($\hat{\eta} \geq 0$), is only postulated for the mixture.

For a constituent φ^α, one axiomatically introduces that the temporal change of the entropy η^α equals the entropy efflux $-\mathbf{q}^\alpha/\Theta^\alpha$, the entropy supply $\rho^\alpha\, r^\alpha/\Theta^\alpha$ and the entropy production $\hat{\eta}^\alpha$:

$$\frac{\mathrm{d}}{\mathrm{d}t} \int_{\mathcal{B}} \rho^\alpha\, \eta^\alpha\, \mathrm{d}v = -\int_{\partial\mathcal{B}} \frac{1}{\Theta^\alpha}\, \mathbf{q}^\alpha\, \mathrm{d}a + \int_{\mathcal{B}} \frac{1}{\Theta^\alpha}\, \rho^\alpha\, r^\alpha\, \mathrm{d}v + \int_{\mathcal{B}} \hat{\eta}^\alpha\, \mathrm{d}v\,. \tag{2.78}$$

Therein, Θ^α is *Kelvin*'s temperature of φ^α. Note that the formulations for the entropy efflux and the entropy supply come from *a priori* constitutive assumptions. As usual, the following identifications of the mechanical quantity, the efflux, the supply and the production terms can be carried out:

$$\Psi^\alpha = \rho^\alpha\, \eta^\alpha\,, \quad \boldsymbol{\phi}^\alpha = -\frac{1}{\Theta^\alpha}\, \mathbf{q}^\alpha\,, \quad \sigma^\alpha = \frac{1}{\Theta^\alpha}\, \rho^\alpha\, r^\alpha\,, \quad \hat{\Psi}^\alpha = \hat{\eta}^\alpha\,. \tag{2.79}$$

The entropy production term $\hat{\eta}^\alpha$ of the constituent φ^α can be split into a direct and an indirect term: $\hat{\eta}^\alpha = \hat{\zeta}^\alpha + \hat{\rho}^\alpha\, \eta^\alpha$. Taking into account the mass balances (2.52), the local form of the entropy balances for the constituents φ^α yields

$$\rho^\alpha\, (\eta^\alpha)'_\alpha = \mathrm{div}\, (-\frac{1}{\Theta^\alpha}\, \mathbf{q}^\alpha) + \frac{1}{\Theta^\alpha}\, \rho^\alpha\, r^\alpha + \hat{\zeta}^\alpha\,. \tag{2.80}$$

Using the constraint $\hat{\eta} = \sum_{\alpha=1}^{k} \hat{\eta}^\alpha$ [48, 53], the entropy inequality for the mixture can be written as follows

$$\hat{\eta} = \sum_{\alpha=1}^{k} \hat{\eta}^\alpha = \sum_{\alpha=1}^{k} [\, \rho^\alpha\, (\eta^\alpha)'_\alpha + \hat{\rho}^\alpha\, \eta^\alpha + \mathrm{div}\, (\frac{1}{\Theta^\alpha}\, \mathbf{q}^\alpha) - \frac{1}{\Theta^\alpha}\, \rho^\alpha\, r^\alpha\,] \geq 0\,. \tag{2.81}$$

By introduction of mass specific constituent free energy functions ψ^α (*Helmholtz* free energy functions) via

$$\psi^\alpha = \varepsilon^\alpha - \Theta^\alpha\, \eta^\alpha\,, \tag{2.82}$$

and the use of (2.77), one obtains the following formulation for the entropy inequality:

$$\sum_{\alpha=1}^{k} \frac{1}{\Theta^\alpha} \{\, \mathbf{T}^\alpha \cdot \mathbf{L}_\alpha - \rho^\alpha\, [\, (\psi^\alpha)'_\alpha + (\Theta^\alpha)'_\alpha\, \eta^\alpha\,] - \hat{\mathbf{p}}^\alpha \cdot \overset{'}{\mathbf{x}}_\alpha - $$
$$- \hat{\rho}^\alpha\, [\, \psi^\alpha + \tfrac{1}{2}\, \overset{'}{\mathbf{x}}_\alpha \cdot \overset{'}{\mathbf{x}}_\alpha\,] - \frac{1}{\Theta^\alpha}\, \mathbf{q}^\alpha \cdot \mathrm{grad}\, \Theta^\alpha + \hat{e}^\alpha\, \} \geq 0\,. \tag{2.83}$$

The above equation is the starting point for the evaluation of the entropy inequality, which results in restrictions for the constitutive assumptions. The description of this procedure will not be shown in this thesis, only the final results for the constitutive settings are discussed in the next section. The reader who is interested in more information on this topic is referred to the work by *Ehlers* [48, 53].

2.3　Constitutive settings

In order to determine all unknown quantities of a continuum mechanical model, the kinematic and the balance relations do not provide enough equations. Consequently, further equations, namely, the constitutive equations, have to be developed in order to close the particular model under consideration. Within these constitutive settings, the characteristics of the respective mechanical model and of the viewed material can be taken into account, e. g., the neglect of acceleration terms or the assumption of a specific material behavior. However, the decisions for the respective constitutive assumptions are not arbitrary, one has to meet the restrictions coming from the evaluation of the entropy inequality (2.83) for a thermodynamically consistent model. As already mentioned in the previous section, the development of the constitutive assumptions, including the explanation of the thermodynamically correct approach, is not discussed in this thesis. Here, only the final equations are presented based on their physical motivation.

Within this section, the constitutive settings for a triphasic model consisting of a materially incompressible solid skeleton, a materially incompressible viscous liquid phase and a materially compressible viscous gaseous phase are pointed out, cf. *Ehlers* [53], *Blome* [18], *Ehlers et al.* [62]. Furthermore, a biphasic model is presented, which can be found easily by leaving out the gaseous phase from the triphasic formulation, cf. *Diebels et al.* [44], *Ehlers & Ellsiepen* [59].

2.3.1　Adaption of the balance equations

The model under consideration is developed to describe typical geotechnical problems like consolidation processes or slope failure problems. For a proper description of such problems, the balance relations presented in the previous section can be simplified by the following assumptions:

　* no mass exchange between the constituents $\rightsquigarrow \hat{\rho}^{\alpha} = 0$.

　* constant and identical body force for all constituents (gravitation $\mathbf{g}$) $\rightsquigarrow \mathbf{b}^{\alpha} = \mathbf{g}$.

　* constant and identical temperature for all constituents (isothermal conditions) $\rightsquigarrow \Theta^{\alpha} = \Theta = \text{const.}$

　* quasi-static conditions $\rightsquigarrow \overset{\prime\prime}{\mathbf{x}}_{\alpha} = \mathbf{0}$.

Furthermore, by assuming that the occurring deformations of the problems under study are small, the kinematical relations presented in Section 2.1 can also be simplified, i. e.,

the finite deformation theory can be reduced to a geometrically linear approach. Thus, one has to distinguish no longer between the reference and the current configuration, which leads to the following approximations for the gradient and divergence operators:

$$\operatorname{Grad}_\alpha(\cdot) \approx \operatorname{grad}(\cdot), \qquad \operatorname{Div}_\alpha(\cdot) \approx \operatorname{div}(\cdot). \tag{2.84}$$

In the remainder of this thesis, therefore, spatial gradient and divergence operators are used. The reader who is interested in the discussion of multiphasic models in the context of large deformations for elastic, viscoelastic or elasto-plastic material behavior is referred to the work by *Eipper* [65], *Mahnkopf* [103] and *Markert* [104].

Using the solid displacement vector $\mathbf{u}_S$ and the seepage velocities $\mathbf{w}_\beta$ from Equation (2.23), the above simplifications lead to the following resulting balance relations for the solid, the liquid and the gaseous phases:

∗ volume (mass) balances:

$$(n^S)'_S + n^S \operatorname{div}(\mathbf{u}_S)'_S \qquad\qquad\qquad = 0,$$

$$(n^L)'_S + n^L \operatorname{div}(\mathbf{u}_S)'_S + \operatorname{div}(n^L \mathbf{w}_L) \qquad\qquad = 0, \tag{2.85}$$

$$n^G(\rho^{GR})'_S + (n^G)'_S \rho^{GR} + n^G \rho^{GR} \operatorname{div}(\mathbf{u}_S)'_S + \operatorname{div}(n^G \rho^{GR} \mathbf{w}_G) = 0.$$

∗ momentum balances:

$$\mathbf{0} = \operatorname{div}\mathbf{T}^S + n^S \rho^{SR}\mathbf{g} + \hat{\mathbf{p}}^S,$$

$$\mathbf{0} = \operatorname{div}\mathbf{T}^L + n^L \rho^{LR}\mathbf{g} + \hat{\mathbf{p}}^L, \tag{2.86}$$

$$\mathbf{0} = \operatorname{div}\mathbf{T}^G + n^G \rho^{GR}\mathbf{g} + \hat{\mathbf{p}}^G.$$

Note again that the mass balances can be reduced to volume balances in the case of materially incompressible constituents, cf. remark on Page 19. The volume (mass) balances $(2.85)_{2,3}$ are written by use of (2.9) with respect to the skeleton motion, i. e., the material time derivative $(\cdot)'_\beta$ of the fluid motion is formulated in relation to the skeleton time derivative $(\cdot)'_S$ by a modification of the convective part:

$$(\Gamma)'_\beta = (\Gamma)'_S + \operatorname{grad}\Gamma \cdot \mathbf{w}_\beta. \tag{2.87}$$

By a time integration of the volume balance of the solid skeleton $(2.85)_1$, the following relation can be found:

$$n^S = n^S_{0S}(\det\mathbf{F}_S)^{-1}. \tag{2.88}$$

Therein, n^S_{0S} is the initial volume fraction of φ^S. In the framework of a geometrically linear theory, the above relation can be formally linearized around the natural state of φ^S:

$$n^S \approx n^S_{0S}(1 - \operatorname{div}\mathbf{u}_S). \tag{2.89}$$

The isothermal triphasic model under consideration is governed by five primary variables given by the solid displacement $\mathbf{u}_S$, the seepage velocities $\mathbf{w}_L$ and $\mathbf{w}_G$ and the effective

pore-fluid pressures p^{LR} and p^{GR}. Taking into account the assumption of a quasi-static approach, a coupling of the seepage velocities and the effective fluid pressures via the individual fluid momentum balances $(2.86)_{2,3}$ in the shape of linear *Darcy*-like relations can be obtained, cf. Section 2.3.4. Thus, the number of primary variables is reduced from five to three: the solid displacement $\mathbf{u}_S$ and the fluid pressures p^{LR} and p^{GR}. The corresponding set of governing equations is given by the following relations:

$$\mathbf{0} = \operatorname{div} \mathbf{T} + \rho \, \mathbf{g} \, ,$$

$$(n^L)'_S + n^L \operatorname{div}(\mathbf{u}_S)'_S + \operatorname{div}(n^L \, \mathbf{w}_L) = 0 \, , \tag{2.90}$$

$$n^G(\rho^{GR})'_S + (n^G)'_S \, \rho^{GR} + n^G \rho^{GR} \operatorname{div}(\mathbf{u}_S)'_S + \operatorname{div}(n^G \rho^{GR} \mathbf{w}_G) = 0 \, .$$

Therein, $(2.90)_1$ represents the momentum balance of the mixture given by the summation of the partial momentum balances (2.86) over all constituents φ^S, φ^L and φ^G. Additionally, the Equations (2.9), $(2.53)_{1,3}$ and $(2.61)_{2,4}$ have been taken into account to get the final form of $(2.90)_1$:

$$\hat{\mathbf{p}}^S + \hat{\mathbf{p}}^L + \hat{\mathbf{p}}^G = \mathbf{0} \, , \quad \mathbf{T} := \mathbf{T}^S + \mathbf{T}^L + \mathbf{T}^G \, , \quad \rho = n^S \rho^{SR} + n^L \rho^{LR} + n^G \rho^{GR} \, . \tag{2.91}$$

Note that in the case of quasi-static conditions, the dyadic product of the diffusion velocities $\mathbf{d}_\alpha$ from $(2.61)_2$ does not occur.

Remark: The governing equations of the triphasic model (2.90) are directly connected with the set of primary variables: the overall momentum balance $(2.90)_1$ corresponds to the displacement vector $\mathbf{u}_S$, the liquid volume balance $(2.90)_2$ corresponds to the pore-liquid pressure p^{LR} and the gas mass balance $(2.90)_3$ is connected to the pore-gas pressure p^{GR}. Consequently, for the biphasic model, where the fluid phase is represented by only one materially incompressible constituent, the set of governing equations can be reduced to the overall momentum balance $(2.90)_1$ and the liquid volume balance $(2.90)_2$. $\qquad\square$

To finally close the triphasic model, constitutive equations are required for the partial *Cauchy* stress tensors $\mathbf{T}^\alpha$, the linear momentum productions $\hat{\mathbf{p}}^\beta$ of the pore-fluids, the liquid saturation s^L and the effective gas pressure p^{GR}. However, since p^{GR} is chosen as a primary variable, the constitutive equation for p^{GR} will be given in an inverse form as an equation for the effective density ρ^{GR}.

2.3.2 Effective stress concept

The evaluation of the entropy inequality (2.83) shows that the solid and fluid stresses $\mathbf{T}^S$ and $\mathbf{T}^\beta$ as well as the momentum production terms $\hat{\mathbf{p}}^\alpha$ consist of two terms, cf. *Bowen* [32], *Ehlers* [49, 53]:

$$\begin{aligned}
\mathbf{T}^S &= -n^S p^{FR} \mathbf{I} + \mathbf{T}^S_E \, , \\
\mathbf{T}^\beta &= -n^\beta p^{\beta R} \mathbf{I} + \mathbf{T}^\beta_E \, , \\
\hat{\mathbf{p}}^\beta &= p^{\beta R} \operatorname{grad} n^\beta + \hat{\mathbf{p}}^\beta_E \, .
\end{aligned} \tag{2.92}$$

Therein, the first terms are governed by the pore pressure variables, where the effective pore pressure $p = p^{FR}$ is obtained by the well-known *Dalton*'s law,

$$p = s^L p^{LR} + s^G p^{GR}, \tag{2.93}$$

whereas the second terms, the so-called extra terms, result from the solid deformation (effective stress) or the pore-fluid flow (frictional stress), respectively.

As usual for geotechnical applications, the frictional fluid forces $\mathbf{f}_E^\beta = \operatorname{div} \mathbf{T}_E^\beta$ can be neglected in comparison with the viscous interaction terms $\hat{\mathbf{p}}_E^\beta$, cf. *Ehlers et al.* [56]. Assuming therefore for the extra terms of the fluid $\mathbf{T}_E^\beta \approx \mathbf{0}$, the overall *Cauchy* stress tensor can be found via a summation of $(2.92)_{1,2}$ with $\beta = L$, G and by using the Equations (2.5), (2.11) and (2.93):

$$\mathbf{T} = -p\,\mathbf{I} + \mathbf{T}_E^S. \tag{2.94}$$

The above equation represents the well-known concept of effective stress [17, 130], which was already formulated by *Terzaghi* [139] in 1925 .

2.3.3 Solid skeleton

Within a geometrically linear approach, one starts from a linearized strain tensor $\boldsymbol{\varepsilon}_S$ for the description of the deformation of the solid skeleton. This strain tensor $\boldsymbol{\varepsilon}_S$ can be found by a linearization of the *Green-Lagrange*an strain tensor $\mathbf{E}_S$ around the natural state of φ^S:

$$\lin(\mathbf{E}_S) = \boldsymbol{\varepsilon}_S = \tfrac{1}{2}\left[\operatorname{grad}\mathbf{u}_S + (\operatorname{grad}\mathbf{u}_S)^T\right]. \tag{2.95}$$

Decomposing the overall strain $\boldsymbol{\varepsilon}_S$ into a purely elastic and a purely plastic part,

$$\boldsymbol{\varepsilon}_S = \boldsymbol{\varepsilon}_{Se} + \boldsymbol{\varepsilon}_{Sp}, \tag{2.96}$$

the solid extra stresses $\mathbf{T}_E^S$ can be described by the generalized *Hooke*an law:

$$\mathbf{T}_E^S \approx \boldsymbol{\sigma}_E^S = 2\,\mu^S\,\boldsymbol{\varepsilon}_{Se} + \lambda^S\,(\,\boldsymbol{\varepsilon}_{Se}\cdot\mathbf{I}\,)\,\mathbf{I}. \tag{2.97}$$

Therein, the *Cauchy* stress tensor $\mathbf{T}_E^S$ is approximately equal to $\boldsymbol{\sigma}_E^S$, which is the solid stress tensor under small strain conditions, and μ^S and λ^S are the *Lamé* constants of the solid skeleton. Note again that, within the geometrically linear approach, no difference between the stress tensors presented in Section 2.1.4 must be made, which leads to $\mathbf{T}_E^S \approx \boldsymbol{\tau}_E^S \approx \mathbf{P}_E^S \approx \mathbf{S}_E^S \approx \boldsymbol{\sigma}_E^S$.

Considering plastic deformations, the solid materials under study, as, e. g., sand or clayey silt, have to be modeled as so-called frictional materials. In contrast to metallic, non-porous materials, a major characteristic of such materials is that the concept of plastic incompressibility is not valid, i. e., frictional materials can undergo plastic deformations under purely hydrostatic load conditions. Furthermore, *Lade & Duncan* [99] found dilatant or contractant plastic material behavior in their triaxial tests on cohesionless soil. Consequently, an adequate yield criterion, which allows for the representation of all these
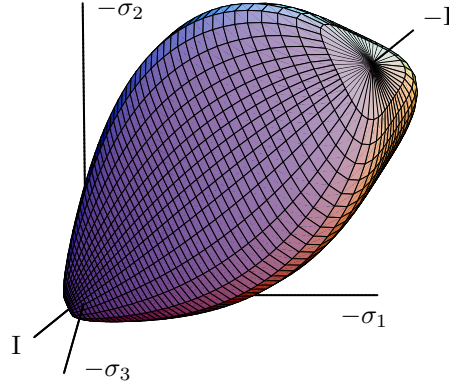
Figure 2.3: Single-surface yield criterion for cohesive-frictional materials in the principal stress space (tension positive).

effects, has to be used for a proper description. Following this, the single-surface yield criterion F by *Ehlers* [49, 50] is applied, cf. Figure 2.3:

$$
\begin{aligned}
F &= \Phi^{1/2} + \beta\, \mathrm{I} + \epsilon\, \mathrm{I}^2 - \kappa = 0\,, \\
\Phi &= \mathrm{II}^D (1 + \gamma\, \vartheta)^m + \tfrac{1}{2}\, \alpha\, \mathrm{I}^2 + \delta^2\, \mathrm{I}^4\,, \\
\vartheta &= \mathrm{III}^D / (\mathrm{II}^D)^{3/2}.
\end{aligned}
\tag{2.98}
$$

Therein, I, II^D and III^D correspond to the first principal invariant of $\boldsymbol{\sigma}_E^S$ and the (negative) second and third principal invariants of the effective stress deviator $(\boldsymbol{\sigma}_E^S)^D$, cf. Appendix A.2.2. Altogether seven material parameters,

$$
\mathcal{S}_h = \{\alpha,\, \beta,\, \delta,\, \epsilon,\, \kappa\}\,, \qquad \mathcal{S}_d = \{\gamma,\, m\}\,,
\tag{2.99}
$$

govern the shape of the yield surface in the hydrostatic ($\mathcal{S}_h$) and in the deviatoric plane ($\mathcal{S}_d$), respectively. Within this thesis, the perfect plasticity concept is assumed for using (2.98) and, therefore, the parameters included in $\mathcal{S}_h$ and in $\mathcal{S}_d$ are kept constant during the deformation process. The reader who is interested in parameter identification of $\mathcal{S}_h$ and $\mathcal{S}_d$ and in an approach to an isotropic hardening concept for the single-surface criterion (2.98) is referred to *Müllerschön* [112].

For frictional materials, the associated plasticity concept cannot be applied, for details cf., e. g., *Lade & Duncan* [99] or *Davis & Selvadurai* [40]. Thus, an additional plastic potential G has to be defined [103]:

$$
\begin{aligned}
G &= \Gamma^{1/2} + \psi_2\, \mathrm{I} + \epsilon\, \mathrm{I}^2\,, \\
\Gamma &= \psi_1\, \mathrm{II}^D + \tfrac{1}{2}\, \alpha\, \mathrm{I}^2 + \delta^2\, \mathrm{I}^4\,.
\end{aligned}
\tag{2.100}
$$

Therein, ψ_1 and ψ_2 serve to relate the dilatation angle to experimental data. Within the non-associated plasticity concept, the flow rule reads

$$
(\boldsymbol{\varepsilon}_{Sp})_S' = \Lambda\, \frac{\partial\, G}{\partial\, \boldsymbol{\sigma}_E^S}\,,
\tag{2.101}
$$

where Λ is the so-called plastic multiplier, which has to be determined in an elasto-plasticity concept via the *Kuhn-Tucker* conditions:

$$F \leq 0 \,, \qquad \Lambda \geq 0 \,, \qquad \Lambda\, F = 0 \,. \tag{2.102}$$

Remark: Dilatant or contractant plastic material behavior can be described by the above presented approach for the description of solid plasticity due to two reasons. First of all, the non-associated plasticity concept allows for a free choice of the plastic potential, and, therefore, a flow direction $(\boldsymbol{\varepsilon}_{Sp})'_S$, which is directed towards the negative direction of the hydrostatic axis I, can be modeled. The second aspect is due to the closed shape of the yield criterion. Changes of the hydrostatic pressure lead to yield points either in the brittle or in the ductile regime, thus, leading to dilatant or contractant plastic material behavior, cf. Figure 2.4. The latter effect was shown by the numerical simulation of biaxial tests by *Ehlers et al.* [60].
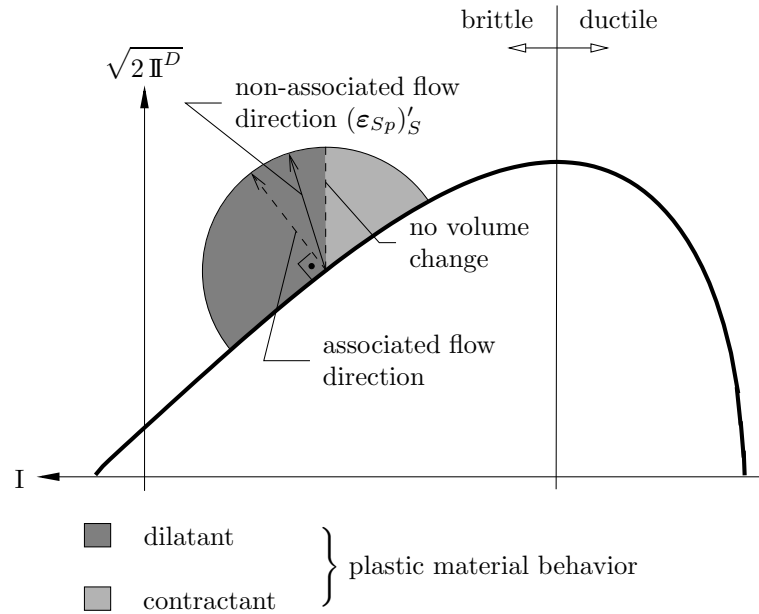

Figure 2.4: Yield criterion [49, 50] plotted in the hydrostatic plane.

$\square$

2.3.4 Fluid constituents

The triphasic model under study contains two fluid components, a liquid and a gaseous phase, whereas in the biphasic model, the fluid phase is represented only by a liquid phase. Thus, the complexity within the field of constitutive relations for the triphasic model is much higher than for the biphasic case. On the other hand, the triphasic model is a much more powerful tool to describe geotechnical problems realistically, since partially saturated conditions in soils can be described with that model. In the following section, therefore, the constitutive relations for the triphasic model [62] are first presented, and,
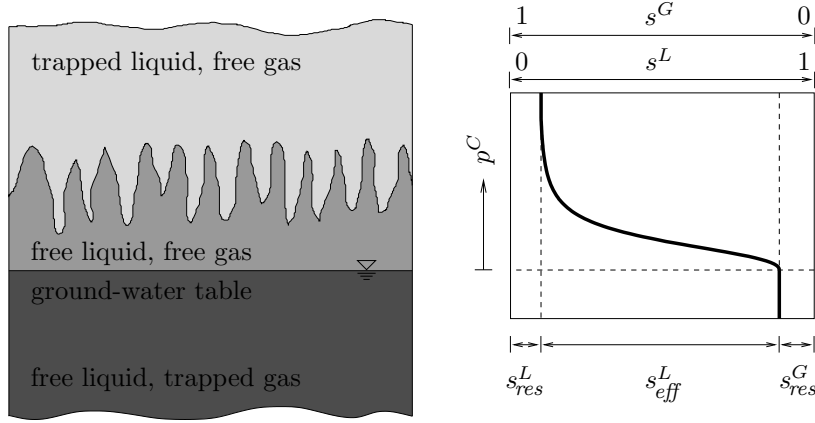
Figure 2.5: Zones of a partially saturated soil.

after that, these relations are simplified with respect to the necessary constitutive settings for the fluid phase φ^F of the biphasic model.

Triphasic model

The extra momentum production terms $\hat{\mathbf{p}}_E^\beta$ are related to the seepage velocities $\mathbf{w}_\beta$ via

$$\hat{\mathbf{p}}_E^\beta = -(n^\beta)^2\,\gamma^{\beta R}\,(\mathbf{K}_r^\beta)^{-1}\,\mathbf{w}_\beta\,, \tag{2.103}$$

where $\gamma^{\beta R}$ is the specific weight and $\mathbf{K}_r^\beta$ the relative permeability tensor of the constituent φ^β. Note that the tensor $\mathbf{K}_r^\beta$ includes both the relative permeabilities depending on the saturation of φ^β and the *Darcy* permeabilities, which are specified under fully saturated conditions, i. e., $s^\beta = 1$. The relative permeability tensor $\mathbf{K}_r^\beta$ is defined via the product between the so-called relative permeability factor κ_r^β and the *Darcy* permeability tensor $\mathbf{K}^\beta$:

$$\mathbf{K}_r^\beta = \kappa_r^\beta\,\mathbf{K}^\beta\,. \tag{2.104}$$

For a proper determination of the relative permeability factor κ_r^β, one usually defines three different zones within a partially saturated soil, cf. Figure 2.5 (left). In the zone beneath the ground-water table, most of the pore-space is filled with the pore-liquid. In this so-called saturated domain, the mobility of the pore-liquid is governed by the *Darcy* permeability and only a residual saturation of trapped pore-gas s_{res}^G is present. In a certain height above the ground-water table, in the so-called empty domain, the situation is the other way round, which means that the pore-gas is mobile and a small amount of pore-liquid is trapped with the residual saturation s_{res}^L. In the partially saturated or unsaturated domain, which is located in between these two zones, both the pore-liquid and the pore-gas are mobile. This domain is defined by a lower bound and an upper bound for the effective saturation of the liquid: $0 < s_{eff}^L < 1$, cf. Figure 2.5 (right). A relation between the saturation s^L and the effective saturation s_{eff}^L can be found easily by
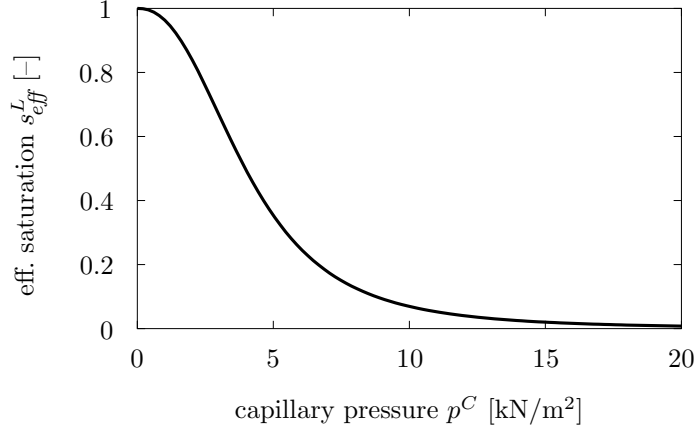
Figure 2.6: Capillary-pressure-saturation relation by *van Genuchten* [77].

the following two constraints, cf. *Finsterle* [73]:

$$s^L(s_{eff}^L = 0) = s_{res}^L \quad \text{and} \quad s^L(s_{eff}^L = 1) = 1 - s_{res}^G$$

$$\rightsquigarrow \quad s^L = s_{eff}^L (1 - s_{res}^L - s_{res}^G) + s_{res}^L . \tag{2.105}$$

In order to include the above mentioned different fluid mobilities through a relation between the pore pressures and the effective liquid saturation, the capillary pressure p^C is introduced via

$$p^C = p^{GR} - p^{LR} . \tag{2.106}$$

Following this procedure, relations between the effective liquid saturation s_{eff}^L and the capillary pressure p^C were set up by *Brooks & Corey* [37] or *van Genuchten* [77]. In the framework of this thesis, the ansatz by *van Genuchten* is used, cf. Figure 2.6:

$$s_{eff}^L = [\, 1 + (\alpha_{gen}\, p^C)^{j_{gen}}\,]^{-h_{gen}} . \tag{2.107}$$

Therein, α_{gen}, j_{gen} and h_{gen} are material parameters. Finally, the relative permeability factors κ_r^L and κ_r^G are defined within the *van Genuchten* model by

$$
\begin{aligned}
\kappa_r^L &= (s_{eff}^L)^{\epsilon_{gen}} \{\, 1 - [\, 1 - (s_{eff}^L)^{1/h_{gen}}\,]^{h_{gen}}\, \}^2 , \\
\kappa_r^G &= (1 - s_{eff}^L)^{\gamma_{gen}} [\, 1 - (s_{eff}^L)^{1/h_{gen}}\,]^{2\, h_{gen}}
\end{aligned}
\tag{2.108}
$$

with the additional material parameters ϵ_{gen} and γ_{gen}. Following this, a trapped pore-liquid ($\kappa_r^L = 0$) is obtained for a vanishing effective saturation, whereas a fully mobile pore-liquid ($\kappa_r^L = 1$) is obtained in the saturated domain, viz $s_{eff}^L = 1$. Looking at the pore-gas, equivalent statements hold, cf. Figure 2.7. For a more detailed description on the interaction of different pore-fluids, the interested reader is referred to the work by *Helmig* [89].
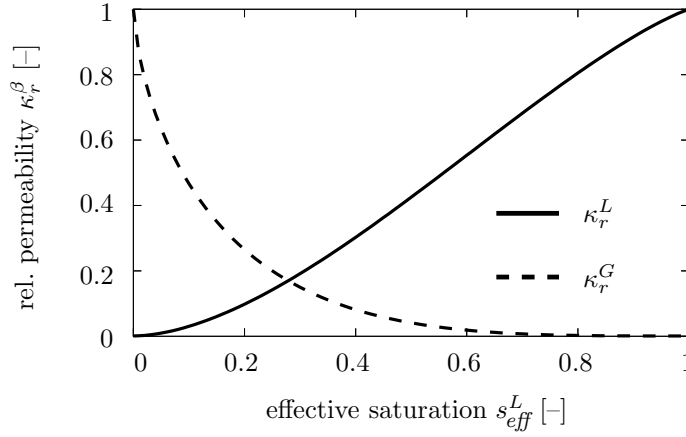
Figure 2.7: Relative permeability factors by *van Genuchten* [77].

Looking at the *Darcy* permeabilities, a relation between $\mathbf{K}^{\beta}$ and the intrinsic permeability tensor $\mathbf{K}^{S}$ is given by

$$\mathbf{K}^{\beta} = \frac{\gamma^{\beta R}}{\mu^{\beta R}} \mathbf{K}^{S},\tag{2.109}$$

where $\mu^{\beta R}$ is the effective shear viscosity of the fluid β. For the description of the deformation dependence of $\mathbf{K}^{S}$, the ansatz of *Eipper* [65] is chosen:

$$\mathbf{K}^{S} = \left(\frac{1 - n^{S}}{1 - n_{0S}^{S}}\right)^{\pi} \mathbf{K}_{0S}^{S}.\tag{2.110}$$

Therein, the actual volume fraction n^{S} of the solid is determined by (2.88). In the above equation, π is a material parameter and $\mathbf{K}_{0S}^{S}$ represents the intrinsic permeability tensor of the undeformed skeleton. In case of an isotropic solid material, this tensorial quantity is reduced to a scalar coefficient K_{0S}^{S},

$$\mathbf{K}_{0S}^{S} = K_{0S}^{S} \mathbf{I},\tag{2.111}$$

which, in analogy to (2.109), again can be related to an initial *Darcy* permeability coefficient k_{0S}^{β}:

$$k_{0S}^{\beta} = \frac{\gamma^{\beta R}}{\mu^{\beta R}} K_{0S}^{S}.\tag{2.112}$$

Insertion of (2.103) into the quasi-static fluid momentum balances $(2.86)_{2,3}$ gives the already mentioned *Darcy*-like equations:

$$n^{\beta} \mathbf{w}_{\beta} = -\frac{\mathbf{K}_{r}^{\beta}}{\gamma^{\beta R}} \left(\operatorname{grad} p^{\beta R} - \rho^{\beta R} \mathbf{g}\right).\tag{2.113}$$

Note again that with the above equations ($\beta = L, G$), the seepage velocities $\mathbf{w}_{\beta}$ can be dropped as primary variables.

Finally, the constitutive setting for the effective gas density ρ^{GR} is chosen by means of the ideal gas law by *Boyle*:

$$\rho^{GR} = \frac{p^{GR} + p_{0}}{\bar{R}^{G} \theta}.\tag{2.114}$$

Therein, p_0 denotes the ambient pressure, $\bar{R}^G$ the specific gas constant of the pore-gas and θ the absolute Kelvin's temperature, which, within this thesis, is constant ($\theta = \text{const.}$) due to the assumption of an overall isothermal problem.

Biphasic model

In the biphasic model, the pore-liquid is the only fluid component ($\varphi^L = \varphi^F$), thus, the above derived equations for the triphasic model have to be modified accordingly. By leaving the pore-gas from the equations for the triphasic model, the following relations can be concluded straightforwardly:

$$s^L = 1 \quad \rightsquigarrow \quad s^L_{\mathit{eff}} = 1 \quad \rightsquigarrow \quad \kappa^L_r = 1 \,. \tag{2.115}$$

Due to these relations, the tensor $\mathbf{K}^\beta_r$, which includes both the relative and the *Darcy* permeabilities, can be simplified resulting in the *Darcy* permeability tensor $\mathbf{K}^F$ from (2.109). According to (2.103), this leads to the following relation for the extra momentum production term,

$$\hat{\mathbf{p}}^F_E = -(n^F)^2 \, \gamma^{FR} \, (\mathbf{K}^F)^{-1} \, \mathbf{w}_F \,, \tag{2.116}$$

and, finally, to the well-known *Darcy* equation for the description of the fluid flow in a fully saturated porous medium, cf. (2.113):

$$n^F \mathbf{w}_F = -\frac{\mathbf{K}^F}{\gamma^{FR}} \left(\operatorname{grad} p - \rho^{FR} \mathbf{g} \right) . \tag{2.117}$$

Chapter 3:
Spatial and temporal discretization

For the numerical realization of the porous media models, which were presented in the last chapter, all the describing quantities, like, e. g., displacement or pore-liquid pressure, have to be discretized in both the spatial and the temporal domain. Thereby, it is a common procedure to carry out the spatial and the temporal discretization sequentially by two different methods, i. e., first the discretization in space by use of the finite element method (FEM) and, second, the discretization in time by use of a finite difference scheme. After that, the resulting nonlinear system of equations has to be solved accordingly for a reliable numerical solution of the prescribed governing equations.

Within this chapter, the above mentioned discretization methods are introduced very briefly, with special emphasis of the numerical difficulties coming from the multiphasic character of the considered models. Subsequently, the solution of the resulting system of nonlinear equations is discussed. The reader who is interested in a more fundamental introduction of the FEM is referred to the works by *Strang & Fix* [134], *Oden & Reddy* [116], *Hughes* [92], *Bathe* [7], *Schwarz* [127], *Eriksson et al.* [68], *Braess* [34], *Ellsiepen* [66] and *Zienkiewicz & Taylor* [156, 157]. Detailed information on the numerical time integration of ordinary differential equations and differential-algebraic equations can be found in the works by *Hairer et al.* [82, 83], *Wood* [154], *Törnig & Spellucci* [140] and *Strehmel & Weiner* [135].

Besides the above mentioned sequential combination of the two different discretization methods, other strategies exist, which try to deal with the numerical realization of the resulting system of differential equations in a more uniform way. In these strategies, the finite element method is chosen for both the spatial and the temporal domain. The first papers on this topic were published in 1969 by *Argyris & Scharpf* [2], *Fried* [75] and *Oden* [115]. Further developments in this field with different emphasis can be found, e. g., in the works by *Hughes & Hulbert* [93], *Hulbert & Hughes* [94], *Borri & Bottasso* [23], *Betsch & Steinmann* [14, 15] and *Ehlers & Ammann* [54]. Thereby, as far as the author is aware, the only paper which applies the FEM in time and space to multiphasic problems was published by *Steeb et al.* [131] in 2003. In the framework of this thesis, these discretization methods are only mentioned here and should not be further investigated.

3.1   Finite element method

3.1.1   Strong and weak formulation

For the spatial discretization, in a first step, the governing equations of the bi- and triphasic models have to be transformed from the strong into a weak formulation. In the following, this procedure is going to be presented using the example of the governing

equations of the triphasic model, cf. (2.90):

$$\text{div}\,(\boldsymbol{\sigma}_E^S - p\,\mathbf{I}) + \rho\,\mathbf{g} = \mathbf{0}\,,$$

$$(n^L)'_S + n^L\,\text{div}\,(\mathbf{u}_S)'_S + \text{div}\,(n^L\,\mathbf{w}_L) = 0\,, \qquad (3.1)$$

$$n^G(\rho^{GR})'_S + (n^G)'_S\,\rho^{GR} + n^G\rho^{GR}\,\text{div}\,(\mathbf{u}_S)'_S + \text{div}\,(n^G\rho^{GR}\,\mathbf{w}_G) = 0\,.$$

Equations (3.1) together with the corresponding initial and boundary conditions represent the so-called strong formulation of the initial boundary-value problem. This is due to the fact that in the above relations, equilibrium is fulfilled at each point $\mathbf{x}$ of the underlying domain Ω of the body $\mathcal{B}$. Obviously, this requirement is too strict for the numerical investigation of arbitrary problems, and, therefore, the weak formulation has to be introduced at this point. In order to obtain such a weak formulation, the single Equations (3.1) have to be (scalarly) multiplied with a corresponding test function and integrated over the domain Ω. After the application of the chain rule and of the *Gaussian* integral theorem, the so-called *Neumann* (or natural) boundary terms can be identified. In this final form of the weak formulation, equilibrium is no longer fulfilled point-wise but only in an integral manner, i. e., in a weak sense.

As already stated in the remark on Page 26, the governing equations of the triphasic model (3.1) are directly connected with the respective primary variables. In this connection, the choice of the corresponding test functions is straightforward. Consequently, the trial and test spaces for the resulting displacement-pressure-pressure formulation are defined as follows:

$$
\begin{aligned}
\mathcal{S}_u(t) &= \{\,\mathbf{u}_S && \in H^1(\Omega)^D : \mathbf{u}_S(\mathbf{x}) && = \bar{\mathbf{u}}_S(\mathbf{x},\,t) && \text{on } \Gamma_u\,\}\,, \\[4pt]
\mathcal{S}_{pl}(t) &= \{\,p^{LR} && \in H^1(\Omega) \;\; : p^{LR}(\mathbf{x}) && = \bar{p}^{LR}(\mathbf{x},\,t) && \text{on } \Gamma_{pl}\,\}\,, \\[4pt]
\mathcal{S}_{pg}(t) &= \{\,p^{GR} && \in H^1(\Omega) \;\; : p^{GR}(\mathbf{x}) && = \bar{p}^{GR}(\mathbf{x},\,t) && \text{on } \Gamma_{pg}\,\}\,, \\[4pt]
\mathcal{T}_u &= \{\,\delta\mathbf{u}_S && \in H^1(\Omega)^D : \delta\mathbf{u}_S(\mathbf{x}) && = \mathbf{0} && \text{on } \Gamma_u\,\}\,, \\[4pt]
\mathcal{T}_{pl} &= \{\,\delta p^{LR} && \in H^1(\Omega) \;\; : \delta p^{LR}(\mathbf{x}) && = 0 && \text{on } \Gamma_{pl}\,\}\,, \\[4pt]
\mathcal{T}_{pg} &= \{\,\delta p^{GR} && \in H^1(\Omega) \;\; : \delta p^{GR}(\mathbf{x}) && = 0 && \text{on } \Gamma_{pg}\,\}\,.
\end{aligned}
\qquad (3.2)
$$

Therein, $D \in \{1,\,2,\,3\}$ represents the spatial dimension of the problem and $H^1(\Omega)$ is the standard *Sobolev* space. Furthermore, $\bar{\mathbf{u}}_S$, $\bar{p}^{LR}$ and $\bar{p}^{GR}$ are the *Dirichlet* (or essential) boundary conditions of the problem under consideration. As usual, *Dirichlet* boundary conditions are exactly fulfilled by the proper choice of the trial (or ansatz) functions $\mathbf{u}_S$, p^{LR} and p^{GR}. Additionally, the corresponding test functions $\delta\mathbf{u}_S$, δp^{LR} and δp^{GR} vanish at *Dirichlet* boundaries.

For each governing equation from (3.1), *Neumann* and *Dirichlet* boundary conditions have to be defined. By doing this, the boundary $\Gamma = \partial\Omega$ of the domain Ω is split up for each

of the three governing equations in the following way:

$$\Gamma = \Gamma_u \cup \Gamma_t, \qquad \emptyset = \Gamma_u \cap \Gamma_t,$$

$$\Gamma = \Gamma_{pl} \cup \Gamma_v, \qquad \emptyset = \Gamma_{pl} \cap \Gamma_v, \tag{3.3}$$

$$\Gamma = \Gamma_{pg} \cup \Gamma_q, \qquad \emptyset = \Gamma_{pg} \cap \Gamma_q.$$

The above equations state that for each unknown quantity $\mathbf{u}_S$, p^{LR} or p^{GR} the boundary Γ is divided into a *Dirichlet* boundary Γ_u, Γ_{pl} and Γ_{pg} and a *Neumann* boundary Γ_t, Γ_v and Γ_q. Furthermore, boundary parts are not permitted, on which both *Dirichlet* and *Neumann* boundary conditions for one unknown quantity are defined.

For the derivation of the weak formulation of the overall momentum balance $(3.1)_1$, in a first step, this equation is scalarly multiplied with the test function for the solid displacement $\delta\mathbf{u}_S$ and integrated over the domain Ω:

$$\int_\Omega \left[\operatorname{div}(\boldsymbol{\sigma}_E^S - p\,\mathbf{I}) + \rho\,\mathbf{g} \right] \cdot \delta\mathbf{u}_S \, \mathrm{d}v = 0 \quad \forall \quad \delta\mathbf{u}_S \in \mathcal{T}_u. \tag{3.4}$$

Additional application of the chain rule

$$\operatorname{div}(\boldsymbol{\sigma}_E^S - p\,\mathbf{I}) \cdot \delta\mathbf{u}_S = \operatorname{div}\left[(\boldsymbol{\sigma}_E^S - p\,\mathbf{I})^T \delta\mathbf{u}_S\right] - (\boldsymbol{\sigma}_E^S - p\,\mathbf{I}) \cdot \operatorname{grad}\delta\mathbf{u}_S \tag{3.5}$$

and of the *Gaussian* integral theorem

$$\int_\Omega \operatorname{div}\left[(\boldsymbol{\sigma}_E^S - p\,\mathbf{I})^T \delta\mathbf{u}_S\right] \mathrm{d}v \;=\; \int_{\Gamma_t} \left[(\boldsymbol{\sigma}_E^S - p\,\mathbf{I})^T \delta\mathbf{u}_S\right] \cdot \mathbf{n} \, \mathrm{d}a$$

$$= \int_{\Gamma_t} \delta\mathbf{u}_S \cdot \underbrace{\left[(\boldsymbol{\sigma}_E^S - p\,\mathbf{I})\,\mathbf{n}\right]}_{\bar{\mathbf{t}}} \mathrm{d}a \tag{3.6}$$

finally yields the weak formulation of $(3.1)_1$:

$$\int_\Omega (\boldsymbol{\sigma}_E^S - p\,\mathbf{I}) \cdot \operatorname{grad}\delta\mathbf{u}_S \, \mathrm{d}v - \int_\Omega \rho\,\mathbf{g} \cdot \delta\mathbf{u}_S \, \mathrm{d}v = \int_{\Gamma_t} \bar{\mathbf{t}} \cdot \delta\mathbf{u}_S \, \mathrm{d}a \quad \forall \quad \delta\mathbf{u}_S \in \mathcal{T}_u. \tag{3.7}$$

As the above equation is the weak formulation of the momentum balance of the mixture, the surface traction $\bar{\mathbf{t}}$ acts on all constituents, i. e., the solid, the liquid and the gaseous phase. Note that this property is important for the modeling of a boundary-value problem, as no separation of the boundary conditions into actions on the different phases is needed and, thus, physically reasonable boundary conditions can be defined.

After multiplication of Equation $(3.1)_2$ with the corresponding test function δp^{LR} and application of the above mentioned steps in an analogous way, the weak formulation of the pore-liquid volume balance reads:

$$\int_\Omega \left[(n^L)'_S + n^L \operatorname{div}(\mathbf{u}_S)'_S \right] \delta p^{LR} \, \mathrm{d}v -$$

$$- \int_\Omega n^L \mathbf{w}_L \cdot \operatorname{grad}\delta p^{LR} \, \mathrm{d}v = \int_{\Gamma_v} \bar{v}^L \, \delta p^{LR} \, \mathrm{d}a \quad \forall \quad \delta p^{LR} \in \mathcal{T}_{pl}. \tag{3.8}$$

Therein, $\bar{v}^L = n^L \, \mathbf{w}_L \cdot \mathbf{n}$ represents the efflux of liquid.

Multiplying the pore-gas mass balance $(3.1)_3$ with the test function δp^{GR} and, again, applying the chain rule and the *Gaussian* integral theorem, the weak formulation for the determination of the pore-gas pressure p^{GR} is found as

$$
\int_\Omega \left[\, (n^G \, \rho^{GR})'_S + n^G \, \rho^{GR} \, \mathrm{div} \, (\mathbf{u}_S)'_S \, \right] \delta p^{GR} \, \mathrm{d}v -
$$

$$
- \int_\Omega n^G \, \rho^{GR} \, \mathbf{w}_G \cdot \mathrm{grad} \, \delta p^{GR} \, \mathrm{d}v = \int_{\Gamma_q} \bar{q}^G \, \delta p^{GR} \, \mathrm{d}a \quad \forall \quad \delta p^{GR} \in \mathcal{T}_{pg} \, ,
\tag{3.9}
$$

where $\bar{q}^G = n^G \, \rho^{GR} \, \mathbf{w}_G \cdot \mathbf{n}$ is interpreted as the efflux of gaseous mass through the *Neumann* boundary Γ_q.

3.1.2   Finite element mesh and *Bubnov-Galerkin* method

The spatial discretization of the domain Ω, which contains the body $\mathcal{B}$ under study, requires the partition into non-overlapping subdomains, the so-called finite elements (or cells) C:

$$
\Omega \approx \Omega^h = \bigcup_{C \in \mathcal{C}} C \, .
\tag{3.10}
$$

The spatially discretized domain Ω^h is also called the finite element mesh. In the three-dimensional (3-d) case, each cell $C \in \mathcal{C}$, with $\mathcal{C}$ representing the set of all cells in the mesh, consists of faces $F(C)$, edges $E(C)$ and nodes (or points) $P(C)$, cf. Figure 3.1. Reducing the dimension of the problem under study towards the 2-d case, no faces are
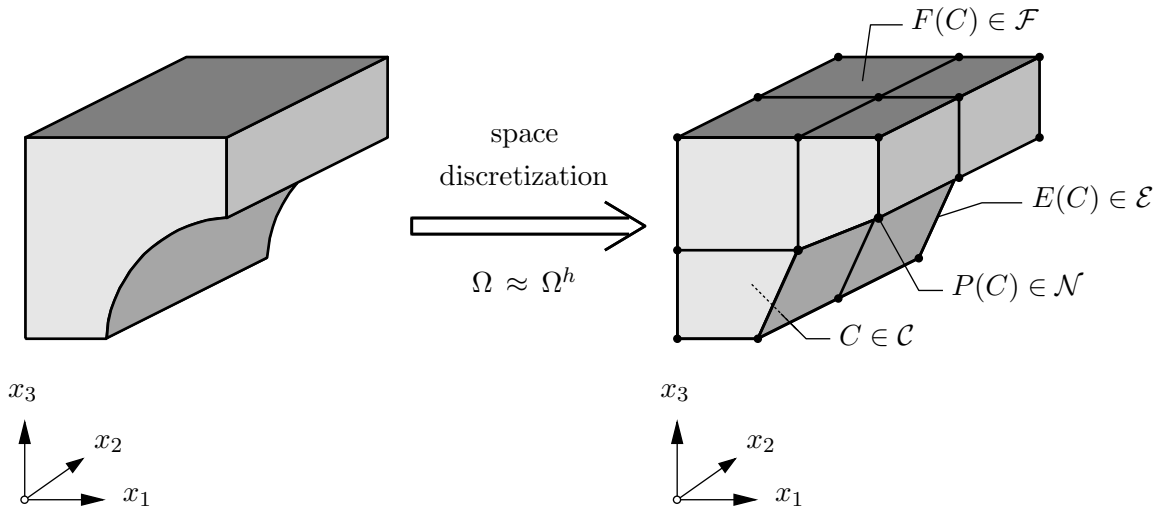

Figure 3.1: Space discretization with finite elements (hexahedra).

available and, consequently, in the 1-d case, no faces and edges are defined. Furthermore, the set of all faces $\mathcal{F}$, all edges $\mathcal{E}$ and all nodes $\mathcal{N}$ of the FE mesh are given by

$$\mathcal{F} = \bigcup_{F \in \mathcal{F}} F(C) \,, \qquad \mathcal{E} = \bigcup_{E \in \mathcal{E}} E(C) \,, \qquad \mathcal{N} = \bigcup_{P \in \mathcal{N}} P(C) \,. \tag{3.11}$$

In the next step, the weak formulations (3.7) – (3.9), which are up to now defined continuously in the infinite-dimensional spaces of the ansatz and test functions (3.2), are approximated by finite-dimensional (N-dimensional) subspaces. For an abstract setting of this procedure, the interested reader is referred to *Ellsiepen* [66] and *Ehlers & Ellsiepen* [59]. Here, this procedure is discussed using the example of the displacement-pressure-pressure formulation (3.1). Following this, on a mesh with N nodal points, the following space discrete ansatz and test functions are introduced:

$$
\begin{aligned}
\mathbf{u}_S(\mathbf{x}, t) &\approx \mathbf{u}_S^h(\mathbf{x}, t) &= \bar{\mathbf{u}}_S^h(\mathbf{x}, t) &+ \sum_{j=1}^{N} \boldsymbol{\phi}_u^j(\mathbf{x}) \, \mathbf{u}_S^j(t) & \in \mathcal{S}_u^h(t) \,, \\
p^{LR}(\mathbf{x}, t) &\approx p^{LRh}(\mathbf{x}, t) &= \bar{p}^{LRh}(\mathbf{x}, t) &+ \sum_{j=1}^{N} \phi_{pl}^j(\mathbf{x}) \, p^{LRj}(t) & \in \mathcal{S}_{pl}^h(t) \,, \\
p^{GR}(\mathbf{x}, t) &\approx p^{GRh}(\mathbf{x}, t) &= \bar{p}^{GRh}(\mathbf{x}, t) &+ \sum_{j=1}^{N} \phi_{pg}^j(\mathbf{x}) \, p^{GRj}(t) & \in \mathcal{S}_{pg}^h(t) \,, \\
\delta\mathbf{u}_S(\mathbf{x}) &\approx \delta\mathbf{u}_S^h(\mathbf{x}) &= &\sum_{j=1}^{N} \boldsymbol{\phi}_u^j(\mathbf{x}) \, \delta\mathbf{u}_S^j & \in \mathcal{T}_u^h \,, \\
\delta p^{LR}(\mathbf{x}) &\approx \delta p^{LRh}(\mathbf{x}) &= &\sum_{j=1}^{N} \phi_{pl}^j(\mathbf{x}) \, \delta p^{LRj} & \in \mathcal{T}_{pl}^h \,, \\
\delta p^{GR}(\mathbf{x}) &\approx \delta p^{GRh}(\mathbf{x}) &= &\sum_{j=1}^{N} \phi_{pg}^j(\mathbf{x}) \, \delta p^{GRj} & \in \mathcal{T}_{pg}^h \,.
\end{aligned}
\tag{3.12}
$$

Therein, $\{\bar{\mathbf{u}}_S^h, \bar{p}^{LRh}, \bar{p}^{GRh}\}$ define the *Dirichlet* boundary conditions and $\{\boldsymbol{\phi}_u^j, \phi_{pl}^j, \phi_{pg}^j\}$ represent the global basis functions of the trial or test functions, respectively. For the global basis functions of the displacement, the following relation holds: $\boldsymbol{\phi}_u^j = [\phi_{u_1}^j, \dots, \phi_{u_D}^j]$. The basis functions introduced above are in each case linearly independent and fulfill the homogeneous *Dirichlet* boundary conditions

$$
\begin{aligned}
\phi_{u_d}^j &= 0 \quad \text{on } \Gamma_{u_d}^h \,, & j = 1, \dots, N \,, \quad d = 1, \dots, D \,, \\
\phi_{pl}^j &= 0 \quad \text{on } \Gamma_{pl}^h \,, & j = 1, \dots, N \,, \\
\phi_{pg}^j &= 0 \quad \text{on } \Gamma_{pg}^h \,, & j = 1, \dots, N \,,
\end{aligned}
\tag{3.13}
$$

where $D \in \{1, 2, 3\}$ represents the spatial dimension of the problem under study. Note that the global basis functions of the trial functions $\{\boldsymbol{\phi}_u^j, \phi_{pl}^j, \phi_{pg}^j\}$ depend only on the

spatial position $\mathbf{x}$ and the unknown nodal quantities $\{\mathbf{u}_S^j, p^{LRj}, p^{GRj}\}$, which are also called degrees of freedom, are only time-dependent.

When regarding the definitions for the approximated trial and test functions (3.12), one recognizes that the same basis functions $\{\boldsymbol{\phi}_u^j, \phi_{pl}^j, \phi_{pg}^j\}$ are used for the respective approximations. Such an approach is known as *Bubnov-Galerkin* method (or simply *Galerkin* method). Obviously, it is alternatively possible to choose different basis functions for the trial and test spaces. This more general case is known as *Petrov-Galerkin* method. Applications of this approach can be found, e. g., in the framework of numerical stabilization techniques [61] and of time integration methods [54].

For an efficient implementation of the trial and test functions, each nodal point $\bar{P} \in \mathcal{N}$ is assigned to a basis function ϕ_{dof}^j with supports only in the finite elements $C \in \mathcal{C}_{\bar{P}}$, i. e., elements C, which are attached to the respective node $\bar{P}$:

$$\phi_{dof}^j(\mathbf{x}) = 0 \,, \qquad \text{if} \quad \mathbf{x} \notin \bigcup_{C \in \mathcal{C}_{\bar{P}}} C \,, \qquad dof \in \{u_d,\, pl,\, pg\} \,. \tag{3.14}$$

This choice for the basis functions leads to simple structures of the resulting linear system of equations, i. e., to sparse matrices. Furthermore, the chosen basis functions ϕ_{dof}^j are normalized, viz:

$$\phi_{dof}^j(\mathbf{x}_i) = \delta_i^j \,, \qquad i,\, j = 1, \ldots, N \,. \tag{3.15}$$

Therein, δ_i^j is the *Kronecker* symbol, which gives for $i = j$ the value 1 and otherwise the value 0. By choosing this property for the basis functions, it is assured that the nodal quantities $\{\mathbf{u}_S^i, p^{LRi}, p^{GRi}\}$ at the node i exactly correspond to the value of the approximated solution, such that, for example, the following relation holds for the pore-liquid pressure p^{LRh}:

$$\underline{\text{PSfrag replacements}} \qquad p^{LRh}(\mathbf{x}_i) = \sum_{j=1}^{N} \phi_{pl}^j(\mathbf{x}_i)\, p^{LRj} = p^{LRi} \,. \tag{3.16}$$

The properties (3.14) and (3.15) are illustrated in Figure 3.2 at a simple one-dimensional example for the linear basis function $\phi^3(x)$ at the node P_3 in a FE mesh with 4 elements.
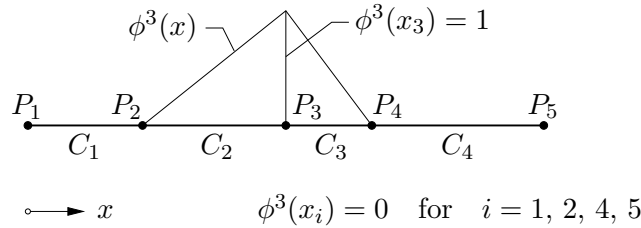

Figure 3.2: Illustration of the properties (3.14) and (3.15) for the basis functions.

In order to obtain the required number of equations for the determination of all degrees of freedom, the test functions are interpreted in a certain way, cf. *Ellsiepen* [66]. This

strategy is now shown exemplarily at the example of the weak formulation of the overall momentum balance. Equation (3.7) states that the weak formulation has to be fulfilled for all test functions $\delta \mathbf{u}_S \in \mathcal{T}_u$. Consequently, after the space discretization, this must hold for all $\delta \mathbf{u}_S^h \in \mathcal{T}_u^h$. For a spatial discretization by a FE mesh with N nodal points, the weak formulation (3.7) results for a general D-dimensional case in a system with $D \cdot N$ degrees of freedom $\mathbf{u}_S^j = \left[u_{S1}^j, \ldots, u_{SD}^j \right]^T$ with $j = 1, \ldots, N$. Choosing for the test functions

$$\delta u_{S1}^1 = 1, \qquad \delta u_{S1}^j = 0 \quad \text{for} \quad j = 2, \ldots, N \quad \text{and}$$

$$\delta u_{Sd}^j = 0 \quad \text{for} \quad j = 1, \ldots, N, \quad d = 2, \ldots, D, \tag{3.17}$$

the equation for the determination of the "first degree of freedom of the horizontal solid displacement" is obtained. Proceeding analogously for the other degrees of freedom leads to a system of $D \cdot N$ linearly independent equations.

3.1.3   Mixed finite elements

The spatial discretization of the underlying biphasic or triphasic models within the FEM results in so-called mixed finite element formulations. This is due to the fact that, in addition to the primary variable (solid) displacement $\mathbf{u}_S$, other primary variables, e. g., in case of the triphasic model the pore-liquid pressure p^{LR} and the pore-gas pressure p^{GR}, have to be considered.
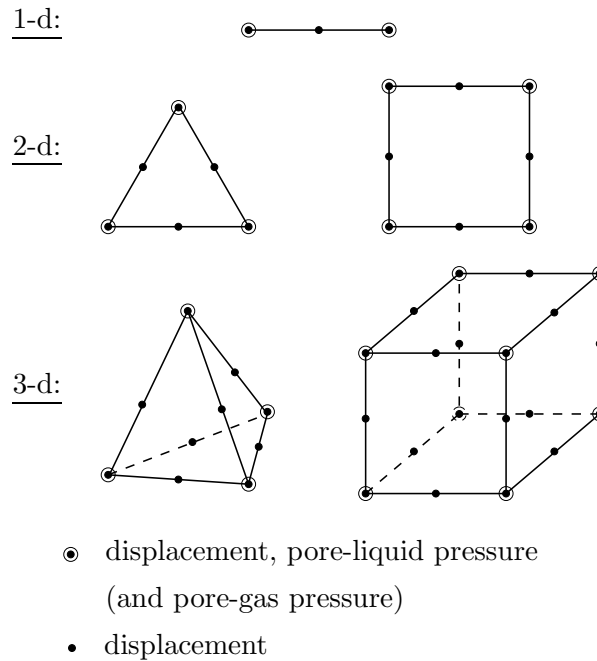

Figure 3.3: *Taylor-Hood* elements in all spatial dimensions.

The main difficulty within such a mixed finite element formulation consists of the correct choice of the proper ansatz functions, e. g., in case of the triphasic model, the ansatz functions included in $(3.12)_{1-3}$. There, the chosen ansatz functions are not arbitrary but have to fulfill the so-called inf-sup condition (*Babuška-Brezzi* condition) for a stable finite element formulation. The reader who is interested in more information on this topic, e. g., the mathematical background of the inf-sup condition or a survey of possible mixed finite element formulations, is referred to the works by *Brezzi & Fortin* [35], *Braess* [34], *Langtangen & Tveito* [100] and *Wieners* [149].

Within the framework of this thesis, quadratic ansatz functions for the solid displacement $\mathbf{u}_S^h$ and linear ansatz functions for the pressure terms p^{LRh} and p^{GRh} are chosen. This combination fulfills the above mentioned inf-sup condition [35] and, therefore, provides a stable finite element formulation. Mixed finite elements of this type are well-known under the name of *Taylor-Hood* elements and are very often introduced in the literature in the context of the *Stokes* problem [34, 100], which is a model coming from fluid mechanics with the primary variables velocity and pressure. Examples for *Taylor-Hood* elements are given in Figure 3.3, where in the 1-d case a line, in the 2-d case a triangle and a quadrilateral and in the 3-d case a tetrahedron and a hexahedron are exemplarily shown.

3.1.4   Element-wise evaluation of the weak formulations

Within a finite element program, all essential quantities for the solution of the problem, like, e. g., the residual or the tangent coming from the consistent linearization (cf. Section 3.3.2), are evaluated locally on the element level and, thereafter, these quantities are assembled to the global system. Furthermore, within this element-wise evaluation, the necessary trial and test functions are always expressed with respect to a so-called reference element, which leads directly to the introduction of the geometry transformation and of the local coordinates $\boldsymbol{\xi}$.

Starting from a reference element C_r described within local coordinates $\boldsymbol{\xi}$, a relation to the physical coordinate system $\mathbf{x}$ can be established by the following equation:

$$\mathbf{x}(\boldsymbol{\xi}) = \sum_{j=1}^{N_g} \boldsymbol{\phi}_{geo}^j(\boldsymbol{\xi}) \, \mathbf{x}_j \, . \tag{3.18}$$

Therein, $\mathbf{x}(\boldsymbol{\xi})$ describes an arbitrary position within a finite element depending on the local coordinates $\boldsymbol{\xi}$, N_g is the number of nodes in the element and $\mathbf{x}_j$ are the global (physical) coordinates of the nodal points in this element. Furthermore, $\boldsymbol{\phi}_{geo}^j(\boldsymbol{\xi})$ are the basis functions of the geometry transformation fulfilling the properties (3.14) and (3.15). Note that in contrast to the basis functions ϕ_{dof}^j discussed up to now, the basis functions in (3.18) are formulated with respect to a local coordinate system.

Looking at the geometry transformation, different basis functions $\boldsymbol{\phi}_{geo}^j$ can be chosen. If the basis function for the approximation of the primary variables ϕ_{dof}^j is equal to the one for the geometry transformation $\boldsymbol{\phi}_{geo}^j$, it is called an isoparametric mapping. Otherwise, the terms subparametric (ansatz for geometry transformation lower than for approximation
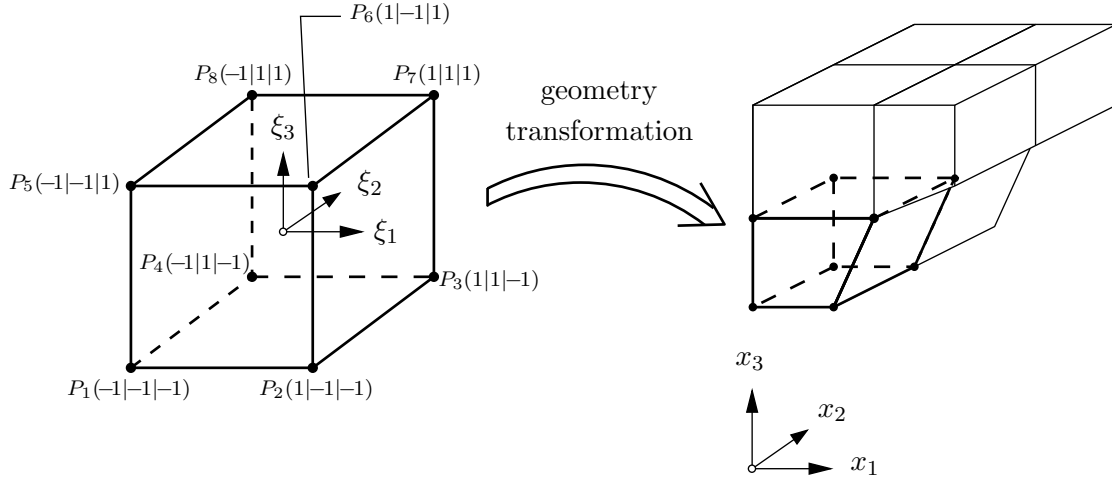
Figure 3.4: Geometry transformation for hexahedra with linear ansatz functions.

of primary variables) and superparametric (ansatz for geometry transformation higher than for approximation of primary variables) mapping are used. Obviously, in a mixed finite element formulation, where the single primary variables have to be approximated with different ansatz functions due to stability reasons, these classifications can be used no longer for the description of the entire ansatz. Therein, it is only possible to classify the ansatz functions with regard to the respective primary variables. Choosing quadratic ansatz functions for the geometry transformation together with the *Taylor-Hood* elements introduced in the last section, one can call this an isoparametric mapping for the solid displacement and superparametric mappings for the pressure terms.

Figure 3.4 shows an example of a geometry transformation for hexahedra with linear ansatz functions. Looking at the reference element on the left part of Figure 3.4, the fixed local coordinates of the 8 nodal points representing the (tri-)linear ansatz are shown.

The weak formulations, which are the basis for the finite element calculation, are expressed in an integral form, cf. the weak formulations (3.7), (3.8) and (3.9) of the triphasic model under study. For the element-wise evaluation of these formulations within a reference element C_r, the single integrals have to be reformulated with respect to the local coordinates $\boldsymbol{\xi}$ using the substitution rule of the integral calculus

$$\int_C f(\mathbf{x}) \, dv = \int_{C_r} f\left(\mathbf{x}(\boldsymbol{\xi})\right) J_C(\boldsymbol{\xi}) \, dv_r \,, \tag{3.19}$$

where dv_r is the incremental volume element of C_r and J_C is the *Jacobi*an determinant, which is defined by

$$J_C(\boldsymbol{\xi}) = \det\left(\frac{d\mathbf{x}(\boldsymbol{\xi})}{d\boldsymbol{\xi}}\right) \,. \tag{3.20}$$

Note that for quantities, which are containing derivatives with respect to the global coordinates like, e. g., the gradient or divergence operators, the above mentioned reformulation

gives the following relation:

$$\frac{\mathrm{d}f(\mathbf{x})}{\mathrm{d}\mathbf{x}} = J_C^{-1} \, \frac{\mathrm{d}f\left(\mathbf{x}(\boldsymbol{\xi})\right)}{\mathrm{d}\boldsymbol{\xi}}\,. \tag{3.21}$$

Within a FE code, the actual integration of the weak formulations is realized by a numerical integration, e. g., by the so-called *Gauss* quadrature. Therein, depending on the underlying reference element, an integral is evaluated using the $\tilde{K}$ integration points $\boldsymbol{\xi}_k$ and weight factors w_k:

$$\int_C f(\mathbf{x})\,\mathrm{d}v \approx \sum_{k=1}^{\tilde{K}} f\left(\mathbf{x}(\boldsymbol{\xi}_k)\right)\, J_C(\boldsymbol{\xi}_k)\, w_k\,. \tag{3.22}$$

Note that due to the geometry transformation to reference elements, the numerical evaluation of each integral within a FE computation is carried out with fixed integration points and weight factors for each type of reference element, which allows for a straightforward implementation of this procedure.

A crucial point within the numerical integration is the choice of the proper integration order, i. e., the necessary number of integration points for a sufficiently accurate result. Using the *Gauss* quadrature, a numerical integration with $\tilde{K}$ integration points exactly evaluates an integral containing polynomials of order $(2\,\tilde{K} - 1)$. Consequently, the use of less integration points results in an approximation error, which can lead to unphysical results in a FE calculation, e. g., when using a tri-quadratic ansatz for the solid displacement in a FE mesh with hexahedra (isoparametric approach), an 8-point *Gauss* quadrature was found to result in an insufficiently accurate integration [151]. As this problem leads to polynomials of sixth order, even an integration with 27 integration points $(3\cdot 3\cdot 3$ points$)$ does not give exact results, but leads to results, where the integration error does not produce remarkable disadvantages concerning the accuracy of the whole computation.

Specifications of integration points and weight factors for different reference elements and integration orders can be taken from the literature, cf., e. g., *Stroud* [137] or *Zienkiewicz & Taylor* [156].

3.1.5   Semi-discrete initial-value problem

After the spatial discretization, a so-called semi-discrete initial-value problem can be formulated, in which the time dependence is still described continuously. For the description of this problem, the abstract setting of *Ellsiepen* [66] will be used in this thesis. Therein, for a FE mesh with N nodal points and K integration points, the space-discrete variables of the triphasic model under study (3.1) are combined by the following vectors:

$$\left.\begin{aligned}
\boldsymbol{u} &= [(\mathbf{u}_S^1,\, p^{LR1},\, p^{GR1}),\dots,(\mathbf{u}_S^N,\, p^{LRN},\, p^{GRN})]^T\,,\\
\boldsymbol{q} &= [(\boldsymbol{\varepsilon}_{Sp}^1,\, \Lambda^1),\dots,(\boldsymbol{\varepsilon}_{Sp}^K,\, \Lambda^K)]^T\,,
\end{aligned}\right\} \quad \boldsymbol{y} = (\boldsymbol{u}^T,\, \boldsymbol{q}^T)^T, \tag{3.23}$$

where $\boldsymbol{u}$ represents the vector containing all the degrees of freedom (nodal quantities) of the FE mesh and $\boldsymbol{q}$ is the vector, in which all the internal variables are collected. Note that

for the sake of clarity, the different ansatz functions for the solid displacement (quadratic ansatz) and the pressure terms (linear ansatz) are not regarded within this formulation. For an efficient implementation of a finite element code, the pressure terms are of course only defined at the corner nodes of the finite elements, and, therefore, less than N nodal points have to be considered for them.

The internal variables (or history variables) $\boldsymbol{q}$ result from the (elasto-)plastic material behavior of the solid skeleton, which is described by the flow rule (2.101) and the restrictions resulting from the *Kuhn-Tucker* conditions (2.102). In contrast to the nodal quantities, these internal variables are evaluated in the sense of the collocation method element-wise at the integration points of the numerical quadrature. Finally, $\boldsymbol{u}$ and $\boldsymbol{q}$ are combined to one vector $\boldsymbol{y}$ representing all the unknown quantities of the problem.

Combining both the system of equations coming from the discretization of the governing equations ($\boldsymbol{F}_1 = \boldsymbol{0}$) and the plastic evolution equations ($\boldsymbol{F}_2 = \boldsymbol{0}$), the entire semi-discrete initial-value problem of first order in the variable time t can be described by:

$$\boldsymbol{F}(t, \boldsymbol{y}, \boldsymbol{y}') = \left[\begin{array}{c} \boldsymbol{F}_1(t, \boldsymbol{u}, \boldsymbol{u}', \boldsymbol{q}) \\ \boldsymbol{F}_2(t, \boldsymbol{q}, \boldsymbol{q}', \boldsymbol{u}) \end{array} \right] = \left[\begin{array}{c} \boldsymbol{M}\boldsymbol{u}' + \boldsymbol{k}(\boldsymbol{u}, \boldsymbol{q}) - \boldsymbol{f} \\ \boldsymbol{A}\boldsymbol{q}' - \boldsymbol{g}(\boldsymbol{q}, \boldsymbol{u}) \end{array} \right] \overset{!}{=} \boldsymbol{0} \,. \tag{3.24}$$

Therein, for convenience, the abbreviation $(\,\cdot\,)' = (\,\cdot\,)'_S$ is used. In (3.24), $\boldsymbol{M}$ is the generalized mass matrix, $\boldsymbol{k}$ is the generalized stiffness vector containing nonlinear dependencies on $(\boldsymbol{u}, \boldsymbol{q})$, and $\boldsymbol{f}$ is the vector of the external forces. The initial conditions of (3.24) are given by $\boldsymbol{y}(t_0) = \boldsymbol{y}_0$ with the initial time $t_0 \leq t$. Furthermore, the plastic evolution equations yield:

$$\boldsymbol{A}\boldsymbol{q}' - \boldsymbol{g}(\boldsymbol{q}, \boldsymbol{u}) = \left[\begin{array}{c} (\boldsymbol{\varepsilon}_{Sp})' \\ \\ 0 \end{array} \right] - \left[\begin{array}{c} \Lambda \, \dfrac{\partial G}{\partial \boldsymbol{\sigma}^S_E} \\ \\ F(\boldsymbol{\sigma}^S_E) \end{array} \right] = \boldsymbol{0} \,. \tag{3.25}$$

From the above equation, it is evident that $\boldsymbol{A} = \mathrm{blockdiag}(\boldsymbol{I}, 0)$. The missing *Kuhn-Tucker* conditions in (3.25) are fulfilled both in an elastic and a plastic step via an appropriate algorithm on the element level [66].

Remark: Within this thesis, the abstract description of the underlying problem illustrated above is only mentioned here, since with this representation, the type of differential equations can be specified in a clear way. Looking at (3.24)$_1$, the generalized mass matrix $\boldsymbol{M}$ results in a non-regular matrix for both the bi- and triphasic model, as no temporal derivative of a primary variable is present in the overall momentum balance (3.1)$_1$. With this property, (3.24)$_1$ turns out to be a system of differential-algebraic equations (DAE) of index one in the time variable. Furthermore, (3.24)$_2$ results in the same way in a system of DAE, because $\boldsymbol{A}$ is also a singular matrix. If the matrices $\boldsymbol{M}$ or $\boldsymbol{A}$ were regular, the resulting system would be called a system of ordinary differential equations (ODE). Details on the solution of DAE systems in combination with the development of efficient time adaptive strategies can be found, e. g., in *Ellsiepen* [66] and *Diebels et al.* [45]. $\square$

3.2   Time integration

Finally, as already mentioned in the previous section, the formulation (3.24) has to be discretized in the temporal domain for a numerical calculation of the problem under study. In the triphasic model (3.1), several time dependent quantities $(\,\cdot\,)'_S$ (or with the abbreviation $(\,\cdot\,)' = (\,\cdot\,)'_S$) are present, especially in the pore-liquid volume balance (3.8), the pore-gas mass balance (3.9) and the flow rule (3.25)$_1$. Within this thesis, the well-known *Euler* difference schemes will be used for the discretization of these quantities. Therein, two totally different approaches, namely the forward and the backward *Euler* difference schemes, have to be distinguished.

For the illustration of the forward *Euler* difference scheme, a simple nonlinear problem can be established in the following form

$$\boldsymbol{u}'(t_{n-1}) = \boldsymbol{h}(\boldsymbol{u}_{n-1},\, t_{n-1})\,, \tag{3.26}$$

where the arbitrary function $\boldsymbol{h}$ contains a nonlinear dependence on a vector $\boldsymbol{u}$ representing the unknown quantities to determine. Furthermore, the temporal derivative is represented with the symbol $\boldsymbol{u}' = \mathrm{d}\boldsymbol{u}/\mathrm{d}t$, and this time derivative of first order should now be discretized as follows:

$$\boldsymbol{u}'(t_{n-1}) = \frac{\boldsymbol{u}_n - \boldsymbol{u}_{n-1}}{\Delta t_n} \qquad \leadsto \qquad \boldsymbol{u}_n = \boldsymbol{u}_{n-1} + \boldsymbol{u}'(t_{n-1})\,\Delta t_n\,. \tag{3.27}$$

Therein, the time increment Δt_n is defined via $\Delta t_n = t_n - t_{n-1}$. Insertion of (3.26) into (3.27) yields the forward *Euler* method

$$\boldsymbol{u}_n = \boldsymbol{u}_{n-1} + \boldsymbol{h}(\boldsymbol{u}_{n-1},\, t_{n-1})\,\Delta t_n\,, \tag{3.28}$$

in which the unknown quantity $\boldsymbol{u}_n$ is calculated on the basis of quantities from the last time step t_{n-1}. In contrast to this, the backward *Euler* method can be derived via a nonlinear problem formulated at the time t_n,

$$\boldsymbol{u}'(t_n) = \boldsymbol{h}(\boldsymbol{u}_n,\, t_n)\,, \tag{3.29}$$

where the quantity $\boldsymbol{u}'(t_n)$ is discretized by

$$\boldsymbol{u}'(t_n) = \frac{\boldsymbol{u}_n - \boldsymbol{u}_{n-1}}{\Delta t_n} \qquad \leadsto \qquad \boldsymbol{u}_n = \boldsymbol{u}_{n-1} + \boldsymbol{u}'(t_n)\,\Delta t_n\,, \tag{3.30}$$

describing a discretization of the time derivative $\boldsymbol{u}'(t_n)$ with respect to the actual and the last time step (backward in time). Insertion of (3.29) into (3.30) leads to the final formulation of the backward *Euler* method:

$$\boldsymbol{u}_n - \boldsymbol{u}_{n-1} - \boldsymbol{h}(\boldsymbol{u}_n,\, t_n)\,\Delta t_n = 0\,. \tag{3.31}$$

Comparing (3.28) and (3.31), the difference between these two methods is evident. Within the forward *Euler* method, a new solution at the time t_n is obtained by the straightforward evaluation of the governing equations with respect to the last time step t_{n-1}, whereas in

the backward *Euler* method, the actual solution $\boldsymbol{u}_n$ cannot be obtained explicitly but has to be evaluated during an iterative procedure like, e. g., the *Newton-Raphson* method, cf. Section 3.3.2. This characteristics motivates the specification "explicit time integration" for (3.28) and "implicit time integration" for the formula (3.31).

Consequently, the question, which of the two approaches, the explicit or the implicit time integration method, is the more suitable one for the numerical solution of the problem under study, has to be discussed in a next step. Obviously, at first sight, the explicit time integration scheme seems to be the more efficient method, since the determination of a new quantity $\boldsymbol{u}_n$ is much easier than in case of the implicit *Euler* method. But the special type of differential equations resulting from (3.24) has also to be considered for the proper decision about that question.

The presented discretization strategy, i. e., using the finite element method for the spatial and a finite difference scheme like the *Euler* method for the temporal discretization, leads to a stepwise time integration of a fixed spatial discretization. By doing this, the fully discretized problem becomes a system of stiff differential equations [66]. Having such stiff differential equations, it is well-known that the application of explicit time integration schemes leads to unstable solutions for too large time steps [83]. On the other hand, implicit schemes do not show such an unstable behavior and, therefore, such schemes, like, e. g., the backward *Euler* method, have to be used for an unconditionally stable solution of the discretized problem. Further discussions on the stability conditions necessary for stable time integration methods can be found, e. g., in *Ellsiepen* [66].

Nevertheless, the application of explicit time integration methods on coupled multiphasic problems cannot be totally excluded. In case of dynamical problems, the use of implicit methods can lead to unstable numerical solutions and, thus, explicit methods, after the identification of a critical time step size, are an alternative in such cases, cf. *Danilov* [39].

Proceeding from quasi-static conditions for the numerical simulations, the backward *Euler* method is used for the temporal discretization within this thesis. Therein, an *a priori* fixed time series $t_0 < t_1 < t_2 < \ldots < t_{N_t}$ is processed until the end of the simulation is reached after N_t time steps.

3.3   Solution of the resulting nonlinear system

After the spatial and temporal discretization of the bi- or triphasic problem, the resulting nonlinear system has finally to be solved in order to obtain a result from the numerical simulation. This procedure will be discussed within this section. Therein, one main focus is put on a detailed description of the fully discretized weak formulations and evolution equations. In contrast to the abstract setting in Section 3.1.5, this description will be carried out explicitly at the example of the triphasic model (3.1), whereby the dependencies of all secondary variables, like, e. g., the extra stress $\boldsymbol{\sigma}_E^S$ of the solid skeleton or the liquid saturation function s^L, on the primary variables are discussed for a better understanding of the structure of the discretized model. After this, the *Newton-Raphson* method together with the consistent linearization of the governing equations are discussed, and, finally, a local assembling interface describing the single steps within the nonlinear so-

lution procedure on the element level is introduced. This interface provides a coupling of two different FE codes, whereas, e. g., one FE code contains the implementation of a specific material behavior and the other program exhibits a nonlinear solver together with parallel data structures, cf. Section 5.2.

The strategy for the solution of the resulting nonlinear system denoted above is chosen in accordance to *Wieners et al.* [151], where a similar illustration of such a solution procedure was presented using the example of the biphasic problem. Starting from the abstract setting presented in Section 3.1.5, an analogous approach is shown in the works by *Ellsiepen* [66] and *Ehlers & Ellsiepen* [59].

3.3.1   Description of the fully discretized triphasic model

For convenience, the following definitions are introduced for the discretized primary and history variables at time t_n:

$$\text{solid displacement:}\quad \mathbf{u}_S^{h,n}\,,\quad \text{effective pore-liquid pressure:}\quad p_L^{h,n} := p^{LRh,n}\,,$$

$$\text{effective pore-gas pressure:}\qquad p_G^{h,n} := p^{GRh,n}\,,\qquad (3.32)$$

$$\text{plastic multiplier:}\quad \Lambda^{h,n}\,,\quad \text{solid plastic strain:}\qquad \boldsymbol{\varepsilon}_p^{h,n} := \boldsymbol{\varepsilon}_{Sp}^{h,n}\,.$$

In order to represent the discretized weak formulations (3.7) – (3.9) and the plastic evolution equations (3.25) in a compact way, secondary variables are going to be defined together with their dependencies on the primary or history variables, respectively, cf. *Wieners et al.* [153]:

$$
\begin{aligned}
\boldsymbol{\varepsilon}\,(\mathbf{u}_S^{h,n}) &:= \boldsymbol{\varepsilon}_S : \text{total solid strain from (2.95)}\,,\\[4pt]
\boldsymbol{\sigma}^S\,(\mathbf{u}_S^{h,n},\,\boldsymbol{\varepsilon}_p^{h,n}) &= \mathbb{C}\,[\,\boldsymbol{\varepsilon}(\mathbf{u}_S^{h,n}) - \boldsymbol{\varepsilon}_p^{h,n}\,] := \boldsymbol{\sigma}_E^S : \text{solid stress from (2.97)}\,,\\[4pt]
s^L\,(p_L^{h,n},\,p_G^{h,n}) &:= s^L : \text{liquid saturation from (2.105) – (2.107)}\,,\\[4pt]
s^G\,(p_L^{h,n},\,p_G^{h,n}) &:= s^G : \text{gaseous saturation from (2.12)}\,,\\[4pt]
n^S\,(\mathbf{u}_S^{h,n}) &:= n^S : \text{solid volume fraction from (2.89)}\,,\\[4pt]
n^L\,(\mathbf{u}_S^{h,n},\,p_L^{h,n},\,p_G^{h,n}) &:= n^L : \text{liquid volume fraction from }(2.11)_1 \text{ and}\\[2pt]
&\qquad\qquad n^F = 1 - n^S\,,\\[4pt]
n^G\,(\mathbf{u}_S^{h,n},\,p_L^{h,n},\,p_G^{h,n}) &:= n^G : \text{gaseous volume fraction from }(2.11)_1\,,\\[4pt]
\rho^{GR}\,(p_G^{h,n}) &:= \rho^{GR} : \text{gaseous density from (2.114)}\,,\\[4pt]
\tilde{\mathbf{w}}_L\,(\mathbf{u}_S^{h,n},\,p_L^{h,n},\,p_G^{h,n}) &:= n^L\,\mathbf{w}_L : \text{liquid filter velocity from (2.104) – (2.113)}\,,\\[4pt]
\tilde{\mathbf{w}}_G\,(\mathbf{u}_S^{h,n},\,p_L^{h,n},\,p_G^{h,n}) &:= n^G\,\mathbf{w}_G : \text{gaseous filter velocity from (2.104) – (2.113)}\,.
\end{aligned}
\tag{3.33}
$$

Therein, $\mathbb{C} := \overset{4}{\mathbf{C}} = 2\,\mu^S\,(\mathbf{I}\otimes\mathbf{I})^{\overset{23}{T}} + \lambda^S\,(\mathbf{I}\otimes\mathbf{I})$ denotes the fourth order elasticity tensor,

where the transposition $(\,\cdot\,)^{\overset{ik}{T}}$ indicates an exchange of the i-th and k-th basis systems included into the tensor basis of higher order tensors, cf. Appendix A.1.3.

Using the above definitions, the weak formulation of the overall momentum balance reads

$$
\int_{\Omega^h} \{\boldsymbol{\sigma}^S(\mathbf{u}_S^{h,n},\,\boldsymbol{\varepsilon}_p^{h,n}) - [s^L(p_L^{h,n},\,p_G^{h,n})\,p_L^{h,n} + s^G(p_L^{h,n},\,p_G^{h,n})\,p_G^{h,n}]\,\mathbf{I}\} \cdot \operatorname{grad}\delta\mathbf{u}_S^h\,\mathrm{d}v -
$$
$$
- \int_{\Omega^h} [n^S(\mathbf{u}_S^{h,n})\,\rho^{SR} + n^L(\mathbf{u}_S^{h,n},p_L^{h,n},p_G^{h,n})\,\rho^{LR}+
$$
$$
+ n^G(\mathbf{u}_S^{h,n},p_L^{h,n},p_G^{h,n})\,\rho^{GR}\,(p_G^{h,n})]\,\mathbf{g}\cdot\delta\mathbf{u}_S^h\,\mathrm{d}v = \int_{\Gamma_t^h}\bar{\mathbf{t}}^h\cdot\delta\mathbf{u}_S^h\,\mathrm{d}a\,,
\tag{3.34}
$$

where the constant densities ρ^{SR} and ρ^{LR} (incompressible constituents) and the gravitation $\mathbf{g}$ are interpreted as material parameters. Furthermore, the *Neumann* boundary condition $\bar{\mathbf{t}}^h$ (surface traction) is also a given quantity depending on the respective initial boundary-value problem.

Looking at the plastic evolution equations (3.25), the discretized formulation results in

$$
\boldsymbol{\varepsilon}_p^{h,n} = \boldsymbol{\varepsilon}_p^{h,n-1} + \Delta t_n\,\Lambda^{h,n}\,\frac{\partial G(\boldsymbol{\sigma}^S(\mathbf{u}_S^{h,n},\,\boldsymbol{\varepsilon}_p^{h,n}))}{\partial\boldsymbol{\sigma}^S}\,,
$$
$$
F(\boldsymbol{\sigma}^S(\mathbf{u}_S^{h,n},\,\boldsymbol{\varepsilon}_p^{h,n})) = 0\,.
\tag{3.35}
$$

Note that this local system is solved on the element level, i. e., for each finite element, a so-called trial stress $\boldsymbol{\sigma}_{trial}^{Sn} = \mathbb{C}\,[\,\boldsymbol{\varepsilon}(\mathbf{u}_S^{h,n}) - \boldsymbol{\varepsilon}_p^{h,n-1}\,]$ is determined on the basis of the current value $\mathbf{u}_S^{h,n}$ of the solid displacement and the old value $\boldsymbol{\varepsilon}_p^{h,n-1}$ (value from the last time step t_{n-1}) of the plastic strains. If this trial stress violates the yield criterion $(3.25)_2$, the local system (3.35) is entered and a compatible plastic strain increment $\Delta\boldsymbol{\varepsilon}_p^{h,n} = \boldsymbol{\varepsilon}_p^{h,n} - \boldsymbol{\varepsilon}_p^{h,n-1}$ is determined by solving (3.35). Thus, Equations (3.35) can be reformulated with respect to these considerations in the following way: Find the plastic strain increment $\Delta\boldsymbol{\varepsilon}_p^{h,n}$ and the incremental plastic multiplier $\Lambda^{h,n}$ such that

$$
\Delta\boldsymbol{\varepsilon}_p^{h,n} = \Delta t_n\,\Lambda^{h,n}\,\frac{\partial G(\boldsymbol{\sigma}_{trial}^{Sn} - \mathbb{C}\,\Delta\boldsymbol{\varepsilon}_p^{h,n})}{\partial\boldsymbol{\sigma}^S}\,,
$$
$$
F(\boldsymbol{\sigma}_{trial}^{Sn} - \mathbb{C}\,\Delta\boldsymbol{\varepsilon}_p^{h,n}) = 0\,.
\tag{3.36}
$$

Inserting the new stress state $\boldsymbol{\sigma}^{Sn} = \boldsymbol{\sigma}_{trial}^{Sn} - \mathbb{C}\,\Delta\boldsymbol{\varepsilon}_p^{h,n}$, the following equivalent form of (3.36) can be obtained [151]: For a given trial stress $\boldsymbol{\sigma}_{trial}^{Sn}$, find the stress response $\boldsymbol{\sigma}^{Sn}$ and the plastic multiplier $\Lambda^{h,n}$ such that

$$
\boldsymbol{\sigma}^{Sn} = \boldsymbol{\sigma}_{trial}^{Sn} - \Delta t_n\,\Lambda^{h,n}\,\mathbb{C}\,\frac{\partial G(\boldsymbol{\sigma}^{Sn})}{\partial\boldsymbol{\sigma}^S}\,,
$$
$$
F(\boldsymbol{\sigma}^{Sn}) = 0\,.
\tag{3.37}
$$

The solution of the nonlinear problem (3.37) defines the stress response by

$$
\boldsymbol{\sigma}^{Sn} = \bar{\mathbf{P}}^n(\boldsymbol{\sigma}_{trial}^{Sn}) = \bar{\mathbf{P}}^n(\mathbf{u}_S^{h,n},\,\boldsymbol{\varepsilon}_p^{h,n-1})\,,
\tag{3.38}
$$

where the stress response function $\bar{\mathbf{P}}^n$ includes all the incremental plastic evolution relations from (3.35). Furthermore, this formulation also incorporates the correct representation of the *Kuhn-Tucker* conditions in the elastic regime, as for $F(\boldsymbol{\sigma}_{trial}^{S\,n}) < 0$ the value $\Lambda^{h,n} = 0$ for the plastic multiplier is obtained and $\bar{\mathbf{P}}^n(\boldsymbol{\sigma}_{trial}^{S\,n}) = \boldsymbol{\sigma}_{trial}^{S\,n}$ yields a linear (elastic) stress response.

Insertion of the stress response $\bar{\mathbf{P}}^n$ into (3.34) leads to the final formulation of the fully discretized triphasic formulation: For given values $\{\,\mathbf{u}_S^{h,n-1},\ p_L^{h,n-1},\ p_G^{h,n-1},\ \boldsymbol{\varepsilon}_p^{h,n-1}\,\}$ of the primary and history variables (last time step), find the solid displacement $\mathbf{u}_S^{h,n}$ and the pressure variables $p_L^{h,n}$ and $p_G^{h,n}$ such that the following weak formulations are fulfilled:

Overall momentum balance:

$$\int_{\Omega^h} \{\bar{\mathbf{P}}^n(\mathbf{u}_S^{h,n}, \boldsymbol{\varepsilon}_p^{h,n-1}) - [s^L(p_L^{h,n}, p_G^{h,n})\,p_L^{h,n} + s^G(p_L^{h,n}, p_G^{h,n})\,p_G^{h,n}]\,\mathbf{I}\} \cdot \operatorname{grad}\delta\mathbf{u}_S^h\,\mathrm{d}v -$$

$$- \int_{\Omega^h} [n^S(\mathbf{u}_S^{h,n})\,\rho^{SR} + n^L(\mathbf{u}_S^{h,n}, p_L^{h,n}, p_G^{h,n})\,\rho^{LR} +$$

$$+ n^G(\mathbf{u}_S^{h,n}, p_L^{h,n}, p_G^{h,n})\,\rho^{GR}(p_G^{h,n})]\,\mathbf{g}\cdot\delta\mathbf{u}_S^h\,\mathrm{d}v = \int_{\Gamma_t^h} \bar{\mathbf{t}}^h\cdot\delta\mathbf{u}_S^h\,\mathrm{d}a\,,$$

Pore-liquid volume balance:

$$\int_{\Omega^h} [\,n^L(\mathbf{u}_S^{h,n}, p_L^{h,n}, p_G^{h,n}) + n^L(\mathbf{u}_S^{h,n}, p_L^{h,n}, p_G^{h,n})\operatorname{div}(\mathbf{u}_S^{h,n} - \mathbf{u}_S^{h,n-1})\,]\,\delta p_L^h\,\mathrm{d}v -$$

$$- \Delta t_n \int_{\Omega^h} \tilde{\mathbf{w}}_L(\mathbf{u}_S^{h,n}, p_L^{h,n}, p_G^{h,n})\cdot\operatorname{grad}\delta p_L^h\,\mathrm{d}v =$$

(3.39)

$$= \int_{\Omega^h} n^L(\mathbf{u}_S^{h,n-1}, p_L^{h,n-1}, p_G^{h,n-1})\,\delta p_L^h\,\mathrm{d}v + \Delta t_n \int_{\Gamma_v^h} \bar{v}^{L\,h}\,\delta p_L^h\,\mathrm{d}a\,,$$

Pore-gas mass balance:

$$\int_{\Omega^h} \{\,[n^G(\mathbf{u}_S^{h,n}, p_L^{h,n}, p_G^{h,n}) - n^G(\mathbf{u}_S^{h,n-1}, p_L^{h,n-1}, p_G^{h,n-1})]\,\rho^{GR}(p_G^{h,n}) +$$

$$+ n^G(\mathbf{u}_S^{h,n}, p_L^{h,n}, p_G^{h,n})\,[\rho^{GR}(p_G^{h,n}) - \rho^{GR}(p_G^{h,n-1})] +$$

$$+ n^G(\mathbf{u}_S^{h,n}, p_L^{h,n}, p_G^{h,n})\,\rho^{GR}(p_G^{h,n})\operatorname{div}(\mathbf{u}_S^{h,n} - \mathbf{u}_S^{h,n-1})\,\}\,\delta p_G^h\,\mathrm{d}v -$$

$$- \Delta t_n \int_{\Omega^h} \rho^{GR}(p_G^{h,n})\,\tilde{\mathbf{w}}_G(\mathbf{u}_S^{h,n}, p_L^{h,n}, p_G^{h,n})\cdot\operatorname{grad}\delta p_G^h\,\mathrm{d}v = \Delta t_n \int_{\Gamma_q^h} \bar{q}^{G\,h}\,\delta p_G^h\,\mathrm{d}a\,.$$

Therein, $\delta p_L^h := \delta p^{LRh}$ and $\delta p_G^h := \delta p^{GRh}$ are the abbreviated notations of the test functions introduced in (3.12). Furthermore, the *Neumann* boundary conditions $\bar{v}^{Lh}$ (efflux of liquid) and $\bar{q}^{Gh}$ (efflux of gaseous mass) are user-defined quantities.

The solution of (3.39) finally gives the new plastic strain via

$$\varepsilon_p^{h,n} = \varepsilon\left(\mathbf{u}_S^{h,n}\right) - \mathbb{C}^{-1}\,\bar{\mathbf{P}}^n(\mathbb{C}\,[\,\varepsilon(\mathbf{u}_S^{h,n}) - \varepsilon_p^{h,n-1}\,])\,. \tag{3.40}$$

Remark: According to Equations (3.12) and (3.13), the *Dirichlet* boundary conditions are always fulfilled by the solutions $\{\,\mathbf{u}_S^{h,n},\,p_L^{h,n},\,p_G^{h,n}\,\}$ of the system (3.39), i. e.,

$$\mathbf{u}_S^{h,n} = \bar{\mathbf{u}}_S^h(\mathbf{x},\,t_n) \quad \text{on } \Gamma_u^h\,,$$

$$p_L^{h,n} = \bar{p}^{LRh}(\mathbf{x},\,t_n) \quad \text{on } \Gamma_{pl}^h\,, \tag{3.41}$$

$$p_G^{h,n} = \bar{p}^{GRh}(\mathbf{x},\,t_n) \quad \text{on } \Gamma_{pg}^h\,.$$

$\square$

3.3.2 *Newton-Raphson* method and consistent linearization

By a reformulation of (3.39), the following residual terms can be identified (dependencies on the primary and history variables are omitted for convenience):

$$\begin{aligned}
\mathcal{R}_{MM}^{h,n} &= \int_{\Omega^h} \{\bar{\mathbf{P}}^n - (s^{Ln}\,p_L^{h,n} + s^{Gn}\,p_G^{h,n})\,\mathbf{I}\} \cdot \operatorname{grad}\delta\mathbf{u}_S^h\,dv - \\
&\quad - \int_{\Omega^h} (n^{Sn}\,\rho^{SR} + n^{Ln}\,\rho^{LR} + n^{Gn}\,\rho^{GRn})\,\mathbf{g}\cdot\delta\mathbf{u}_S^h\,dv - \int_{\Gamma_t^h} \bar{\mathbf{t}}^h\cdot\delta\mathbf{u}_S^h\,da\,, \\[4pt]
\mathcal{R}_{VL}^{h,n} &= \int_{\Omega^h} [n^{Ln} - n^{Ln-1} + n^{Ln}\,\operatorname{div}(\mathbf{u}_S^{h,n} - \mathbf{u}_S^{h,n-1})]\,\delta p_L^h\,dv - \\
&\quad - \Delta t_n \int_{\Omega^h} \tilde{\mathbf{w}}_L^n\cdot\operatorname{grad}\delta p_L^h\,dv - \Delta t_n \int_{\Gamma_v^h} \bar{v}^{Lh}\,\delta p_L^h\,da\,, \tag{3.42} \\[4pt]
\mathcal{R}_{MG}^{h,n} &= \int_{\Omega^h} [\,(n^{Gn} - n^{Gn-1})\,\rho^{GRn} + n^{Gn}\,(\rho^{GRn} - \rho^{GRn-1}) + \\
&\quad + n^{Gn}\,\rho^{GRn}\,\operatorname{div}(\mathbf{u}_S^{h,n} - \mathbf{u}_S^{h,n-1})\,]\,\delta p_G^h\,dv - \\
&\quad - \Delta t_n \int_{\Omega^h} \rho^{GRn}\,\tilde{\mathbf{w}}_G^n\cdot\operatorname{grad}\delta p_G^h\,dv - \Delta t_n \int_{\Gamma_q^h} \bar{q}^{Gh}\,\delta p_G^h\,da\,.
\end{aligned}$$

Therein, $\mathcal{R}_{MM}^{h,n}$, $\mathcal{R}_{VL}^{h,n}$ and $\mathcal{R}_{MG}^{h,n}$ denote the residual terms resulting from the momentum balance of the mixture, the pore-liquid volume balance and the pore-gas mass balance, respectively. With these definitions, the global problem is obtained by the evaluation of the single test functions as described in Equation (3.17). For N nodal points and a general D-dimensional case, the following global problem is defined: For given values of the vectors $\boldsymbol{u}_{n-1}$ and $\boldsymbol{q}_{n-1}$ (last time step), determine the new quantities $\boldsymbol{u}_n$ and $\boldsymbol{q}_n$ such that

$$\boldsymbol{\mathcal{R}}^{h,n}(t_n, \boldsymbol{u}_n, \boldsymbol{q}_n) = \begin{bmatrix} \boldsymbol{\mathcal{R}}_{MM}^{h,n}(t_n, \boldsymbol{u}_n, \boldsymbol{q}_n) \\[1mm] \boldsymbol{\mathcal{R}}_{VL}^{h,n}(t_n, \boldsymbol{u}_n) \\[1mm] \boldsymbol{\mathcal{R}}_{MG}^{h,n}(t_n, \boldsymbol{u}_n) \end{bmatrix} \overset{!}{=} \boldsymbol{0}\,, \tag{3.43}$$

where, according to (3.23), the temporally discretized unknown quantities are collected in the vectors $\boldsymbol{u}_n$ and $\boldsymbol{q}_n$. Furthermore, $\boldsymbol{\mathcal{R}}_{MM}^{h,n}$, $\boldsymbol{\mathcal{R}}_{VL}^{h,n}$ and $\boldsymbol{\mathcal{R}}_{MG}^{h,n}$ are defined as follows:

$$\begin{aligned} \boldsymbol{\mathcal{R}}_{MM}^{h,n}(t_n, \boldsymbol{u}_n, \boldsymbol{q}_n) &= \left[\mathcal{R}_{MM}^{h,n}(t_n, \boldsymbol{u}_n, \boldsymbol{q}_n; \phi_{u_1}^1), \ldots, \mathcal{R}_{MM}^{h,n}(t_n, \boldsymbol{u}_n, \boldsymbol{q}_n; \phi_{u_D}^N) \right]^T, \\[1mm] \boldsymbol{\mathcal{R}}_{VL}^{h,n}(t_n, \boldsymbol{u}_n) &= \left[\mathcal{R}_{VL}^{h,n}(t_n, \boldsymbol{u}_n; \phi_{pl}^1), \ldots, \mathcal{R}_{VL}^{h,n}(t_n, \boldsymbol{u}_n; \phi_{pl}^N) \right]^T, \\[1mm] \boldsymbol{\mathcal{R}}_{MG}^{h,n}(t_n, \boldsymbol{u}_n) &= \left[\mathcal{R}_{MG}^{h,n}(t_n, \boldsymbol{u}_n; \phi_{pg}^1), \ldots, \mathcal{R}_{MG}^{h,n}(t_n, \boldsymbol{u}_n; \phi_{pg}^N) \right]^T. \end{aligned} \tag{3.44}$$

Therein, $\{\boldsymbol{\phi}_u^i, \phi_{pl}^i, \phi_{pg}^i\}$ with $i = 1, \ldots, N$ represent the global basis functions defined in (3.12).

As already denoted in the previous section, a combination of several substeps is used for the solution of the problem (3.43), cf. *Wieners* [148], *Ehlers & Ellsiepen* [59] and *Wieners et al.* [151]:

* compute the residual $\boldsymbol{\mathcal{R}}^{h,n,j}$ on the basis of the current vector $\boldsymbol{u}_n^j$. Note that within this substep the stress response is determined at every integration point from the numerical quadrature by a *Newton-Raphson* method for (3.37). This evaluation at the integration points leads to the determination of the current vector of the internal variables: $\boldsymbol{q}_n^j = \boldsymbol{q}_n^j(\boldsymbol{u}_n^j)$.

* compute the consistent tangent $\mathrm{D}\boldsymbol{\mathcal{R}}^{h,n,j} = \mathrm{d}\boldsymbol{\mathcal{R}}^{h,n,j} / \mathrm{d}\boldsymbol{u}_n^j$ of the global system (3.43).

* solve the sparse global linear system (3.49) for $\Delta\boldsymbol{u}_n^j$.

* update the global variables $\boldsymbol{u}_n^{j+1} = \boldsymbol{u}_n^j - \Delta\boldsymbol{u}_n^j$.

Therein, the index j denotes the current *Newton* iteration step.

As the solution of the local system (3.37) is carried out for fixed values of the primary variables $\boldsymbol{u}_n^j$, the new vector $\boldsymbol{q}_n^j$ of the internal variables is a function of $\boldsymbol{u}_n^j$. Taking this fact into account within the computation of the tangent for the *Newton-Raphson* method leads directly to the term "algorithmically consistent linearization", which was established in the framework of nonlinear finite element calculations of elasto-plastic materials by

Simo & Taylor [129]. Further information about this topic can be found, e. g., in the work by *Wriggers* [155] or *Eipper* [65].

According to this, the algorithmically consistent tangent $\mathrm{D}\boldsymbol{\mathcal{R}}^{h,n,j}$ reads

$$\mathrm{D}\boldsymbol{\mathcal{R}}^{h,n,j} = \frac{\mathrm{d}\boldsymbol{\mathcal{R}}^{h,n,j}}{\mathrm{d}\boldsymbol{u}_n^j} = \frac{\partial \boldsymbol{\mathcal{R}}^{h,n,j}}{\partial \boldsymbol{u}_n^j} + \frac{\partial \boldsymbol{\mathcal{R}}^{h,n,j}}{\partial \boldsymbol{q}_n^j} \frac{\mathrm{d}\boldsymbol{q}_n^j}{\mathrm{d}\boldsymbol{u}_n^j}\,, \tag{3.45}$$

where the dependence of $\boldsymbol{q}_n^j$ on the primary variables $\boldsymbol{u}_n^j$ can be determined by the derivation of the local system (3.37) with respect to $\boldsymbol{u}_n^j$:

$$\boldsymbol{\mathcal{R}}_{local}^{h,n,j} \overset{!}{=} \boldsymbol{0}\,, \quad \frac{\mathrm{d}\boldsymbol{\mathcal{R}}_{local}^{h,n,j}}{\mathrm{d}\boldsymbol{u}_n^j} = \frac{\partial \boldsymbol{\mathcal{R}}_{local}^{h,n,j}}{\partial \boldsymbol{u}_n^j} + \frac{\partial \boldsymbol{\mathcal{R}}_{local}^{h,n,j}}{\partial \boldsymbol{q}_n^j} \frac{\mathrm{d}\boldsymbol{q}_n^j}{\mathrm{d}\boldsymbol{u}_n^j} = \boldsymbol{0}$$

$$\rightsquigarrow \quad \frac{\mathrm{d}\boldsymbol{q}_n^j}{\mathrm{d}\boldsymbol{u}_n^j} = -\left[\frac{\partial \boldsymbol{\mathcal{R}}_{local}^{h,n,j}}{\partial \boldsymbol{q}_n^j}\right]^{-1} \frac{\partial \boldsymbol{\mathcal{R}}_{local}^{h,n,j}}{\partial \boldsymbol{u}_n^j}\,. \tag{3.46}$$

Therein, $\boldsymbol{\mathcal{R}}_{local}^{h,n,j}$ is the residual formulation of the local system (3.35) (index j of the current *Newton* iteration is omitted for convenience)

$$\boldsymbol{\mathcal{R}}_{local}^{h,n}(t_n, \boldsymbol{u}_n, \boldsymbol{q}_n) \quad = \quad \begin{bmatrix} \boldsymbol{\mathcal{R}}_{local\ 1}^{h,n}(t_n, \boldsymbol{u}_n, \boldsymbol{q}_n) \\ \cdot \\ \cdot \\ \cdot \\ \boldsymbol{\mathcal{R}}_{local\ K}^{h,n}(t_n, \boldsymbol{u}_n, \boldsymbol{q}_n) \end{bmatrix} \overset{!}{=} \boldsymbol{0} \quad \text{with}$$

$$\boldsymbol{\mathcal{R}}_{local\ k}^{h,n}(t_n, \boldsymbol{u}_n, \boldsymbol{q}_n) \quad = \quad \begin{bmatrix} \boldsymbol{\varepsilon}_p^{h,n} - \boldsymbol{\varepsilon}_p^{h,n-1} - \Delta t_n\, \Lambda^{h,n}\, \dfrac{\partial G(\boldsymbol{\sigma}^S(\mathbf{u}_S^{h,n}, \boldsymbol{\varepsilon}_p^{h,n}))}{\partial \boldsymbol{\sigma}^S} \\ F(\boldsymbol{\sigma}^S(\mathbf{u}_S^{h,n}, \boldsymbol{\varepsilon}_p^{h,n})) \end{bmatrix}_{\mathbf{x}=\mathbf{x}_k}\,, \tag{3.47}$$

where $\boldsymbol{\mathcal{R}}_{local\ k}^{h,n}$ is obtained at each integration point k ($k = 1, \dots, K$) of the underlying FE mesh with the global position $\mathbf{x}_k$. Note that the matrix $\partial \boldsymbol{\mathcal{R}}_{local}^{h,n,j} / \partial \boldsymbol{q}_n^j$ is block-diagonal, i. e., the linear system $(3.46)_2$ can be solved in a decoupled way by solving a small linear system for the internal variables at each integration point.

Insertion of the above result in (3.45) gives the final form of the algorithmically consistent tangent:

$$\mathrm{D}\boldsymbol{\mathcal{R}}^{h,n,j} = \frac{\partial \boldsymbol{\mathcal{R}}^{h,n,j}}{\partial \boldsymbol{u}_n^j} - \frac{\partial \boldsymbol{\mathcal{R}}^{h,n,j}}{\partial \boldsymbol{q}_n^j} \left[\frac{\partial \boldsymbol{\mathcal{R}}_{local}^{h,n,j}}{\partial \boldsymbol{q}_n^j}\right]^{-1} \frac{\partial \boldsymbol{\mathcal{R}}_{local}^{h,n,j}}{\partial \boldsymbol{u}_n^j}\,. \tag{3.48}$$

With this tangent, the global linear system

$$\mathrm{D}\boldsymbol{\mathcal{R}}^{h,n,j}\, \Delta \boldsymbol{u}_n^j = \boldsymbol{\mathcal{R}}^{h,n,j} \tag{3.49}$$

is solved for the global *Newton* increment $\Delta \boldsymbol{u}_n^j$. After that, the global solution vector is updated,

$$\boldsymbol{u}_n^{j+1} = \boldsymbol{u}_n^j - \lambda\, \Delta \boldsymbol{u}_n^j\,, \tag{3.50}$$

and, based on this new solution vector, the new residual $\mathcal{R}^{h,n,j+1}$ is evaluated again. In (3.50), λ is a damping parameter, which is determined by minimizing the new *Euclid*ian defect $||\mathcal{R}^{h,n,j+1}||$. The above mentioned procedure is repeated until the norm of the residual fulfills a user-defined tolerance:

$$||\mathcal{R}^{h,n,j+1}|| < tol. \tag{3.51}$$

3.3.3   Local assembling interface

Within a FE program, the evaluation of many substeps for the solution of the nonlinear system is carried out on the element level. This fact leads directly to the following scheme of a local assembling interface defined for each cell C, which contains all the main steps of the nonlinear solution procedure: evaluation of the *Dirichlet* and *Neumann* boundary conditions, calculation of the residual (3.43), determination of the algorithmically consistent tangent (3.48) and, finally, the update of the internal variables at the end of a time step:

* $D_C(t_n, (\boldsymbol{u}_n)_C)$: mark all components corresponding to *Dirichlet* boundary points on Γ_u, Γ_{pl} and Γ_{pg} and assign the corresponding *Dirichlet* boundary values at time t_n in the element solution vector $(\boldsymbol{u}_n)_C$.

* $R_C(t_n, \Delta t_n, (\boldsymbol{u}_n)_C, (\boldsymbol{u}_{n-1})_C, (\boldsymbol{q}_{n-1})_C)$: for a given *Newton* iterate $(\boldsymbol{u}_n)_C = (\boldsymbol{u}_n^j)_C$, the old element solution vector $(\boldsymbol{u}_{n-1})_C$ and the old element vector of the internal variables $(\boldsymbol{q}_{n-1})_C$, compute the element-wise residual $(\mathcal{R}^{h,n,j})_C$ of the global problem (3.43). If the cell C contains an edge (or surface) at the boundary of the domain, additionally, the *Neumann* boundary conditions are evaluated and added to the residual $(\mathcal{R}^{h,n,j})_C$ within this function.

* $T_C(t_n, \Delta t_n, (\boldsymbol{u}_n)_C, (\boldsymbol{u}_{n-1})_C, (\boldsymbol{q}_{n-1})_C)$: for a given *Newton* iterate $(\boldsymbol{u}_n)_C = (\boldsymbol{u}_n^j)_C$, the old element solution vector $(\boldsymbol{u}_{n-1})_C$ and the old element vector of the internal variables $(\boldsymbol{q}_{n-1})_C$, compute the element-wise consistent tangent $(\mathrm{D}\mathcal{R}^{h,n,j})_C$.

* $U_C(t_n, (\boldsymbol{u}_n)_C, (\boldsymbol{q}_n)_C)$: for a given *Newton* solution $(\boldsymbol{u}_n)_C$, update the vector of the internal variables $(\boldsymbol{q}_{n-1})_C = (\boldsymbol{q}_n)_C$ (old vector for the next time step) by an element-wise evaluation of (3.40).

With the definition of this local assembling interface, the strategy of solving one time step for the nonlinear system (3.43) reads as follows:

* call D_C for all elements and assemble the element-wise information $(\boldsymbol{u}_n)_C$ of the *Dirichlet* data into the global solution vector $\boldsymbol{u}_n$. This procedure is carried out once at the beginning of a time step.

* start the *Newton-Raphson* method:

  ▷ call R_C for all elements and assemble the element-wise information $(\mathcal{R}^{h,n,j})_C$ (including the *Neumann* data) to the global residual $\mathcal{R}^{h,n,j}$ and check for convergence, i. e., $||\mathcal{R}^{h,n,j}|| < tol$.

    ▷ if the residual norm does not meet the stopping criterion, call T_C for all elements and assemble the global consistent tangent $\mathrm{D}\boldsymbol{\mathcal{R}}^{h,n,j}$.

    ▷ solve the global system $\mathrm{D}\boldsymbol{\mathcal{R}}^{h,n,j}\,\Delta\boldsymbol{u}_n^j = \boldsymbol{\mathcal{R}}^{h,n,j}$ and determine an appropriate damping factor λ for the update of the global solution vector $\boldsymbol{u}_n^{j+1} = \boldsymbol{u}_n^j + \lambda\,\Delta\boldsymbol{u}_n^j$.

∗ if the stopping criterion of the *Newton-Raphson* method is reached, call the update function U_C for all elements. If the maximum number of *Newton* iterations is reached, i. e., no convergence within the *Newton-Raphson* method is obtained, bisect the time step size and start the *Newton* iteration with the smaller time increment once again (until a minimum time step size is reached, which leads to a termination of the whole program).

Note that the presented local assembling interface allows for a coupling of two different FE codes, whereas, e. g., one finite element code contains the implementation of a specific material behavior and the other program exhibits efficient linear solvers. In Section 5.2.2, the idea of this interface will be picked up again, when a sequentially implemented finite element code is parallelized by coupling it with a program, which already contains parallel data structures.

Chapter 4: Regularization techniques

With the theoretical and numerical information given in the last two chapters, one now is in principle provided with all the necessary information for the numerical simulations of strongly coupled solid-fluid problems based on the finite element method. However, a major problem occurs within finite element calculations, when the elastic range of the solid skeleton is exceeded and the plastic deformations result in a softening material behavior of the solid skeleton. In soil mechanics, such material behavior can be observed in the numerical investigations of localization phenomena, as, for example, in the well-known base failure and slope failure problems. Carrying out FE calculations of these problems, the development of shear bands can be found, which result from local concentrations of plastic strains and which lead to the failure of the investigated geometries.

In such cases, the results of FE simulations based on the presented plasticity model from Section 2.3.3 show a strong dependence on the chosen spatial discretization with finite elements, which is of course spurious and unphysical. This so-called mesh-dependent behavior can be avoided by the application of regularization techniques.

After some remarks on mesh-dependent behavior and an overview of existing regularization techniques, within this chapter, three different regularization techniques are discussed in detail, namely a viscoplastic ansatz, a micropolar continuum theory and a non-local model. After the presentation of the theoretical aspects and the numerical realization of the single regularization techniques, numerical simulations are shown, which clarify the properties of the single approaches.

4.1   Mesh-dependent behavior

The above mentioned problem in the numerical simulation of localization phenomena resulting from softening material behavior can be recognized, for example, in the width of the localization zone. It can be observed that the width of the shearing domain strongly depends on the chosen spatial discretization through the mesh size and the mesh orientation. For example, each mesh refinement leads to a decrease of the shear band width until, in theory, one obtains a singular surface for an infinitely fine FE mesh.

Obviously, such a mesh-dependent behavior leads to unphysical results, as from experimental investigations, it can be seen that the width of the shear band is directly connected with a micro-structural length scale, like, e. g., the average size of the grains in a sandy soil. However, the presented plasticity model from Section 2.3.3, suffers from the drawback that no material parameter is involved in the model, which is capable of defining the width of the shear band independently of the spatial discretization, and, as a consequence, the element size serves as an internal length scale. Therefore, this plasticity model is not applicable for the numerical simulation of localization problems.

From the mathematical point of view, the reason of this pathological mesh sensitivity is

due to the fact that the type of the partial differential equations changes from elliptic to hyperbolic right at the moment, when the material behavior switches from non-softening to softening or, in other words, the well-posed problem becomes an ill-posed problem. The terms "well-posed problem" and "ill-posed problem" were originally introduced by *Hadamard* [81] based on the following definition: a problem is well-posed when a solution exists, is unique and depends continuously on the initial data. It is ill-posed when it fails to satisfy at least one of these three criteria.

Within the framework of this thesis, the question, which of the three criteria is not fulfilled at the onset of softening material behavior, is not going to be discussed. Here, a problem will be classified as ill-posed or not regularized, when the numerical calculations with several, uniformly refined FE meshes lead to different results concerning the shear band width, the absolute value of the plastic strains and the stress-displacement development at a specific point or area. For a more detailed information on the classification and the regularization of ill-posed problems with emphasis on the mathematical viewpoint, the interested reader is referred to, e. g., *Morozov* [108] or *Louis* [102].

Note that mesh-dependent behavior is a phenomenon, which is associated with elasto-plastic and softening material behavior of a solid constituent. The simultaneous consideration of pore-fluids in a porous material does not deteriorate but can weaken the ill-posed behavior, cf. *Ehlers & Volk* [64]. This effect is due to a more or less pronounced viscosity of the respective pore-fluids. Within the framework of this thesis, such effects are not going to be discussed and, therefore, single-phasic (solid) materials are viewed for further discussions within this chapter.

For the sake of simplicity, mesh-dependent behavior is going to be illustrated at the
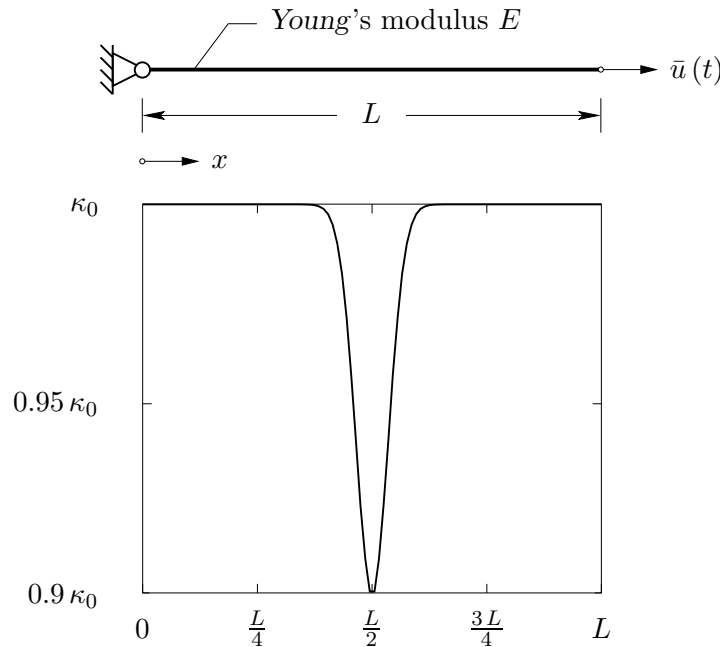

Figure 4.1: One-dimensional boundary-value problem (top) and weakening of the initial equivalent stress κ_0 (bottom).

example of a simple one-dimensional problem, which is also going to be used for the discussion of the single regularization techniques in Section 4.6.1. This example concerns a bar, which is supported at $x = 0$ and which is pulled at the right end $(x = L)$ by an increasing displacement $\bar{u}(t)$, cf. Figure 4.1 (top). The following set of equations describes the kinematics, the equilibrium condition and the constitutive relations for this model problem:

$$
\begin{aligned}
\varepsilon &= \mathrm{d}u/\mathrm{d}x & &\text{(kinematic compatibility)}\,, \\
\mathrm{d}\sigma/\mathrm{d}x &= 0 & &\text{(momentum balance)}\,, \\
\sigma &= E\,\varepsilon_e & &\text{(\textit{Hooke}an elasticity law)}\,, \\
\varepsilon &= \varepsilon_e + \varepsilon_p & &\text{(strain decomposition)}\,, \\
F &= \sigma - \overset{\star}{\kappa} & &\text{(yield criterion)}\,, \\
\overset{\star}{\kappa} &= \kappa_0 - h\,\varepsilon_p & &\text{(hardening/softening law)}\,, \\
\mathrm{d}\varepsilon_p/\mathrm{d}t &= \Lambda\,\mathrm{d}F/\mathrm{d}\sigma & &\text{(plastic flow rule)}\,, \\
\Lambda\,F &= 0\,, \quad \Lambda \geq 0\,, \quad F \leq 0 & &\text{(\textit{Kuhn-Tucker} conditions)}\,.
\end{aligned}
\tag{4.1}
$$

Therein, the following values for the material parameters are chosen: *Young*'s modulus $E = 210 \cdot 10^3\,\mathrm{kN/m^2}$ and initial equivalent stress $\kappa_0 = 240\,\mathrm{kN/m^2}$. For the parameter h, three different values are chosen in order to illustrate linear softening $(h = 1\,000\,\mathrm{kN/m^2})$ and linear hardening $(h = -1\,000\,\mathrm{kN/m^2})$ material behavior as well as the limiting case of ideal or *Prandtl-Reuss* plasticity $(h = 0\,\mathrm{kN/m^2})$. The length L of the bar is $0.2\,\mathrm{m}$ and the *Dirichlet* boundary condition $\bar{u}(t)$ at $x = L$ results due to a linear increase of $\bar{u}$ in the final displacement of $0.9\,\mathrm{mm}$ at $t = 6\,\mathrm{s}$. In order to initiate a "shear band" (shear zone) in a predefined area of the bar, the initial equivalent stress κ_0 is weakened as shown in Figure 4.1 (bottom).
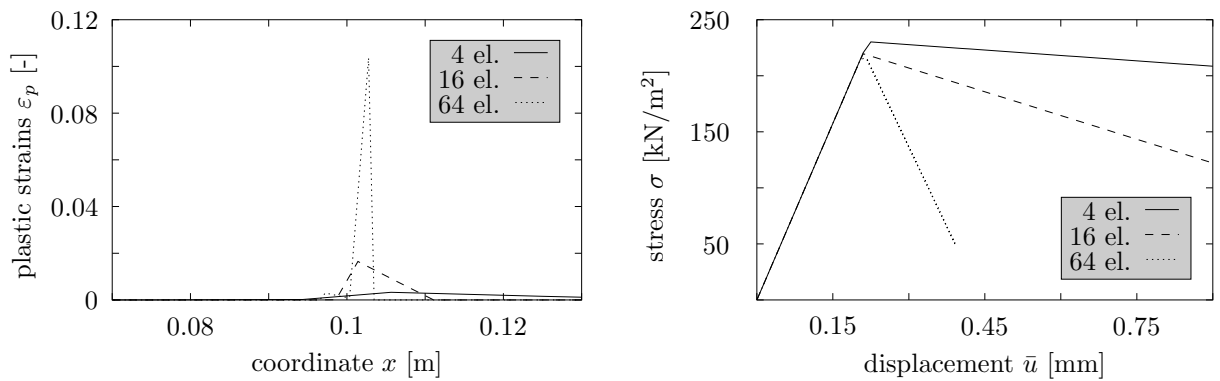

Figure 4.2: Distribution of the plastic strains ε_p [-] in the bar (left) and development of the stress σ [kN/m^2] at $x = L$ (right) for $h = 1\,000\,\mathrm{kN/m^2}$.

For an evaluation of the posedness of the respective problem, FE calculations were carried out with different meshes. Starting from a spatial discretization with 4 elements, 5 regular
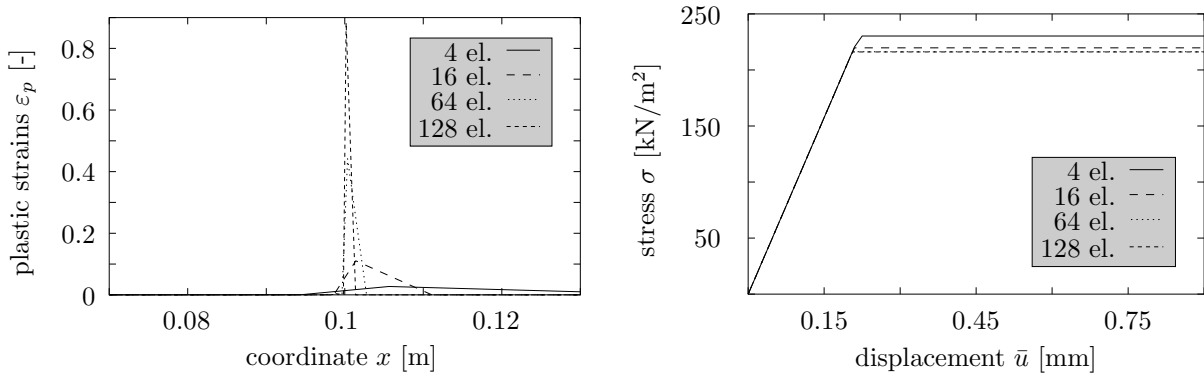
Figure 4.3: Distribution of the plastic strains ε_p [-] in the bar (left) and development of the stress σ [kN/m^2] at $x = L$ (right) for $h = 0$ kN/m^2.

refinement steps result in a rather fine mesh with 128 elements. Therein, one regular refinement step divides each element into 2 elements of identical size, and, therefore, doubles the number of elements. Within each element, a quadratic ansatz is chosen for the displacement u and the numerical quadrature is carried out as shown in Section 3.1.4 with an integration order 5, which results in 3 integration points per element.

Concerning the results of the computations carried out with $h = 1\,000$ kN/m^2, the mesh-dependent behavior is quite obvious. The stress-displacement relationship (Figure 4.2, right) shows a softening material behavior, which strongly depends on the spatial discretization, i. e., each refinement of the mesh leads to a huge decrease in the stress response such that already the mesh with 64 elements would give negative stresses at the final displacement of $\bar{u} = 0.9$ mm. As the simple model problem from (4.1) contains no saturation constraint, which would prevent a softening towards the negative range of the stresses, the simulations were terminated whenever the resulting stress of any integration point in the mesh was negative.

In order to compare the shear zones in this example, the plastic strains at $\bar{u} = 0.3$ mm are plotted over the length of the bar for three different FE meshes, cf. Figure 4.2 (left). Therein, the ill-posedness of this problem is also well reflected. The width of the shear zone as well as the absolute values of the plastic strains are totally different in the calculations with the varying meshes. Furthermore, the location of the maximum value of the plastic strain changes and is never exactly at $x = L/2 = 0.1$ m, where the weakening of κ_0 is maximum.

In Figure 4.3, the results for $h = 0$ kN/m^2 are shown. Therein, the stress remains constant after the yield stress is reached, which in this example corresponds to 216 kN/m^2 in the weakened area of the bar at $x = L/2$. Due to the fact that for $h = 0$ kN/m^2, the stress response is specified *a priori* in the plastic regime, the resulting stress-displacement relationship shows a well-posed behavior, where the numerical results converge to a reference solution for the refined meshes, cf. Figure 4.3 (right). Nevertheless, the problem is still ill-posed, as the distribution of the plastic strains at $\bar{u} = 0.9$ mm shows again a mesh-dependent behavior, cf. Figure 4.3 (left), like in the previous example.

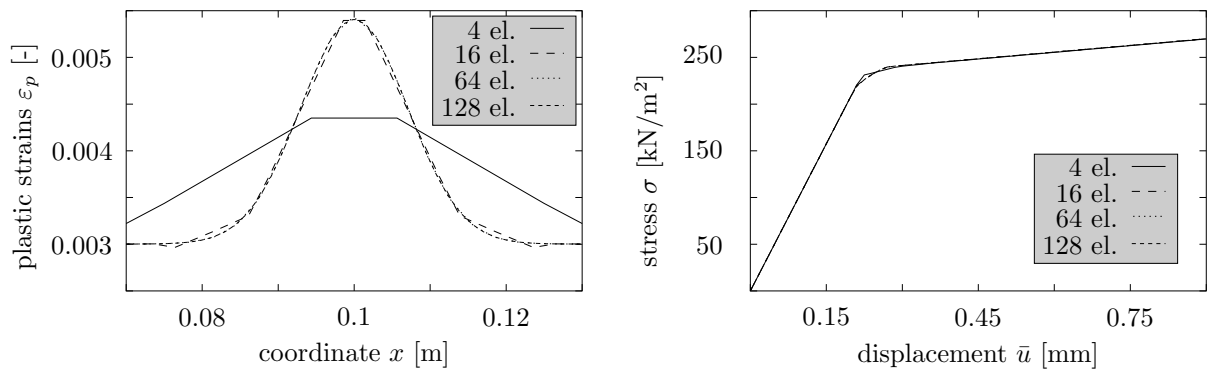Finally, in Figure 4.4, the parameter h is set to a negative value such that a hardening

Figure 4.4: Distribution of the plastic strains ε_p [-] in the bar (left) and development of the stress σ [kN/m^2] at $x = L$ (right) for $h = -1\,000\,\text{kN/m}^2$.

material behavior is obtained. This example results in a well-posed problem, as both the stress-displacement relationship and the distribution of the plastic strains show a mesh-independent behavior. Note that in this case, the whole bar undergoes plastic deformations, whereas in the middle area of the bar, the given weakening of κ_0 is reflected.

4.2 Overview of regularization techniques

In order to overcome the pathological mesh sensitivity illustrated in the last section, the ill-posed problem has to be regularized and, therewith, to be transferred into a well-posed problem. For this procedure, many different strategies can be found in the literature, cf. for an excellent survey on some methods, e. g., *Brinkgreve* [36]. Within this section, three main branches of regularization methods are discussed shortly concerning their advantages and disadvantages on the basis of important publications dealing with the respective methods.

Before this discussion, it is very important to be aware of the fact that, within most regularization methods, the actual mathematical formulation, which, from a theoretical point of view, describes the physical problem under study correctly, is changed such that the numerical realization of this formulation yields a well-posed problem. This is usually achieved by the introduction of an internal length scale, by which the influence of the regularization method on the physical model can be controlled. Applying a regularization technique, it is therefore always a crucial point to what extent the physical problem has to be changed in order to obtain a regularizing effect, i. e., an objective result.

The first branch of the regularization techniques to be discussed here are methods, which take advantage of a possible rate-dependent behavior of the material under study. Such a material behavior allows for the introduction of viscosity in the model, which prevents the pathological mesh dependence *a priori*. This is due to the fact that the numerical solutions for rate-dependent materials always remain well-posed even in the case of softening material behavior, cf. *Needleman* [113]. A common approach, which can be found in the literature, cf. [44, 121, 146] (among others), is to regard the rate-dependent behavior only

for its regularizing effect in the plastic regime, which leads to the term "viscoplasticity".

The actual realization of such rate-dependent regularization techniques are carried out within the constitutive theory, where, e. g., in case of the common *Perzyna* viscoplasticity [118], the viscosity is added within the formula for the plastic flow rule. In connection with this, it is remarkable that, although there are no parameters in such regularization methods with the dimensions of length involved, material rate dependence implicitly introduces an internal length scale in the governing equations, which affects the width of the shear band [113]. Furthermore, it was pointed out by *Belytschko et al.* [11] and *Wang et al.* [146] that, in case of viscoplasticity, the size of the imperfection can significantly influence the initial width of the shear band. Note that in the computational analysis of failure, imperfections in the geometry or the material parameters are very often used to initialize the localization zone, cf. the 1-d example from the last section.

Concerning the advantages and disadvantages of viscoplastic models, the most obvious drawback of this model is due to the rate dependence. Viscoplastic models do not work at all for purely static simulations. Adequate applications for this regularization technique are dynamic or, at least, quasi-static problems. Furthermore, for relatively slow processes, the amount of viscosity to retain well-posedness can become unrealistically high such that so-called artificial viscosities are incorporated in the respective boundary-value problem [36].
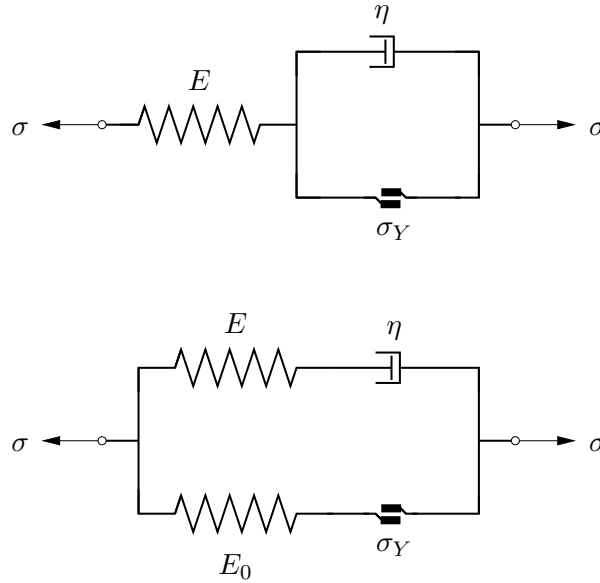

Figure 4.5: Rheological models for rate-dependent material behavior following *Perzyna* [118] (top) and *Dias da Silva* [41] (bottom).

Nevertheless, for dynamic or quasi-static problems, the viscoplastic model is a powerful tool for the regularization procedure. Moreover, following *Perzyna* [118], each material has a more or less pronounced time-dependent behavior, which furthermore motivates the application of viscoplasticity on a physical basis. *di Prisco & Imposimato* [120] prove even time-dependent material behavior for loose sand within experimental investigations (load

controlled triaxial tests). To be more precise, in a continuative publication, where the numerical simulation of this sand is discussed in detail, *di Prisco et al.* [121] admit that the identified viscosity is too low to reliably regularize their strain-softening problems such that they would have to choose artificial viscosities to obtain objective results, which is not surprising for this kind of material. To overcome this problem, *di Prisco et al.* expand their viscoplastic model with respect to a further regularization technique, namely a non-local model (see below). By this combination, they obtain objective results from their numerical simulations.

In a recent work by *Dias da Silva* [41], the difficulty of ill-posedness within low viscous or even inviscid circumstances is solved by a modification of the underlying rheological model. Therein, instead of the classical viscoplastic rheological model following *Perzyna* (Figure 4.5, top), a parallel assembly of a viscoelastic *Maxwell* model (E, η) and an elasto-plastic element (E_0, σ_Y) is used (Figure 4.5, bottom). Obviously, by this modification, viscosity is regarded in both the elastic and the plastic regime.

Finally, from a numerical point of view, viscoplastic models are very convenient, since they do not need any additional discretization on the global level, which makes the implementation of such a model within an existing FE program quite easy.

Another possibility of a regularization method is based on the application of the so-called micropolar theory, which dates back to the work by *Cosserat & Cosserat* [38] and which is, therefore, also called the *Cosserat* (continuum) theory. The micropolar theory is a physically motivated extension of the standard *Boltzmann* continuum. The basic idea of this extended continuum theory is to assign each material point in addition to the standard translational degrees of freedom also independent rotational degrees of freedom. By doing this, the distortion of the material points against each other has an influence on the macroscopic behavior.

PSfrag replacements

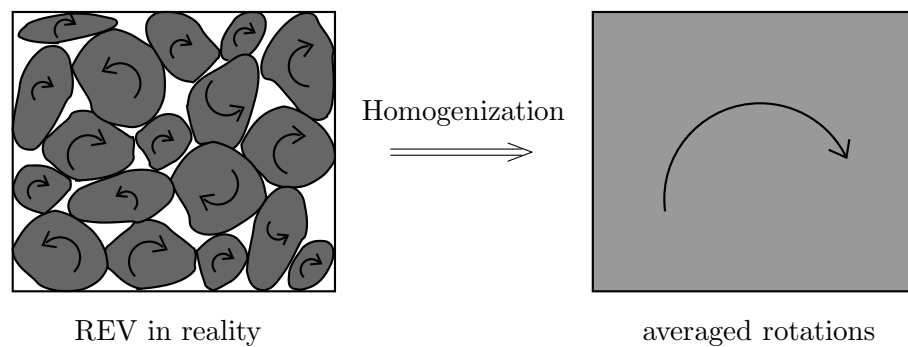REV in reality   Homogenization   averaged rotations

Figure 4.6: Physical motivation of the *Cosserat* theory [144].

Typical representatives of this micropolar class are granular materials, whose material points must have a spatial expanse in the order of magnitude of the single grains. Thus, the smallest possible unit of the micropolar material is a so-called micro rigid body, which consists of the three translational and the three rotational degrees of freedom of a rigid body. These rotational degrees of freedom may not be identified by the rotations of the single grains, as the virtual averaging process, cf. Section 2.1.1, has to be carried

out also in this case. Due to this reason, the additional rotational degrees of freedom correspond, from a physical point of view, to the averaged rotations of the single grains over a Representative Elementary Volume (REV), cf. Figure 4.6.

Interestingly enough, the micropolar theory by the *Cosserat* brothers received only little attention in the first half of the last century, which was probably caused by its relative complexity [26]. Nevertheless, after a dormant period of some 50 years, renewed interest arose by the work by, e. g., *Günther* [80], *Schaefer* [122], *Besdo* [13], *Eringen & Kafadar* [71] or *Steinmann* [132] (among others), in which the original formulation by the *Cosserat* brothers was extended and improved towards a generalized continuum mechanical theory. Publications with a focus on micropolar porous media on the basis of the Theory of Porous Media can be found in the group of *Ehlers*, cf., e. g., the work by *Diebels & Ehlers* [43], *Ehlers & Volk* [64], *Volk* [144], *Diebels* [42] or *Ehlers* [53].

The regularizing effect of the *Cosserat* theory within the numerical simulation of strain-softening problems was discovered almost 20 years ago, thus leading to many publications with emphasis on this topic, cf., e. g., *Mühlhaus & Vardoulakis* [111], *de Borst* [24, 25, 26], *Steinmann & Willam* [133], *Dietsche et al.* [47], *Tejchman & Wu* [138], *Ehlers & Volk* [64] or *Ehlers et al.* [60]. This regularizing effect is due to the introduction of the additional quantities couple stress and curvature [29], which are related to each other by a constitutive relation containing usually an internal length scale [24]. By this approach, the internal length scale, by which the width of the shear band can be controlled in the case of the numerical investigations of localization phenomena, is already introduced within the elastic regime.

Discussing the characteristics of the micropolar theory as a regularization method, *de Borst & Mühlhaus* [27] and *Brinkgreve* [36] claim that the *Cosserat* theory is only efficient as a regularization tool, if shear deformations play a dominant role in the respective boundary-value problem under study. This fact can lead to unrealistic results in the numerical simulation of fracture problems, like, e. g., of a mode-I fracture [26]. However, for the numerical investigations of shear bands, the *Cosserat* theory works well as a regularization technique. Therein, it can be observed that the rotational degrees of freedom and, as a consequence, the quantities couple stress and curvature are only active, i. e., non-zero, within the shearing domain.

Furthermore, due to the physical motivation of the *Cosserat* continuum, the micropolar theory can only be applied to certain classes of materials. Typical materials are in this context, e. g., materials with a granular or a beam-like microstructure. However, *Diepolder* [46] applied the micropolar theory even for the numerical simulation of torsion experiments of metal bars. He motivates this approach by experimental investigations of torsion bars, which show a modified surface structure after a torsional load. Following *Diepolder*, this change in composition of the surface is due to a change of the orientation of the single polycrystals in the metal bar.

From a numerical point of view, the application of the *Cosserat* theory significantly increases the numerical effort of solving a boundary-value problem, because of the introduction of the rotations as additional degrees of freedom. Nevertheless, *de Borst & Mühlhaus* [27] suggest an approach such that the classical format of computational plas-

ticity can be recovered and, thus, minimize the programming effort for the realization of the *Cosserat* theory in existing finite element programs.

Finally, the third main branch of regularization methods is discussed, the so-called non-local models. Except of the other two already discussed branches, the application of the non-local models is, as far as the author is aware, not restricted with respect to certain types of boundary-value problems or specific materials. For a clear classification of these models, the different approaches can be grouped into integral- and gradient-type models. In *Jirásek* [95], an excellent overview of both the integral- and gradient-type non-local methods is given.

Starting with the integral-type models, the first publications on this topic date back to the late sixties of the last century and focus on non-local formulations for elasticity, cf. *Kröner* [97] and *Eringen & Edelen* [70]. Later, this was extended by *Eringen* [69] towards plasticity. These ideas were first applied to regularization methods by *Pijaudier-Cabot & Bažant* [119] in the context of damage models and by *Bažant et al.* [8] or *Belytschko et al.* [10] for strain-softening problems. In *Strömberg & Ristinmaa* [136], a detailed description of a possible numerical solution procedure for an integral-type non-local plasticity model within the FE method is presented. A comprehensive publication on integral-type methods with an emphasis on damage models is given by *Bažant & Jirásek* [9].

Generally speaking, the idea of a non-local approach consists of replacing a certain "local" field function $f(\mathbf{x})$ by its non-local counterpart $\bar{\bar{f}}(\mathbf{x})$ obtained by a weighted averaging over a spatial neighborhood of each point under consideration [95]. This leads directly to the definition of an integral-type non-local (averaged) quantity

$$\bar{\bar{f}}(\mathbf{x}) = \frac{1}{V_r(\mathbf{x})} \int\limits_{\Omega} w(\mathbf{x} - \mathbf{y}) \, f(\mathbf{y}) \, \mathrm{d}v \,, \tag{4.2}$$

where w is an averaging function and $V_r(\mathbf{x})$ is the so-called representative volume defined by

$$V_r(\mathbf{x}) = \int\limits_{\Omega} w(\mathbf{x} - \mathbf{y}) \, \mathrm{d}v \,. \tag{4.3}$$

Note that the volume integrals in (4.2) and (4.3) are carried out over the whole domain Ω for fixed position vectors $\mathbf{x}$ and variable position vectors $\mathbf{y}$. The influence of the surrounding area of $\mathbf{x}$ on the averaged function $\bar{\bar{f}}(\mathbf{x})$ is given by the distance vector $(\mathbf{x} - \mathbf{y})$ included in the function w. Thus, the above definition yields for constant field functions, $f(\mathbf{x}) = \text{const.}$, the identity $\bar{\bar{f}}(\mathbf{x}) \equiv f(\mathbf{x})$. In this approach, the averaging function w contains the internal length scale, by which the influence of the regularization method on the numerical solution can be controlled, cf. [95, 136, 36] or Section 4.5.1.

In a fully integral-type non-local method, a relation is established between average stresses and average strains. Using a non-local approach as a regularization technique, usually only one variable is evaluated in an averaged sense. Following *Jirásek* [95], the choice of the variable to be averaged remains to some extent arbitrary, whereby at least one basic requirement has to be satisfied. The extended model should coincide with the standard

"local" continuum as long as the material behavior remains in the elastic range. Except for a homogeneous strain state, averaged strains always differ from local strains, thus leading to a different model behavior already for purely elastic deformations. For this reason, it is not possible to simply use averaged strains instead of the local ones and apply them to the standard constitutive relations. A possible choice, which fulfills this requirement, is to average the variable, which controls the softening behavior of the material under study [95, 136, 36]. According to the 1-d formulation (4.1) of the last section and (4.2), the plastic strain incorporated in the softening law can be averaged, which leads to the following modified non-local formulation of $(4.1)_6$: $\overset{\star}{\kappa} = \kappa_0 - h\,\bar{\bar{\varepsilon}}_p$.

From the integral formulation (4.2) for the averaged quantity $\bar{\bar{f}}(\mathbf{x})$, a relation in terms of gradients of the quantity f can be derived making use of the following *Taylor* series expansion [110, 67]:

$$
\begin{aligned}
f(\mathbf{y}) \;=\;& f(\mathbf{x}) + \nabla f(\mathbf{y})|_{\mathbf{y}=\mathbf{x}} \cdot (\mathbf{y}-\mathbf{x}) + \tfrac{1}{2!}\,\nabla\nabla f(\mathbf{y})|_{\mathbf{y}=\mathbf{x}} \cdot [\,(\mathbf{y}-\mathbf{x}) \otimes (\mathbf{y}-\mathbf{x})\,] + \\[4pt]
&+\;\tfrac{1}{3!}\,\nabla\nabla\nabla f(\mathbf{y})|_{\mathbf{y}=\mathbf{x}} \cdot [\,(\mathbf{y}-\mathbf{x}) \otimes (\mathbf{y}-\mathbf{x}) \otimes (\mathbf{y}-\mathbf{x})\,] + \\[4pt]
&+\;\tfrac{1}{4!}\,\nabla\nabla\nabla\nabla f(\mathbf{y})|_{\mathbf{y}=\mathbf{x}} \cdot [\,(\mathbf{y}-\mathbf{x}) \otimes (\mathbf{y}-\mathbf{x}) \otimes (\mathbf{y}-\mathbf{x}) \otimes (\mathbf{y}-\mathbf{x})\,] + \ldots
\end{aligned}
\tag{4.4}
$$

Therein, the notation $\nabla(\cdot) = \mathrm{grad}\,(\cdot)$ has been used. Insertion of this expression in (4.2) and evaluation of the integral on $\mathbb{R}^3$ gives the following gradient-type non-local representation of f, cf. Appendix B:

$$
\bar{\bar{f}}(\mathbf{x}) = f(\mathbf{x}) + C_1\,\Delta f(\mathbf{x}) + C_2\,\Delta\Delta f(\mathbf{x}) + \ldots,
\tag{4.5}
$$

where the abbreviations $\Delta(\cdot) = \mathrm{div}[\nabla(\cdot)]$ and $\Delta\Delta(\cdot) = \Delta^2(\cdot)$ have been used for convenience. Note that the odd derivatives from (4.4) vanish due to isotropy properties of the averaging function w, cf. Section 4.5.1. Furthermore, note that for the gradient-type models, the internal length scale is included in the constants C_i $(i = 1, 2, \ldots)$.

Many different gradient-type models can be found in the literature, where most of these models contain second-order gradients, i. e., the fourth- and higher-order gradients from (4.5) are neglected there. Initially, the idea to add gradients to the constitutive relations dates back to the work by *Mindlin* [106] from 1965. In the context of regularization methods, this idea was first picked up by *Aifantis* [1], who added a second-order gradient of the hardening/softening variable in the constitutive relation for the yield stress. First remarks on the numerical realization of the gradient-type models can be found in *Lasry & Belytschko* [101]. The connection between the integral- and gradient-type models, cf. (4.4) and (4.5), was discovered by *Mühlhaus & Aifantis* [110]. They furthermore established a variational formulation for the gradient-type models, where *de Borst & Mühlhaus* [27, 28] intensively investigated the numerical realization of this variational formulation by introducing the plastic multiplier as an additional degree of freedom. *de Borst & Pamin* [30] discuss the problems coming along with the numerical realization of these models, e. g., the proper consideration of the additional boundary terms from the variational formulation or the choice of C^0- or C^1-continuous finite elements for a correct approximation of the higher-order gradient terms. Even in the last few years, the work

on this topic is still up to date, e. g., *Askes et al.* [3] analytically examined second-order gradient models and created a new strain-gradient model including fourth-order gradients.

In accordance with the 1-d formulation (4.1) of the last section, a gradient-type non-local formulation of $(4.1)_6$ could be formulated as

$$\overset{\star}{\kappa} = \kappa_0 - h \left(\varepsilon_p + l^2 \, \Delta \varepsilon_p \right) = \kappa_0 - h \left(\varepsilon_p + l^2 \, \frac{\partial^2 \varepsilon_p}{\partial x^2} \right) , \qquad (4.6)$$

where l is the internal length scale. The effect of this relation is obvious: as long as the solution remains uniform, the plastic strain is constant in space, its second derivative vanishes identically, and (4.6) is reduced to the standard formulation $(4.1)_6$. After the onset of localization, the higher-order term is activated and, thus, the formulation preserves its well-posedness [95].

Due to the above mentioned problems in the numerical realization of the gradient-type models, the development and the application of so-called implicit gradient-type methods receive more and more attention, cf., e. g., *Engelen et al.* [67] or *Zimmermann* [158] (among others). In this context, models of the type (4.6) are called "explicit", as the corresponding non-local quantity, $\varepsilon_p + l^2 \, \Delta \varepsilon_p$, can be directly calculated from the local field ε_p. In contrast to this, implicit models can be derived by taking the second-order derivative Δ of (4.5), thus, after some reformulation, ending up with the following partial differential equation of *Helmholtz* type [67]:

$$\bar{\bar{f}}(\mathbf{x}) - C_1 \, \Delta \bar{\bar{f}}(\mathbf{x}) = f(\mathbf{x}) . \qquad (4.7)$$

By adding the above relation to the set of governing equations and by solving it on the global level, a C^0-continuous interpolation is sufficient for the weak formulation of (4.7). Furthermore, the problems coming along with the boundary terms are no longer present, as the boundary terms of the implicit formulation are defined on the external boundary and not on the moving boundary of the plastic domain, as it is the case for the explicit gradient-type models [67, 30].

Finally, it should be mentioned at the end of this section that physically meaningful combinations between different regularization methods can lead to improved results concerning the well-posedness or the numerical behavior, cf., e. g., *di Prisco et al.* [121] or *Volk* [144].

4.3   Viscoplasticity

4.3.1   Theoretical aspects

A widespread strategy to include rate-dependent plastic material behavior in a continuum mechanical model is the approach suggested by *Perzyna* [118] in the middle of the sixties of the last century. Therein, the plastic multiplier Λ included in the flow rule (2.101) is given by

$$\Lambda = \frac{1}{\eta} \left\langle \frac{F(\boldsymbol{\sigma})}{\sigma_0} \right\rangle^r , \qquad (4.8)$$

where η is the relaxation time (viscosity), σ_0 is the reference stress for which the relation $\sigma_0 \equiv \kappa_0$ is usually used, r is the viscoplastic exponent and $\langle \cdot \rangle$ are the *Macauley* brackets defined by $\langle x \rangle = \max\{0, x\}$.

Remark: Note that the quantities introduced in Chapter 2 are used here without the usual indices marking the different constituents of a porous material. As was already mentioned in Section 4.1, plastic material behavior is restricted to the solid phase ($\alpha = S$) and, therefore, all indices regarding this are omitted for convenience in this chapter. Following this, e. g., the linearized stress tensor (of the solid constituent) is given by $\boldsymbol{\sigma}$ instead of $\boldsymbol{\sigma}_E^S$. $\square$

In the viscoplastic approach, the relation (4.8) is used for the determination of Λ instead of the *Kuhn-Tucker* conditions (2.102), thus allowing for overstresses, i. e., $F(\boldsymbol{\sigma}) > 0$, whose amounts depend on the values chosen for the viscoplastic material parameters η and r. This overstress character is getting more clear by a reformulation of (4.8):

$$\Lambda \, \eta \, \langle \sigma_0 \rangle^r = \langle F(\boldsymbol{\sigma}) \rangle^r \ . \tag{4.9}$$

From the above relation, both the rate-independent as well as the rate-dependent case can be deduced, cf. *Hartmann et al.* [84], where the limiting case ($\eta = 0$) represents elasto-plasticity and $\eta > 0$ leads to viscoplastic material behavior.

Note that due to the use of the *Macauley* brackets in (4.8), the restriction for the plastic multiplier defined in (2.102)$_2$, i. e., $\Lambda \geq 0$, is still valid for the viscoplastic case. Consequently, this leads to $\Lambda = 0$ for the elastic regime and to some $\Lambda > 0$ resulting from the evaluation of (4.8) in the plastic regime. Following this, the evaluation of (2.101) yields $\boldsymbol{\varepsilon}_p' = \mathbf{0}$ for $\Lambda = 0$ and some non-zero value for the plastic strain tensor $\boldsymbol{\varepsilon}_p$ for $\Lambda > 0$.

4.3.2 Numerical realization

Starting from an existing implementation of the elasto-plasticity model as described in Section 3, the numerical realization of the rate-dependent concept is straightforward, cf. *Ellsiepen* [66], *Ehlers & Ellsiepen* [59] or *Wieners et al.* [151]. The spatial and temporal discretized formulation of the plastic evolution equations introduced in (3.35) have to be changed with respect to the viscoplastic approach:

$$\boldsymbol{\varepsilon}_p^{h,n} = \boldsymbol{\varepsilon}_p^{h,n-1} + \Delta t_n \, \Lambda^{h,n} \, \frac{\partial G(\boldsymbol{\sigma}(\mathbf{u}^{h,n}, \boldsymbol{\varepsilon}_p^{h,n}))}{\partial \boldsymbol{\sigma}} \ ,$$

$$\Lambda^{h,n} = \frac{1}{\eta} \left\langle \frac{F(\boldsymbol{\sigma}(\mathbf{u}^{h,n}, \boldsymbol{\varepsilon}_p^{h,n}))}{\sigma_0} \right\rangle^r \ . \tag{4.10}$$

Note that with the explicit equation (4.10)$_2$ for the plastic multiplier $\Lambda^{h,n}$, the local system (4.10) could be reduced to one vector-valued relation by inserting (4.10)$_2$ into (4.10)$_1$. This simplification is not going to be carried out in order to keep the possibility to easily switch from the rate-dependent to the rate-independent case, in which (4.10)$_2$ is replaced again by (3.35)$_2$.

The actual evaluation of (4.10) is carried out in an analogous way as described in Section 3 for the rate-independent model. Thus, from a numerical point of view, the use of the viscoplastic approach as a regularization technique does not increase the computational effort at all, as one scalar relation $(3.35)_2$ is replaced by another one $(4.10)_2$ and, even more important, the evaluation of the plastic evolution equations can still be carried out element-wise on a local level.

4.4 Micropolar theory

4.4.1 Theoretical aspects

Within this section, a very brief summary of the micropolar theory is given. Therein, the changes due to this theory within the governing equations, i. e., the geometrically linear kinematics, the moment of momentum balance relation and the constitutive relations, are going to be presented. The reader who is interested in a more detailed description of the *Cosserat* theory is referred to the citations on this topic already given in Section 4.2.

Considering besides translational also rotational degrees of freedom for each material point, consequently, an additional primary kinematic variable besides the displacement vector $\mathbf{u}$ has to be taken into account for a proper formulation of the kinematic relations, namely the independent micropolar rotation $\overset{*}{\boldsymbol{\varphi}}$. Together with the continuum rotation $\boldsymbol{\varphi}$, which is directly connected with the skew-symmetric part $\mathbf{H}_{\mathrm{skw}}$ of the displacement gradient $\mathbf{H}$,

$$\mathbf{H} = \operatorname{grad} \mathbf{u} \,, \qquad \mathbf{H}_{\mathrm{skw}} = \tfrac{1}{2} \left(\mathbf{H} - \mathbf{H}^T \right) , \tag{4.11}$$

this defines the total average grain rotation $\bar{\boldsymbol{\varphi}}$ by

$$\bar{\boldsymbol{\varphi}} = \boldsymbol{\varphi} + \overset{*}{\boldsymbol{\varphi}} \,, \qquad \boldsymbol{\varphi} = -\tfrac{1}{2} \overset{3}{\mathbf{E}} \, \mathbf{H}_{\mathrm{skw}} \,. \tag{4.12}$$

Therein, $\overset{3}{\mathbf{E}}$ denotes the *Ricci* permutation tensor, cf. Appendix A.1.3. As a consequence of the introduction of $\bar{\boldsymbol{\varphi}}$, one is able to define the linear *Cosserat* strain tensor $\bar{\boldsymbol{\varepsilon}}$ and the linear curvature tensor $\bar{\boldsymbol{\kappa}}$:

$$\bar{\boldsymbol{\varepsilon}} = \mathbf{H} + \overset{3}{\mathbf{E}} \, \bar{\boldsymbol{\varphi}} \,, \qquad \bar{\boldsymbol{\kappa}} = \operatorname{grad} \bar{\boldsymbol{\varphi}} \,. \tag{4.13}$$

From the above definition, it is obvious that the *Cosserat* strain tensor $\bar{\boldsymbol{\varepsilon}}$ does not necessarily have to be a symmetric tensor, as it is the case for the strain tensor $\boldsymbol{\varepsilon}$ from the non-polar continuum theory, cf. Equation (2.95). Thus, the symmetric and the skew-symmetric parts of the *Cosserat* strain are described by

$$
\begin{aligned}
\bar{\boldsymbol{\varepsilon}}_{\mathrm{sym}} &= \tfrac{1}{2} \left(\mathbf{H} + \mathbf{H}^T \right) &&= \boldsymbol{\varepsilon} \,, \\
\bar{\boldsymbol{\varepsilon}}_{\mathrm{skw}} &= \tfrac{1}{2} \left(\mathbf{H} - \mathbf{H}^T \right) + \overset{3}{\mathbf{E}} \, \bar{\boldsymbol{\varphi}} &&= \overset{3}{\mathbf{E}} \, \overset{*}{\boldsymbol{\varphi}} \,.
\end{aligned}
\tag{4.14}
$$

Furthermore, *Ehlers & Volk* [64] derived a relation between the *Cosserat* strain and the linear curvature tensor. This so-called micropolar compatibility condition can be obtained

by use of the Equations $(4.11)_1$ and (4.13) and the *Schwarz*ian exchangeability rule of partial derivatives, cf. *Volk* [144] for a detailed derivation:

$$\bar{\boldsymbol{\kappa}} = \tfrac{1}{2} \{ \overset{3}{\mathbf{E}} [\operatorname{grad} \bar{\boldsymbol{\varepsilon}} + (\operatorname{grad} \bar{\boldsymbol{\varepsilon}})^{\overset{13}{T}} - (\operatorname{grad} \bar{\boldsymbol{\varepsilon}})^{\overset{23}{T}}] \}^{\underline{2}}. \tag{4.15}$$

As already mentioned, the transpositions $(\cdot)^{\overset{ik}{T}}$ indicate an exchange of the i-th and k-th basis systems included into the tensor basis of higher order tensors. The additional superscript $\{ \cdot \}^{\underline{n}}$ defines the included contraction $\{ \cdot \}$ to yield a tensor of n-th order, cf. Appendix A.1.5.

In a next step, the micropolar moment of momentum balance relation is going to be discussed, in which additional quantities compared to the standard moment of momentum balance, cf. Section 2.2.4, have to be regarded. Referring to the general balance relation $(2.41)_2$, the following values for the efflux $\boldsymbol{\Phi}$, the supply $\boldsymbol{\sigma}$ and the production term $\hat{\boldsymbol{\Psi}}$ have to be considered for a proper determination of the temporal change of the micropolar angular momentum, which is the mechanical quantity $\boldsymbol{\Psi}$ in this case:

$$\boldsymbol{\Psi} = \mathbf{x} \times \rho \, \dot{\mathbf{x}} + \rho \, \bar{\boldsymbol{\Theta}} \, \bar{\boldsymbol{\omega}} \,, \qquad \boldsymbol{\Phi} = \mathbf{x} \times \mathbf{T} + \mathbf{M} \,, \qquad \boldsymbol{\sigma} = \mathbf{x} \times \rho \, \mathbf{b} + \rho \, \mathbf{c} \,, \qquad \hat{\boldsymbol{\Psi}} = \mathbf{0} \,. \tag{4.16}$$

Therein, $\bar{\boldsymbol{\Theta}}$ is the tensor of microinertia, $\bar{\boldsymbol{\omega}} = \dot{\bar{\boldsymbol{\varphi}}}$ is the rotational velocity, $\mathbf{M}$ denotes the couple stress tensor and $\mathbf{c}$ is the volume-specific body couple stress vector.

With the above relation and $(2.42)_2$ together with the consideration of the "lower" balance relations, i. e., the mass and the momentum balances, the following local moment of momentum balance relation is obtained:

$$\rho \, (\bar{\boldsymbol{\Theta}} \, \bar{\boldsymbol{\omega}})^{\boldsymbol{\cdot}} = \mathbf{I} \times \mathbf{T} + \operatorname{div} \mathbf{M} + \rho \, \mathbf{c} \,. \tag{4.17}$$

Restricting the considerations to the case of quasi-static processes $(\dot{\bar{\boldsymbol{\omega}}} = \mathbf{0})$ and, furthermore, applying the simplifying assumption $\dot{\bar{\boldsymbol{\Theta}}} = \mathbf{0}$ [64], the balance equation of angular momentum finally reads

$$\mathbf{0} = \mathbf{I} \times \mathbf{T} + \operatorname{div} \mathbf{M} + \rho \, \mathbf{c} \,. \tag{4.18}$$

The above relation serves as an equation for the determination of the total rotation $\bar{\boldsymbol{\varphi}}$. Furthermore, as a direct consequence of Equation (4.18), the micropolar stress tensor $\mathbf{T}$ (or $\boldsymbol{\sigma}$, cf. $(4.19)_1$) usually is non-symmetric.

Remark: As was already mentioned in the remark on Page 68, the character $\boldsymbol{\sigma}$ will be used as a symbol for the stress tensor under small strain conditions. The supply term from (4.16), which unfortunately has the same symbol, is not going to be used in the further discussions in this thesis. □

Following *Ehlers & Volk* [64], the constitutive expressions for the stress $\boldsymbol{\sigma}$ and the couple stress $\mathbf{M}$ are given by

$$\begin{aligned} \boldsymbol{\sigma} &= 2 \, \mu \, \bar{\boldsymbol{\varepsilon}}_{e \, \mathrm{sym}} + 2 \, \mu_c \, \bar{\boldsymbol{\varepsilon}}_{e \, \mathrm{skw}} + \lambda \, (\bar{\boldsymbol{\varepsilon}}_{e \, \mathrm{sym}} \cdot \mathbf{I}) \, \mathbf{I} \,, \\[2mm] \mathbf{M} &= 2 \, \mu_c \, l_c^2 \, \bar{\boldsymbol{\kappa}}_e \,, \end{aligned} \tag{4.19}$$

whereby, in analogy to the non-polar theory, cf. (2.96), the *Cosserat* strain $\bar{\varepsilon}$ and the curvature tensor $\bar{\kappa}$ are additively decomposed into elastic and plastic parts:

$$\bar{\varepsilon} = \bar{\varepsilon}_e + \bar{\varepsilon}_p \,, \qquad \bar{\kappa} = \bar{\kappa}_e + \bar{\kappa}_p \,. \tag{4.20}$$

In (4.19), μ and λ are the standard *Lamé* constants, whereas μ_c is an additional parameter governing the influence of the skew-symmetric part of the elastic *Cosserat* strain on the stress tensor $\boldsymbol{\sigma}$. Note that the symmetric part of $\boldsymbol{\sigma}$ is equivalent to the stress tensor (2.97) of the non-polar formulation, whereas the skew-symmetric part is directly related to the independent micropolar rotation $\overset{*}{\boldsymbol{\varphi}}$ through (4.14)$_2$. Finally, as was pointed out, e. g., by *de Borst* [24], l_c represents an intrinsic length scale parameter relating the couple stress to the elastic curvature. Using this parameter, the regularizing effect of the micropolar theory can be controlled.

In order to expand the micropolar theory to plastic material behavior, all the stress quantities introduced in (4.19) have to be considered for a consistent formulation of the yield criterion. Starting from the extension of the single-surface yield criterion (2.98) towards micropolar cohesive-frictional materials given in [64], a simple micropolar yield criterion could be formulated via

$$\bar{F} = \sqrt{\mathbb{II}_{\mathrm{sym}}^D + k_\sigma \, \mathbb{II}_{\mathrm{skw}}} + \tfrac{1}{2} \, k_M \sqrt{\mathbb{II}_M} - \overset{\star}{\kappa} \,, \tag{4.21}$$

whereby, for simplicity, the parameters $\{\alpha,\, \beta,\, \delta,\, \epsilon\,,\gamma\,,m\}$ from (2.98) are all set to zero and the constant parameter κ is replaced by a proper softening law $\overset{\star}{\kappa}$ to be discussed in Section 4.6.2. In the yield criterion introduced above, $\mathbb{II}_{\mathrm{sym}}^D$ is the second principal invariant of symmetric part of the stress deviator $\boldsymbol{\sigma}^D$, $\mathbb{II}_{\mathrm{skw}}$ defines the second principal invariant of the skew-symmetric part of $\boldsymbol{\sigma}$, and $\mathbb{II}_M$ is the second principal invariant of the couple stress $\mathbf{M}$, cf. Appendix A.2.2. Furthermore, k_σ and k_M are additional material parameters.

As was pointed out by *Ehlers & Volk* [64], there exists no evolution equation for the plastic rate of the curvature tensor independent of both the evolution equation for the plastic strains, cf. (2.101),

$$\bar{\varepsilon}'_p = \Lambda \, \frac{\partial \bar{G}}{\partial \boldsymbol{\sigma}} \,, \tag{4.22}$$

and the micropolar compatibility condition (4.15). Thus, once the plastic strain rate is given via Equation (4.22), the most convenient possibility to obtain an evolution equation for $\bar{\kappa}_p$ directly results from (4.15), leading to the following expression:

$$\bar{\kappa}'_p = \tfrac{1}{2} \, \{ \overset{3}{\mathbf{E}} \, [\, \mathrm{grad}\, \bar{\varepsilon}'_p + (\mathrm{grad}\, \bar{\varepsilon}'_p)^{\overset{13}{T}} - (\mathrm{grad}\, \bar{\varepsilon}'_p)^{\overset{23}{T}} \,] \, \}^{\underline{2}}. \tag{4.23}$$

Note that within the further discussions in this chapter, the concept of associated plasticity is applied for simplicity. Therefore, the micropolar plastic potential $\bar{G}$ from (4.22) is equal to the yield criterion (4.21), thus leading to $\bar{G} = \bar{F}$.

4.4.2   Numerical realization

As was shown in Section 3.1.1, the strong formulation (4.18) of the moment of momentum balance has to be transferred into a weak formulation. Therefore, the necessary trial and test spaces are defined in a way analogous to (3.2):

$$
\begin{aligned}
\mathcal{S}_\varphi(t) &= \left\{\, \bar{\boldsymbol{\varphi}} \ \in H^1(\Omega)^r \,:\, \bar{\boldsymbol{\varphi}}(\mathbf{x}) \ = \bar{\boldsymbol{\varphi}}(\mathbf{x},\, t) \ \text{on } \Gamma_\varphi \,\right\}, \\
\mathcal{T}_\varphi &= \left\{\, \delta\bar{\boldsymbol{\varphi}} \in H^1(\Omega)^r \,:\, \delta\bar{\boldsymbol{\varphi}}(\mathbf{x}) = \mathbf{0} \qquad \text{on } \Gamma_\varphi \,\right\}.
\end{aligned}
\tag{4.24}
$$

Therein, the index r is related to the spatial domain, i. e., it holds $r = 1$ for a 2-d problem and $r = 3$ for a 3-d problem. Note that the only rotational degree of freedom in two-dimensional problems is defined by a possible "in-plane" rotation of a grain around the axis perpendicular to the defined plane. Following this, it is not possible to formulate a *Cosserat* theory within a purely one-dimensional model, as no rotational degree of freedom can be identified therein. Note that in "hybrid" models like the *Timoshenko* beam such independent rotations can be identified again, cf. *Günther* [80]. In the framework of this thesis, such models, which exhibit expanded 1-d formulations but which are not globally valid 2-d models, are not going to be discussed.

By a scalar multiplication of (4.18) with the test function $\delta\bar{\boldsymbol{\varphi}}$, integration over the domain Ω and application of the usual reformulations shown in Section 3.1.1, the weak formulation of the moment of momentum balance relation is obtained:

$$
\int_\Omega \mathbf{M} \cdot \operatorname{grad} \delta\bar{\boldsymbol{\varphi}} \, \mathrm{d}v - \int_\Omega (\mathbf{I} \times \boldsymbol{\sigma}) \cdot \delta\bar{\boldsymbol{\varphi}} \, \mathrm{d}v = 0 \quad \forall \quad \delta\bar{\boldsymbol{\varphi}} \in \mathcal{T}_\varphi.
\tag{4.25}
$$

Therein, it has been assumed that there is no external loading by couple vectors $\mathbf{c}$ and surface couples $\mathbf{m} = \mathbf{M}\,\mathbf{n}$.

The above relation and the weak formulation of the momentum balance (3.7), in which the pore pressure p has to be set to zero for a single phase material, build the set of governing equations for the (single phase) micropolar formulation to be discussed in this chapter. According to *Volk* [144], the convergence behavior of this model can be significantly improved by applying the viscoplastic ansatz shown in Section 4.3 instead of the elasto-plastic approach. Therefore, this combination is going to be used in the numerical simulations shown in Section 4.6.2.

Remark: Combining the two regularization methods, it is, at first sight, not clear, which approach is regularizing the numerical simulation of a strain-softening problem. To demonstrate the regularizing effect of the *Cosserat* theory, an adequately small value for the viscosity η will be chosen in the numerical example in Section 4.6.2. Before this, it will be shown that this value for the viscosity leads to an ill-posed behavior, if numerical simulations are carried out with the viscoplastic approach as the only regularization technique.   □

Another point to be discussed in this section is the numerical evaluation of the gradient terms included in the compatibility condition (4.15) or (4.23). The difficulty involved

there is that the (plastic) strains are variables, whose values are only calculated at the integration points of the numerical integration, cf. Section 3.1. Therefore, the determination of the gradient of these only point-wise defined quantities is not straightforward. A simple solution to overcome this problem is suggested by *Volk* [144]. Therein, without changing the point-wise representation of the strains, an approximation method to determine the gradient of $\bar{\varepsilon}$ is presented based on ansatz functions of the FEM. The basic idea of this approach is to use the ansatz functions within each finite element to determine the exact nodal values of the strains, i. e., from the viewpoint of the usual evaluation procedure of the ansatz functions, an inverse problem is solved. The task of this inverse problem is to find the nodal values of the strains such that the evaluation of the ansatz functions at the integration points exactly yields the respective values of $\bar{\varepsilon}$. In two dimensions, this strategy can be realized with only little numerical effort. Using three integration points in a triangle and four integration points in a quadrilateral, the linear ansatz functions, which are defined by three or four nodal points in a triangle or quadrilateral, lead to small systems of linear equations, which can be solved without high numerical effort. In three dimensions, very often a higher integration order has to be chosen for a stable numerical quadrature, thus leading to a number of integration points, which is not equal to the number of nodes necessary for an arbitrary order of an ansatz function. For example, in a hexahedron, an integration of fifth order defines altogether 27 integration points, whereas a linear or a quadratic ansatz is defined by 8 or 20 nodal points, respectively. In such a case, the approach suggested by *Volk* would have the consequence of an enormous numerical overhead, as this over-determined system has to be solved by a time consuming procedure as, e. g., the least-squares method [140].

A direct consequence of the approach described above for the evaluation of the gradient of the (plastic) strains is that the local systems for the determination of the current plastic strain increment and the plastic multiplier cannot be evaluated any longer in a point-wise manner. Due to the additional consideration of the couple stress in the yield criterion and the use of the compatibility condition for the determination of the plastic curvatures $\bar{\boldsymbol{\kappa}}_p$, the values for the plastic strains $\bar{\boldsymbol{\varepsilon}}_p$ at each integration point depend on the respective values at the other integration points. Consequently, all integration points of a finite element have to be included in the solution of the local system. However, this results in only a small increase of the numerical effort of the local solution procedure, as, e. g., in a quadrilateral instead of four nonlinear equations with six unknowns, namely the entries of the non-symmetric plastic strain tensor and the plastic multiplier, now one nonlinear system with altogether 24 unknowns has to be solved.

4.5 Non-local model

4.5.1 Theoretical aspects

In the framework of this section, an integral-type non-local model is discussed in detail, which is based on the definitions for the determination of an averaged quantity $\bar{\bar{f}}$ given
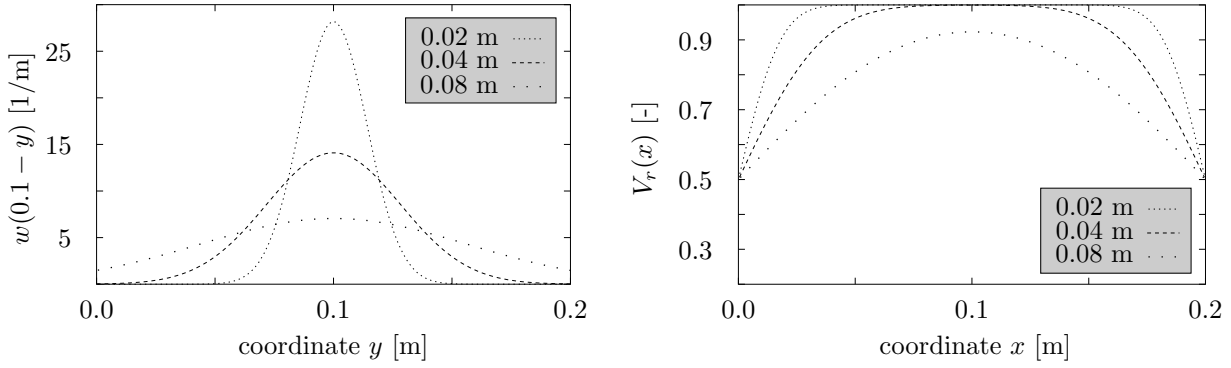
Figure 4.7: Weighting function w (left) and representative volume V_r (right) evaluated for different values of the internal length scale l.

by Equations (4.2) and (4.3):

$$\bar{\bar{f}}(\mathbf{x}) = \frac{1}{V_r(\mathbf{x})} \int\limits_\Omega w(\mathbf{x} - \mathbf{y})\, f(\mathbf{y})\, \mathrm{d}v\,, \quad V_r(\mathbf{x}) = \int\limits_\Omega w(\mathbf{x} - \mathbf{y})\, \mathrm{d}v\,, \tag{4.26}$$

In order to complete these definitions, the weighting function w has to be specified. Following *Brinkgreve* [36], a possible choice for this weighting function is given by

$$w(\mathbf{x} - \mathbf{y}) = \frac{1}{l\sqrt{\pi}} \exp\left[-\frac{(\mathbf{x} - \mathbf{y}) \cdot (\mathbf{x} - \mathbf{y})}{l^2}\right]\,. \tag{4.27}$$

Other choices can be found in the literature on non-local theories, cf. *Strömberg & Ristinmaa* [136] or *Jirásek* [95] and the citations therein. The important properties of the above introduced exponential, *Gauss*ian bell-shaped function are that it has a maximum at $\mathbf{y} = \mathbf{x}$, it is symmetric about that point and, finally, it depends on an internal length scale l. These properties can be recognized in Figure 4.7 (left), where the function (4.27) is plotted within a 1-d example for different values of l at the position $x = 0.1$ m. Obviously, the sphere of influence of the weighting function increases with increasing values of the internal length scale. Looking at the representative volume (Figure 4.7, right), the influence of l as well as of the boundary of the domain on the result of the averaging procedure can be deduced. If l is relatively small compared with the dimensions of the domain Ω, the representative volume results in the constant value 1.0, except close to the boundaries of the domain, where the value for V_r decreases to the minimum value 0.5. This behavior of V_r has the consequence that values of functions that are to be averaged at points close to boundaries are more weighted, since they do not get "contributions" from points outside the boundaries [136]. This is illustrated in Figure 4.8 (left), where the function $w(x - y)/V_r(x)$ is plotted as a function of x for $l = 0.04$ m and for various constant values of y, viz $y = 0$ m, 0.05 m, 0.1 m, 0.15 m, 0.2 m.

Using the proposed averaging procedure, it can be observed that for small enough values of l, the non-local function is equal to the local one. This effect is shown in Figure 4.8 (right), where the local function $f(x) = 20 - 9^4\, x^2 + 10^6\, x^5$ is transferred for three different internal length scales into its non-local representation $\bar{\bar{f}}(x)$. Starting from a rather big
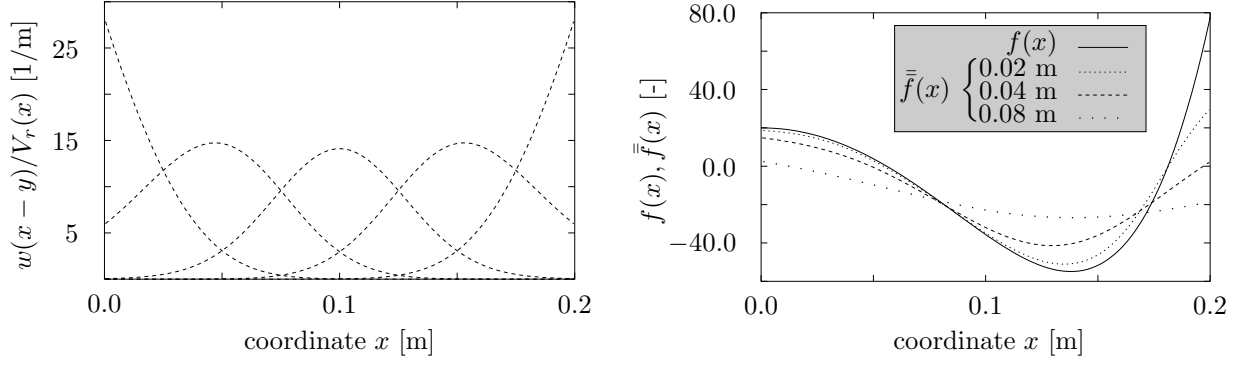
Figure 4.8: Weighting behavior for different values for y (left) and non-local representations $\bar{\bar{f}}(x)$ of the local function $f(x) = 20 - 9^4\,x^2 + 10^6\,x^5$ for different values of the internal length scale l (right).

value for l, where the similarity with the local function is almost vanished, the differences between the local and the non-local functions are getting smaller for smaller values of l.

As already depicted in Section 4.2, a possible choice for the variable to be averaged within a non-local theory is a scalar reference value of the plastic strain tensor $\boldsymbol{\varepsilon}_p$, which is incorporated in the softening law $\overset{\star}{\kappa}$. Very often, the so-called accumulated plastic strain

$$\varepsilon_{pv} := ||\boldsymbol{\varepsilon}_p|| = \sqrt{\boldsymbol{\varepsilon}_p \cdot \boldsymbol{\varepsilon}_p} \tag{4.28}$$

is used for this purpose, thus leading to $\overset{\star}{\kappa}(\bar{\bar{\varepsilon}}_{pv})$. This choice is interesting from a numerical point of view, as it can cause major changes in the numerical procedure, cf. the next section.

Based on the work by *Brinkgreve* [36], an additional parameter α is introduced, by which the influence of both the local and the non-local parts of the plastic strain on the averaged plastic strain can be weighted:

$$\bar{\bar{\varepsilon}}_{pv}(\mathbf{x}) = \langle 1 - \alpha \rangle\,\varepsilon_{pv}(\mathbf{x}) + \frac{\alpha}{V_r(\mathbf{x})} \int\limits_{\Omega} w(\mathbf{x} - \mathbf{y})\,\varepsilon_{pv}(\mathbf{y})\,\mathrm{d}v\,. \tag{4.29}$$

Therein, $\langle \cdot \rangle$ are the *Macauley* brackets already introduced in Equation (4.8). Note that for $\alpha = 1$, the formulation $(4.26)_1$ is obtained. *Brinkgreve* motivates the introduction of the additional parameter α by a better convergence behavior within his 1-dimensional numerical studies of the non-local method. In Section 4.6.2, the importance of this parameter in order to obtain mesh-independent results will be emphasized.

4.5.2 Numerical realization

Upon a closer look at (4.29), it is apparent that the usual local, element-wise evaluation of the yield criterion as described in Section 3.3 can no longer be carried out. Obviously, the calculation of $\bar{\bar{\varepsilon}}_{pv}$ depends not only on the local quantities of the plastic strain tensor

$\boldsymbol{\varepsilon}_p$ but also on the plastic strains of the surrounding integration points. For a consistent evaluation of Equation (4.29), the non-local character of this formulation has to be considered. Therefore, two different approaches for the numerical realization are going to be discussed within this section, whereby the first approach leads to an exact but very inefficient evaluation of (4.29), and the second approach is based on a simplification, which makes the evaluation procedure more efficient.

In order to realize the formulation (4.29) exactly, a straightforward approach is to determine the plastic strains for a given *Newton* iterate $\boldsymbol{u}_n^j$ globally before the standard element-wise evaluation procedure is carried out. By doing this, it is ensured that each element contains the up to date plastic strains corresponding to the current *Newton* iterate. However, a global system containing all plastic strains and plastic multipliers at each integration point has to be solved in this approach for each *Newton* iterate, cf. Equation (3.47). Note that in contrast to the usual local formulation, this procedure now leads to a coupled system, in which, due to the non-local formulation of the softening law $\overset{\star}{\kappa}(\bar{\bar{\varepsilon}}_{pv})$, the single plastic strains depend on each other. Obviously, this additional solution of such a coupled, global system implies a very inefficient strategy, which is therefore only applied for the calculation of the 1-dimensional numerical example in Section 4.6.1.

For the realization of the 2-dimensional example, a different procedure is chosen based on the work by *Brinkgreve* [36] and *Schanz* [123]. In this approach, it is assumed that the change of the elastic strain $\boldsymbol{\varepsilon}_e$ from one time step to the other one is negligible within the plastic deformation process, thus leading to the assumption $\boldsymbol{\varepsilon}_e^{h,n,j} \approx \boldsymbol{\varepsilon}_e^{h,n-1}$. Applying this simplification to the evaluation of (4.29), a fundamental difference for the numerical realization is achieved:

$$
\begin{aligned}
\bar{\bar{\varepsilon}}_{pv}^{h,n,j}(\mathbf{x}) &= \langle 1 - \alpha \rangle \, \varepsilon_{pv}^{h,n,j}(\mathbf{x}) + \frac{\alpha}{V_r(\mathbf{x})} \int\limits_{\Omega} w(\mathbf{x} - \mathbf{y}) \, \varepsilon_{pv}^{h,n,j}(\mathbf{y}) \, \mathrm{d}v \,, \\[2mm]
&\approx \langle 1 - \alpha \rangle \, \varepsilon_{pv}^{h,n,j}(\mathbf{x}) + \frac{\alpha}{V_r(\mathbf{x})} \int\limits_{\Omega} w(\mathbf{x} - \mathbf{y}) \, \tilde{\varepsilon}_{pv}^{h,n,j}(\mathbf{y}) \, \mathrm{d}v \,, \qquad (4.30) \\[2mm]
\tilde{\varepsilon}_{pv}^{h,n,j} &= \sqrt{ \underbrace{\left(\boldsymbol{\varepsilon}^{h,n,j} - \boldsymbol{\varepsilon}_e^{h,n-1} \right)}_{\approx \, \boldsymbol{\varepsilon}_p^{h,n,j}} \cdot \underbrace{\left(\boldsymbol{\varepsilon}^{h,n,j} - \boldsymbol{\varepsilon}_e^{h,n-1} \right)}_{\approx \, \boldsymbol{\varepsilon}_p^{h,n,j}} } \,.
\end{aligned}
$$

Using the above relation, the standard element-wise (or, more exactly, integration-point-wise) evaluation procedure for the flow rule and the yield criterion can be maintained. The current total strain $\boldsymbol{\varepsilon}^{h,n,j}$ depends only on the current solution vector $\boldsymbol{u}_n^j$ and the elastic strain $\boldsymbol{\varepsilon}_e^{h,n-1}$ from the last time step t_{n-1} is even constant within each *Newton* iterate j.

For an efficient evaluation of (4.29) or (4.30), it is also very important that the effort for the calculation of the integral term is adapted depending on the internal length scale. Carrying out an integration over the whole domain Ω, i. e., executing a loop over all finite elements, with a relatively small value for l mostly leads to the summation of "zero values", as the sphere of influence of the weighting function in such a case is only in the closest neighborhood of the regarded integration point. In order to prevent such an

inefficient strategy, at the beginning of the calculation, the set of elements, which have an influence on the non-local quantity, can be determined by calculating the distance between the respective points and comparing this distance with some reference value, which depends on the internal length scale.

In accordance to the remark on Page 72, it finally has to be mentioned that the numerical calculations with the non-local regularization approach as well as the simulations with the micropolar strategy show a significantly better convergence behavior, when the viscoplastic approach is additionally applied. Therefore, these combinations are going to be used for the 2-dimensional simulations in Section 4.6.2.

4.6 Numerical examples and discussion

In this section, the regularization methods presented above are going to be applied to a tensile bar, and their effect on the respective numerical solutions will be discussed. Starting with a purely 1-dimensional formulation, in which, as already mentioned, the *Cosserat* theory cannot be applied, a discussion of a 2-dimensional tensile bar follows, wherein all the three regularization methods are used.

Note that within this section, no effort was made to describe the softening behavior of a realistic material. Here, the main focus is put on the discussion, to which extent the single regularization techniques are suitable to obtain a well-posed behavior.

4.6.1 1-d tensile bar

For the 1-dimensional simulation, the example from Section 4.1 is picked up again and the set of governing equations (4.1) is changed with respect to the viscoplastic or the non-local regularization method, respectively. Following the viscoplastic approach, the *Kuhn-Tucker* conditions $(4.1)_8$ are replaced by

$$\Lambda = \frac{1}{\eta} \left\langle \frac{F(\sigma)}{\kappa_0} \right\rangle^r , \qquad (4.31)$$

and for the non-local method, the softening law $(4.1)_6$ containing the local value for the plastic strains is replaced by its non-local representation:

$$\overset{\star}{\kappa}(x) = \kappa_0 - h\, \bar{\bar{\varepsilon}}_p(x), \qquad \bar{\bar{\varepsilon}}_p(x) = \langle 1 - \alpha \rangle\, \varepsilon_p(x) + \frac{\alpha}{V_r(x)} \int\limits_{\Omega} w(x - y)\, \varepsilon_p(y)\, \mathrm{d}v. \qquad (4.32)$$

Note that, within this 1-d example, the representative volume $V_r(x)$ denotes a representative length and the volume integral $\int_{\Omega}(\cdot)\,\mathrm{d}v$ reduces to a line integral. Furthermore, the same material parameters as already used in Section 4.1 are applied here for the simulations with the two regularization methods. In order to obtain a softening material behavior, the parameter of the linear softening law is set to $h = 1\,000\,\mathrm{kN/m^2}$. The *Dirichlet* boundary condition $\bar{u}(t)$ at the right end of the bar is linearly increased with the displacement velocity $0.15\,\mathrm{mm/s}$ up to the final displacement of $0.9\,\mathrm{mm}$ at $t = 6\,\mathrm{s}$.
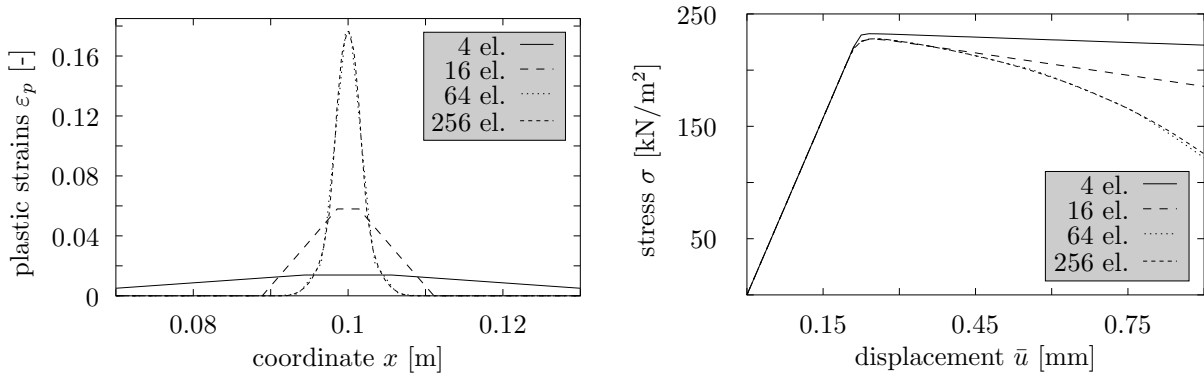
Figure 4.9: Viscoplastic approach: distribution of the plastic strains ε_p [-] in the bar (left) and development of the stress σ [kN/m^2] at $x = L$ (right) for $\eta = 5$ s.

Applying the viscoplastic approach, the viscosity η is set to 5 s (unless other values are explicitly specified) and the viscoplastic exponent r is set to 1. Looking at the results illustrated in Figure 4.9, an obvious mesh-independent behavior can be recognized. The width of the shear zone and the maximum plastic strain converge for discretizations with increasing number of finite elements to fixed values (Figure 4.9, left). The well-posed behavior can also be identified in the stress-displacement diagram, in which no fundamental difference can be detected for results obtained by FE meshes with 64 or more elements (Figure 4.9, right). Note that although a linear softening law is applied, the stress-displacement development results due to the viscoplastic regularization in a nonlinear behavior.

The influence of the viscosity η on the solution of the numerical simulation is illustrated in Figure 4.10, where three different values of η are chosen for the calculations on a constant FE mesh with 256 elements. Therein, due to the overstresses coming along with the viscoplastic regularization, a dependence of the shear zone on the viscosity is obtained, cf. Figure 4.10 (left). For increasing values of η, the width of the shear zone increases and, simultaneously, the maximum value of the plastic strain decreases, until for a rather large
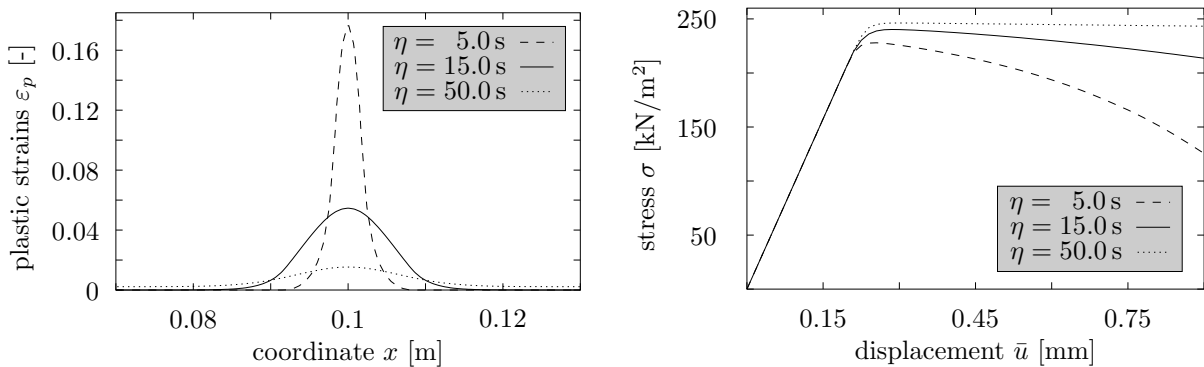
Figure 4.10: Viscoplastic approach: influence of the viscosity η on the shear zone (left) and the stress development (right).

PSfrag replacements
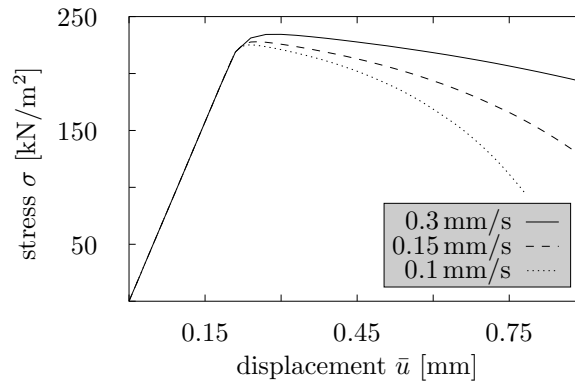
Figure 4.11: Viscoplastic approach: influence of the displacement velocity on the development of the stress σ [kN/m^2].

value of $\eta = 50.0$ s, the plastic strains are distributed over the whole length of the bar. Looking at the stress-displacement progression in Figure 4.10 (right), the effect of η on the solution becomes even more obvious, as the softening behavior is completely different for the varying values of the viscosity. For $\eta = 50.0$ s, almost no decrease of stress with respect to the displacement of the right boundary of the bar can be recognized.

Finally, the rate-dependent material behavior of the viscoplastic approach is illustrated in Figure 4.11, where the stress-displacement development is shown for three different displacement velocities specified within the boundary condition $\bar{u}(t)$. Therein, a typical behavior of a viscous material can be identified. The material shows a stiffer behavior for increasing values of the displacement velocity, whereas for rather slow processes, the viscous part of the model opposes only a small force against the specified displacement.

Discussing the regularizing effect of the non-local approach, the internal length scale l is set to 0.2 mm and the additional parameter α is set to 2, which is a proper choice for α referring to the numerical investigations on 1-d problems by *Brinkgreve* [36]. Analogously PSfrag replacements to the simulations with the viscoplastic regularization method, calculations were carried

PSfrag replacements
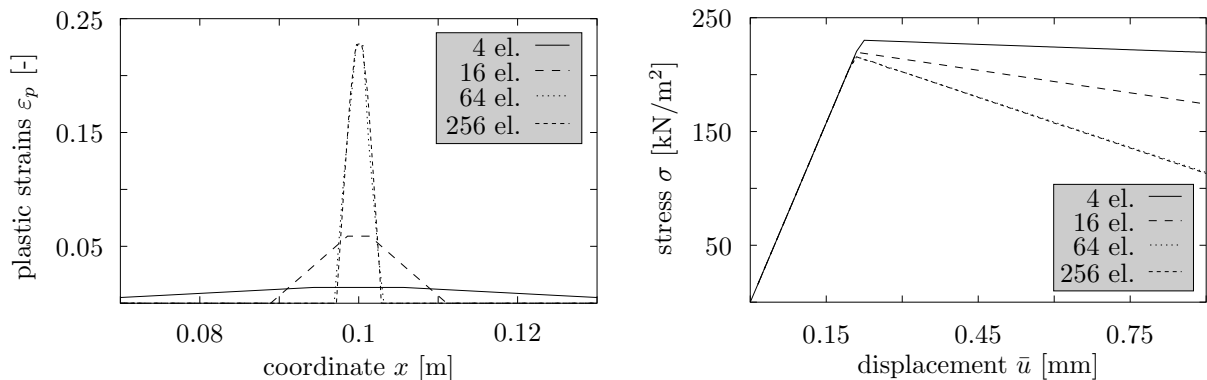
Figure 4.12: Non-local approach: distribution of the plastic strains ε_p [-] in the bar (left) and development of the stress σ [kN/m^2] at $x = L$ (right) for $l = 0.002$ m.

out on different meshes consisting of 4 up to 256 finite elements. Again, a well-posed behavior can be recognized in Figure 4.12, where in the left picture, the distribution of the plastic strains over the length of the bar is shown and, in the right picture, the stress-displacement development is illustrated. Starting the calculations with a spatial resolution of 64 elements, each mesh refinement leads to almost equal results concerning the width of the shear zone, the maximum value of the plastic strains and the progression of the stress-displacement diagram.

Changing the values of the internal length scale, the influence of the non-local approach on the solution can be recognized, cf. Figure 4.13. From a numerical point of view, the simulations get less "critical", if the internal length scale is increased. By doing this, an increase of the shear zone width, a decrease of the maximum plastic strain and a lower softening behavior are obtained.

Finally, it can be concluded that both the viscoplastic and the non-local approaches show an excellent regularizing effect within this example. However, as already denoted in Section 4.5.2, the simulations with the non-local approach are realized numerically very inefficiently in this 1-d problem, which leads to enormous computing times for such a simple example. Comparing the computing times of both regularization methods, the calculations carried out on the finest FE mesh with 256 elements took around 1 minute for the viscoplastic approach and around 1 week for the non-local approach. This fact clearly motivates the more efficient realization of the non-local strategy for the simulations of 2-d or even 3-d problems as shown in (4.30).

Furthermore, it can be seen from, e. g., Figures 4.10 (left) and 4.13 (left) that the application of different regularization methods gives different results concerning the characteristics of the solution. In the viscoplastic case, a smooth transition from the elastic to the plastic zones can be detected, whereas by the non-local approach, an abrupt change from elastic to plastic material behavior is obtained.
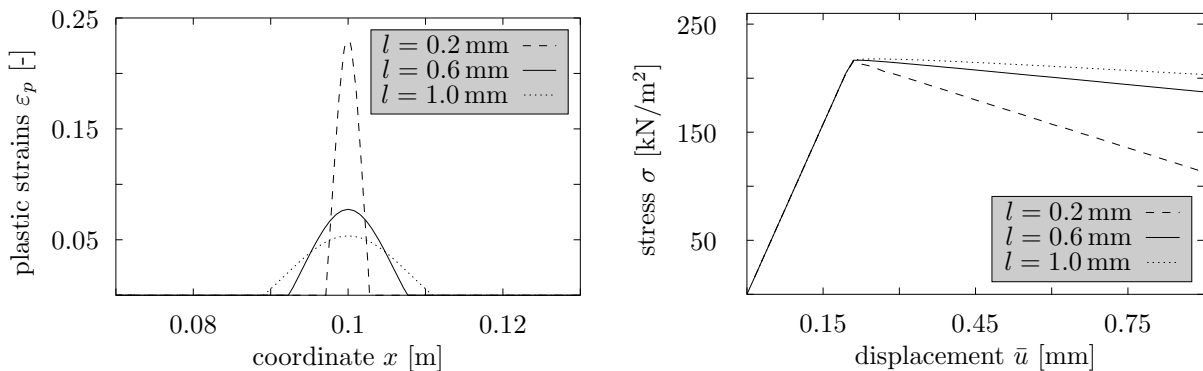

Figure 4.13: Non-local approach: influence of the internal length scale l on the shear zone (left) and the stress development (right).

4.6.2   2-d tensile bar

Expanding the set of governing equations (4.1) from the one-dimensional case to two dimensions, the following equations can be identified:

$$
\begin{aligned}
\boldsymbol{\varepsilon} &= \tfrac{1}{2}\left[\,\mathrm{grad}\,\mathbf{u} + (\mathrm{grad}\,\mathbf{u})^T\,\right] && (\textit{kinematic compatibility})\,,\\[4pt]
\mathrm{div}\,\boldsymbol{\sigma} &= \mathbf{0} && (\textit{momentum balance})\,,\\[4pt]
\boldsymbol{\sigma} &= 2\,\mu\,\boldsymbol{\varepsilon}_e + \lambda\,(\,\boldsymbol{\varepsilon}_e\cdot\mathbf{I}\,)\,\mathbf{I} && (\textit{Hookean elasticity law})\,,\\[4pt]
\boldsymbol{\varepsilon} &= \boldsymbol{\varepsilon}_e + \boldsymbol{\varepsilon}_p && (\textit{strain decomposition})\,,\\[4pt]
F &= \sqrt{\mathbb{II}^D} - \overset{\star}{\kappa} && (\textit{von Mises-type yield criterion})\,, \quad (4.33)\\[4pt]
\overset{\star}{\kappa} &= \kappa_0\left\{1 - h_{sat}\left[1 - \exp\left(-h_e\,\varepsilon_{pv}\right)\right]\right\} && (\textit{softening law})\,,\\[4pt]
(\boldsymbol{\varepsilon}_p)' &= \Lambda\,\frac{\partial F}{\partial\boldsymbol{\sigma}} && (\textit{plastic flow rule})\,,\\[4pt]
\Lambda &= \frac{1}{\eta}\left\langle\frac{F(\boldsymbol{\sigma})}{\kappa_0}\right\rangle^r && (\textit{viscoplasticity})\,.
\end{aligned}
$$

Therein, the softening law $\overset{\star}{\kappa}$ is assumed to be given by an exponential-type function, which progression can be controlled by the two material parameters h_{sat} and h_e. Note again that the concept of associated plasticity is applied in this example, cf. $(4.33)_7$.

As already mentioned in the remark on Page 72, the viscoplastic approach will be used within all simulations of the 2-d tensile bar. This fact leads to combinations of the
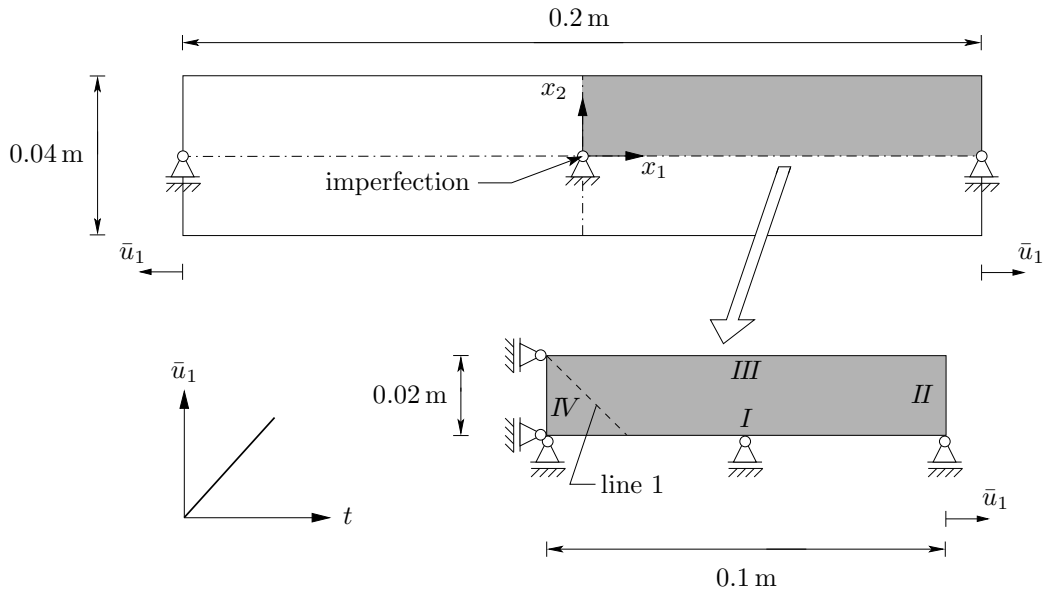
Figure 4.14: Two-dimensional boundary-value problem (top) and reduced system due to symmetry (bottom).

Lamé constants	$\mu = 81\,000 \,\mathrm{kN/m}^2$, $\lambda = 118\,000 \,\mathrm{kN/m}^2$
initial equivalent stress	$\kappa_0 = 400 \,\mathrm{kN/m}^2$
softening behavior	$h_{sat} = 0.99$, $h_e = 40$
viscoplastic exponent	$r = 1$

Table 4.1: 2-d tensile bar: material parameters.

viscoplastic approach with both the non-local as well as the micropolar regularization techniques. Following this, the equations given in (4.33), which already contain the viscoplastic regularization, describe the basic equations for the simulations in this section. Within the simulations, where the non-local approach is studied, the accumulated plastic strain ε_{pv} in the softening law $(4.33)_6$ is replaced by its non-local representation $\bar{\bar{\varepsilon}}_{pv}$ given by Equation (4.30). Combining the viscoplastic and the micropolar approach, the strains $\boldsymbol{\varepsilon}$ and the stresses $\boldsymbol{\sigma}$ have to be replaced with respect to their micropolar representations, which are given in Equations $(4.13)_1$ and $(4.19)_1$. Furthermore, the additional moment of momentum balance relation (4.18) together with the definition $(4.19)_2$ of the couple stresses $\mathbf{M}$ have to be considered within the *Cosserat* theory. In contrast to $(4.19)_2$, where a split of the curvature $\bar{\boldsymbol{\kappa}}$ into elastic and plastic parts is included, this split of $\bar{\boldsymbol{\kappa}}$ is, for the sake of simplicity, not assumed in the simulations within this section, i. e., the curvature remains in the elastic range and can be directly computed from $(4.13)_2$ or the compatibility condition (4.15). Finally, the additional material parameters k_σ and k_M of the micropolar yield criterion (4.21) are both set to zero in order to obtain comparable results with respect to the other two regularization techniques.

The material parameters, which are included in the above mentioned set of equations and which are constant for all the different simulations presented in this section, are given in Table 4.1. The characterizing material parameters of the respective regularization
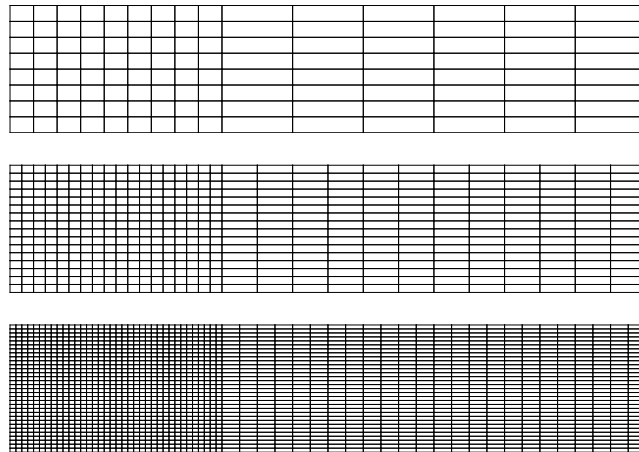

Figure 4.15: FE meshes: level 0 with 120 (top), level 1 with 480 (middle) and level 2 with 1 920 (bottom) elements.
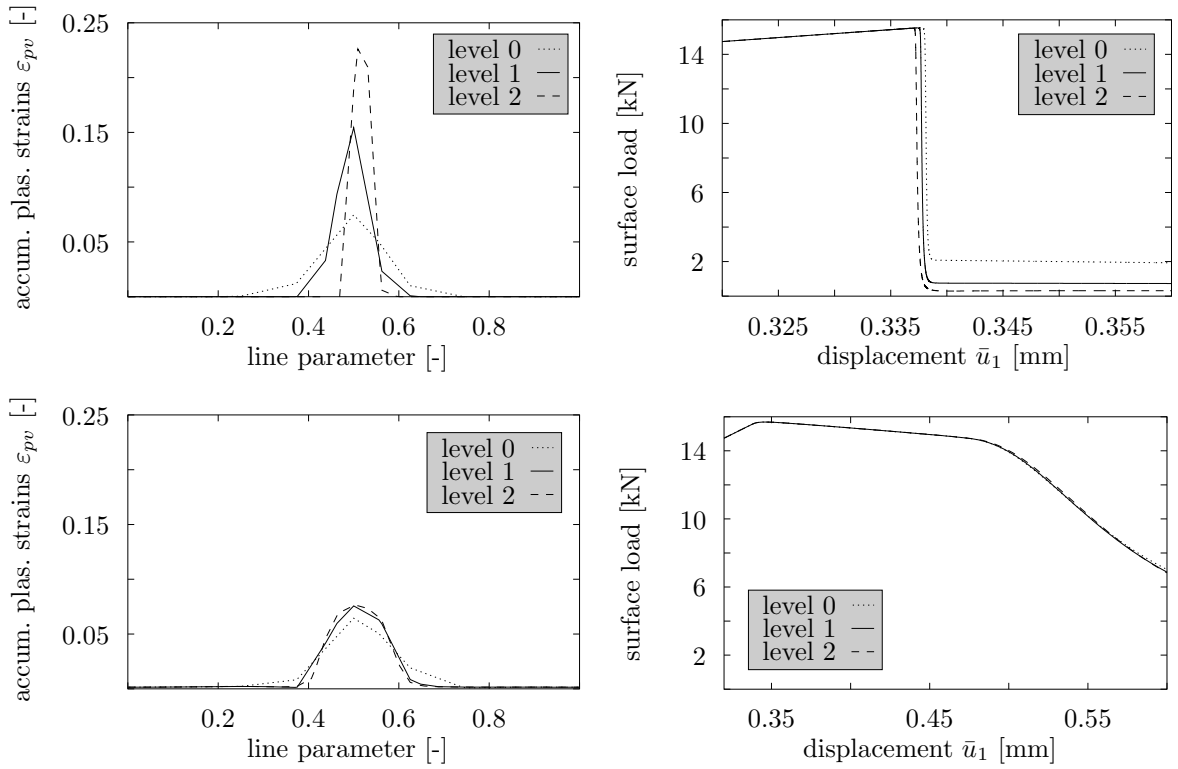
Figure 4.16: Viscoplastic approach: distribution of the accumulated plastic strains ε_{pv} [-] along line 1, cf. Figure 4.14, (left) and development of the surface load [kN] at $x_1 = 0.1\,\mathrm{m}$ (right) for $\eta = 0.0\,005\,\mathrm{s}$ (upper series) and for $\eta = 0.5\,\mathrm{s}$ (lower series).

techniques, namely the viscosity η, the internal length l and the scaling parameter α, as well as the additional micropolar material parameters l_c and μ_c, are specified for each simulation.

The initial boundary-value problem, which is going to be discussed in this section, is illustrated in Figure 4.14. In the upper part of this figure, the entire bar (length $0.2\,\mathrm{m}$, width $0.04\,\mathrm{m}$) and the boundary conditions of the underlying problem are shown. At the left and the right end of the bar, a linearly increasing *Dirichlet* boundary condition $\bar{u}_1$ is applied with $\bar{u}_1' = 1\,\mathrm{mm/s}$ until the limit of the elastic regime is reached and the softening material behavior can be observed. In order to initiate a shear band in this homogeneous problem, the *Lamé* constants are weakened at the position $x_1 = 0\,\mathrm{m}$, $x_2 = 0\,\mathrm{m}$. Due to symmetry reasons, only a quarter of the bar has to be discretized, cf. Figure 4.14 (bottom). The respective symmetry boundary conditions are applied at the edges *I* and *IV*, where the displacements in the x_2- or the x_1-directions are set to zero. In the simulations with the micropolar approach, the rotations are also set to zero at these edges.

For a proper discussion of the regularizing properties of the single approaches, the described boundary-value problem was calculated on three different FE meshes, where the coarsest mesh, cf. Figure 4.15 (top), contains 120 quadrilateral elements. Starting from this mesh (refinement level 0), two uniform refinements result into the finest spatial discretization (refinement level 2) with altogether 1 920 elements. On all three FE meshes,
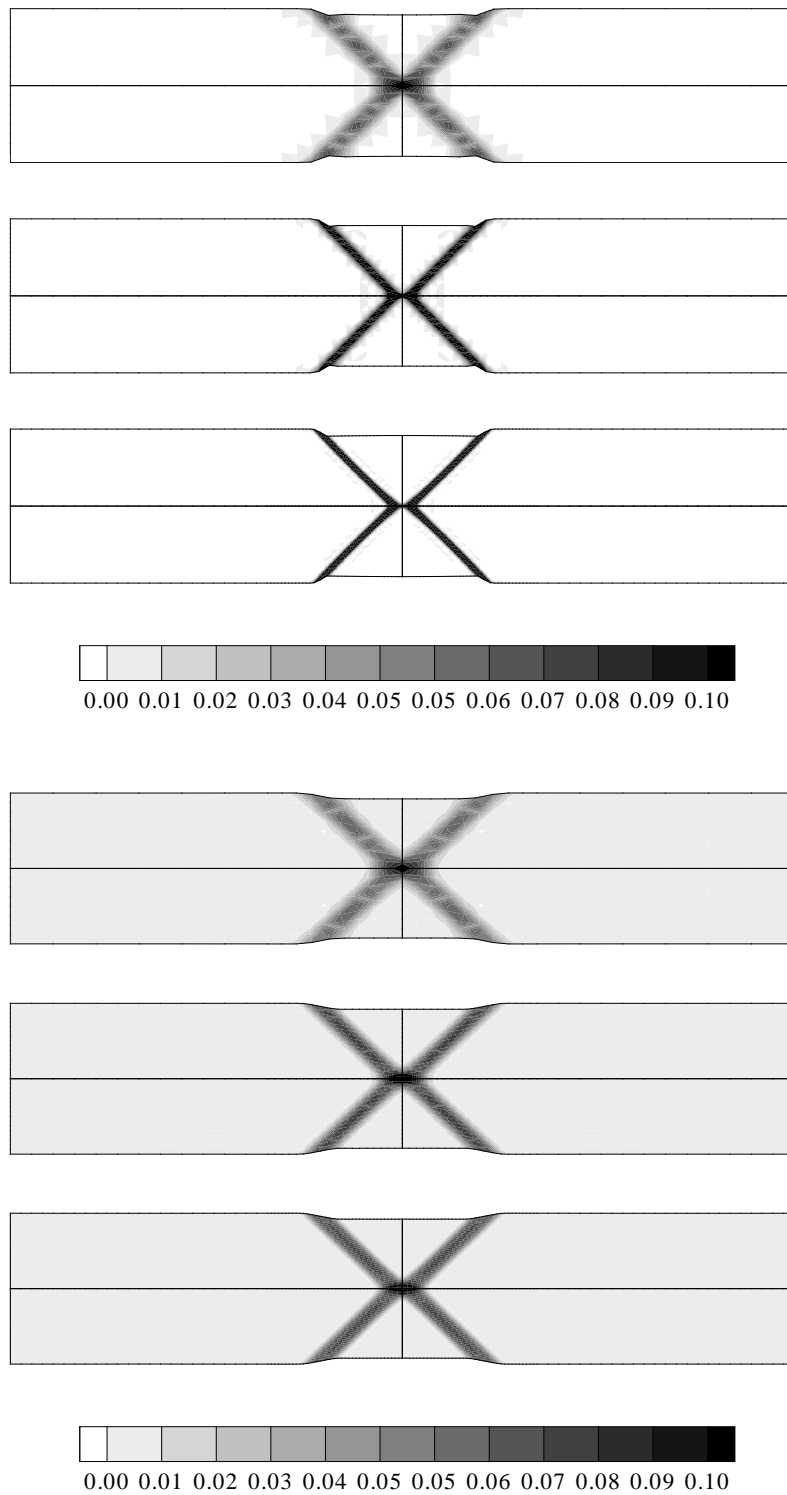
Figure 4.17: Viscoplastic approach: accumulated plastic strains ε_{pv} [-] for $\eta = 0.0\,005\,\text{s}$ (upper series) and $\eta = 0.5\,\text{s}$ (lower series). In each series: coarse mesh (top), medium mesh (middle) and fine mesh (bottom), deformation scaled five times.
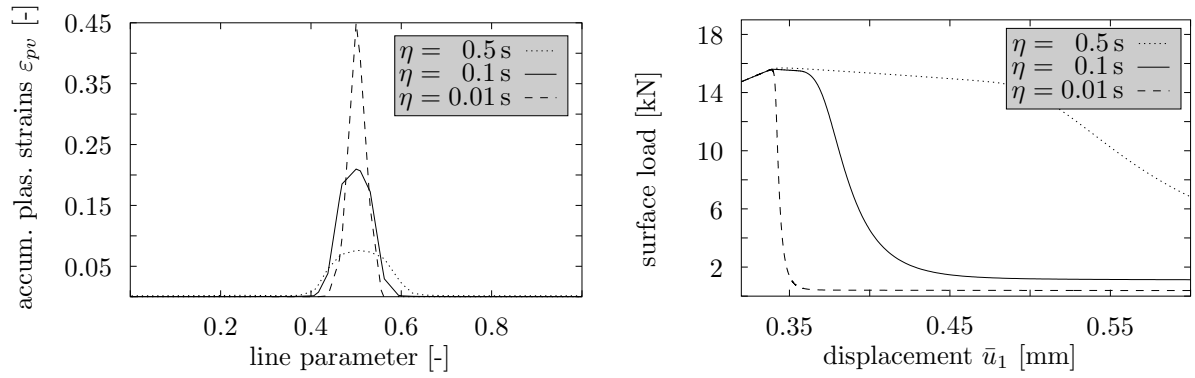
Figure 4.18: Viscoplastic approach: influence of the viscosity η on the shear band width (left) and on the surface load [kN] at $x_1 = 0.1\,\mathrm{m}$ (right).

the displacement **u** is discretized by quadratic ansatz functions, whereas, in the case with the micropolar approach, linear ansatz functions are chosen for the rotation $\bar{\varphi}$. Furthermore, an integration order 3 is chosen for the numerical quadrature, which results in 4 integration points per element.

The first regularization technique to be discussed here, is the viscoplastic approach. In Figure 4.16, the shear band widths (left) and the load-displacement curves (right) for the three different meshes are shown. In the upper series, a rather small viscosity $\eta = 0.0\,005\,\mathrm{s}$
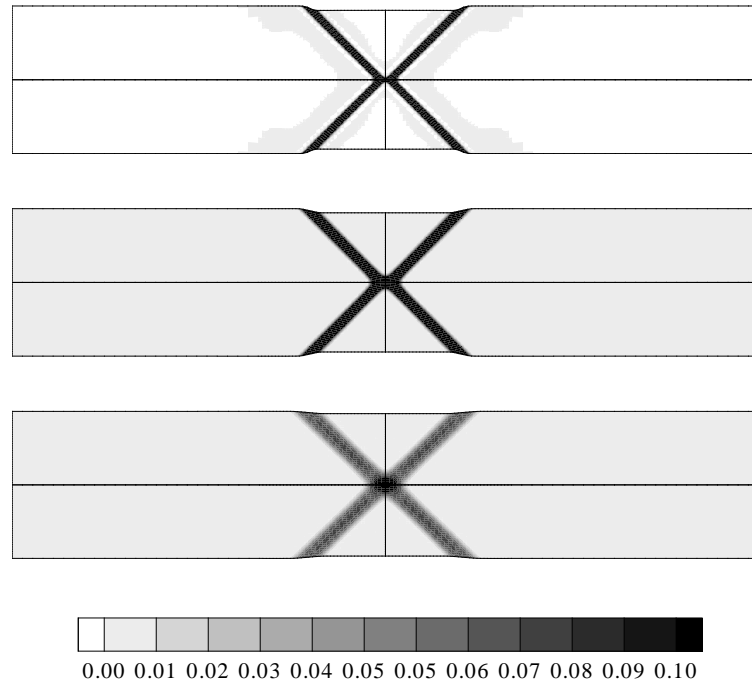
Figure 4.19: Viscoplastic approach: influence of the viscosity η on the shear band width; $\eta = 0.01\,\mathrm{s}$ (top), $\eta = 0.1\,\mathrm{s}$ (middle) and $\eta = 0.5\,\mathrm{s}$ (bottom), deformation scaled two times.

is chosen, whereas, in the lower series, the results coming from the simulations with a viscosity $\eta = 0.5\,\text{s}$ are shown. In these results, an obvious difference with respect to mesh-independent behavior can be observed. The calculations with the smaller value of η lead to mesh-dependent results, as the shear band widths decrease and the maximum values of the accumulated plastic strains increase for finer spatial discretizations. Furthermore, the single load-displacement curves show also mesh-dependent results. Following this, an ill-posed behavior is obtained and, therefore, this value of η will be taken for the combinations of the viscoplastic approach with the non-local and the micropolar regularization techniques in the further simulations in this section.

In contrast to this mesh-dependent behavior, the results coming from the simulations with a viscosity, which is larger by the factor 1000, show a much better characteristics. Both the shear band widths, the maximum values of the accumulated plastic strains and the progressions of the load-displacement curves give comparable results independent of the spatial discretization. The same characteristics can be observed in Figure 4.17, in which the accumulated plastic strains are plotted for the different values of η and the different spatial discretizations.

In order to obtain a mesh-independent behavior with the viscoplastic approach for the three FE meshes shown in Figure 4.15, a rather large value for the viscosity has to be chosen. Therefore, the viscoplastic regularization technique has a big influence on the physical behavior of the modeled bar, cf., e. g., Figure 4.16 (lower series, right), where a softening material behavior is obtained only for very large values of $\bar{u}_1$. Furthermore, the overstresses coming along with the viscoplastic approach can be observed in Figure 4.17. Therein, the large value of η leads to plastic deformations in the whole bar (lower series), whereas for the small value of η, plastic strains are only detected in shear bands (upper series).

For a clarification of the influence of the viscosity on the shear band width, the maximum value of the plastic strains and the characteristics of the load-displacement curve, three further simulations were carried out on the fine FE mesh (1 920 elements) with different values of the viscosity, namely $\eta = 0.01\,\text{s},\ 0.1\,\text{s},\ 0.5\,\text{s}$. Figures 4.18 and 4.19 show the results of these simulations and confirm this influence significantly.

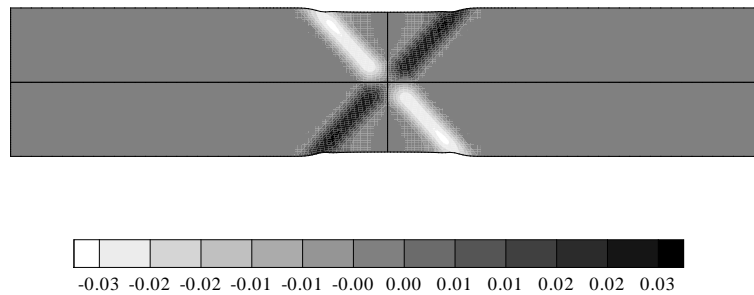In a next step, the properties of the micropolar approach as a regularization technique are

Figure 4.20: Micropolar approach: total rotations $\bar{\varphi}$ for $l_c = 0.5\,\text{mm}$ and $\mu_c = 10^5\,\text{kN/m}^2$, deformation scaled five times.
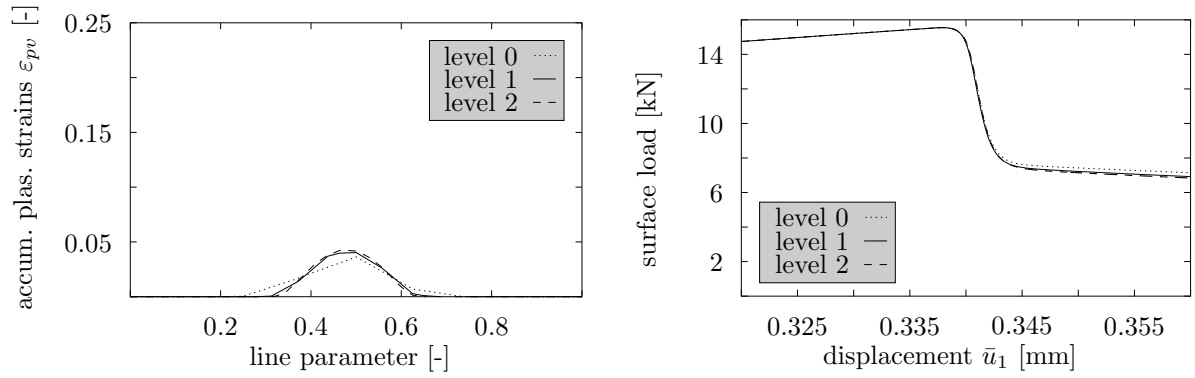
Figure 4.21: Micropolar approach: distribution of the accumulated plastic strains ε_{pv} [-] along line 1, cf. Figure 4.14, (left) and development of the surface load [kN] at $x_1 = 0.1\,\mathrm{m}$ (right) for $l_c = 0.5\,\mathrm{mm}$ and $\mu_c = 10^5\,\mathrm{kN/m^2}$.

going to be discussed. Due to the constitutive assumptions presented in Section 4.4, the influence of the two additional material parameters l_c and μ_c incorporated in this theory have to be taken into account for this discussion. Carrying out a parameter study on the influence of these two material parameters on the regularizing effect of the *Cosserat* theory, it was observed that the order of magnitude of the value of μ_c must be large enough to obtain such an effect. In the simulations of the tensile bar, mesh-dependent behavior was
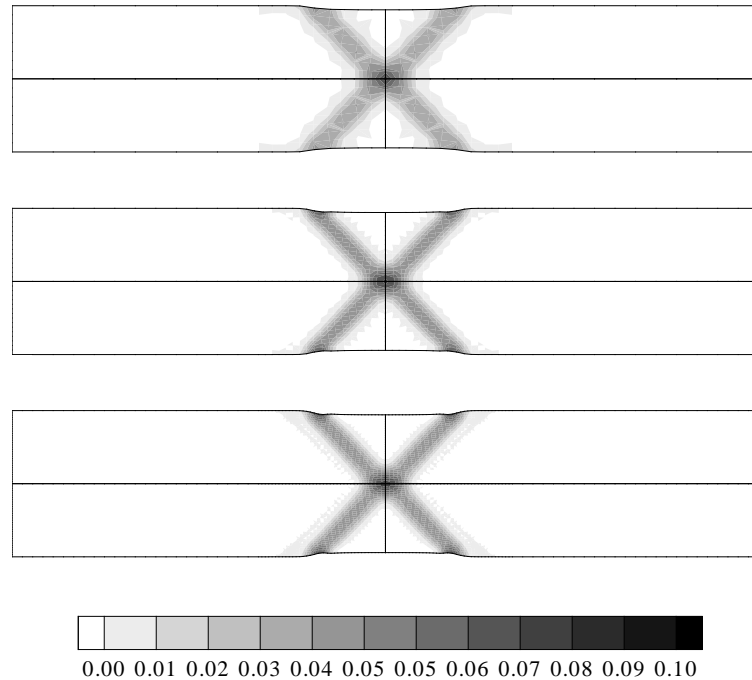
Figure 4.22: Micropolar approach: accumulated plastic strains ε_{pv} [-] for $l_c = 0.5\,\mathrm{mm}$ and $\mu_c = 10^5\,\mathrm{kN/m^2}$. Coarse mesh (top), medium mesh (middle) and fine mesh (bottom), deformation scaled five times.
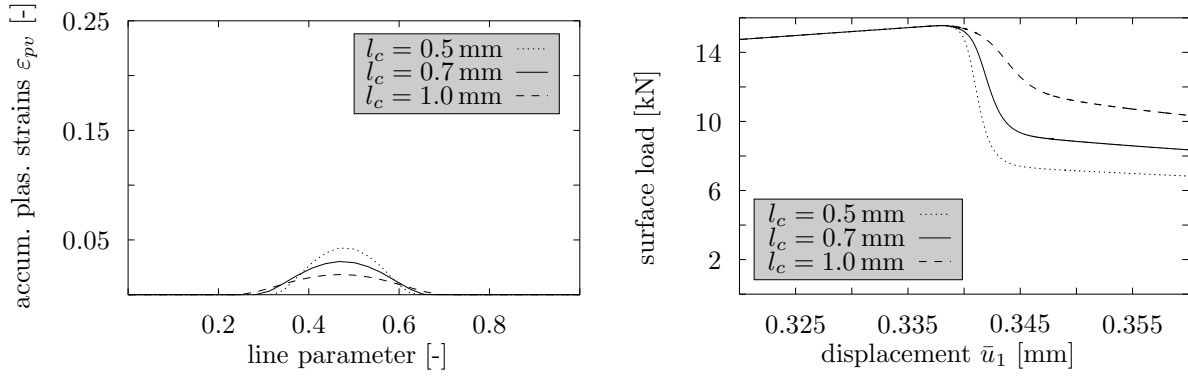
Figure 4.23: Micropolar approach: influence of the internal length l_c on the shear band width (left) and on the surface load [kN] at $x_1 = 0.1$ m (right).

found for values of μ_c smaller than the order of magnitude of approximately 10^4 kN/m². For such values, even significant modifications of l_c do not lead to mesh-independent results.

Assuming $l_c = 0.5$ mm and $\mu_c = 10^5$ kN/m² for the simulation of the described boundary-value problem, the results illustrated in Figures 4.21 and 4.22 were obtained. Therein, the regularizing effect of the *Cosserat* theory is clearly demonstrated by the constant shear band widths, the comparable maximum values for the plastic strains and the analogous
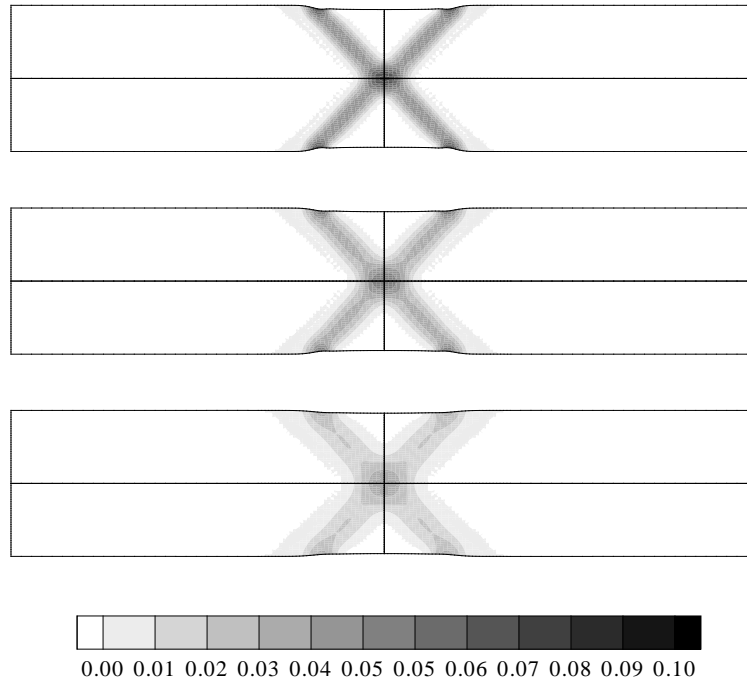

Figure 4.24: Micropolar approach: influence of the internal length l_c on the shear band width; $l_c = 0.5$ mm (top), $l_c = 0.7$ mm (middle) and $l_c = 1.0$ mm (bottom), deformation scaled five times.
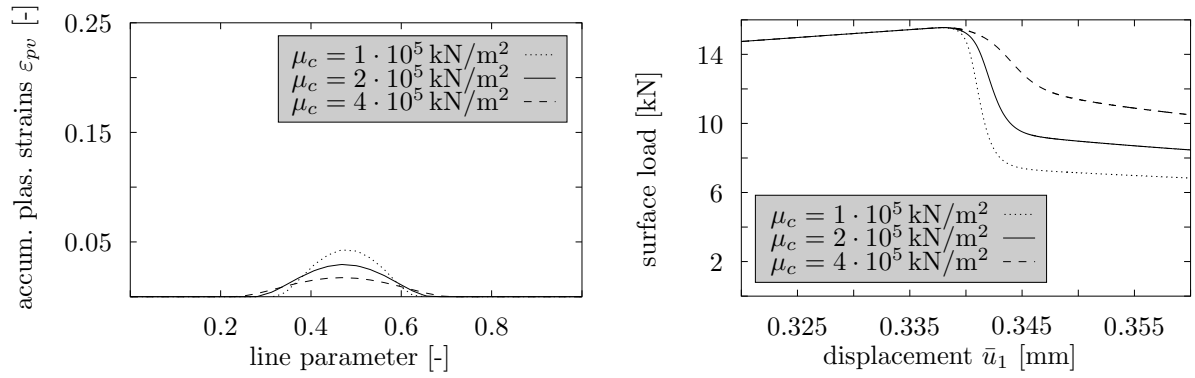
Figure 4.25: Micropolar approach: influence of the parameter μ_c on the shear band width (left) and on the surface load [kN] at $x_1 = 0.1\,\mathrm{m}$ (right).

progressions of the load-displacement curves. Furthermore, the typical distribution of the total rotation can be observed in Figure 4.20. Following this, the rotations are approximately zero outside the shear bands. Inside the shear bands, the rotation is either positive or negative. As a result, the rotation is zero at the crossing point of positively and negatively rotating shear bands. In the present example, such a point is given at the imperfection, which causes the shear band initiation, cf. Figure 4.14.

Following these results, it can be deduced that the influence of the skew-symmetric part
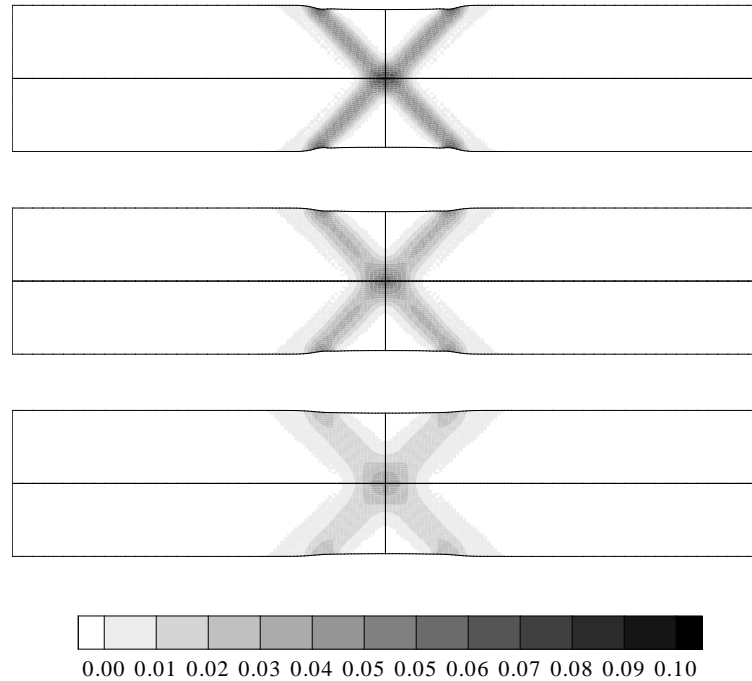

Figure 4.26: Micropolar approach: influence of the parameter μ_c on the shear band width; $\mu_c = 10^5\,\mathrm{kN/m^2}$ (top), $\mu_c = 2{\cdot}10^5\,\mathrm{kN/m^2}$ (middle) and $\mu_c = 4{\cdot}10^5\,\mathrm{kN/m^2}$ (bottom), deformation scaled five times.
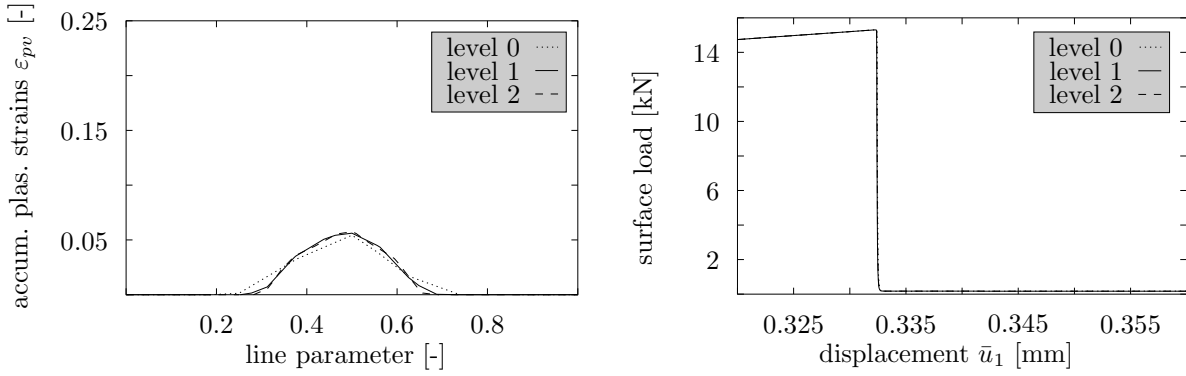
Figure 4.27: Non-local approach: distribution of the accumulated plastic strains ε_{pv} [-] along line 1, cf. Figure 4.14, (left) and development of the surface load [kN] at $x_1 = 0.1$ m (right) for $l = 2.0$ mm.

of the micropolar strain $\bar{\varepsilon}_{e\,\text{skw}}$ on the calculation of the stress tensor by Equation $(4.19)_1$ has to be large enough in order to obtain a substantial regularizing influence of the micropolar theory in this example under study. Furthermore, it was recognized in the numerical studies on the tensile bar that with both micropolar parameters l_c and μ_c the shear band width can be modified. In order to prove this statement, both parameters were modified in FE calculations on the fine mesh with 1 920 elements. In Figures 4.23
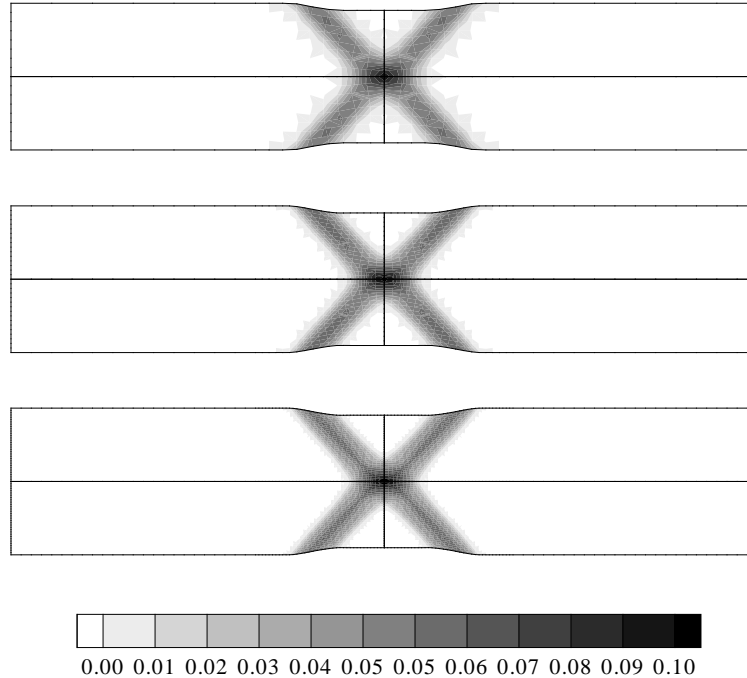

Figure 4.28: Non-local approach: accumulated plastic strains ε_{pv} [-] for $l = 2.0$ mm. Coarse mesh (top), medium mesh (middle) and fine mesh (bottom), deformation scaled five times.
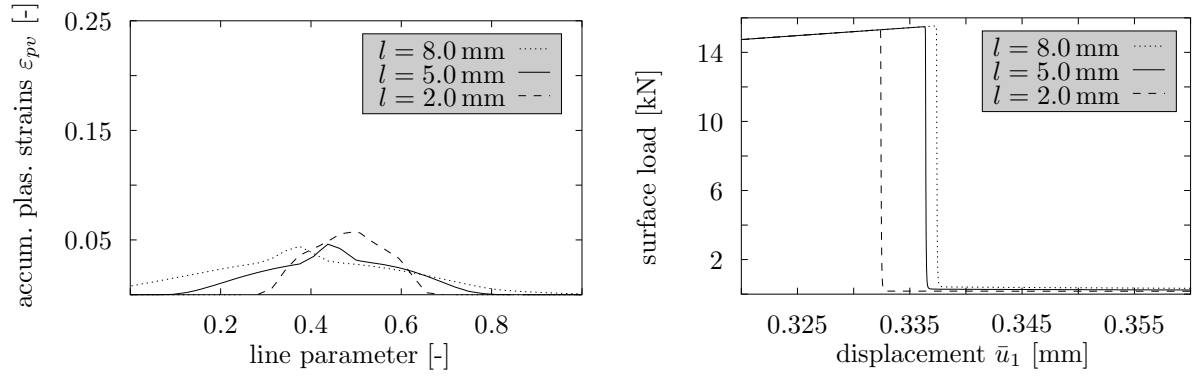
Figure 4.29: Non-local approach: influence of the internal length l on the shear band width (left) and on the surface load [kN] at $x_1 = 0.1\,\mathrm{m}$ (right).

and 4.24, the results for three different values for l_c are shown, and in Figures 4.25 and 4.26, qualitatively similar results are obtained by modifications of the material parameter μ_c.

Finally, the non-local regularization technique is going to be discussed. Like the previous two methods, the non-local approach is also capable of realizing mesh-independent solutions for the chosen tensile bar. In Figures 4.27 and 4.28, the results of the simulations with an internal length of $l = 2.0\,\mathrm{mm}$ on the three different FE meshes are shown. In con-
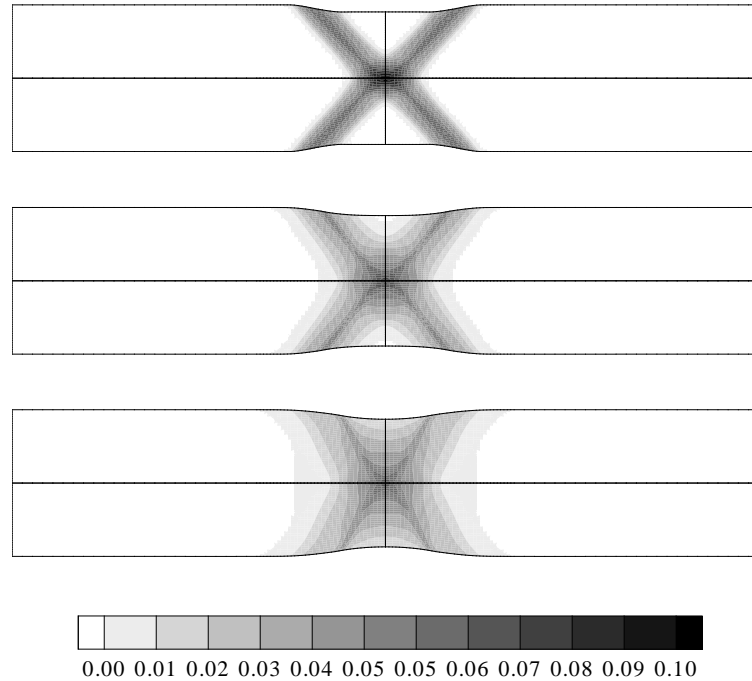

Figure 4.30: Non-local approach: influence of the internal length l on the shear band width; $l = 2.0\,\mathrm{mm}$ (top), $l = 5.0\,\mathrm{mm}$ (middle) and $l = 8.0\,\mathrm{mm}$ (bottom), deformation scaled five times.

trast to the 1-d example presented in the last section, these mesh-independent results can only be realized by increasing the influence of the non-local part of (4.30), i. e., the value of α, which rules this influence, was chosen to 4. For smaller values of α and independent of the chosen values of the internal length l, mesh-dependent results were obtained in this numerical example.

Furthermore, the non-local approach is the only regularization technique presented in this section to give a well-posed behavior and to model the strong softening material behavior, which is governed by the choice of the values for the material parameters h_{sat} and h_e. By setting $h_{sat} = 0.99$, only 1% of the initial stiffness should be obtained at the end of the softening process. Whereas the other two regularization methods can model well-posed behavior only by a significant delay to obtain this final stiffness, cf. Figures 4.16 (bottom, right) and 4.21 (right), the non-local approach can combine well-posedness and the rapid decrease of stiffness, cf. Figure 4.27 (right).

By changing the values of the internal length l, an influence on the width of the shear band, the maximum value of the plastic strains and the characteristics of the results can be obtained, cf. Figures 4.29 and 4.30, in which the results for the simulations on the fine FE mesh with different values of l are illustrated.

Chapter 5:
Parallelization of finite element simulations

Due to the enormous speed of development in computer technologies in the last decades, the possibility to use parallel computers has improved strongly. Nowadays, it is affordable for many companies or research institutes to buy and use parallel computers, because most of these machines are based on hardware coming from standard personal computers (PCs). The physical limitations of the problem size an engineer or scientist is able to compute numerically are therefore no longer given by the system memory or processing speed of a single computer, but by the amount of processors, which are available within a parallel computer system. For example, a FE simulation of a frontal crash of a car against a wall can be computed with such a realistic accuracy that the number of expensive crash experiments was reduced dramatically in recent years by the automotive industry.

In order to be able to run parallel computations, obviously, not only the hardware but also the software, the FE code, has to provide parallel structures. Therefore, in this chapter, the parallelization of finite element simulations is discussed in detail. Starting with general remarks on some aspects of parallel computing, in the second section of this chapter, special emphasis is put on the parallel simulation of multiphasic problems. Thereby, the interface of the sequentially implemented FE code PANDAS (Porous media Adaptive Nonlinear finite element solver based on Differential Algebraic Systems) [58, 117] and the parallel solver M++ (Meshes, Multigrid and more) [147] is presented, which is the basis for the large scale FE simulations following in the Sections 6.2 and 6.3.

5.1 General remarks on parallel computing

In this section, a general basis on parallel computing is established, which is necessary for a better understanding of the further discussions in this thesis. Very briefly, the most important notions and concepts are introduced based upon the works by *Bastian* [6] and *Hinkelmann* [90, 91]. The reader who is interested in a more detailed description of the main concepts in this field is referred to the standard literature on this topic like, e. g., *Kumar et al.* [98], *van de Felde* [72] or the above mentioned works by *Bastian* and *Hinkelmann*.

5.1.1 Computer architectures

A common way to classify different computer architectures dates back to the work by *Flynn* [74] in 1972. This classification is based on the notion of a stream of information. Two different types of information flow into a processor: instructions and data. The taxonomy of *Flynn* classifies machines according to whether they have one stream or more than one stream of each type, which leads to altogether four classes of computer

architectures (whereof one class is empty):

* SISD (single instruction stream, single data stream): this class is represented by the well-known *von Neumann* computer [114, 79], where one processor is connected to one memory, and the commands are carried out sequentially on one data stream. This is the way, a classical PC or workstation operates.

* SIMD (single instruction stream, multiple data stream): in case of a SIMD architecture, there are more than one processor, which are controlled by one instruction stream, i. e., every processor carries out the same command (at the same time) on different data streams. An example of an application that can take advantage of SIMD is one, where the same value is added to a large number of data points, which is a common operation in many multimedia applications. One example would be changing the brightness of an image. Each pixel of an image consists of three 8-bit values for the brightness of the red, green and blue portions of the color. To change the brightness, the R, G and B values are read from the memory, a value is added (or subtracted) from it, and the resulting value is written back out to the memory. A member of this class is the so-called array processor.

* MISD (multiple instruction stream, single data stream): this class is empty.

* MIMD (multiple instruction stream, multiple data stream): these types of parallel machines consist of several *von Neumann* computers, which are connected with a shared memory or which interact with each other via an interconnection network. The obvious difference to the SIMD architecture is due to the fact that the MIMD consists of several stand-alone processors, where each processor has its own instruction stream, i. e., the processors can operate fully independently of each other.

In the framework of this thesis, the parallel algorithms, which are going to be presented, are designed for the class of the MIMD architectures. As already mentioned above, this class can be divided into two main groups, which consider the different ways of data interchange or memory distribution, respectively:

* shared memory systems: all processors access with equal rights a common memory (global address space), which not only acts as program memory but also as a communication interface. Computers of this type are usually limited to only few processors and require a special control of the management of the memory access.

* distributed memory systems, cf. Figure 5.1: this class is characterized by the fact that each processor must use its locally attached memory (local address space). The data interchange is carried out via an interconnection network, which is an important part of the whole parallel computer, as the capacity and the latency of the network interface cards, obviously, have a big influence on the capability of the parallel system.

The main advantage of the distributed memory systems in comparison with the shared memory systems is the expense for comparable parallel machines. The single *von Neumann* computers within a distributed memory system, which are also called (compute)
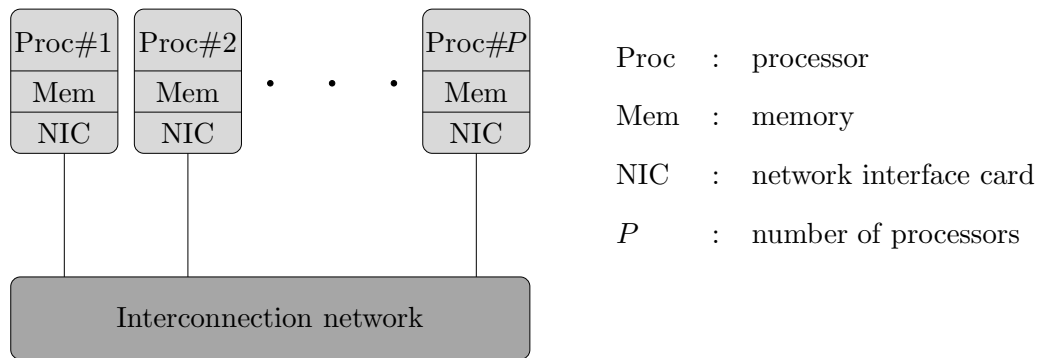
Figure 5.1: Distributed memory system.

nodes, consist of standard PC hardware mass products. Therefore, these computer architectures directly profit from the development of the semiconductor industry, which approximately results in a doubling of the complexity every 18 months, cf. *Moore*'s law [107]. Independently of this fast development of the compute nodes, the interconnection network can be designed depending on the respective power demand of each research institute or company, respectively.

5.1.2 Programming model

The algorithms within the parallel code M++ are designed for the above mentioned distributed memory systems. The necessary data transfer in such a computer architecture can be realized essentially by a programming model, which is based on the so-called functional parallelism. This programming model is characterized by splitting a sequential algorithm in parallel executable segments. The communication between those segments is realized via a message passing, which is implemented directly in the source code based on a certain communication interface, like, e. g., the Message Passing Interface (MPI; *Walker & Dongarra* [145]) or the Parallel Virtual Machine (PVM; *Geist et al.* [76]).

In the current version of M++, the MPI library is used as the communication interface. Thereby, the following small subset of MPI functions is used, cf. *Wieners et al.* [152]:

  ∗ `MPI_Init`: all MPI programs must contain a call to `MPI_Init`. This routine initializes the MPI environment and must be called before any other MPI routine.

  ∗ `MPI_Finalize`: all processes must call this routine before exiting. The number of running processes is undefined after this routine is called.

  ∗ `MPI_Comm_size`: determines the number of processors, which are involved in the parallel run.

  ∗ `MPI_Comm_rank`: each processor in a parallel run is assigned a unique identifier (or rank). `MPI_Comm_rank` determines the rank of the respective processor (or process).

  ∗ `MPI_Bcast`: broadcasts a message from the process with the rank `root` (specified as an input variable of this function) to all other processes of the parallel run.

* MPI_Allreduce: carries out a global operation and distributes the result back to all processes.

* MPI_Isend: begins a non-blocking send (see below).

* MPI_Irecv: begins a non-blocking operation to receive data (see below):

* MPI_Wait: waits for a non-blocking send or receive to complete (see below).

Both the sending and receiving processes in a communication interface can be carried out via a blocking (synchronous) or a non-blocking (asynchronous) communication. In case of a blocking communication, the sending and receiving processes are blocked until the message is transferred or a receipt confirmation is given, respectively. In case of the asynchronous communication, the execution of the program is directly continued such that a temporal overlapping of communication and program execution occurs. A blocking can be forced in this type of communication with the function MPI_Wait, which forces a block until the message passing is completed. Obviously, the asynchronous communication is the faster alternative, whereas the synchronous communication is less fault-prone.

Some of the above comments and explanations on the MPI routines have been taken from [109].

Within M++, a separate parallel processor interface is defined, where the above functions are called internally. Thus, it is easy to replace the MPI library by any other message passing protocol.

5.1.3   Load balancing

A crucial point of a parallel FE simulation is the distribution of the finite elements on the single compute nodes. For an efficient distribution, mainly two aspects have to be considered: equal load on each processor and minimal communication between the processors. Obviously, an equally distributed load on each compute node is important to prevent unbalanced processes, i. e., the waiting time of a processor for the others to finish a calculation step should be minimized. At the same time, the communication should be minimized by choosing contiguous and compact subdomains.

Applying parallel FE simulations to geotechnical questions, the geometrical complexity of the problems under study is usually rather simple, cf., e. g., Figure 5.2, where a slope is discretized with hexahedra. Following this, a standard geometrically oriented method, e. g., the so-called Recursive Coordinate Bisection (RCB; *Berger & Bokhari* [12]), can be chosen for the domain decomposition of such problems [151]. In the RCB, the computational domain is first divided into two regions by a cutting plane orthogonal to one of the coordinate axes so that half the work load is in each of the subdomains. The splitting direction is determined by computing, in which coordinate direction the set of objects is most elongated, based upon the geometrical locations of the objects. The subdomains are then further divided by recursive application of the same splitting algorithm until the number of subdomains equals the number of processors. Although a strict application of this recursive algorithm would lead to 2^k subdomains, where k is
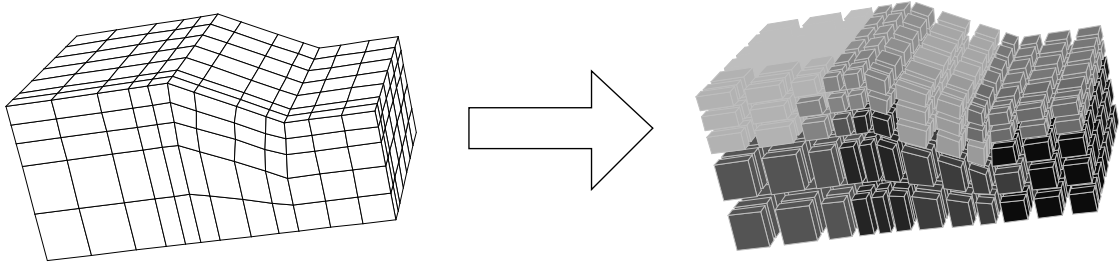
Figure 5.2: Load balancing on 16 processors by the RCB method.

the number of the divisions, any number of equally sized subdomains can be created by a modification of the dividing planes.

Another rather simple load balancing strategy was applied in [153]. There, each FE mesh was distributed onto the processors by a simple lexicographic ordering of the cell midpoints X^C. By application of the rule

$$X^{C_1} < X^{C_2} \iff \quad \begin{aligned} & x_1^{C_1} < x_1^{C_2} \text{ or} \\ & x_1^{C_1} = x_1^{C_2} \text{ and } x_2^{C_1} < x_2^{C_2} \text{ or} \\ & x_1^{C_1} = x_1^{C_2} \text{ and } x_2^{C_1} = x_2^{C_2} \text{ and } x_3^{C_1} < x_3^{C_2} , \end{aligned} \tag{5.1}$$

a unique ordering of the cells can be obtained. In the above equation, X^{C_1} and X^{C_2} denote two cell midpoints, which are defined by their coordinates $x_1^{C_i}$, $x_2^{C_i}$ and $x_3^{C_i}$ ($i = 1, 2$). Note that this load balancing minimizes the number of neighboring processors, but for more complex geometries, it is not optimal with respect to the size of the processor interfaces. Thus, enhanced methods have to be used for general geometries. A discussion on other load balancing methods can be found, e. g., in *Hinkelmann* [90].

Remark: If a constant spatial discretization is used, the domain decomposition is carried out once at the beginning of each parallel computation, after the number of processors is known and the FE mesh is read or generated. This static load balancing is no longer the appropriate strategy, when space adaptive methods are applied. In such cases, dynamic load balancing methods have to be used in order to guarantee a proper load balancing of the adaptively refined mesh, cf. *Bastian* [5].   □

Following Equation (3.10), the spatially discretized domain Ω^h is represented by finite elements C, which together build the FE mesh:

$$\Omega^h = \bigcup_{C \in \mathcal{C}} C . \tag{5.2}$$

Using a load balancing method, the FE mesh is distributed onto P processors,

$$\mathcal{C} = \bigcup_{p \in \mathcal{P}} \mathcal{C}_p , \qquad \Omega^h = \Omega_1^h \cup \ldots \cup \Omega_P^h , \qquad \Omega_p^h = \bigcup_{C \in \mathcal{C}_p} C , \tag{5.3}$$

where $\mathcal{C}_p$ denotes the set of all elements located on the processor p and $\mathcal{P} = \{1, 2, ..., P\}$ represents the set of processors or, more precisely, the identification numbers of the parallel processes. Note that for an admissible distribution of the mesh, each element C has to be uniquely assigned to one processor p, whereas the other geometrical quantities, i. e., the faces $\mathcal{F}$, edges $\mathcal{E}$ and nodes $\mathcal{N}$, can be represented on more than one processor.

5.1.4   Representation of vectorial quantities

Within the FEM, vectorial quantities like the global solution vector $\boldsymbol{u}_n$ from (3.23) or the consistent tangent $\mathrm{D}\boldsymbol{\mathcal{R}}^{h,n,j}$ from (3.48) are tied to the nodes of the finite element mesh. Therefore, it is a logical consequence of the above introduced domain decomposition that according to the respective node, a component of a vector is possibly distributed on several processors.

Following *Bastian* [5], two different algebraic representations are used for the vectorial quantities:

* ∗ consistent representation: a global vector $\boldsymbol{a}$ is stored consistently, if for all components $\boldsymbol{a}_p$ on the processor p the following holds:

$$\boldsymbol{a}_p = (\boldsymbol{a})_{\Omega_p^h} \ . \tag{5.4}$$

  This means that in all copies of the entries, which are tied to a certain node, the same values are stored.

* ∗ inconsistent or additive representation: a global vector $\boldsymbol{a}$ is stored inconsistently, if the following relation holds:

$$\boldsymbol{a} = \sum_{p \in \mathcal{P}} \boldsymbol{a}_p \ . \tag{5.5}$$

  This means that the global entries, which are tied to a certain node, are only obtained by a summation over all processors p this node is represented on.

5.1.5   Capability of the parallel code

Each parallel implementation of a FE program can lead to different results concerning the total computing time. Furthermore, the fact that a source code is executable in parallel does not necessarily lead to a decrease of computing time of a numerical simulation. Therefore, measures for the classification of the capability of a parallel code have to be defined. Generally, three important measures are known: speed-up, efficiency and scale-up [96].

The parallel speed-up S_P is defined as the ratio of the computing time on one processor to the computing time on P processors:

$$S_P = \frac{T_{1,K}}{T_{P,K}} \ . \tag{5.6}$$

Therein, $T_{P,K}$ denotes the computing time on P processors of a problem with the complexity K, and $T_{1,K}$ represents the sequential computing time of this problem. In the framework of this thesis, the complexity of a problem is defined by the number of finite elements, which are used for the spatial discretization of the computational domain.

In Figure 5.3 (left), a possible development of the speed-up S_P is shown. Looking at this figure, it is obvious that a close progression of the identified curve of S_P to the theoretically possible curve corresponds to a good speed-up of the parallel code. In the practical applications, the speed-up S_P is always smaller than P. This is due to the so-called parallel overhead, which arises from, e. g., a lot of communication between the compute nodes or a load imbalance.
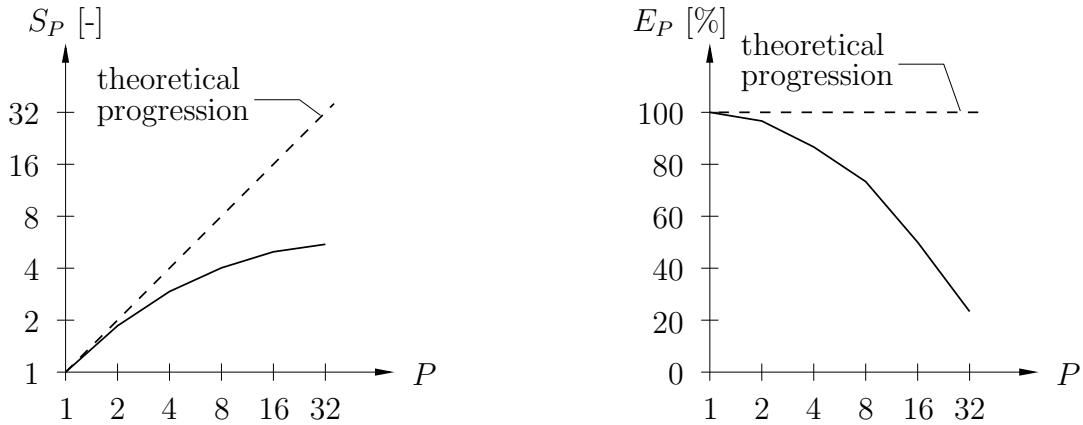

Figure 5.3: Speed-up S_P and efficiency E_P [90].

The parallel efficiency E_P is defined as the ratio of the speed-up S_P with respect to the number of compute nodes P:

$$E_P = \frac{S_P}{P} = \frac{T_{1,K}}{P\,T_{P,K}}\,. \tag{5.7}$$

E_P can be understood as a scaling of the speed-up S_P with respect to the processors P. In general, this results in an efficiency $E_P < 1$ ($< 100\%$), which decreases for an increasing number of compute nodes, cf. Figure 5.3 (right).

The parallel scale-up U_P is defined via the relation

$$U_P = \frac{T_{P,(K*P)}}{T_{1,K}}\,. \tag{5.8}$$

U_P provides a statement about the question: how many compute nodes are necessary for an increasing complexity of the problem in order to keep the computing time constant? Coming along with this definition of U_P is the term "scalable algorithm". A scalable algorithm is an algorithm, which results in a more or less constant scale-up U_P, when the complexity $K * P$ and the number of processors P are increased.

The above introduced measures, speed-up S_P and efficiency E_P, are defined with respect to a constant complexity K of the problems and varying number of processors P. Based on

a varying complexity and a constant number of compute nodes, the following definitions for the "slow-down" S_K and the efficiency E_K can be introduced:

$$S_K = \frac{T_{P,(K*m)}}{T_{P,K}}, \qquad E_K = \left(\frac{S_K}{m}\right)^{-1} = \left(\frac{T_{P,(K*m)}}{m\,T_{P,K}}\right)^{-1}. \tag{5.9}$$

Therein, m is the factor, by which the complexity of the problem is increased, i. e., in the framework of this thesis, the factor, by which the number of elements is multiplied. Thinking about a regular refinement of the FE mesh in 2-d (or 3-d) in order to increase the complexity, this factor results in 4 (or 8) for a single refinement step. Furthermore, S_K and E_K are not only measures for the rating of the capability of the parallel code, but also measures on how much an increase of the complexity at a constant number of processors effects the total computing time.

5.2   Parallel simulations of multiphasic problems

Due to high numerical costs, finite element simulations of realistic porous media problems in soil mechanics are a difficult task for the numerical realization. Adaptive strategies in time and space proved to be very effective in the simulation of a variety of challenging 2-d problems, cf. *Ellsiepen* [66] and *Ehlers et al.* [59, 60, 55, 62]. Nevertheless, new strategies have to be considered for a numerical realization of porous media models in 3-d.

Therefore, in the framework of this thesis, the parallelization of the FE code is applied as a new strategy. In this section, the interface of the sequentially implemented FE tool PANDAS [58, 117] and the parallel solver M++ [147], together with the underlying parallel data structure, the so-called Distributed Point Objects [150, 152], are presented.

5.2.1   Complexity of FE simulations of porous media models

The high numerical costs coming along with the simulation of realistic boundary-value problems for porous media models are caused by mainly three reasons: complex mechanical models, the choice of the finite element ansatz functions and the necessity of 3-d computations.

From the mechanical point of view, the modeling of porous media results in systems with more than one type of degree of freedom, i. e., for example, in the presented triphasic model, the displacement $\mathbf{u}_S$ of the solid skeleton, the pore-liquid pressure p^{LR} and the pore-gas pressure p^{GR}, cf. Chapter 2. Furthermore, due to stability reasons of the resulting system of equations, the order of the ansatz functions for the single degrees of freedom cannot be chosen arbitrarily but have to fulfill certain conditions, cf. Section 3.1.3. This fact leads to the application of the *Taylor-Hood* elements, which result in quadratic ansatz functions for the solid displacement $\mathbf{u}_S$ and linear ansatz functions for the pressure terms p^{LR} and p^{GR}. Finally, for the calculation of practical applications, the geometry of a problem has to be discretized very often in all three dimensions. A simplification towards a 2-d problem is only possible, when plane strain or plain stress conditions can be assumed for the solid deformation and plane flow conditions exist for the fluid flow.
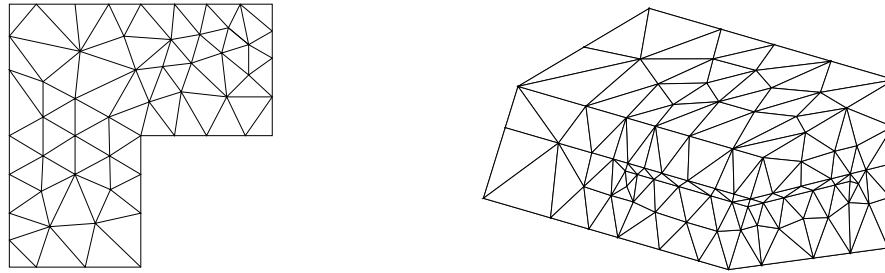
Figure 5.4: 2-d [128] and 3-d [124, 125] finite element meshes.

In Figure 5.4, two exemplary FE meshes are shown. The 2-d mesh, which consists of triangular elements [128], results in 79 finite elements and 55 or 188 nodes for a linear or quadratic ansatz, respectively. The 3-d mesh contains altogether 1 005 tetrahedra [124, 125] and 240 or 1 598 nodes (again for linear or quadratic ansatz functions). From this example, it becomes evident that there is an enormous difference in the numerical effort of handling, one the one hand, systems with linear or with quadratic ansatz functions, and, on the other hand, 2-d or 3-d calculations. In the presented example, the factor between the linear and the quadratic ansatz functions is in the 2-d case approximately 3.4 and in the 3-d case approximately 6.7.

5.2.2 Definition of the interface M++/PANDAS

In order to be able to run FE calculations in parallel, the sequentially implemented FE code PANDAS has to be modified. Within this FE program, almost any imaginable mechanical model, like, e. g., the presented triphasic model, can be implemented straightforward, and problems based on this model can be solved with advanced adaptive techniques and a variety of linear solvers, but the complexity of a problem is limited to only one processor. At this point, there are mainly two possibilities to start the parallelization process: rewrite the whole FE code based on a parallel data structure or define an interface between the sequential program and a code, which already contains parallel data structures. As the first alternative would take a lot of time, possibly many years, until the first problem could be calculated in parallel, the second alternative turns out to be very efficient.

The program M++ is a tool, which is based on a parallel data structure and which contains parallel linear solvers. It is furthermore implemented in such a universal manner that it was possible to realize the above mentioned interface within that program. This interface finally contains only a few callback functions for the necessary communication between the two programs. Note that with this strategy, it was made possible to run parallel computations with the material models from PANDAS without changing anything in the source code of PANDAS. This strategy is of course not restricted to the parallelization of PANDAS but is capable to be applied also to other sequential programs.

Based on the local assembling interface, which was presented in Section 3.3.3, the following

callback routines define the interface between M++ and PANDAS:

* `Pandas_Init`: initialization of PANDAS for the required types of finite elements and the reading of the material parameters.

* `Pandas_Dirichlet`: evaluation of the *Dirichlet* boundary conditions D_C.

* `Pandas_Defect`: evaluation of the *Neumann* boundary conditions and calculation of the residual R_C for every element.

* `Pandas_Tangent`: computation of the algorithmically consistent tangent T_C.

* `Pandas_Update`: update U_C of the internal variables in PANDAS.

The actual interaction between the two programs is controlled by M++, which initializes PANDAS only in the background. Except for the two routines, which arrange the initialization of PANDAS at the beginning of each computation, and the update function `Pandas_Update`, which updates the internal variables at the end of each time step, the above functions are called element-wise and fairly often within each *Newton* iteration from M++ in order to build the necessary global quantities. Thereby, the only information about the initial boundary-value problem explicitly known in M++ are the FE mesh and the number of unknowns (degrees of freedom) at each node. All further information on boundary conditions and material parameters are defined via the usual input files of and in PANDAS.

5.2.3   Distributed Point Objects

The underlying parallel data structure of M++ are the Distributed Point Objects (DPO). This structure was developed by *Wieners* [150] in order to establish a transparent basis for modifications or extensions of the parallel code and its applications like, e. g., PANDAS [152].

The DPO are a geometrical model, which is based on a finite set of points $\mathcal{X} \subset \mathbb{R}^D$ with $D \in \{1, 2, 3\}$ representing the spatial dimension of the problem. For the description of different geometrical quantities, respective types of points are introduced: corner points X^V, edge midpoints X^E, face midpoints X^F, cell midpoints X^C and an exception point $X^{Ex} = \infty$, cf. Figure 5.5.

With these different types of points, a FE mesh $\mathcal{M} = (\bar{\mathcal{C}}, \bar{\mathcal{F}}, \bar{\mathcal{E}}, \bar{\mathcal{V}}, \bar{\mathcal{B}})$ is defined by the following mappings:

* cell mapping $\bar{\mathcal{C}} \colon \mathcal{X} \longrightarrow \bigcup_{N_C} \mathcal{X}^{N_C}$, which assigns every cell midpoint X^C the cell represented by the vector of N_C corner points, where, e. g., $N_C = 4$ for tetrahedra or $N_C = 8$ for hexahedra:

$$C = \bar{\mathcal{C}}(X^C) = (X^1, \dots, X^{N_C}) \quad \in \mathcal{X}^{N_C} . \tag{5.10}$$
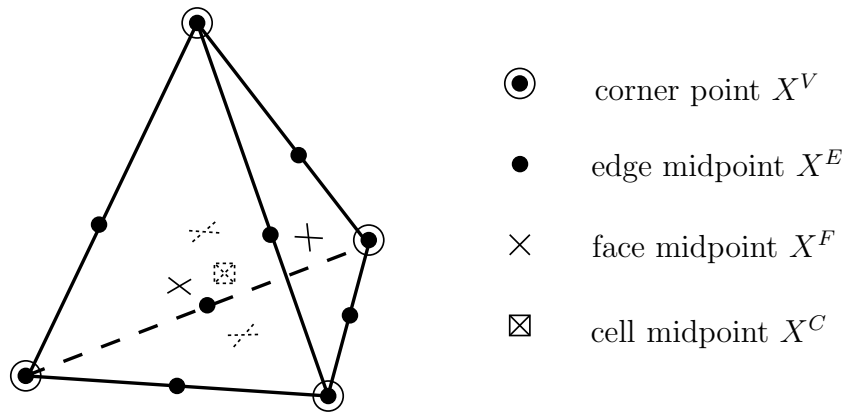
Figure 5.5: Different types of points in a tetrahedron.

* face mapping $\bar{\mathcal{F}}\colon \mathcal{X} \longrightarrow \mathcal{X}^2$, which assigns every face midpoint X^F the two adjacent elements represented by their midpoints $X^{C\,\text{left}}$ and $X^{C\,\text{right}}$:

$$F = \bar{\mathcal{F}}(X^F) = (X^{C\,\text{left}}, X^{C\,\text{right}}) \quad \in \mathcal{X}^2 \,. \tag{5.11}$$

* edge mapping $\bar{\mathcal{E}}\colon \mathcal{X} \longrightarrow \mathcal{X}^2$, which assigns every edge midpoint X^E the two adjacent vertices $X^{V\,\text{left}}$ and $X^{V\,\text{right}}$ and which counts for each edge midpoint X^E the number of cells with $X^E \in C$:

$$E = \bar{\mathcal{E}}(X^E) = (X^{V\,\text{left}}, X^{V\,\text{right}}) \quad \in \mathcal{X}^2 \,. \tag{5.12}$$

* vertex mapping $\bar{\mathcal{V}}$, which represents a list of vertices X^V and counts for each vertex X^V the number of cells with $X^V \in C$.

* boundary mapping $\bar{\mathcal{B}}$, which represents a list of boundary faces identified by their markers for the definition of boundary conditions. Boundary faces are a special type of faces F characterized by $X^{C\,\text{right}} = X^{Ex} = \infty$.

Note that all mappings return an empty object for point arguments of the wrong type. For convenience, the abbreviations $C \in \bar{\mathcal{C}}$ (instead of $C \in \bar{\mathcal{C}}(\mathcal{X})$), $F \in \bar{\mathcal{F}}$ (instead of $F \in \bar{\mathcal{F}}(\mathcal{X})$), etc. are used. Furthermore, the notation $X \in \mathcal{X}_{\bar{\mathcal{C}}}$ for the cell midpoints X^C, etc. is used.

Until now, point objects based on a finite set of points $\mathcal{X}$ have been described. For the representation of the parallel distribution of $\mathcal{X}$, a partition map π is introduced,

$$\pi\colon \mathcal{X} \longrightarrow 2^{\mathcal{P}} \,, \tag{5.13}$$

which is assigning to every point $X \in \mathcal{X}$ the subset $\pi(X) \subset \mathcal{P}$ of processors, where this point is represented. Note that the notation in (5.13) defines π as the power set of $\mathcal{P}$, i. e., the set of all subsets of $\mathcal{P}$. With the definition of the partition map π at hand, it is straightforward to define a unique master processor for every point X,

$$\mu(X) = \min \pi(X) \,, \tag{5.14}$$

and an overlapping partition for the distributed point sets $\mathcal{X}_p$:

$$\mathcal{X} = \mathcal{X}_1 \cup \ldots \cup \mathcal{X}_P\,, \qquad \mathcal{X}_p = \{X \in \mathcal{X} \colon p \in \pi(X)\}\,. \tag{5.15}$$

From this, the local mesh $\mathcal{M}_p = (\bar{\mathcal{C}}_p, \bar{\mathcal{F}}_p, \bar{\mathcal{E}}_p, \bar{\mathcal{V}}_p, \bar{\mathcal{B}}_p, \pi_p)$ on processor p is obtained by restricting all mappings to $\mathcal{X}_p$.

In order to determine an admissible distribution of the mesh $\mathcal{M}$ onto P processors, every cell $C \in \bar{\mathcal{C}}$ is assigned exactly one destination processor $\mathrm{dest}\,(C) \in \mathcal{P}$. This defines a disjoint partition for the cells and overlapping partitions for the faces, edges and vertices:

$$\begin{aligned}
\pi(X^C) &= \{\mathrm{dest}\,(C)\}, & C &\in \bar{\mathcal{C}}, \\
\pi(X^F) &= \{\mathrm{dest}\,(C) \colon X^C \in F\}, & F &\in \bar{\mathcal{F}}, \\
\pi(X^E) &= \{\mathrm{dest}\,(C) \colon E \subset C\}, & E &\in \bar{\mathcal{E}}, \\
\pi(X) &= \{\mathrm{dest}\,(C) \colon X \in C\}, & X &\in \bar{\mathcal{V}}.
\end{aligned} \tag{5.16}$$

Remark: Note that the Distributed Point Objects already provide a parallel uniform refinement rule for a cell in the FE mesh, cf. *Wieners* [150]. With this additional feature, the DPO are also qualified for the application of space adaptive strategies. □

5.2.4 Parallel algorithm

Based on the DPO, the parallel algorithm can be defined, which manages the single steps within the *Newton-Raphson* method as they were described in Section 3.3.2. For convenience, the following abbreviations are introduced for the further discussions within this section:

$$\begin{aligned}
\bar{\boldsymbol{u}} &:= \boldsymbol{u}_n^j & &: \text{global solution vector,} \\
\Delta\bar{\boldsymbol{u}} &:= \Delta\boldsymbol{u}_n^j & &: \textit{Newton } \text{correction vector for } \bar{\boldsymbol{u}}, \\
\bar{\boldsymbol{\mathcal{R}}} &:= \boldsymbol{\mathcal{R}}^{h,n,j} & &: \text{residual vector of the nonlinear problem,} \\
\mathrm{D}\bar{\boldsymbol{\mathcal{R}}} &:= \mathrm{D}\boldsymbol{\mathcal{R}}^{h,n,j} & &: \text{algorithmically consistent tangent.}
\end{aligned} \tag{5.17}$$

The single entries in the vectors $\bar{\boldsymbol{u}}$, $\Delta\bar{\boldsymbol{u}}$, $\bar{\boldsymbol{\mathcal{R}}}$ and in the matrix $\mathrm{D}\bar{\boldsymbol{\mathcal{R}}}$ correspond to the nodes of the FE discretization, i. e., in the context of the DPO, to the corner points X^V and to the edge midpoints X^E. By assigning the number of degrees of freedom $N_X \geq 0$ to every point $X \in \mathcal{X}$, the block vectors

$$\bar{\boldsymbol{u}}[X] \in \mathbb{R}^{N_X}\,, \qquad \Delta\bar{\boldsymbol{u}}[X] \in \mathbb{R}^{N_X} \quad \text{and} \quad \bar{\boldsymbol{\mathcal{R}}}[X] \in \mathbb{R}^{N_X} \tag{5.18}$$

are defined. By a combination of all block vectors, the respective global vector is obtained, e. g., the global solution vector yields

$$\bar{\boldsymbol{u}} = (\bar{\boldsymbol{u}}[X])_{X \in \mathcal{X}} \in \mathbb{R}^{N_{\mathcal{X}}}\,, \qquad N_{\mathcal{X}} = \sum_{X \in \mathcal{X}} N_X\,. \tag{5.19}$$

These global vectors are represented in parallel by local vectors, e. g., for the local solution vector on the processor p holds

$$\bar{\boldsymbol{u}}_p \colon \mathcal{X}_p \longrightarrow \bigcup_{N_p} \mathbb{R}^{N_p} , \qquad N_p = \sum_{X \in \mathcal{X}_p} N_X . \tag{5.20}$$

Based on a 3-dimensional spatial discretization with *Taylor-Hood* elements for the triphasic model, the following degrees of freedom are assigned to the different points:

$$N_X = 5 \ \text{ for } X \in \mathcal{X}_{\bar{\mathcal{V}}} , \quad N_X = 3 \ \text{ for } X \in \mathcal{X}_{\bar{\mathcal{E}}} , \quad N_X = 0 \ \text{ for } X \in \{\mathcal{X}_{\bar{\mathcal{F}}} \cup \mathcal{X}_{\bar{\mathcal{C}}}\} . \tag{5.21}$$

Following the introduction in Section 5.1.4, two representations of distributed vectorial quantities are distinguished:

* a consistent representation is chosen for solution and correction vectors, where, e. g., the unique block vector $\bar{\boldsymbol{u}}[X]$ is represented on all processors $p \in \pi(X)$, viz $\bar{\boldsymbol{u}}_p[X] = \bar{\boldsymbol{u}}[X]$.

* an additive representation is chosen for residual vectors and tangent matrices, where, e. g., the block vector $\bar{\boldsymbol{\mathcal{R}}}[X]$ has a non-unique parallel representation $\bar{\boldsymbol{\mathcal{R}}}[X] = \sum_{p \in \pi(X)} \bar{\boldsymbol{\mathcal{R}}}_p[X]$.

Within the presented interface M++/PANDAS, almost every callback routine (except the function `Pandas_Init`) is evaluated on the element level. This motivates the introduction of cell vectors $\bar{\boldsymbol{u}}[C] , \Delta\bar{\boldsymbol{u}}[C] , \bar{\boldsymbol{\mathcal{R}}}[C]$ and cell matrices $\mathrm{D}\bar{\boldsymbol{\mathcal{R}}}[C]$:

$$\begin{aligned}
\bar{\boldsymbol{u}}[C] &= (\bar{\boldsymbol{u}}[X])_{X \in \mathcal{X}_C} & \in \mathbb{R}^{N_C} , \\
\Delta\bar{\boldsymbol{u}}[C] &= (\Delta\bar{\boldsymbol{u}}[X])_{X \in \mathcal{X}_C} & \in \mathbb{R}^{N_C} , \\
\bar{\boldsymbol{\mathcal{R}}}[C] &= (\bar{\boldsymbol{\mathcal{R}}}[X])_{X \in \mathcal{X}_C} & \in \mathbb{R}^{N_C} , \\
\mathrm{D}\bar{\boldsymbol{\mathcal{R}}}[C] &= (\mathrm{D}\bar{\boldsymbol{\mathcal{R}}}[X,Y])_{X,Y \in \mathcal{X}_C} & \in \mathbb{R}^{N_C,N_C} .
\end{aligned} \tag{5.22}$$

Therein, $\mathcal{X}_C = \{X \in \mathcal{X} \cap \mathrm{conv}(C) \colon N_X > 0\}$ defines the nodal points of the cell C and $N_C = \sum_{X \in \mathcal{X}_C} N_X$ denotes the number of the degrees of freedom, which are associated to the nodal points $X \in \mathcal{X}_C$. Furthermore, $\mathrm{conv}(C) \subset \mathbb{R}^D$ gives the convex hull of the corner points X^V of the cell C.

The above definition of cell vectors and cell matrices requires an efficient access to the block vectors (5.18) and, especially, to the block matrices:

$$\mathrm{D}\bar{\boldsymbol{\mathcal{R}}}[X,Y] \quad \in \mathbb{R}^{N_X,N_Y} , \quad X,Y \in \mathcal{X}_C . \tag{5.23}$$

In the current version of M++, this is realized by hash tables, where the keys for these tables are points. By this choice for the data access, pointers can be completely avoided in the parallel data structure described above.

Remark: Within a programming language, a pointer is a datatype, whose value is an address, which is used to refer to ("point to") another value stored elsewhere in the

computer memory. On the one side, the use of pointers can provide a more efficient data access than realized in the model with the hash tables, but, on the other side, the fact that no pointers are needed is essential for a transparent and expandable parallel code, cf. *Wieners et al.* [152]. □

For the parallel assembling of the global linear system (3.49), the following routines of the interface M++/PANDAS are called for each element C:

∗ `Pandas_Dirichlet`: the local function D_C assigns the respective *Dirichlet* values to the cell vector $\bar{\boldsymbol{u}}[C]$. This procedure is performed in parallel without communication. After D_C is called for all cells C, the *Dirichlet* data has to be exchanged at the processor interfaces in order to guarantee consistent start values on all processors p.

∗ `Pandas_Defect`: based on the consistent solution vectors $\bar{\boldsymbol{u}}[C]$, the local residual function R_C is called in parallel (no communication) for every cell on each processor p. This procedure results in additive representations of the residual vectors $\bar{\boldsymbol{\mathcal{R}}}_p$:

$$\bar{\boldsymbol{\mathcal{R}}}_p = \sum_{\mu(C)=p} \bar{\boldsymbol{\mathcal{R}}}[C] \,. \tag{5.24}$$

∗ `Pandas_Tangent`: based on the consistent solution vectors $\bar{\boldsymbol{u}}[C]$, the local tangent function T_C is called in parallel (no communication) for every cell on each processor p. This procedure results in additive representations of the algorithmically consistent tangents $\mathrm{D}\bar{\boldsymbol{\mathcal{R}}}_p$:

$$\mathrm{D}\bar{\boldsymbol{\mathcal{R}}}_p = \sum_{\mu(C)=p} \mathrm{D}\bar{\boldsymbol{\mathcal{R}}}[C] \,. \tag{5.25}$$

In the above relations, the notation $\mu(C)$ has been used for the unique master processor of each cell C,

$$\mu(C) \;\in\; \pi(C) \,, \quad \pi(C) = \bigcap_{X \in \mathcal{X}_C} \pi(X) \,, \tag{5.26}$$

which is a logical consequence of the chosen strategy (5.16) for the mesh distribution.

In principle, the above described assembling process leads to the global linear system (3.49), which has to be solved within each *Newton* step:

$$\mathrm{D}\bar{\boldsymbol{\mathcal{R}}} \, \Delta\bar{\boldsymbol{u}} = \bar{\boldsymbol{\mathcal{R}}} \qquad \text{with} \quad \mathrm{D}\bar{\boldsymbol{\mathcal{R}}} = \sum_{p \in \mathcal{P}} \mathrm{D}\bar{\boldsymbol{\mathcal{R}}}_p \quad \text{and} \quad \bar{\boldsymbol{\mathcal{R}}} = \sum_{p \in \mathcal{P}} \bar{\boldsymbol{\mathcal{R}}}_p \,. \tag{5.27}$$

The strategy of explicitly assembling the whole problem is not target-oriented, as the solution of the resulting huge linear system (5.27) usually cannot be performed on one processor. Obviously, for this solution process, also parallel strategies have to be applied.

In order to solve linear systems of the type (5.27) in parallel, iterative linear solvers are well suited and very efficient, cf., e. g., *Bastian* [5] or *Wieners et al.* [150, 152, 153]. Therein, for a given start iterate $\Delta\bar{\boldsymbol{u}}^m \in \mathbb{R}^{N_{\mathcal{X}}}$ ($m = 0$), a typical step within a basic iterative linear solver is organized as follows:

∗ compute the residual vector $\boldsymbol{r}_p^m$ for each $p \in \mathcal{P}$ (no communication):

$$\boldsymbol{r}_p^m = \bar{\boldsymbol{\mathcal{R}}}_p - \mathrm{D}\bar{\boldsymbol{\mathcal{R}}}_p \ \Delta\bar{\boldsymbol{u}}_p^m \,. \tag{5.28}$$

Starting with an additive right-hand side $\bar{\boldsymbol{\mathcal{R}}}_p$, the matrix-vector multiplication of an additive matrix $\mathrm{D}\bar{\boldsymbol{\mathcal{R}}}_p$ and a consistent vector $\Delta\bar{\boldsymbol{u}}_p^m$ results in an additive residual vector $\boldsymbol{r}_p^m$.

∗ check for convergence (communication necessary):

$$||\boldsymbol{r}^m|| = \sqrt{(\boldsymbol{r}^m)^T \, \boldsymbol{r}^m} = \sqrt{\sum_{p \in \mathcal{P}} (\boldsymbol{r}_{p,\mathrm{col}}^m)^T \, \boldsymbol{r}_{p,\mathrm{col}}^m} \ < \ tol$$

$$\text{with} \quad \boldsymbol{r}_{p,\mathrm{col}}^m = (\boldsymbol{r}_{p,\mathrm{col}}^m[X])_{X \in \mathcal{X}_p}$$

$$\tag{5.29}$$

$$\text{and} \quad \boldsymbol{r}_{p,\mathrm{col}}^m[X] = \begin{cases} \displaystyle\sum_{q \in \pi(X)} \boldsymbol{r}_q^m[X] & \text{for } p = \mu(X) \,, \\ \boldsymbol{0} & \text{else}\,. \end{cases}$$

To determine the global norm $||\boldsymbol{r}^m||$, the single entries of the local residual vectors $\boldsymbol{r}_p^m$ are collected as defined in $(5.29)_3$. By doing this, a unique additive representation of $\boldsymbol{r}^m$ is obtained on the master nodal points such that the global norm $||\boldsymbol{r}^m||$ can be computed in parallel as shown in $(5.29)_1$. If the user-defined tolerance is not fulfilled, the iteration procedure has to be continued.

∗ determine the correction vector $\boldsymbol{c}_p^m$ for each $p \in \mathcal{P}$ (communication necessary):

$$\boldsymbol{c}_p^m = (\boldsymbol{c}_p^m[X])_{X \in \mathcal{X}_p}$$

$$\text{with} \quad \boldsymbol{c}_p^m[X] = \sum_{p \in \pi(X)} \boldsymbol{c}_{p,\mathrm{add}}^m[X] \,,$$

$$\boldsymbol{c}_{p,\mathrm{add}}^m[X] = \boldsymbol{B}[X,X] \, \boldsymbol{r}_{p,\mathrm{col}}^m[X] \tag{5.30}$$

$$\text{and} \quad \boldsymbol{B}[X,X] = \left(\sum_{p \in \pi(X)} \mathrm{D}\bar{\boldsymbol{\mathcal{R}}}_p[X,X] \right)^{-1} \,.$$

The consistent correction vector $\boldsymbol{c}_p^m$ is obtained within two steps. First of all, the matrix-vector multiplication of a consistent preconditioner $\boldsymbol{B}$ (approximating $\mathrm{D}\bar{\boldsymbol{\mathcal{R}}}^{-1}$) with a (unique) additive residual vector $\boldsymbol{r}_{p,\mathrm{col}}^m$ results in an additive correction vector $\boldsymbol{c}_{p,\mathrm{add}}^m$. After this, the parallel representation of the correction vector is changed to a consistent vector by an interface communication as described in $(5.30)_2$.

The preconditioner presented in $(5.30)_4$ is the so-called point-block *Jacobi* preconditioner, which is assembled by the consistent point-block diagonal entries of the

local tangents $\mathrm{D}\bar{\mathcal{R}}_p$. These point-block objects collect the degrees of freedom corresponding to a single nodal point $X \in \mathcal{X}$. Within the presented model, other, more sophisticated preconditioners can be realized, as, e. g., a block *Jacobi* preconditioner with *Gauß-Seidel* blocks [153] or mutlilevel preconditioners [5].

∗ update the solution vector $\Delta\bar{\boldsymbol{u}}^m$ (no communication):

$$\Delta\bar{\boldsymbol{u}}_p^{m+1} = \Delta\bar{\boldsymbol{u}}_p^m + \boldsymbol{c}_p^m \,. \tag{5.31}$$

Due to the consistent correction vector $\boldsymbol{c}_p^m$, this update can be carried out in parallel without any communication and leads to a consistent representation of $\Delta\bar{\boldsymbol{u}}^{m+1}$ on every processor p.

Note that within the iterative solution process of the global linear system (5.27), it is not necessary to assemble the entries of the global consistent tangent matrix:

$$\mathrm{D}\bar{\mathcal{R}}[X,Y] = \sum_{p \in \pi(X) \cap \pi(Y)} \mathrm{D}\bar{\mathcal{R}}_p[X,Y]\,, \qquad X, Y \in \mathcal{X}_p \,. \tag{5.32}$$

Remark: The presented basic iterative linear solver can be extended straightforward within the underlying parallel data structure towards *Krylov* acceleration methods, like, e. g., the GMRES method (Generalized Minimal RESidual; *Barrett et al.* [4]). In *Wieners et al.* [153], the realization of the GMRES method within the presented model is discussed in detail.   □

5.2.5   Example

In order to clarify the strategies within the DPO and the parallel solution of a linear system of equations, some crucial points are illustrated in this section at the example of a simple FE mesh consisting of two triangles [150, 152], cf. Figure 5.6.

In a first step, the mesh is read on one processor (master processor) by a sequential insertion of the single cells, thus, leading to the point objects, which are stored in $\mathcal{M}$. By insertion of the first triangle $C_1 = (X_1, X_2, X_3)$ in $\mathcal{M}$, the following point set $\mathcal{X}$, edges $\bar{\mathcal{E}}(X^E)$ and faces $\bar{\mathcal{F}}(X^F)$ are obtained:

$$
\begin{aligned}
\mathcal{X} \quad &= \quad \{X_1,\, X_2,\, X_3,\, X_{12} = \tfrac{1}{2}\,(X_1 + X_2),\, X_{13} = \tfrac{1}{2}\,(X_1 + X_3), \\
&\qquad X_{23} = \tfrac{1}{2}\,(X_2 + X_3),\, X_{123} = \tfrac{1}{3}\,(X_1 + X_2 + X_3)\}\,, \\[4pt]
\bar{\mathcal{E}}(X_{12}) \quad &= \quad (X_1,\, X_2)\,, \quad \bar{\mathcal{E}}(X_{23}) \;=\; (X_2,\, X_3)\,, \quad \bar{\mathcal{E}}(X_{13}) \;=\; (X_1,\, X_3)\,, \\[4pt]
\bar{\mathcal{F}}(X_{12}) \quad &= \quad (X_{123},\, \infty)\,, \quad \bar{\mathcal{F}}(X_{23}) \;=\; (X_{123},\, \infty)\,, \quad \bar{\mathcal{F}}(X_{13}) \;=\; (X_{123},\, \infty)\,.
\end{aligned}
\tag{5.33}
$$

The insertion of the second triangle $C_2 = (X_2, X_3, X_4)$ adds the new points

$$X_4,\quad X_{24} = \tfrac{1}{2}\,(X_2 + X_4),\quad X_{34} = \tfrac{1}{2}\,(X_3 + X_4),\quad X_{234} = \tfrac{1}{3}\,(X_2 + X_3 + X_4) \tag{5.34}$$
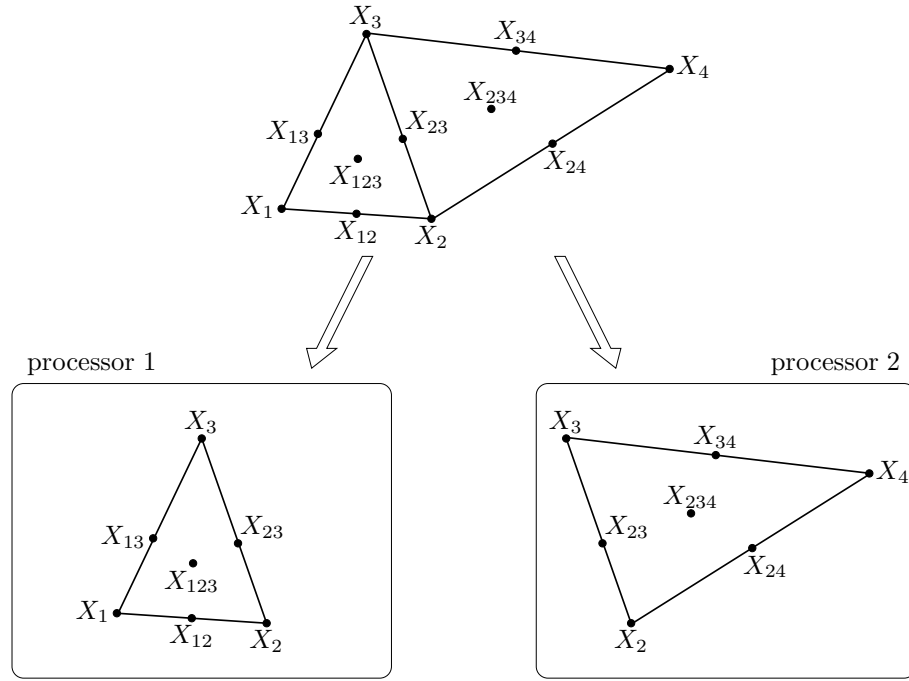
Figure 5.6: Exemplary FE mesh consisting of two triangles.

to the point set $\mathcal{X}$. Furthermore, new edges and faces have to be defined,

$$\bar{\mathcal{E}}(X_{24}) \;=\; (X_2,\, X_4)\,, \quad \bar{\mathcal{E}}(X_{34}) \;=\; (X_3,\, X_4)\,,$$

$$\bar{\mathcal{F}}(X_{24}) \;=\; (X_{234},\, \infty)\,, \quad \bar{\mathcal{F}}(X_{34}) \;=\; (X_{234},\, \infty)\,, \tag{5.35}$$

and, finally, the common face of the two cells is updated:

$$\bar{\mathcal{F}}(X_{23}) \;:=\; (X_{123},\, X_{234})\,. \tag{5.36}$$

After the insertion of all cells is finished, boundary faces can be identified by testing the faces $\bar{\mathcal{F}}(X^F)$ for the exception point: $X^{C\,\mathrm{right}} = X^{Ex} = \infty$.

Assuming $P = 2$ for the number of processors and a parallel distribution with dest $(C_1) = 1$ and dest $(C_2) = 2$, the partition map π results in

$$\pi(X_1) = \pi(X_{12}) = \pi(X_{13}) = \pi(X_{123}) \;=\; \{1\}\,,$$

$$\pi(X_2) = \pi(X_3) = \pi(X_{23}) \;=\; \{1,\, 2\}\,, \tag{5.37}$$

$$\pi(X_4) = \pi(X_{24}) = \pi(X_{34}) = \pi(X_{234}) \;=\; \{2\}\,,$$

thus leading to the Distributed Point Objects with the local point sets $\mathcal{X}_p$:

$$\mathcal{X}_1 \;=\; \{X_1,\, X_2,\, X_3,\, X_{12},\, X_{13},\, X_{23},\, X_{123}\}\,,$$

$$\mathcal{X}_2 \;=\; \{X_2,\, X_3,\, X_4,\, X_{23},\, X_{24},\, X_{34},\, X_{234}\}\,. \tag{5.38}$$

For the discussion of the parallel linear algebra, in a next step, degrees of freedom have to be assigned to the respective points $X \in \mathcal{X}$. Considering *Taylor-Hood* elements for the triphasic model, this results in the assignments

$$N_X = 4 \text{ for } X \in \mathcal{X}_{\bar{\mathcal{V}}}, \quad N_X = 2 \text{ for } X \in \mathcal{X}_{\bar{\mathcal{E}}}, \quad N_X = 0 \text{ for } X \in \{\mathcal{X}_{\bar{\mathcal{F}}} \cup \mathcal{X}_{\bar{\mathcal{C}}}\}, \quad (5.39)$$

which altogether give $N_C = \sum_{X \in \mathcal{X}_C} N_X = 18$ for each triangle $C \in \mathcal{C}$.

On the distributed mesh, the residual vector $\boldsymbol{r}^m$ from (5.28) is represented additively by $\boldsymbol{r}^m = \boldsymbol{r}_1^m + \boldsymbol{r}_2^m$ with

$$
\begin{aligned}
\boldsymbol{r}_1^m &= \left(\boldsymbol{r}_1^m[X_1], \, \boldsymbol{r}_1^m[X_2], \, \boldsymbol{r}_1^m[X_3], \, \boldsymbol{r}_1^m[X_{12}], \, \boldsymbol{r}_1^m[X_{23}], \, \boldsymbol{r}_1^m[X_{13}] \right), \\
\boldsymbol{r}_2^m &= \left(\boldsymbol{r}_2^m[X_2], \, \boldsymbol{r}_2^m[X_4], \, \boldsymbol{r}_2^m[X_3], \, \boldsymbol{r}_2^m[X_{24}], \, \boldsymbol{r}_2^m[X_{34}], \, \boldsymbol{r}_2^m[X_{23}] \right).
\end{aligned}
\quad (5.40)
$$

For the evaluation of the norm $||\boldsymbol{r}^m||$, a unique additive representation is obtained by collecting the residual parts on the processors as described in $(5.29)_3$:

$$
\begin{aligned}
\boldsymbol{r}_{1,\mathrm{col}}^m &= \left(\boldsymbol{r}_1^m[X_1], \, \boldsymbol{r}_1^m[X_2] + \boldsymbol{r}_2^m[X_2], \, \boldsymbol{r}_1^m[X_3] + \boldsymbol{r}_2^m[X_3], \right. \\
&\qquad \left. \boldsymbol{r}_1^m[X_{12}], \, \boldsymbol{r}_1^m[X_{23}] + \boldsymbol{r}_2^m[X_{23}], \, \boldsymbol{r}_1^m[X_{13}] \right) \\
&= \left(\boldsymbol{r}^m[X_1], \, \boldsymbol{r}^m[X_2], \, \boldsymbol{r}^m[X_3], \, \boldsymbol{r}^m[X_{12}], \, \boldsymbol{r}^m[X_{23}], \, \boldsymbol{r}^m[X_{13}] \right), \\
\boldsymbol{r}_{2,\mathrm{col}}^m &= \left(\boldsymbol{0}, \, \boldsymbol{r}_2^m[X_4], \, \boldsymbol{0}, \, \boldsymbol{r}_2^m[X_{24}], \, \boldsymbol{r}_2^m[X_{34}], \, \boldsymbol{0} \right) \\
&= \left(\boldsymbol{0}, \, \boldsymbol{r}^m[X_4], \, \boldsymbol{0}, \, \boldsymbol{r}^m[X_{24}], \, \boldsymbol{r}^m[X_{34}], \, \boldsymbol{0} \right).
\end{aligned}
\quad (5.41)
$$

Obviously, this strategy still yields $\boldsymbol{r}^m = \boldsymbol{r}_{1,\mathrm{col}}^m + \boldsymbol{r}_{2,\mathrm{col}}^m$, but the essential advantage of the collected representation is due to the possibility that now the *Euclid*ian norm can be computed in parallel, cf. $(5.29)_1$:

$$||\boldsymbol{r}^m|| = \sqrt{(\boldsymbol{r}^m)^T \, \boldsymbol{r}^m} = \sqrt{(\boldsymbol{r}_{1,\mathrm{col}}^m)^T \, \boldsymbol{r}_{1,\mathrm{col}}^m + (\boldsymbol{r}_{2,\mathrm{col}}^m)^T \, \boldsymbol{r}_{2,\mathrm{col}}^m}. \quad (5.42)$$

If the residual norm does not meet the stopping criterion, the correction vectors have to be computed by applying the preconditioner $\boldsymbol{B}$ to $\boldsymbol{r}^m$ on all master points, cf. (5.30):

$$
\begin{aligned}
\boldsymbol{c}_{1,\mathrm{add}}^m &= \left(\boldsymbol{B}[X_1, X_1] \, \boldsymbol{r}^m[X_1], \, \boldsymbol{B}[X_2, X_2] \, \boldsymbol{r}^m[X_2], \, \boldsymbol{B}[X_3, X_3] \, \boldsymbol{r}^m[X_3], \right. \\
&\qquad \left. \boldsymbol{B}[X_{12}, X_{12}] \, \boldsymbol{r}^m[X_{12}], \, \boldsymbol{B}[X_{23}, X_{23}] \, \boldsymbol{r}^m[X_{23}], \, \boldsymbol{B}[X_{13}, X_{13}] \, \boldsymbol{r}^m[X_{13}] \right), \\
\boldsymbol{c}_{2,\mathrm{add}}^m &= \left(\boldsymbol{0}, \, \boldsymbol{B}[X_4, X_4] \, \boldsymbol{r}^m[X_4], \, \boldsymbol{0}, \, \boldsymbol{B}[X_{24}, X_{24}] \, \boldsymbol{r}^m[X_{24}], \right. \\
&\qquad \left. \boldsymbol{B}[X_{34}, X_{34}] \, \boldsymbol{r}^m[X_{34}], \, \boldsymbol{0} \right).
\end{aligned}
\quad (5.43)
$$

Finally, the correction vectors are transferred into a consistent representation for the

parallel (local) update of the solution vector:

$$
\begin{aligned}
\boldsymbol{c}_1^m \quad &= \quad (\boldsymbol{c}_{1,\mathrm{add}}^m[X_1],\ \boldsymbol{c}_{1,\mathrm{add}}^m[X_2] + \boldsymbol{c}_{2,\mathrm{add}}^m[X_2],\ \boldsymbol{c}_{1,\mathrm{add}}^m[X_3] + \boldsymbol{c}_{2,\mathrm{add}}^m[X_3], \\
&\qquad \boldsymbol{c}_{1,\mathrm{add}}^m[X_{12}],\ \boldsymbol{c}_{1,\mathrm{add}}^m[X_{23}] + \boldsymbol{c}_{2,\mathrm{add}}^m[X_{23}],\ \boldsymbol{c}_{1,\mathrm{add}}^m[X_{13}]), \\[2mm]
\boldsymbol{c}_2^m \quad &= \quad (\boldsymbol{c}_{1,\mathrm{add}}^m[X_2] + \boldsymbol{c}_{2,\mathrm{add}}^m[X_2],\ \boldsymbol{c}_{1,\mathrm{add}}^m[X_4],\ \boldsymbol{c}_{1,\mathrm{add}}^m[X_3] + \boldsymbol{c}_{2,\mathrm{add}}^m[X_3], \qquad (5.44) \\
&\qquad \boldsymbol{c}_{1,\mathrm{add}}^m[X_{24}],\ \boldsymbol{c}_{1,\mathrm{add}}^m[X_{34}],\ \boldsymbol{c}_{1,\mathrm{add}}^m[X_{23}] + \boldsymbol{c}_{2,\mathrm{add}}^m[X_{23}]), \\[2mm]
\rightsquigarrow \Delta\bar{\boldsymbol{u}}_1^{m+1} \quad &= \quad \Delta\bar{\boldsymbol{u}}_1^m + \boldsymbol{c}_1^m, \qquad \Delta\bar{\boldsymbol{u}}_2^{m+1} \ = \ \Delta\bar{\boldsymbol{u}}_2^m + \boldsymbol{c}_2^m.
\end{aligned}
$$

Chapter 6: Numerical examples

In this chapter, three different numerical examples are presented in order to emphasize and clarify single aspects of the theoretical discussions in this thesis. The first example concerns the numerical simulation of a biaxial test with a micropolar material, which consists of two materially incompressible constituents, namely a solid and a fluid phase. With this example, dilatant and contractant shear band developments are going to be illustrated, cf. *Ehlers et al.* [60]. In contrast to this 2-d simulation, the other two examples are 3-dimensional initial boundary-value problems, which are both dealing with typical failure mechanisms of natural slopes, cf. *Ehlers et al.* [62] and *Wieners et al.* [153]. Therein, the modeled soil is assumed to behave as a non-polar material, which consists of the three different constituents soil, water and air. Consequently, the triphasic model, which was discussed in detail in the Chapters 2 and 3, is used for the description of this soil.
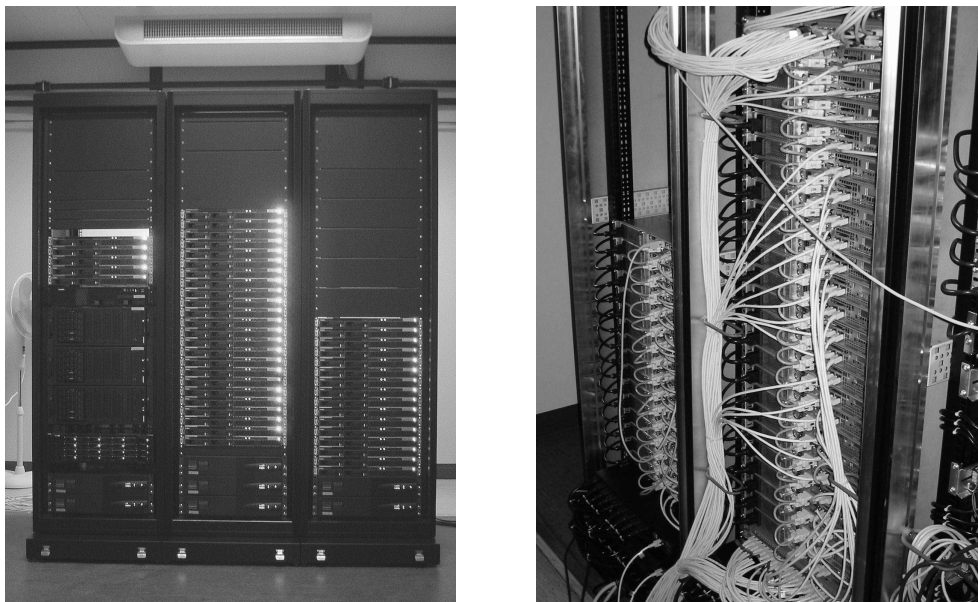

Figure 6.1: Front and back view of the Linux cluster "*Leonardo da Vinci*" of the Institute of Applied Mechanics (Chair 2) at the University of Stuttgart.

As the simulations of the two 3-dimensional boundary-value problems are numerically very expensive, they had to be computed in parallel with the FE code M++/PANDAS, cf. Chapter 5. These parallel computations were carried out on two different Linux clusters, which are located once at the University of Erlangen and second at the University of Stuttgart. The cluster in Erlangen is part of the Institute of Applied Mathematics and consists of 36 Xeon processors (2.2 GHz, 18 dual boards), 18 GB random access memory (500 MB/processor) and one Gigabit network. The second cluster, *Leonardo da Vinci*, is located at the Institute of Applied Mechanics (Chair 2) at the University of Stuttgart, cf. Figure 6.1. This machine consists of altogether 98 Opteron processors (2.2 GHz, 47 dual

boards and 1 quad board), 104 GB random access memory (at least 1 GB/processor) and two Gigabit networks, which share the work coming from the system administration and the data transfer of the parallel computations.

6.1   Biaxial test

In a straightforward extension of *Ehlers et al.* [60], who showed dilatant and contractant shear band developments at the example of non-polar materials, here, these effects are going to be illustrated at the example of a micropolar material, which characterizing material parameters are taken from [64], cf. Table 6.1. The underlying mechanical model is a biphasic model consisting of a materially incompressible, micropolar, elasto-viscoplastic solid skeleton and a materially incompressible, viscous pore-fluid. Due to the fact that such a model was not explicitly discussed in this thesis, all the necessary equations for the numerical realization, which were partly mentioned in Chapter 2 and Section 4.4, are summarized in the following set of equations:

∗ primary variables: solid displacement $\mathbf{u}_S$, pore pressure p and total rotation $\bar{\boldsymbol{\varphi}}_S$.

∗ weak formulations of the balance relations:

$$\int_\Omega (\boldsymbol{\sigma}_E^S - p\mathbf{I}) \cdot \operatorname{grad} \delta\mathbf{u}_S \, \mathrm{d}v - \int_\Omega (n^F \rho^{FR} + n^S \rho^{SR}) \, \mathbf{g} \cdot \delta\mathbf{u}_S \, \mathrm{d}v = \int_{\Gamma_t} \bar{\mathbf{t}} \cdot \delta\mathbf{u}_S \, \mathrm{d}a,$$

$$\int_\Omega [\, (n^F)_S' + n^F \operatorname{div} (\mathbf{u}_S)_S' \,] \, \delta p \, \mathrm{d}v - \int_\Omega n^F \, \mathbf{w}_F \cdot \operatorname{grad} \delta p \, \mathrm{d}v = \int_{\Gamma_v} \bar{v}^F \, \delta p \, \mathrm{d}a, \qquad (6.1)$$

$$\int_\Omega \mathbf{M}^S \cdot \operatorname{grad} \delta\bar{\boldsymbol{\varphi}}_S \, \mathrm{d}v - \int_\Omega (\mathbf{I} \times \boldsymbol{\sigma}_E^S) \cdot \delta\bar{\boldsymbol{\varphi}}_S \, \mathrm{d}v = 0 \,.$$

∗ saturation condition and linearized volume balance of the solid:

$$n^S + n^F = 1 \,, \qquad n^S = n_{0S}^S \, (1 - \operatorname{div} \mathbf{u}_S) \,. \qquad (6.2)$$

∗ kinematic relations for strains and curvatures:

$$\bar{\boldsymbol{\varepsilon}}_S = \operatorname{grad} \mathbf{u}_S + \overset{3}{\mathbf{E}} \, \bar{\boldsymbol{\varphi}}_S \,,$$

$$\bar{\boldsymbol{\kappa}}_S = \frac{1}{2} \, \{ \, \overset{3}{\mathbf{E}} \, [\operatorname{grad} \bar{\boldsymbol{\varepsilon}}_S + (\operatorname{grad} \bar{\boldsymbol{\varepsilon}}_S)^{\overset{13}{T}} - (\operatorname{grad} \bar{\boldsymbol{\varepsilon}}_S)^{\overset{23}{T}} \,] \, \}^{\underline{2}}. \qquad (6.3)$$

∗ additive split of strains and curvatures and micropolar elasticity laws:

$$\bar{\boldsymbol{\varepsilon}}_S = \bar{\boldsymbol{\varepsilon}}_{Se} + \bar{\boldsymbol{\varepsilon}}_{Sp} \,, \qquad\qquad\qquad\qquad \bar{\boldsymbol{\kappa}}_S = \bar{\boldsymbol{\kappa}}_{Se} + \bar{\boldsymbol{\kappa}}_{Sp} \,,$$

$$\boldsymbol{\sigma}_E^S = 2 \, \mu^S \, \bar{\boldsymbol{\varepsilon}}_{Se\,\mathrm{sym}} + 2 \, \mu_c^S \, \bar{\boldsymbol{\varepsilon}}_{Se\,\mathrm{skw}} + \lambda^S \, (\bar{\boldsymbol{\varepsilon}}_{Se\,\mathrm{sym}} \cdot \mathbf{I}) \, \mathbf{I} \,, \quad \mathbf{M}^S = 2 \, \mu_c^S \, (l_c^S)^2 \bar{\boldsymbol{\kappa}}_{Se} \,. \qquad (6.4)$$

Lamé constants	$\mu^S = 5\,583\,\text{kN/m}^2 \,,\; \lambda^S = 8\,375\,\text{kN/m}^2$
effective densities	$\rho^{SR} = 2\,600\,\text{kg/m}^3,\; \rho^{LR} = 1\,000\,\text{kg/m}^3$
solid volume fraction	$n_{0S}^S = 0.67$
effective liquid weight	$\gamma^{FR} = 10\,\text{kN/m}^3$
gravitation	$\mathbf{g} = \mathbf{0}\,\text{m/s}^2$
Darcy permeability coefficient	$k_{0S}^F = 10^{-7}\,\text{m/s}$
yield criterion	$\alpha = 1.074\,0 \cdot 10^{-2},\; \beta = 0.119\,6,\; \gamma = 1.555$
	$\delta = 1.377 \cdot 10^{-4}\,\text{m}^2/\text{kN}\,,\; \epsilon = 4.330 \cdot 10^{-6}\,\text{m}^2/\text{kN}$
	$\kappa = 10.27\,\text{kN/m}^2,\; m = 0.593\,5$
plastic potential	$\psi_1 = 1.33,\; \psi_2 = 0.107$
viscoplasticity	$\eta = 100\,\text{s},\; \sigma_0 = 10.27\,\text{kN/m}^2,\; r = 1$
Cosserat parameters	$l_c^S = 10^{-3}\,\text{m},\; \mu_c^S = 4 \cdot 10^3\,\text{kN/m}^2$
	$k_\sigma = 0,\; k_M = 12$

Table 6.1: Biaxial test: material parameters [64].

∗ evolution equations for plastic strains and plastic curvatures:

$$
\begin{aligned}
(\bar{\boldsymbol{\varepsilon}}_{Sp})'_S &= \frac{1}{\eta} \left\langle \frac{\bar{F}(\boldsymbol{\sigma}_E^S)}{\sigma_0} \right\rangle^r \frac{\partial \bar{G}}{\partial \boldsymbol{\sigma}_E^S}\,, \\
(\bar{\boldsymbol{\kappa}}_{Sp})'_S &= \frac{1}{2}\,\{\, \overset{3}{\mathbf{E}}\, [\, \text{grad}\,(\bar{\boldsymbol{\varepsilon}}_{Sp})'_S + (\text{grad}\,(\bar{\boldsymbol{\varepsilon}}_{Sp})'_S)^{\overset{13}{T}} - (\text{grad}\,(\bar{\boldsymbol{\varepsilon}}_{Sp})'_S)^{\overset{23}{T}}\,]\,\}^{\underline{2}}.
\end{aligned}
\tag{6.5}
$$

∗ micropolar yield function and micropolar plastic potential:

$$
\begin{aligned}
\bar{F} &= \bar{\Phi}^{1/2} + \beta\,\text{I} + \epsilon\,\text{I}^2 + \tfrac{1}{2}\,k_M\,(\mathbf{M}^S \cdot \mathbf{M}^S)^{1/2} - \kappa = 0\,, \\
\bar{\Phi} &= \mathbb{II}^D_{\text{sym}}(1 + \gamma\,\vartheta)^m + k_\sigma\,\mathbb{II}_{\text{skw}} + \tfrac{1}{2}\,\alpha\,\text{I}^2 + \delta^2\,\text{I}^4\,, \\
\bar{G} &= \bar{\Gamma}^{1/2} + \psi_2\,\text{I} + \epsilon\,\text{I}^2\,, \\
\bar{\Gamma} &= \psi_1\,\mathbb{II}^D_{\text{sym}} + k_\sigma\,\mathbb{II}_{\text{skw}} + \tfrac{1}{2}\,\alpha\,\text{I}^2 + \delta^2\,\text{I}^4\,.
\end{aligned}
\tag{6.6}
$$

∗ *Darcy* equation:

$$
n^F\,\mathbf{w}_F = -\frac{k_{0S}^F}{\gamma^{FR}}\,(\text{grad}\,p - \rho^{FR}\,\mathbf{g})\,.
\tag{6.7}
$$

Therein, the definitions of the different invariants in (6.6) are given in Appendix A.2.2.

The initial boundary-value problem describing the numerical simulation of the biaxial test is a 2-d simulation, in which plane strain conditions are prescribed, cf. Figure 6.2. In particular, a fluid-saturated, micropolar and porous material is considered, where during the time period $0 \leq t \leq \tau$ a linearly increasing horizontal stress σ_1 is applied, which is kept constant for $t \geq \tau$. After the consolidation process is finished, which is resulting from
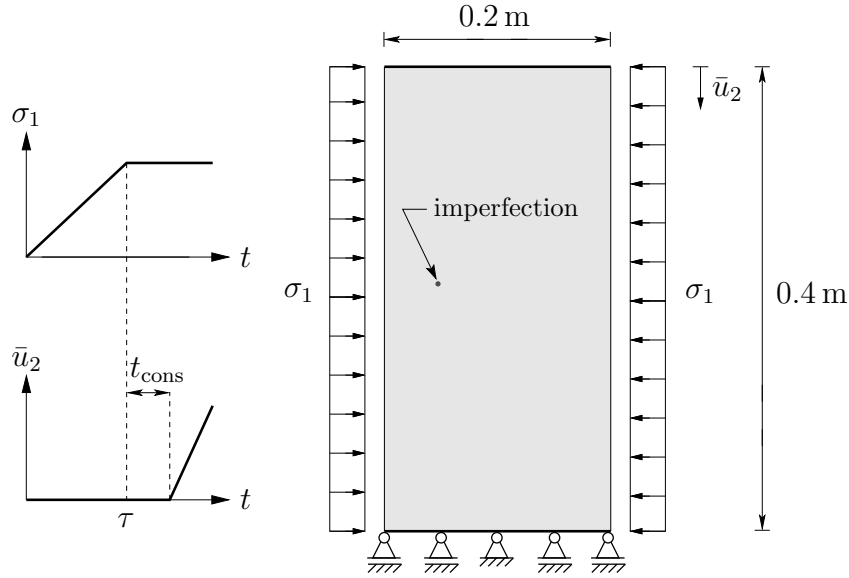
Figure 6.2: Biaxial test: initial boundary-value problem.

the increase of σ_1, the specimen is loaded with a displacement driven vertical stress such that $\bar{u}_2 = (\bar{u}_2)'_S [t - (\tau + t_{\text{cons}})]$. While the top and bottom boundaries of the specimen are impermeable, the side boundaries are assumed to be ideally permeable. Furthermore, the rotation is set to zero at only one FE node at the bottom of the sample, at which, additionally, the horizontal displacement is prevented, cf. Figure 6.2. From the numerical point of view, the prescribed initial boundary-value problem characterizes a homogeneous problem. In order to obtain a shear band localization, an imperfection is included in the sample, cf. Figure 6.2, by a weakening of the *Lamé* constants μ^S and λ^S.

The application of two different lateral loads, namely $\sigma_1 = 110\,\text{kN/m}^2$ and $\sigma_1 = 140\,\text{kN/m}^2$, leads to the development of both dilatant and contractant shear bands. The reason for the onset of the different types of shear bands stems from the fact that, when viscoplastic yielding occurs, the lower lateral load leads to a yield point in the brittle regime, whereas the higher lateral load produces a yield point in the ductile regime, cf. the remark on Page 29. Furthermore, the onset of the weakening material behavior is much earlier in the calculation with the lower lateral load, cf. Figure 6.3.

Both calculations are carried out on a FE mesh with 2 048 quadrilateral elements, in which the displacement $\mathbf{u}_S$ is discretized by quadratic ansatz functions and both the pore-fluid pressure p and the total rotations $\bar{\boldsymbol{\varphi}}_S$ are discretized by linear ansatz functions. This choice leads to altogether 16 964 degrees of freedom for each simulation. Comparing the deformed FE meshes, cf. Figure 6.4, and the accumulated plastic strains, cf. Figures 6.5 and 6.6, it is furthermore seen that the final vertical displacement of $\bar{u}_2 = 6.6\,\text{mm}$ yields comparable shear band developments for the different lateral loads. However, as a result of dilatancy, the maximum value of the accumulated plastic strains is approximately 50 per cent higher in the dilatant case than in the contractant one. The reason for this fact mainly results from the incompressibility constraint of the pore-fluid. To explain this behavior in more detail, one has to take a closer look at the different pore-fluids pressures
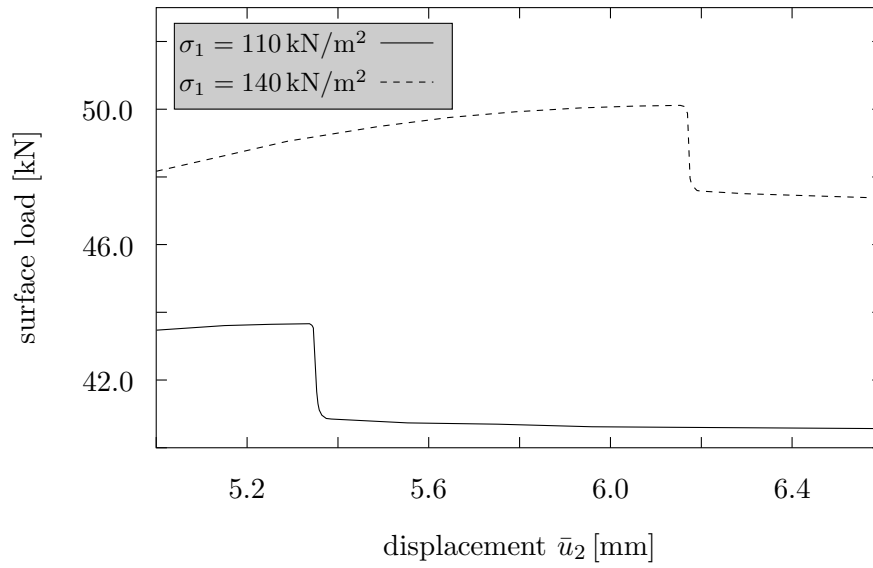
Figure 6.3: Biaxial test: load-deflection curves.

and seepage velocity developments shown in the Figures 6.5 and 6.6. In the case with the higher lateral load, a high pore-fluid pressure is obtained and, as a result of contractancy, the pore-fluid is pressed out of the shear band, whereas, in the case with the lower lateral load, these effects are vice versa, i. e., a seepage flow into the shear band is obtained due to the negative pore-fluid pressure.

Furthermore, proceeding from the porosity of the specimen directly after the lateral load is applied, the final porosity developments in the shearing zones exhibit either an increase or a decrease. These effects are also corresponding to the developments of either dilatant or contractant shear bands, respectively.
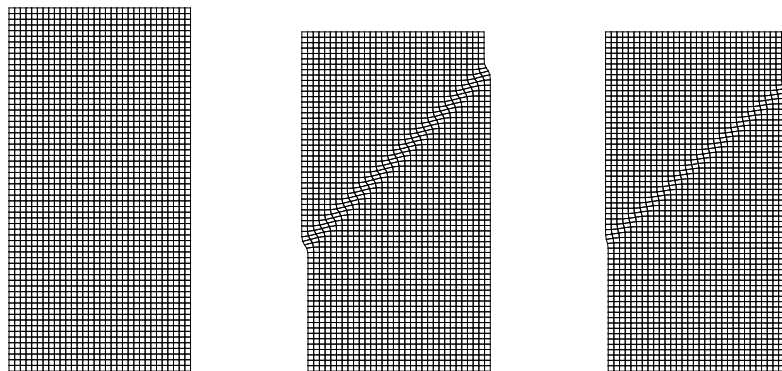
Figure 6.4: Biaxial test: undeformed (left) and deformed FE meshes for $\sigma_1 = 110\,\text{kN/m}^2$ (middle) and $\sigma_1 = 140\,\text{kN/m}^2$ (right), deformation scaled four times.
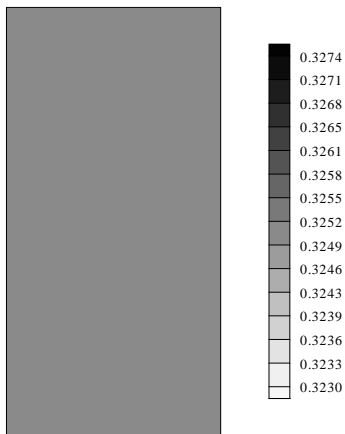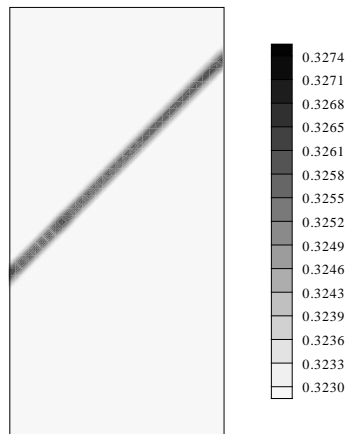
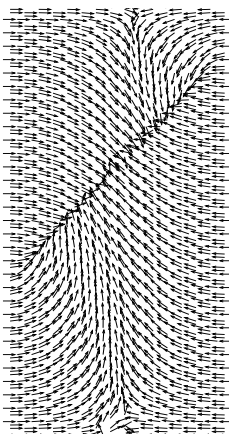accum. plastic strains
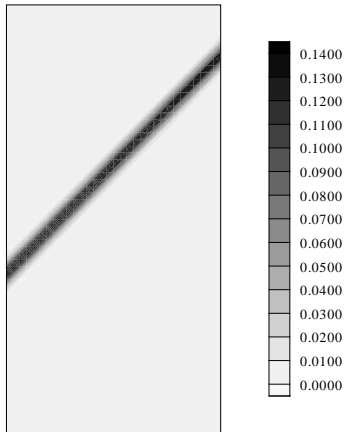
total rotations

inital porosity

final porosity

seepage velocity

pore-fluid pressure

PSfrag replacements
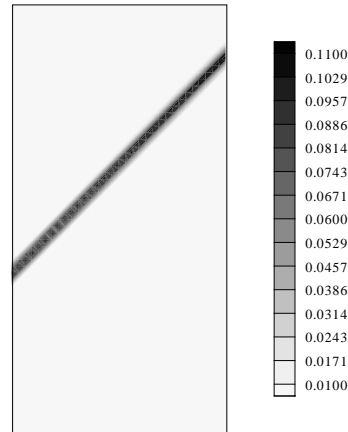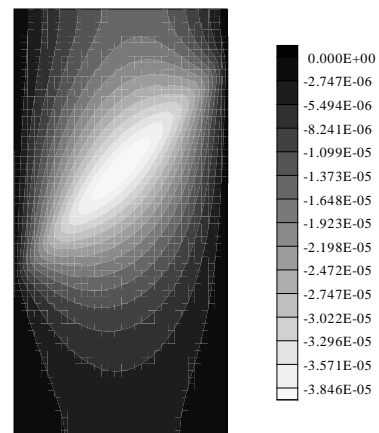
Figure 6.5: Biaxial test: dilatant shear band development ($\sigma_1 = 110\,\text{kN/m}^2$).

accum. plastic strains

total rotations

inital porosity

final porosity

seepage velocity

pore-fluid pressure
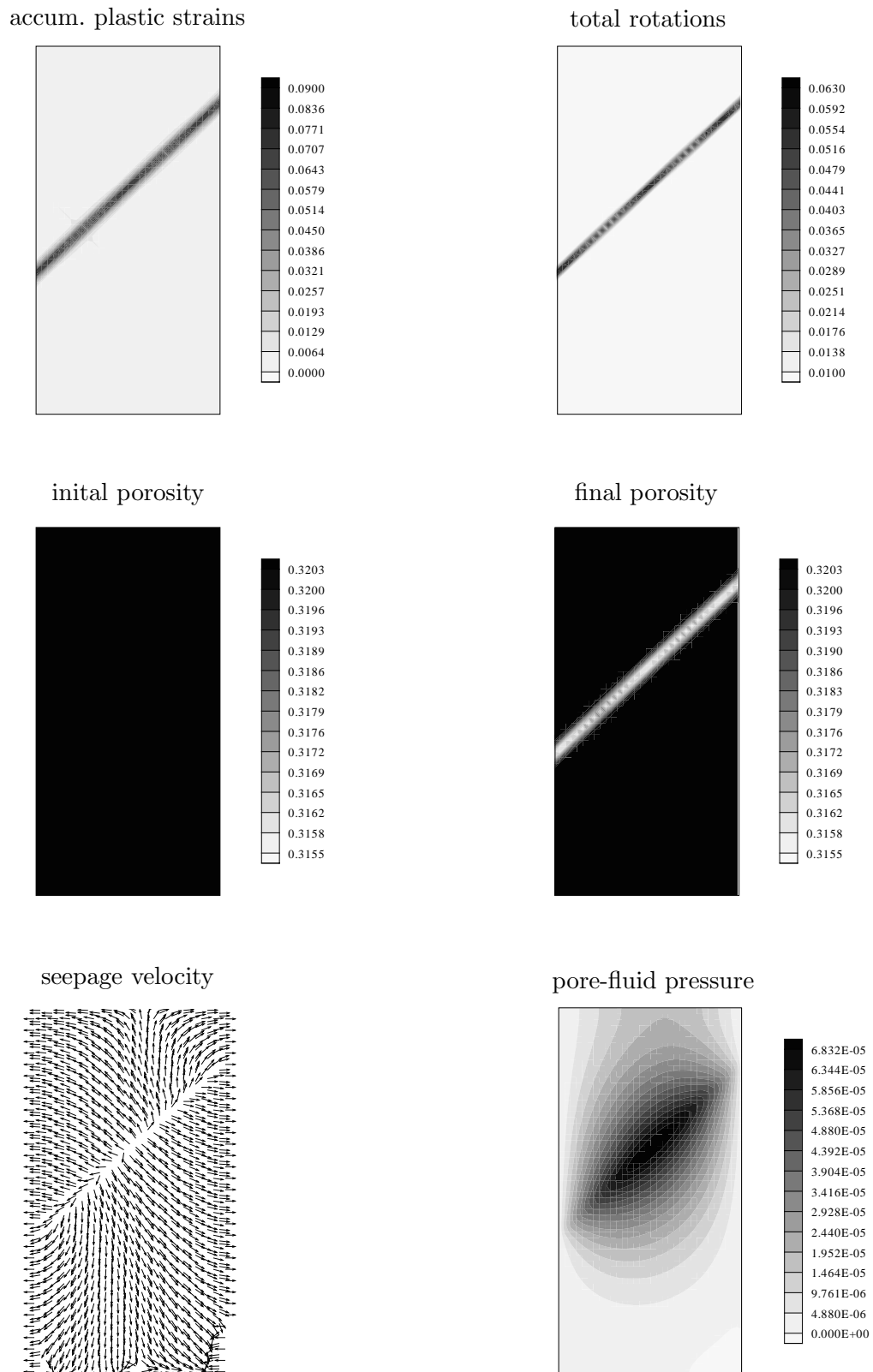
PSfrag replacements

Figure 6.6: Biaxial test: contractant shear band development ($\sigma_1 = 140 \, \mathrm{kN/m^2}$).

6.2   Excavation problem

This example concerns a standard excavation problem carried out at a natural slope shown in Figure 6.7. Therein, the top figure describes the total geometrical situation after the excavation process has been realized and the bottom figure shows a perspective image of half of the problem. Note that due to the symmetry of the configuration, it is sufficient to consider only half of the geometry in the numerical computations. In this example, the modeled soil is assumed to behave like a clayey silt. The characterizing material parameters are given in accordance to [62] in Table 6.2. Note that in contrast to [62], the value for the intrinsic permeability K_{0S}^S was chosen to $10^{-9}\,\mathrm{m}^2$, which is a very large value for realistic soils. This is due to the fact that the current version of the parallel iterative solver is very sensible with respect to small values of K_{0S}^S [153]. This motivates further development on the parallel preconditioner to achieve more robustness. Nevertheless, the obtained results from the parallel simulations show a similar behavior concerning the failure mechanism of the considered slope in comparison with the results of [62].
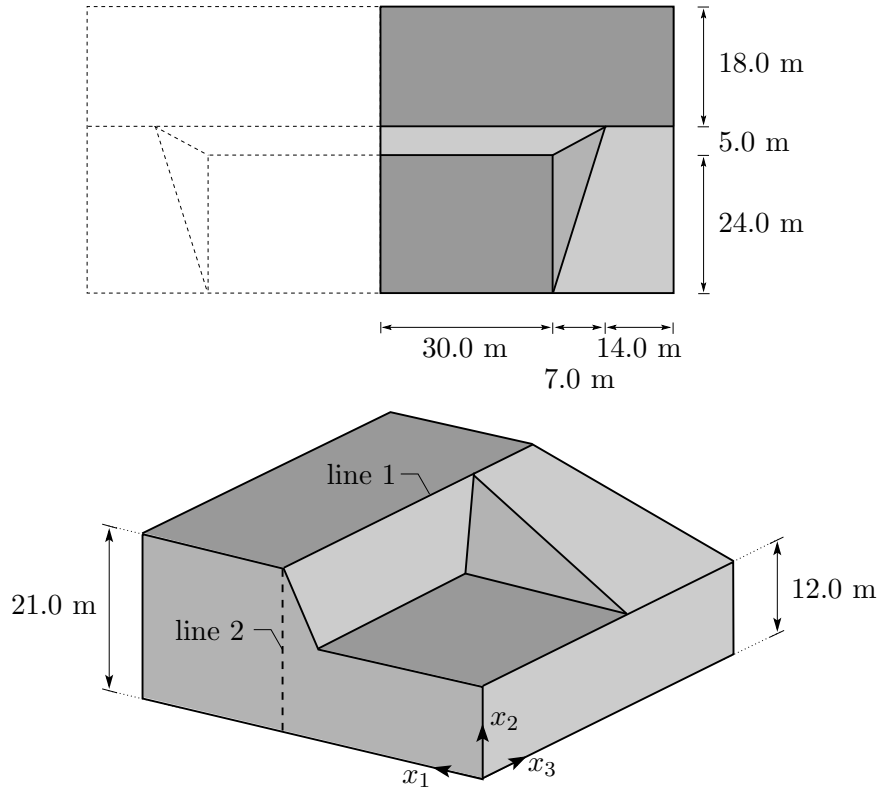
Figure 6.7: Excavation problem: sketch of the whole slope (top) and perspective view on half of the excavated slope (bottom).

As was shown by *Ehlers et al.* [62], it can be observed that the slope under study results in a stable configuration under gravitational load as long as the ground-water table is so low that the pore-liquid does not leak at the slope, cf. Figure 6.8. If this situation is changed by an increase of the ground-water table, cf. Figure 6.9 (top), the failure of the slope is

Lamé constants	$\mu^S = 5\,583\,\text{kN/m}^2$, $\lambda^S = 8\,375\,\text{kN/m}^2$
effective densities	$\rho^{SR} = 2\,720\,\text{kg/m}^3$, $\rho^{LR} = 1\,000\,\text{kg/m}^3$
gas phase	$\bar{R}^G = 287.17\,\text{J/(kg\,K)}$, $\theta = 283\,\text{K}$, $p_0 = 10^5\,\text{N/m}^2$
solid volume fraction	$n_{0S}^S = 0.54$
gravitation	$g = 9.81\,\text{m/s}^2$
fluid viscosities	$\mu^{LR} = 10^{-3}\,\text{N\,s/m}^2$, $\mu^{GR} = 1.8 \cdot 10^{-5}\,\text{N\,s/m}^2$
intrinsic permeability	$K_{0S}^S = 10^{-9}\,\text{m}^2$, $\pi = 1.0$
van Genuchten model	$\alpha_{gen} = 2 \cdot 10^{-4}$, $h_{gen} = 1.5$
	$j_{gen} = 2.3$, $\epsilon_{gen} = 0.5$, $\gamma_{gen} = 0.333$
residual saturations	$s_{res}^L = 0.1$, $s_{res}^G = 0.1$
yield criterion	$\alpha = 1.074\,0 \cdot 10^{-2}$, $\beta = 0.119\,6$, $\gamma = 1.555$
	$\delta = 1.377 \cdot 10^{-4}\,\text{m}^2/\text{kN}$, $\epsilon = 4.330 \cdot 10^{-6}\,\text{m}^2/\text{kN}$
	$\kappa = 10.27\,\text{kN/m}^2$, $m = 0.593\,5$
plastic potential	$\psi_1 = 1.33$, $\psi_2 = 0.107$
viscoplasticity	$\eta = 500\,\text{s}$, $\sigma_0 = 10.27\,\text{kN/m}^2$, $r = 1$

Table 6.2: Material parameters of the modeled soil [62].

initiated, thus leading to a development of a shearing domain with a certain thickness, cf. Figure 6.9 (bottom).

Furthermore, the stream lines presented in Figure 6.10 show clearly that the pore-liquid leaks at the surface of the slope. Note that this fact is important for a realistic modeling of the underlying problem, as the leaking of the pore-liquid prevents the development of a positive pressure (excess pressure) for p^{LR} at the boundary surface of the slope, which would lead to unrealistic results. The leaking of the pore-fluid is realized within the calculation by a flexible setting of the *Dirichlet* boundary conditions $\bar{p}^{LR}$, i. e., if the capillary pressure p^C falls below a critical value at a certain node on the boundary surface due to an increase of the liquid saturation s^L, cf. Figure 2.5 (right) on Page 30, the value of p^{LR} at this node is set to the ambient pressure. At the beginning of the calculation, the values of p^{LR} are not specified at the boundary surface of the slope, in order to prevent a predefined distribution of the liquid saturation $s^L = s^L (p^{LR}, p^{GR})$ on this boundary surface. Such a predefined distribution would occur within the used triphasic model, as *Dirichlet* boundary conditions are already set at the boundary surface of the slope for the effective gas pressure, where p^{GR} is set to the ambient gas pressure.

6.2.1 Convergence behavior and computational expense

For a proper discussion of the convergence behavior of the underlying spatial discretization, the described boundary-value problem was calculated by *Wieners et al.* [153] on four different FE meshes, where the coarsest mesh, cf. Figure 6.11 (left), contains 964 tetrahedra. Starting from this mesh (refinement level 0), three uniform refinements result
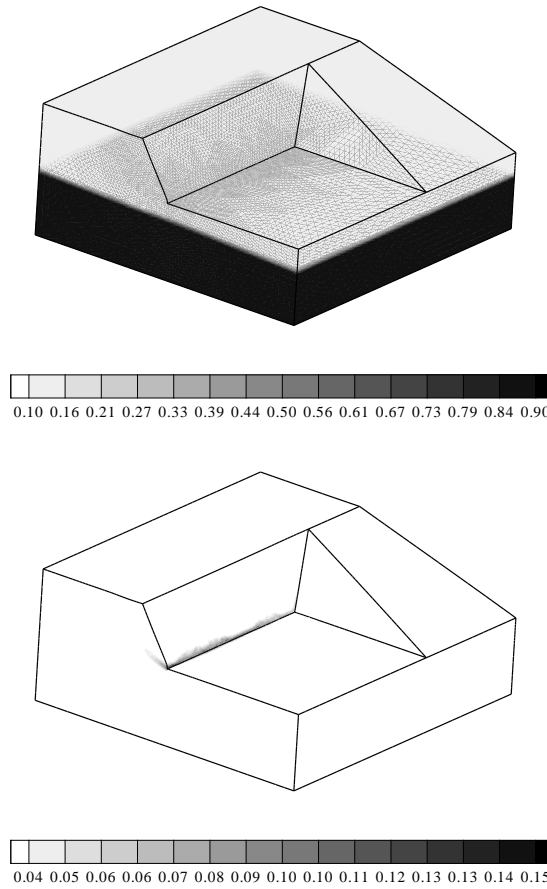
Figure 6.8: Excavation problem with uncritical ground-water table: liquid saturation s^L [-] (top) and accumulated plastic strains ε_{pv} [-] (bottom) after the excavation process (deformation scaled 3 times).

into the finest spatial discretization (refinement level 3) with altogether 493 568 cells, cf. Figure 6.11 (right).

Using *Taylor-Hood* elements with quadratic ansatz functions for the displacement $\mathbf{u}_S$ and linear ansatz functions for the pressure terms p^{LR} and p^{GR}, cf. Figure 3.3 on Page 41, the convergence behavior depicted in Figure 6.12 is obtained. Thereby, the development of the displacements u_1 and u_2 along line 1 ($x_1 = 29\,\text{m}$, $x_2 = 21\,\text{m}$; cf. Figure 6.7) and the liquid saturation s^L along line 2 ($x_1 = 29\,\text{m}$, $x_3 = 0\,\text{m}$; cf. Figure 6.7) are shown exemplarily for the four different meshes. In these three figures, an excellent convergence behavior can be identified for the regularly refined FE meshes.

Note that the number of cells increases by the factor 8 with every uniform refinement step, i. e., each tetrahedron is subdivided into 8 tetrahedra per refinement, cf. Table 6.3. Furthermore, for a stable numerical integration, a quadrature formula of fifth order has to be used [137], which leads to 15 integration points per element, and, thus, to a huge number of internal variables.
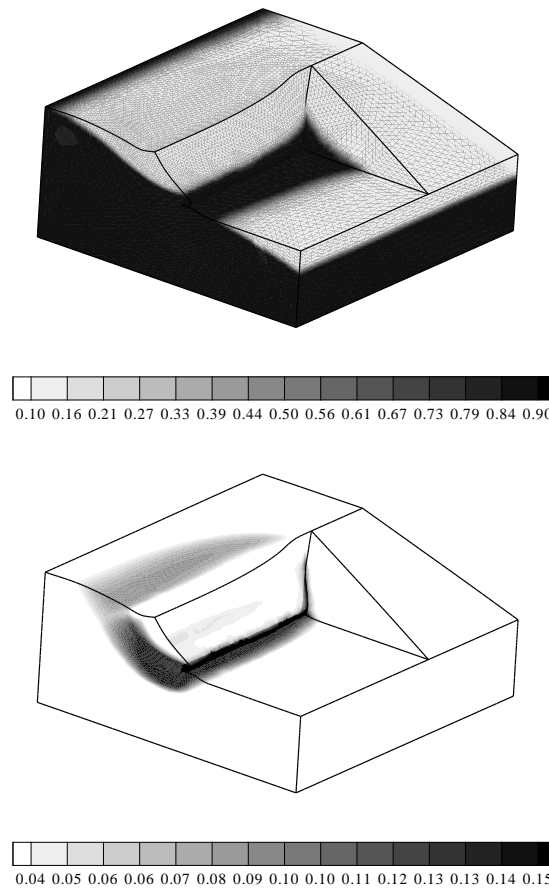
Figure 6.9: Excavation problem with increased ground-water table: liquid saturation s^L [-] (top) and accumulated plastic strains ε_{pv} [-] (bottom) after the excavation process (deformation scaled 3 times).

Figure 6.10: Excavation problem: stream lines of the pore-liquid flow starting from 3 different lines at $x_3 = 1\,\mathrm{m}$, $x_3 = 36\,\mathrm{m}$ and $x_3 = 49\,\mathrm{m}$.

In order to be able to compare the computing times of the different FE meshes, all calculations were carried out on 14 processors of the Linux cluster in Stuttgart. Note that
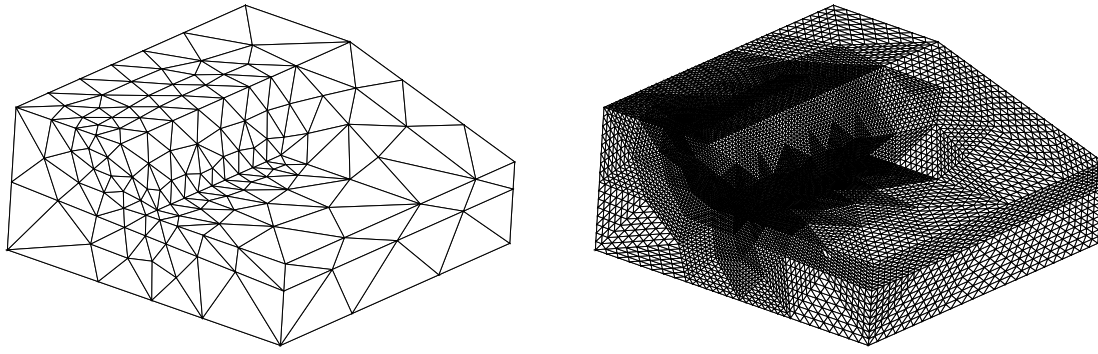
Figure 6.11: Excavation problem: initial finite element mesh (left) and final mesh after three uniform refinement steps (right).

this choice for the number of processors is a compromise between the calculations on the coarsest and the finest FE meshes with rega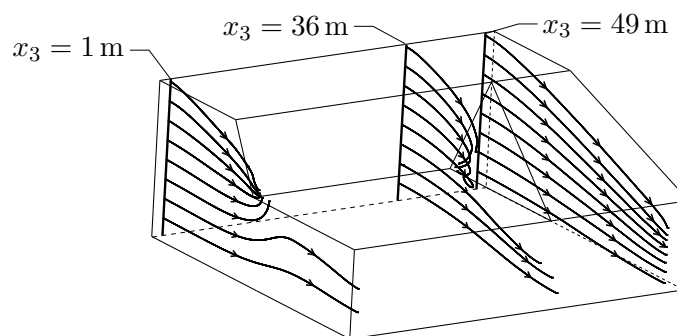rd to the computing time. For example, the computing time of the calculation on the FE mesh with $493\,568$ cells (refinement level 3) can be reduced significantly by choosing more processors, e. g., a parallel calculation with 24 processors on this cluster results in a computing time of approximately 34 hours. In Table 6.3, it can be observed that the computing times for all calculations give reasonable

Figure 6.12: Excavation problem: convergence behavior; displacement u_1 [m] and u_2 [m] plotted along line 1 (top) and liquid saturation s^L [-] plotted along line 2 (bottom).

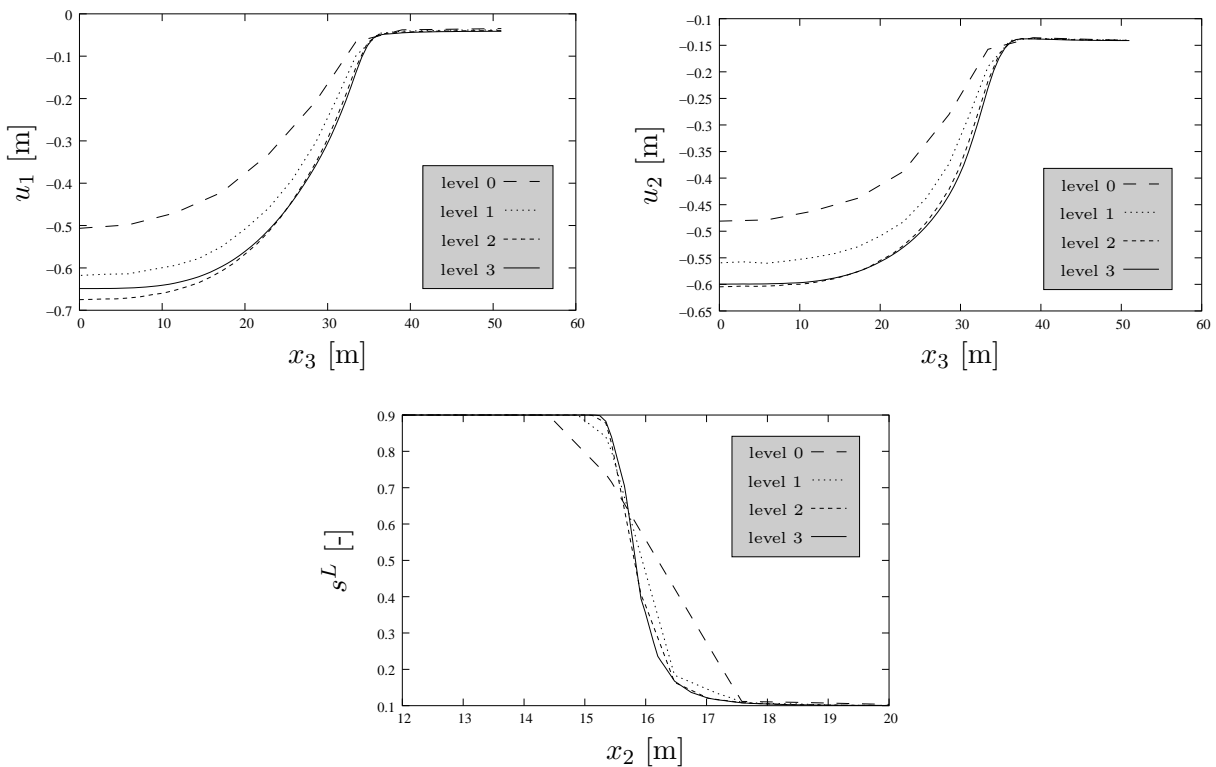|	cells	DOFs	integration points	time [h]	E_K [%]
level 0	964	5 436	14 460	00:04:56	100
level 1	7 712	38 185	115 680	00:37:06	103
level 2	61 696	285 893	925 440	05:56:22	89
level 3	493 568	2 211 941	7 403 520	46:54:11	90

Table 6.3: Excavation problem: computational expense for the full simulation of 280 times steps on different refinement levels.

results concerning the increase of complexity between the single refinement levels. For example, there is a factor of 7.9 in the computing time from level 2 to 3, which is approximately equal to the increase of the number of the cells and which is slightly greater than the increase of the degrees of freedom (DOFs). Nevertheless, looking at the quantity E_K, one can recognize that the efficiency for the calculation on the FE mesh with the refinement level 1 gives an unrealistic value, which is greater than 100 %. This fact indicates that there exists some parallel overhead for less than 40 000 degrees of freedom for calculations of this boundary-value problem on the chosen number of processors.

refinement level	0	1	2	3
Newton iterations (avg.)	2.4	2.8	3.2	3.4
computing time [s] (avg.)	0.8	6.7	70.7	570.7

Table 6.4: Excavation problem: average number of *Newton* iterations per time increment and average computing time for one implicit *Euler* step on different meshes.

For simplicity of the comparison of the results, a common time series was fixed for all refinement levels. In *Wieners et al.* [153], the time steps were chosen in such a way that the simulation on the finest mesh gave a significant increase of average computing time for one implicit *Euler* step, which was associated with the increase in the average number of *Newton* steps and in the average number of iterations within the GMRES method for the solution of one linear problem. Based on these experiences, in this thesis, smaller time steps were chosen such that a moderate increase of computing time is obtained for the simulation on the FE mesh with refinement level 3, cf. Table 6.4. Furthermore, by this choice for the time steps, the average computing time for the solution of one linear

refinement level	0	1	2	3
GMRES iterations (avg.)	25.3	41.8	76.9	149.7
computing time [s] (avg.)	0.2	1.6	15.7	118.2
number of linear problems	695	825	926	985

Table 6.5: Excavation problem: performance of the GMRES solver (average number of iterations per *Newton* step, average computing time for the solution of one linear problem and total number of linear problems for the full simulation of 280 time steps).

problem with the GMRES method reflects the increase of complexity between the single refinement levels quite good, cf. Table 6.5.

### 6.2.2　Influence of the viscoplastic regularization

According to Table 6.2, the material parameters of the modeled soil include a value of $\eta = 500\,\mathrm{s}$ for the viscosity. Changing this value for a parameter study of η, the influence of the viscoplastic regularization technique on the result of the FE simulation of the excavation problem can be illustrated. Therefore, a rather fine FE mesh with $495\,632$ cells leading to altogether $2\,204\,733$ degrees of freedom is generated, which has a comparable complexity to the level 3 mesh of the last section, cf. Figure 6.11 (right). In contrast to the level 3 mesh, the experiences due to the obtained results concerning the failure of the slope, cf. Figure 6.9 (bottom), are used for the generation of this FE mesh. Consequently, a rather fine spatial discretization is chosen for the area, in which a failure of the slope is expected, cf. Figure 6.13 (a).

The results in Figure 6.13 (b)–(f) show the accumulated plastic strains for 5 different values of η, namely $\eta = 500\,\mathrm{s}, 400\,\mathrm{s}, 300\,\mathrm{s}, 200\,\mathrm{s}, 100\,\mathrm{s}$. Interestingly enough, these calculations were not carried out with the increased but with the "uncritical" ground-water table shown in Figure 6.8 (top). From the obtained results, it becomes evident that the value of η has a big influence on the failure behavior of slope under study. As the slope results in a stable configuration for the results shown in Figure 6.13 (b) and (c), any further decrease of the value of η leads to an increase of plastic strains and, thus, to a beginning failure of the slope for the simulation with the smallest value of η. The reason for this behavior is obvious. The decreasing values of the viscosity lead to a decrease of the corresponding overstresses coming along with the viscoplastic regularization method. Thus, yielding occurs for smaller values of the stresses and, furthermore, the developing shear band is limited to a narrower zone in comparison to the simulation with the increased ground-water table, cf. Figure 6.9 (bottom).

The simulations described above were each carried out on 30 processors of the Linux cluster in Stuttgart, where approximately 15 GB memory was used for each computation. Note that the calculation of 250 time steps for the simulation with $\eta = 100\,\mathrm{s}$ took only approximately 20 hours. This fact clearly shows the capability of the interface M++/PANDAS. By using this tool, a flexible testing of large scale initial boundary-value problems can be carried out in a moderate computing time.

6.3　Slope failure problem

In the second parallel simulation, a slope failure problem is discussed, which is caused by an extreme rainfall event [153]. Therein, the slope under study is assumed to consist of three different soil strata, cf. Figure 6.14. The soil stratum at the bottom of the model (stratum 3) should behave purely elastic, whereas the other two strata can show plastic material behavior, if the elastic range of the soil is exceeded. Furthermore, the small soil stratum in the middle (stratum 2) obtains an intrinsic permeability coefficient K_{0S}^{S},
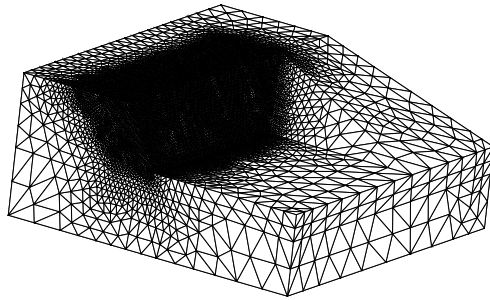
(a) FE mesh with 495 632 cells
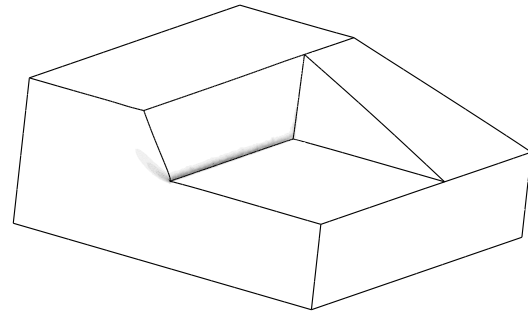
(b) $\eta = 500\,\mathrm{s}$
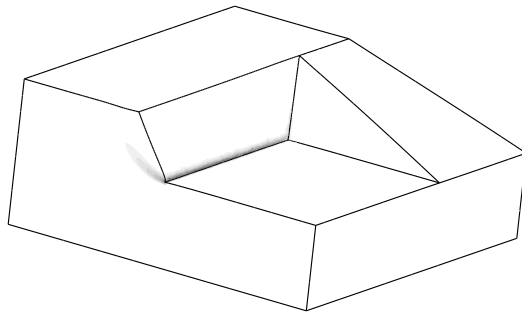
(c) $\eta = 400\,\mathrm{s}$
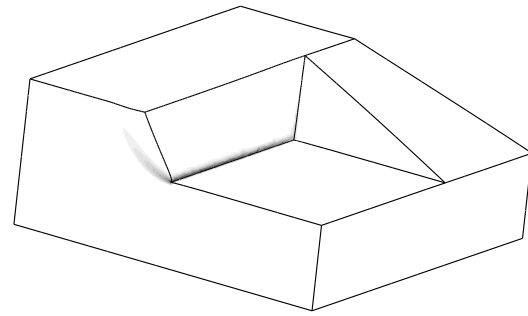
(d) $\eta = 300\,\mathrm{s}$
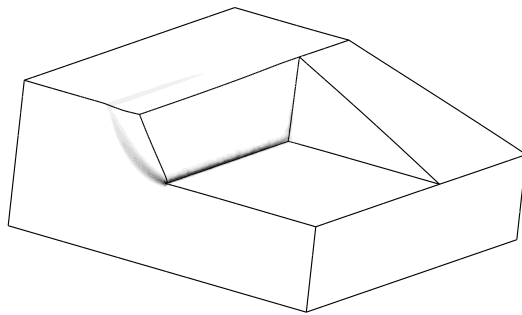
(e) $\eta = 200\,\mathrm{s}$
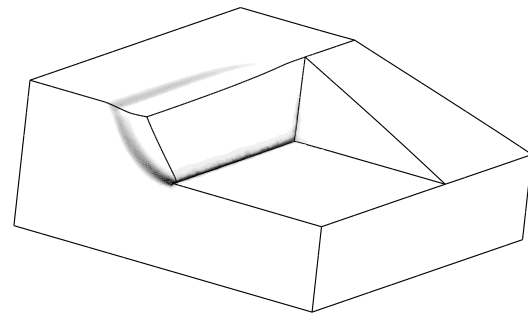
(f) $\eta = 100\,\mathrm{s}$

Figure 6.13: Excavation problem: 5 calculations on a FE mesh with 495 632 cells (a); accumulated plastic strains ε_{pv} [-] for different values of η (b)–(f) (scaled 5 times).

Figure 6.14: Slope failure: perspective view (top) and side view (bottom) on the slope.

which is lower by the factor 1000 than the intrinsic permeability coefficient of the other two soil strata, cf. Table 6.2. Therefore, pore-liquid within the partially saturated soil is prevented from streaming through this "impermeable" stratum.

The slope under study is in a stable situation before the rainfall starts with an infiltration rate (negative efflux) of $\bar{v}^L = -10^{-5}\,\mathrm{m}^3/(\mathrm{m}^2\,\mathrm{s})$ corresponding to $36\,\mathrm{l}/(\mathrm{m}^2\,\mathrm{h})$. In this example, the heavy rainfall event is assumed to last for 2.5 hours, which gives altogether 90 mm rainfall. Due to this heavy rainfall, pore-liquid is accumulated at the top of the impermeable soil stratum, cf. Figures 6.15 and 6.16 (top). Thus, as a result of buoyancy, failure of this part of the slope is initiated, whereas the backward part of the slope remains in its initial stable state, cf. Figures 6.15 and 6.16 (bottom).

6.3.1 Convergence behavior and computational expense

The calculation of this problem is again carried out on four different, uniformly refined FE meshes, where the initial mesh (level 0) and the finest mesh (level 3) are shown in Figure 6.17. Note that it is essential for obtaining reasonable results, that already the initial (coarse) mesh has a sufficient mesh resolution near the impermeable stratum.

Like in the previous example, the convergence behavior of the spatial discretization shows

very good results. In order to illustrate this statement, in Figure 6.18, the distribution of the effective liquid pressure p^L is plotted along line 1 ($x_1 = 21.68$ m, $x_2 = 14.26$ m; cf. Figure 6.14) and the development of the displacement u_1 and the accumulated plastic strains ε_{pv} are plotted along line 2 ($x_1 = 22$ m, $x_2 = 9$ m; cf. Figure 6.14).

	cells	DOFs	integration points	time [h]	E_K [%]
level 0	1 000	5 339	15 000	00:16:11	100
level 1	8 000	38 381	120 000	03:55:02	55
level 2	64 000	291 589	960 000	56:50:30	30
level 3	512 000	2 274 501	7 680 000	633:08:52	22

Table 6.6: Slope failure: computational expense for the full simulation of 800 times steps on different refinement levels.

For a reasonable comparison of the computing times of the four different calculations, all computations were carried out on 24 processors of the Linux cluster in Erlangen. In Table 6.6, the number of cells and integration points, the degrees of freedom, the total
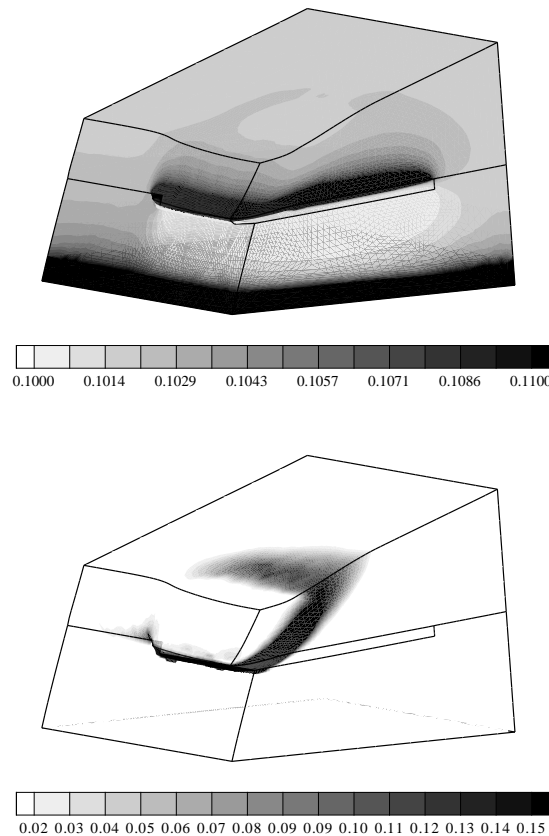

Figure 6.15: Slope failure: liquid saturation s^L [-] (top) and accumulated plastic strains ε_{pv} [-] (bottom) due to a heavy rainfall (scaled 3 times).
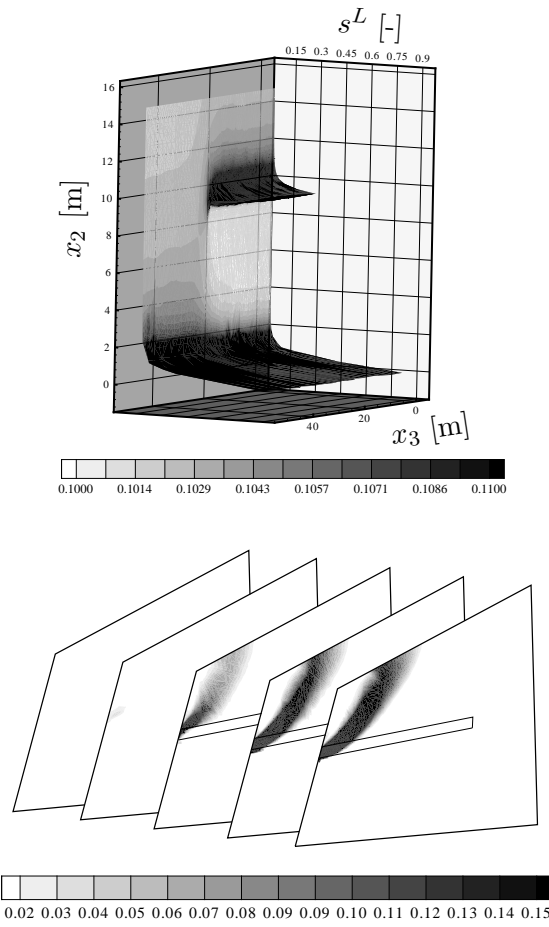
Figure 6.16: Slope failure: distribution of the pore-liquid saturation s^L [-] (top) and development of the accumulated plastic strains ε_{pv} [-] (bottom) in the cutting planes shown in Fig. 6.14 (top).
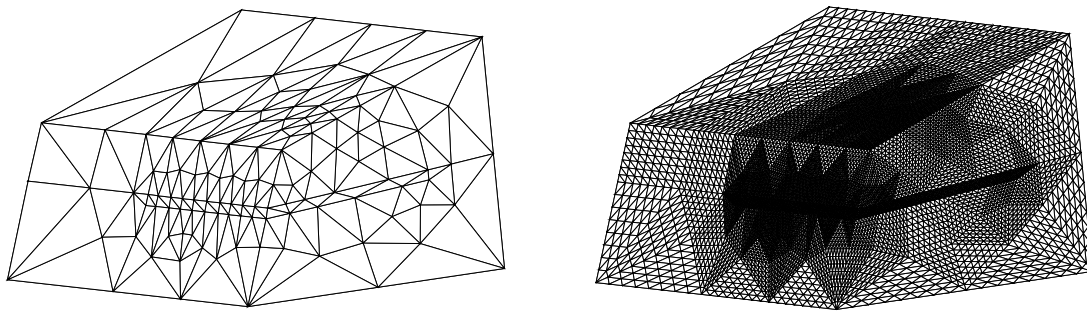

Figure 6.17: Slope failure: initial finite element mesh (left) and final mesh after three uniform refinement steps (right).

computing time and the efficiency E_K for the four FE meshes are shown. Therein, it can be observed that the four FE meshes result in similar problem sizes like in the convergence
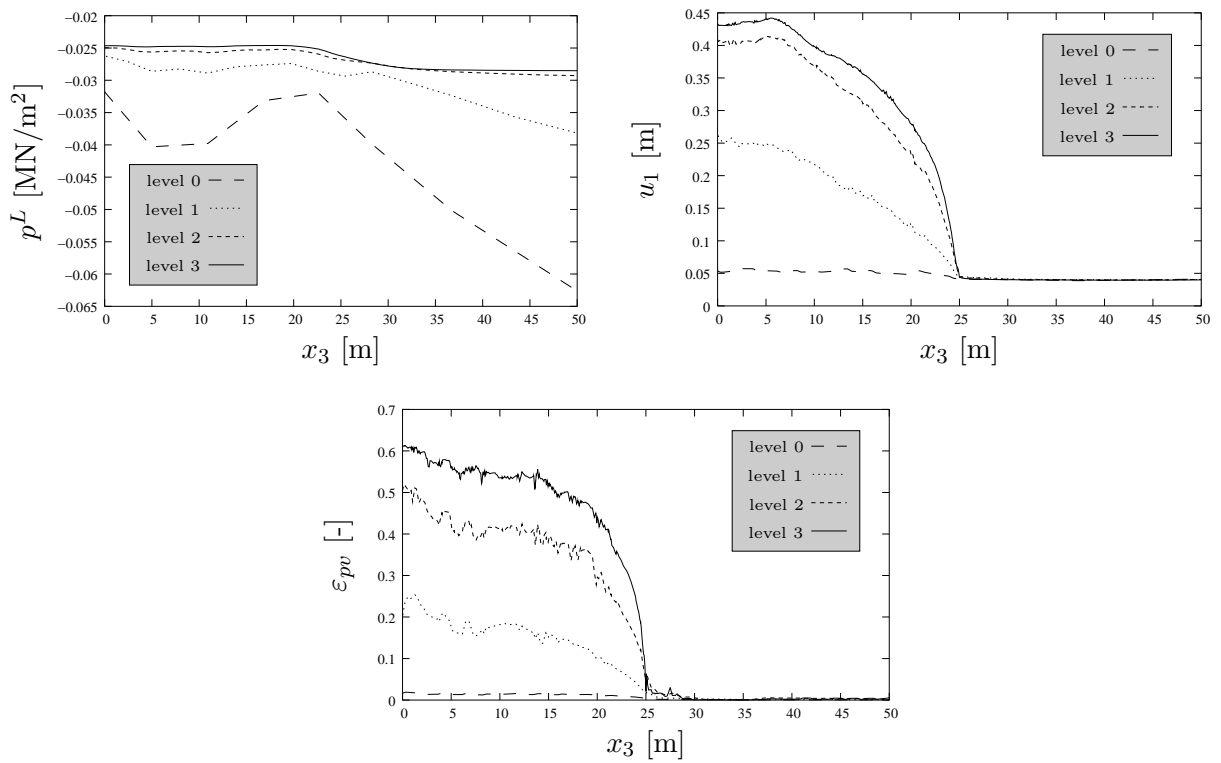
Figure 6.18: Slope failure: convergence behavior; effective liquid pressure p^L [MN/m^2] plotted along line 1 and displacement u_1 [m] and accumulated plastic strains ε_{pv} [-] plotted along line 2.

studies for the excavation problem, cf. Section 6.2.1. Furthermore, one recognizes that the increase of computing time between the different levels is almost constant for the first three levels, i. e., there is approximately a factor of 14.5 between the computing times of the levels 0 and 1 and the levels 1 and 2. Although the total computing time of about 27.5 days for the solution on the finest mesh is rather long, the increase of computing time with respect to the calculation on the level 2 mesh is only around 11.1, which is smaller than for the coarser meshes. The quantity E_K reflects also this good behavior of the level 3 computation, as the decrease of only 8 % efficiency from the level 2 to the level 3 computation is rather small.

refinement level	0	1	2	3
Newton iterations (avg.)	1.6	2.2	3.5	3.7
computing time [s](avg.)	1.2	17.3	253.8	2847.6

Table 6.7: Slope failure: average number of *Newton* iterations per time increment and average computing time for one implicit *Euler* step on different meshes.

Like in the previous example, the time step sizes were chosen in an appropriate manner for all four FE meshes such that no time step has to be repeated because of a non-converging *Newton* method, cf. Table 6.7. Furthermore, Table 6.8 shows a moderate increase of

average computing time for the solution of the linear systems.

refinement level	0	1	2	3
GMRES iterations (avg.)	29.3	64.3	127.7	265.3
computing time [s] (avg.)	1.4	6.5	64.5	702.9
number of linear problems	1 277	1 756	2 836	2 987

Table 6.8: Slope failure: performance of the GMRES solver (average number of iterations per *Newton* step, average computing time for the solution of one linear problem, total number of linear problems for the full simulation of 800 time steps).

6.3.2 Parallel speed-up and efficiency of M++/PANDAS

In order to discuss the parallel scaling properties of M++/PANDAS by use of the quantities speed-up S_P and efficiency E_P, calculations of the slope failure problem were carried out on both FE meshes with the refinement levels 2 and 3, cf. Table 6.6. For convenience, each simulation contains only 20 time steps. The calculations presented in this section were all carried out on the Linux cluster in Stuttgart.

In Table 6.9 and Figure 6.19, the results for the calculations on the mesh with 64 000 cells (refinement level 2) are shown. Starting with a calculation of the whole problem on 1 processor, altogether 12 parallel simulations were carried out with different numbers of processors. Therein, the number of processors is increased by 2 until the mesh is distributed on 24 processors, which results in a calculation with approximately 2 667 cells on each processor. Looking at the computational expense of the single calculations, the

processors	cells/processor	time [h]	S_P [-]	E_P [%]
1	64 000	3:01:40	1.00	100
2	32 000	1:48:25	1.68	84
4	16 000	1:04:32	2.82	70
6	≈ 10 667	0:46:19	3.92	65
8	8 000	0:38:29	4.72	59
10	6 400	0:36:00	5.05	50
12	≈ 5 334	0:34:19	5.29	44
14	≈ 4 572	0:29:29	6.16	44
16	4 000	0:29:46	6.10	38
18	≈ 3 356	0:31:08	5.84	32
20	3 200	0:32:57	5.51	28
22	2 909	0:32:42	5.56	25
24	≈ 2 667	0:34:20	5.29	22

Table 6.9: Slope failure: speed-up and efficiency; 20 time steps on the FE mesh with refinement level 2.
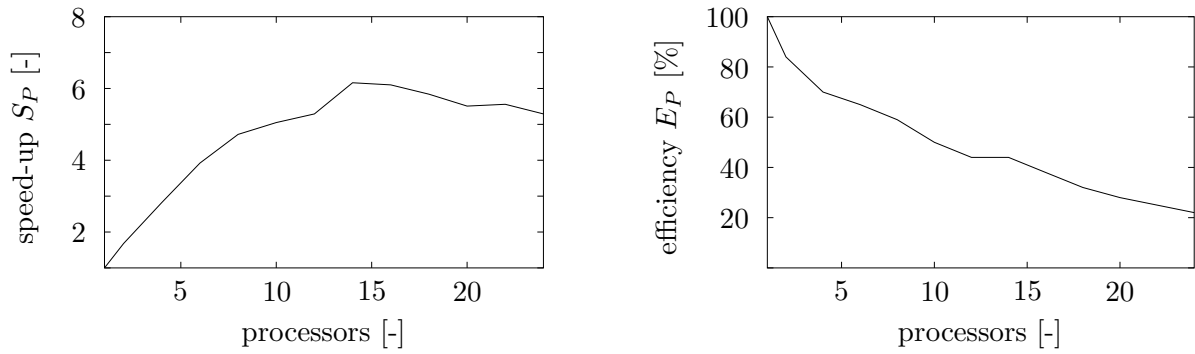
Figure 6.19: Slope failure: progression of speed-up (left) and efficiency (right); 20 time steps on the FE mesh with refinement level 2.

computing time of approximately 3 hours on 1 processor can be maximally reduced by roughly a factor of 6 by the calculations with 14 and 16 processors, respectively. These calculations correspond to a parallel efficiency of around 40 %, i.e., when using 14 (or 16) processors, the theoretically possible speed-up of 14 (or 16) is only reached by a factor around 0.4. By choosing more than 16 processors, in this example, even an increase of computing time is obtained, which is well reflected by the decreasing values for the speed-up.

Table 6.10 shows the results of the simulations on the FE mesh with refinement level 3. Due to the restriction of 1 GB memory per compute node on the cluster in Stuttgart, the

processors	cells/processor	time [h]	S_P [-]	E_P [%]
14	$\approx 36\,572$	5:18:14	1.00	100
16	$32\,000$	4:45:54	1.11	97
18	$\approx 28\,445$	4:41:57	1.13	88
20	$25\,600$	4:14:59	1.25	87
22	$\approx 23\,273$	4:05:37	1.30	82
24	$\approx 21\,334$	3:53:45	1.36	79
26	$\approx 19\,693$	3:52:06	1.37	74
28	$\approx 18\,286$	3:40:46	1.44	72
30	$\approx 17\,067$	3:38:07	1.46	68
32	$16\,000$	3:45:04	1.41	62
34	$\approx 15\,059$	3:43:04	1.43	59
36	$\approx 14\,223$	3:48:28	1.39	54
38	$\approx 13\,474$	3:45:36	1.41	52
40	$12\,800$	3:44:12	1.42	50
42	$\approx 12\,191$	3:49:40	1.38	46

Table 6.10: Slope failure: speed-up and efficiency; 20 time steps on the FE mesh with refinement level 3.

calculation of the slope failure problem on such a fine mesh needs at least 14 processors, which is, therefore, the reference calculation for the quantities speed-up and efficiency in this example. Like in the simulations with the coarser FE mesh, the computing time can be reduced by increasing the number of processors until a minimum computing time is obtained, which is given here by approximately 3 hours and 40 minutes by the calculation on 30 processors. This simulation gives a parallel efficiency of 68 % with respect to the calculation on 14 processors.

Looking at the results given in Tables 6.9 and 6.10, it can be observed that, in both cases, the speed-up S_P increases continuously to a maximum value. After that, depending on the load balancing, i. e., the size of the processor interfaces and, therefore, the amount of parallel communication, the increase of processors can both lead to a decrease or increase of the speed-up. Obviously, a continuous increase of processors after having reached a maximum value for the speed-up leads, in a global sense, to an increase of computing time. Furthermore, due to the obtained results, no *a priori* statement can be made concerning the optimal number of processors for an arbitrary parallel simulation with a certain number of degrees of freedom.

Finally, it can be concluded that the parallel scaling properties of M++/PANDAS are not optimal in comparison with famous commercial parallel FE tools. Nevertheless, recalling the underlying idea of the interface M++/PANDAS, i. e., parallelization of a sequential FE code by coupling with a parallel solver without any change within the sequential code, a comfortable parallel scaling behavior is obtained by M++/PANDAS.

Chapter 7: Summary and outlook

7.1   Summary

In the present thesis, the single steps necessary for the numerical simulations of localization phenomena were presented and discussed. Therein, the numerical aspects of this whole procedure were paid special attention to, namely, to the problems coming along with the modeling of softening material behavior and the problem to efficiently deal with large numbers of unknown quantities within the solution process. By the resulting interface M++/PANDAS, wherein an existing sequential code containing advanced material models is parallelized by coupling with a program containing parallel data structures and efficient parallel solvers, a basis was established for further developments in the field of large scale FE computations of multiphasic problems.

Within the framework of this thesis, the simulations of geotechnical questions were taken as examples of use for the numerical studies. Based on the Theory of Porous Media (TPM), a thermodynamically consistent continuum mechanical model was presented in order to model fully and partially saturated soils properly. The proposed triphasic model, which consists of the constituents solid, liquid and gas, was discussed in detail, whereby a simplified biphasic model was obtained by neglecting the compressible gaseous phase. Subsequently, the numerical realization of this model in the context of the finite element method was pointed out. In addition to the numerical realization of standard single-phasic material models, it was emphasized that the multiphasic character has to be considered in order to obtain stable numerical solutions, for example, by the choice of special ansatz functions for the different unknowns, which finally resulted in the application of the well-known *Taylor-Hood* elements.

In the context of the chapter dealing with the proper numerical treatment of softening material behavior, a comprehensive overview of three main branches of regularization techniques, namely, the rate-dependent models, the micropolar continua and the integral- and gradient-type non-local models, was presented, whereby the history and the main publications of the respective methods were discussed. Therein, it was pointed out that many regularization methods have certain limits for their validity due the respective physical motivation or due to the given application range of the single method. In particular, the viscoplastic ansatz can only be applied in cases of dynamic or quasi-static boundary-value problems of rate-dependent materials, and the use of a micropolar continuum is only recommendable in the context of its regularizing effect in cases of shear dominant problems of materials with a granular or beam-like microstructure. Furthermore, for the non-local models, as far as the author is aware, no appreciable limitations with regard to their validity exist. In the numerical simulation of a tensile bar, each method showed an adequate regularizing effect in order to preserve the well-posedness of the problem. Nevertheless, differences concerning the characteristics of the solution and the numerical convergence behavior between the single regularization methods were recognized. In gen-

eral, it can be concluded that the application of the rate-dependent model clearly shows the best numerical convergence behavior. Following this, whenever the material under study and the respective boundary-value problem are appropriate, the application of such models or at least the combination of them with other regularization methods are strongly recommended for an improvement of the numerical convergence behavior.

In order to enable 3-dimensional FE simulations based on TPM models from a numerical viewpoint, the sequential code PANDAS had to be expanded in terms of parallel strategies. This was carried out by an interface, which combines the two programs M++ and PANDAS, whereby the actual parallel solution process is governed by M++ and no changes with regard to this parallelization procedure had to be additionally implemented into PANDAS. Obviously, this concept is not restricted to the application to PANDAS but can be applied straightforward to other sequential FE codes.

Finally, the capability and efficiency of the presented mechanical models as well as their numerical realizations were proved at challenging numerical examples. In particular, dilatant and contractant shear bands were presented in the framework of a biphasic micropolar continuum. Furthermore, the interface M++/PANDAS was tested at two 3-dimensional simulations of failure mechanisms of natural slopes. Therein, the excellent convergence behavior of the applied model towards a reference solution by uniform refinements of the underlying FE meshes was presented. In addition, the parallel scaling properties of M++/PANDAS were discussed in detail by consideration of the quantities speed-up, efficiency and scale-up.

7.2   Outlook

Realistic FE simulations based on advanced continuum mechanical models are a demanding task, which will become more and more interesting and important in the future. In this context, the developed interface M++/PANDAS can be understood as a prototype implementation, which can be expanded and advanced in many points. First of all, besides the presented triphasic model, other material models containing anisotropy, chemical reactions, damage models, etc. can be integrated in the interface and tested at large scale problems in a reasonable time.

In order to increase the numerical efficiency of the solution process, the tool M++ and, as a consequence, also the interface M++/PANDAS, can be extended with respect to adaptive strategies in time and space. Furthermore, the stability and efficiency of the iterative linear solvers can be increased by special adjustments concerning the respective characteristics of the single problems under consideration.

Finally, the enormous number of internal variables in the presented 3-d examples, which result from the need of many integration points for a stable numerical quadrature, could be a motivation for a completely new approach for the numerical solution procedure. Instead of solving the equations for the determination of the plastic strains and the plastic multiplier locally within each finite element, these quantities could be transferred to the nodes of the FE discretization, such that the respective equations could be solved in a strong sense at these nodes. In combination with parallel solution strategies, this approach

would result in a significant decrease of the computational expense for 3-d simulations, if stable numerical solutions are obtained by the realization of this idea.

Appendix A: Tensor calculus

The main definitions for the tensorial expressions, which were presented within this thesis, are briefly summarized here. Therein, the chosen notation follows the rules and definitions of the absolute tensor notation given in the work by *de Boer* [19] and in the lecture notes on vector and tensor calculus by *Ehlers* [52]. For simplicity, the underlying coordinate system for the following definitions is a normalized *Carte*sian basis, in which no differentiation between covariant or contravariant basis systems has to be carried out. Furthermore, the well-known summation convention of *Einstein* holds for indices appearing twice within a term.

A.1   Tensor algebra

A.1.1   Basic tensor products

Among the variety of different tensor products, here, only the rules for the products, which were used within the discussions of this thesis, are presented, namely the dyadic and scalar products as well as the linear mapping ("contracting product") and the tensor product. For a better understanding of the absolute tensor notation, additionally, an orthonormal basis notation of the respective products is given.

Dyadic product

Within a dyadic tensor product, all the basis vectors $\mathbf{e}_i$ of the involved tensors are combined in a dyadic sense. The order (or rank) of the resulting tensor equals the sum of the ranks of the involved tensors:

$$
\begin{aligned}
\mathbf{C} &= \mathbf{a} \;\otimes\; \mathbf{b} \;=\; a_i\, b_j \quad \mathbf{e}_i \otimes \mathbf{e}_j, \\
\overset{4}{\mathbf{C}} &= \mathbf{A} \;\otimes\; \mathbf{B} \;=\; A_{ij}\, B_{kl} \quad \mathbf{e}_i \otimes \mathbf{e}_j \otimes \mathbf{e}_k \otimes \mathbf{e}_l \,.
\end{aligned}
\tag{A.1}
$$

Note that within the used notation, vectors (or 1-st order tensors) are symbolized by bold, small Latin characters, whereas tensors of n-th order ($n > 1$) are defined by bold, capital Latin characters. Furthermore, the rank of a n-th order tensor is clarified by the superscripted rank for $n > 2$.

Scalar product

The scalar product can only be carried out between tensors of the same order, whereby the single basis vectors are combined scalarly and the result of this product always yields

a scalar value:

$$
\begin{aligned}
\alpha &= \mathbf{a} \cdot \mathbf{b} = a_i\,b_i\,, \\
\alpha &= \mathbf{A} \cdot \mathbf{B} = A_{ij}\,B_{ij}\,.
\end{aligned}
\tag{A.2}
$$

Linear mapping and tensor product

The linear mapping as well as the tensor product are operations, in which the rank of the resulting tensor is reduced (contracted) with respect of the sum of the ranks of all involved tensors. In both operations, the resulting tensor is formed by a combination of both scalar and dyadic products of the basis vectors of the involved tensors:

$$
\begin{aligned}
\mathbf{c} &= \mathbf{A}\,\mathbf{b} = A_{ij}\,b_j && \mathbf{e}_i\,, \\
\mathbf{C} &= \mathbf{A}\,\mathbf{B} = A_{ij}\,B_{jk} && \mathbf{e}_i \otimes \mathbf{e}_k\,, \\
\mathbf{C} &= \overset{4}{\mathbf{A}}\,\mathbf{B} = A_{ijkl}\,B_{kl} && \mathbf{e}_i \otimes \mathbf{e}_j\,.
\end{aligned}
\tag{A.3}
$$

A.1.2 Symmetric and skew-symmetric parts of a tensor

Each arbitrary 2-nd order tensor $\mathbf{A}$ can be uniquely decomposed into symmetric and skew-symmetric parts:

$$
\begin{aligned}
\mathbf{A} &= A_{ij}\,\mathbf{e}_i \otimes \mathbf{e}_j = \mathbf{A}_{\mathrm{sym}} + \mathbf{A}_{\mathrm{skw}}\,, \\
\mathbf{A}_{\mathrm{sym}} &:= \tfrac{1}{2}\,(\mathbf{A} + \mathbf{A}^T) \quad \rightsquigarrow \quad \mathbf{A}_{\mathrm{sym}} = \mathbf{A}_{\mathrm{sym}}^T\,, \\
\mathbf{A}_{\mathrm{skw}} &:= \tfrac{1}{2}\,(\mathbf{A} - \mathbf{A}^T) \quad \rightsquigarrow \quad \mathbf{A}_{\mathrm{skw}} = -\mathbf{A}_{\mathrm{skw}}^T\,,
\end{aligned}
\tag{A.4}
$$

whereby the transpose of a tensor is given by $\mathbf{A}^T = A_{ji}\,\mathbf{e}_i \otimes \mathbf{e}_j$.

A.1.3 Fundamental tensors

A fundamental tensor is a tensor, whose coefficient matrix is exclusively built by combinations of basis vectors and which is independent of any variable quantity.

2-nd order fundamental tensor

The 2-nd order fundamental tensor (or identity tensor) $\mathbf{I}$ leads to an identical map, if it is applied to an arbitrary vector $\mathbf{a}$ or an arbitrary 2nd order tensor $\mathbf{A}$, respectively:

$$
\mathbf{a} = \mathbf{I}\,\mathbf{a}\,, \qquad \mathbf{A} = \mathbf{I}\,\mathbf{A}\,, \qquad \mathbf{I} := \delta_{ij}\,\mathbf{e}_i \otimes \mathbf{e}_j\,,
\tag{A.5}
$$

where δ_{ij} is the so-called *Kronecker* symbol, which takes for $i = j$ the value 1 and otherwise the value 0.

3-rd order fundamental tensor

The 3-rd order fundamental tensor (or *Ricci* permutation tensor) $\overset{3}{\mathbf{E}}$ is defined via the following relation:

$$\overset{3}{\mathbf{E}} := e_{ijk}\left(\mathbf{e}_i \otimes \mathbf{e}_j \otimes \mathbf{e}_k\right), \tag{A.6}$$

whereby the so-called permutation symbol e_{ijk} is given by

$$e_{ijk} = \left\{ \begin{array}{rl} 1 & : \text{even permutation} \\ -1 & : \text{odd permutation} \\ 0 & : \text{double indexing} \end{array} \right. \longrightarrow \left\{ \begin{array}{l} e_{123} = e_{231} = e_{312} = 1 \\ e_{321} = e_{213} = e_{132} = -1 \\ \text{all remaining } e_{ijk} \text{ vanish} \end{array} \right. \tag{A.7}$$

This fundamental tensor is very often used in connection with the outer tensor product of tensors, e. g., the outer tensor product of a vector and a tensor, cf. Section A.1.6.

4-th order fundamental tensors

4-th order fundamental tensors are built by dyadic combinations of the 2-nd order identity tensor $\mathbf{I}$. By additional transpositions of the respective basis vectors, altogether three different 4-th order fundamental tensors can be defined, which have the following properties:

$$\begin{aligned} (\mathbf{I} \otimes \mathbf{I})^{\overset{23}{T}} \mathbf{A} &= \mathbf{A} & (\text{identical map}), \\ (\mathbf{I} \otimes \mathbf{I})^{\overset{24}{T}} \mathbf{A} &= \mathbf{A}^T & (\text{"transposing" map}), \\ (\mathbf{I} \otimes \mathbf{I}) \ \mathbf{A} &= (\mathbf{A} \cdot \mathbf{I})\,\mathbf{I} = (\text{tr}\,\mathbf{A})\,\mathbf{I} & (\text{"tracing" map}). \end{aligned} \tag{A.8}$$

Therein, the transpositions $(\,\cdot\,)^{\overset{ik}{T}}$ indicate an exchange of the i-th and k-th basis systems.

A.1.4 Spherical and deviatoric parts of a tensor

Each arbitrary 2-nd order tensor $\mathbf{A}$ can be decomposed into spherical and deviatoric parts:

$$\begin{aligned} \mathbf{A} &= \mathbf{A}^K + \mathbf{A}^D, \\ \mathbf{A}^K &:= \tfrac{1}{3}\left(\mathbf{A} \cdot \mathbf{I}\right)\mathbf{I}, \\ \mathbf{A}^D &:= \mathbf{A} - \tfrac{1}{3}\left(\mathbf{A} \cdot \mathbf{I}\right)\mathbf{I} = \mathbf{A} - \mathbf{A}^K. \end{aligned} \tag{A.9}$$

By the above definition, the deviatoric part $\mathbf{A}^D$ always results in a traceless tensor, i. e., $\mathbf{A}^D \cdot \mathbf{I} = 0$.

A.1.5   Incomplete mapping

If higher order tensors are applied to other tensors in the sense of incomplete mappings, one has to know how many of the basis vectors have to be linked by scalar products. Therefore, an underlined superscript $(\cdot)^{\underline{n}}$ indicates the order of the desired result after the tensor operation has been carried out. In this context, an incomplete mapping of two 3-rd order tensors results in the following way in a 2-nd order tensor:

$$\mathbf{C} = (\overset{3}{\mathbf{A}}\,\overset{3}{\mathbf{B}})^{\underline{2}} = A_{ijk}\,B_{jkn}\,(\mathbf{e}_i \otimes \mathbf{e}_n)\,. \tag{A.10}$$

A.1.6   Outer tensor product of vector and tensor

The outer tensor product of a vector $\mathbf{a}$ and a 2-nd order tensor $\mathbf{B}$ is defined by

$$\mathbf{a} \times \mathbf{B} = [\,\overset{3}{\mathbf{E}}\,(\mathbf{a} \otimes \mathbf{B})\,]^{\underline{2}} = e_{ijk}\,a_j\,B_{kt}\,(\mathbf{e}_i \otimes \mathbf{e}_t)\,. \tag{A.11}$$

A.2   Invariants

A.2.1   Invariants of a 2-nd order tensor

From the solution of the eigenvalue problem, the principal invariants of an arbitrary 2-nd order tensor $\mathbf{A}$ yield:

$$\begin{aligned}
\mathrm{I}_A &= \mathbf{A} \cdot \mathbf{I} = \operatorname{tr}\mathbf{A}\,, \\
\mathbb{II}_A &= \tfrac{1}{2}\,(\mathrm{I}_A^2 - \mathbf{A}^T \cdot \mathbf{A})\,, \\
\mathbb{III}_A &= \tfrac{1}{6}\,\mathrm{I}_A^3 - \tfrac{1}{2}\,\mathrm{I}_A^2\,(\mathbf{A}\,\mathbf{A} \cdot \mathbf{I}) + \tfrac{1}{3}\,\mathbf{A}^T\,\mathbf{A}^T \cdot \mathbf{A} = \det \mathbf{A}\,.
\end{aligned} \tag{A.12}$$

A.2.2   Specific invariants of the yield criterion

According to the above definitions, the specific invariants of the presented yield criterion can be expressed by the following relations:

∗ Single-surface yield criterion by *Ehlers* [49, 50]:

$$\mathrm{I} = \boldsymbol{\sigma} \cdot \mathbf{I}\,, \quad \mathbb{II}^D = \tfrac{1}{2}\,\boldsymbol{\sigma}^D \cdot \boldsymbol{\sigma}^D\,, \quad \mathbb{III}^D = \det \boldsymbol{\sigma}^D\,. \tag{A.13}$$

∗ Micropolar single-surface yield criterion by *Ehlers & Volk* [64]:

$$\begin{aligned}
\mathrm{I} = \boldsymbol{\sigma} \cdot \mathbf{I}\,, \quad \mathbb{II}_{\mathrm{sym}}^D &= \tfrac{1}{2}\,\boldsymbol{\sigma}_{\mathrm{sym}}^D \cdot \boldsymbol{\sigma}_{\mathrm{sym}}^D\,, \quad \mathbb{III}_{\mathrm{sym}}^D = \det \boldsymbol{\sigma}_{\mathrm{sym}}^D\,, \\
\mathbb{II}_{\mathrm{skw}} &= \tfrac{1}{2}\,\boldsymbol{\sigma}_{\mathrm{skw}} \cdot \boldsymbol{\sigma}_{\mathrm{skw}}\,, \quad \mathbb{II}_M = \tfrac{1}{2}\,\mathbf{M} \cdot \mathbf{M}\,.
\end{aligned} \tag{A.14}$$

Therein, $\boldsymbol{\sigma}$ denotes both the standard and micropolar stress tensors and $\mathbf{M}$ denotes the couple stress tensor of the micropolar theory. Within a multiphasic formulation, both stress quantities are related to the solid constituent.

Appendix B:
Integral- and gradient-type non-local models

In Section 4.2, a connection was established between integral- and gradient-type non-local models. Based on the work by *Engelen et al.* [67], a detailed derivation of this connection will be presented now. Starting point of this derivation is the integral-type formulation of a non-local quantity $\bar{\bar{f}}(\mathbf{x})$:

$$\bar{\bar{f}}(\mathbf{x}) = \frac{1}{V_r} \int_{\mathbb{R}^3} w(\mathbf{x} - \mathbf{y}) \, f(\mathbf{y}) \, \mathrm{d}v \,. \tag{B.1}$$

Following the definitions from Equations (4.3) and (4.27), the representative volume V_r and the weighting function $w(\mathbf{x} - \mathbf{y})$ are given by

$$V_r = \int_{\mathbb{R}^3} w(\mathbf{x} - \mathbf{y}) \, \mathrm{d}v \,,$$

$$w(\mathbf{x} - \mathbf{y}) = \frac{1}{l \sqrt{\pi}} \exp\left[-\frac{(\mathbf{x} - \mathbf{y}) \cdot (\mathbf{x} - \mathbf{y})}{l^2} \right] \,. \tag{B.2}$$

Note that, in contrast to Equations (4.2) and (4.3), the evaluation of the above integrals has to be carried out on $\mathbb{R}^3$ within this derivation, which results in a constant value for the representative volume. Thus, the above integral formulation corresponds to a free boundary problem.

By insertion of the *Taylor* series expansion for $f(\mathbf{y})$ with respect to the point $\mathbf{x}$, cf. Equation (4.4), in (B.1), the following relation is obtained:

$$\begin{aligned}
\bar{\bar{f}}(\mathbf{x}) = \quad & \frac{1}{V_r} \{ \underbrace{\int_{\mathbb{R}^3} w(\mathbf{x} - \mathbf{y}) \, \mathrm{d}v}_{V_r} \, f(\mathbf{x}) + [\underbrace{\int_{\mathbb{R}^3} w(\mathbf{x} - \mathbf{y}) \, (\mathbf{y} - \mathbf{x}) \, \mathrm{d}v}_{\mathbf{r}}] \cdot \nabla f(\mathbf{y})|_{\mathbf{y}=\mathbf{x}} + \\[2mm]
& + \tfrac{1}{2!} [\underbrace{\int_{\mathbb{R}^3} w(\mathbf{x} - \mathbf{y}) \, [(\mathbf{y} - \mathbf{x}) \otimes (\mathbf{y} - \mathbf{x})] \, \mathrm{d}v}_{\mathbf{R}}] \cdot \nabla\nabla f(\mathbf{y})|_{\mathbf{y}=\mathbf{x}} + \\[2mm]
& + \tfrac{1}{3!} [\underbrace{\int_{\mathbb{R}^3} w(\mathbf{x} - \mathbf{y}) \, [(\mathbf{y} - \mathbf{x}) \otimes (\mathbf{y} - \mathbf{x}) \otimes (\mathbf{y} - \mathbf{x})] \, \mathrm{d}v}_{\overset{3}{\mathbf{R}}}] \cdot \nabla\nabla\nabla f(\mathbf{y})|_{\mathbf{y}=\mathbf{x}} + \quad \text{(B.3)} \\[2mm]
& + \tfrac{1}{4!} [\underbrace{\int_{\mathbb{R}^3} w(\mathbf{x} - \mathbf{y}) \, [(\mathbf{y} - \mathbf{x}) \otimes (\mathbf{y} - \mathbf{x}) \otimes (\mathbf{y} - \mathbf{x}) \otimes (\mathbf{y} - \mathbf{x})] \, \mathrm{d}v}_{\overset{4}{\mathbf{R}}}] \cdot \\[2mm]
& \cdot \nabla\nabla\nabla\nabla f(\mathbf{y})|_{\mathbf{y}=\mathbf{x}} + \dots \} \,.
\end{aligned}$$

Therein, as already introduced in (4.4), the notation $\nabla(\cdot) = \mathrm{grad}\,(\cdot)$ has been used for convenience. In the above equation, some integrals turn out to be zero. This is due to the fact that the weighting function $w(\mathbf{x}-\mathbf{y})$ is symmetric and that the terms $(\mathbf{y}-\mathbf{x})$ are skew-symmetric with respect to $\mathbf{y} - \mathbf{x} = \mathbf{0}$. Consequently, the following relations hold:

$$
\begin{aligned}
\mathbf{r} &= \int_{\mathbb{R}^3} w(\mathbf{x} - \mathbf{y})\,(y_i - x_i)\,\mathrm{d}v\,\mathbf{e}_i = \mathbf{0} & \forall\,i\,, \\[2ex]
\mathbf{R} &= \int_{\mathbb{R}^3} w(\mathbf{x} - \mathbf{y})\,(y_i - x_i)\,(y_j - x_j)\,\mathrm{d}v\,(\mathbf{e}_i \otimes \mathbf{e}_j) = \mathbf{0} & i \neq j\,, \\[2ex]
\overset{3}{\mathbf{R}} &= \int_{\mathbb{R}^3} w(\mathbf{x} - \mathbf{y})\,(y_i - x_i)\,(y_j - x_j)\,(y_k - x_k)\,\mathrm{d}v\,(\mathbf{e}_i \otimes \mathbf{e}_j \otimes \mathbf{e}_k) = \overset{3}{\mathbf{0}} & \forall\,i,\,j,\,k\,.
\end{aligned}
$$
(B.4)

Using the same reasoning, *Engelen et al.* [67] concluded that within the series of integrals in front of the fourth-order derivatives of f,

$$
\overset{4}{\mathbf{R}} = \int_{\mathbb{R}^3} w(\mathbf{x} - \mathbf{y})\,(y_i - x_i)\,(y_j - x_j)\,(y_k - x_k)\,(y_l - x_l)\,\mathrm{d}v\,(\mathbf{e}_i \otimes \mathbf{e}_j \otimes \mathbf{e}_k \otimes \mathbf{e}_l)\,,
$$
(B.5)

the integrals are non-zero in the following situations:

$$
\begin{aligned}
&\text{(a)}\quad i = j = k = l\,, \\
&\text{(b)}\quad i = j \,\wedge\, k = l \,\wedge\, i \neq k\,, \\
&\text{(c)}\quad i = k \,\wedge\, j = l \,\wedge\, i \neq j\,, \\
&\text{(d)}\quad i = l \,\wedge\, j = k \,\wedge\, i \neq j\,.
\end{aligned}
$$
(B.6)

Discussing the second-order term $\mathbf{R}$, one concludes to

$$
\begin{aligned}
\mathbf{R} &= \begin{bmatrix} R_{11} & 0 & 0 \\ 0 & R_{22} & 0 \\ 0 & 0 & R_{33} \end{bmatrix} \mathbf{e}_i \otimes \mathbf{e}_j\,, \\[2ex]
R_{11} &= \int_{\mathbb{R}^3} w(\mathbf{x} - \mathbf{y})\,(y_1 - x_1)^2\,\mathrm{d}v\,, \\[2ex]
R_{22} &= \int_{\mathbb{R}^3} w(\mathbf{x} - \mathbf{y})\,(y_2 - x_2)^2\,\mathrm{d}v\,, \\[2ex]
R_{33} &= \int_{\mathbb{R}^3} w(\mathbf{x} - \mathbf{y})\,(y_3 - x_3)^2\,\mathrm{d}v\,.
\end{aligned}
$$
(B.7)

Due to the fact that the integrals are evaluated on $\mathbb{R}^3$ and due to the symmetry properties of $w(\mathbf{x} - \mathbf{y})$, the three integrals R_{11}, R_{22} and R_{33} result all in the same constant value $\bar{C}_1$:

$$\bar{C}_1 := R_{11} = R_{22} = R_{33} \,. \tag{B.8}$$

Thus, the third term in (B.3) gives

$$
\begin{aligned}
\frac{1}{V_r \, 2!} \, \mathbf{R} \cdot \nabla\nabla f(\mathbf{y})\big|_{\mathbf{y}=\mathbf{x}} &= \frac{1}{V_r \, 2!} \, \bar{C}_1 \, (\mathbf{e}_i \otimes \mathbf{e}_i) \cdot \frac{\partial^2 f}{\partial x_l \, \partial x_m} \, (\mathbf{e}_l \otimes \mathbf{e}_m) = \\
&= C_1 \, \frac{\partial^2 f}{\partial x_i^2} = C_1 \, \Delta f(\mathbf{x}) \,.
\end{aligned}
\tag{B.9}
$$

Proceeding analogously with the fourth-order term $\overset{4}{\mathbf{R}}$, finally, the gradient-type non-local formulation from (4.5) is obtained:

$$\bar{\bar{f}}(\mathbf{x}) = f(\mathbf{x}) + C_1 \, \Delta f(\mathbf{x}) + C_2 \, \Delta\Delta f(\mathbf{x}) + \dots \,. \tag{B.10}$$

In the above relations, the abbreviations $\Delta(\cdot) = \operatorname{div}[\nabla(\cdot)]$ and $\Delta\Delta(\cdot) = \Delta^2(\cdot)$ have been used for convenience, cf. Equation (4.5). Note that many authors use the notation $\nabla^2(\cdot) = \Delta(\cdot)$ within this context, cf., e. g., *Engelen et al.* [67] or *Jirásek* [95].

Bibliography

[1] *Aifantis, E. C.*: On the microstructural origin of certain inelastic models. *ASME Journal of Engineering Materials and Technology* **106** (1984), 326–330.

[2] *Argyris, J. H.; Scharpf, D. W.*: Finite elements in time and space. *Nuclear Engineering and Design* **10** (1969), 456–464.

[3] *Askes, H.; Suiker, A. S. J.; Sluys, L. J.*: A classification of higher-order strain-gradient models – linear analysis. *Archive of Applied Mechanics* **72** (2002), 171–188.

[4] *Barrett, R.; Berry, M.; Chan, T.; Demmel, J.; Donato, J.; Dongarra, J.; Eijkhout, V.; Pozo, R.; Romine, C.; van der Vorst, H.*: *Templates for the solution of linear systems.* SIAM, Philadelphia 1994. `ftp://ftp.netlib.org/templates/templates.ps`.

[5] *Bastian, P.*: *Parallele adaptive Mehrgitterverfahren.* Teubner Skripten zur Numerik. Teubner, Stuttgart 1996.

[6] *Bastian, P.*: *Paralleles Rechnen I.* Vorlesungsskript, Universität Heidelberg 2002. `http://hal.iwr.uni-heidelberg.de/lehre/lehre.html`.

[7] *Bathe, K.-J.*: *Finite-Elemente-Methoden.* Springer-Verlag, Berlin 1990.

[8] *Bažant, Z. P.; Belytschko, T.; Chang, T.-P.*: Continuum model for strain softening. *ASCE: Journal of Engineering Mechanics* **110** (1984), 1666–1692.

[9] *Bažant, Z. P.; Jirásek, M.*: Nonlocal integral formulations of plasticity and damage: Survey of progress. *ASCE: Journal of Engineering Mechanics* **128** (2002), 1119–1149.

[10] *Belytschko, T.; Bažant, Z. P.; Hyun, Y.-W.; Chang, T.-P.*: Strain-softening materials and finite-element solutions. *Computers and Structures* **23** (1986), 163–180.

[11] *Belytschko, T.; Moran, B.; Kulkarni, M.*: On the crucial role of imperfections in quasistatic viscoplastic solutions. *Journal of Applied Mechanics* **58** (1991), 658–665.

[12] *Berger, M. J.; Bokhari, S. H.*: A partitioning strategy for nonuniform problems on multiprocessors. *IEEE Transactions on Computers* **36** (1987), 570–580.

[13] *Besdo, D.*: Ein Beitrag zur nichtlinearen Theorie des Cosserat-Kontinuums. *Acta Mechanica* **20** (1974), 105–131.

[14] *Betsch, P.; Steinmann, P.*: Conservation properties of a time FE method. Part I: Time-stepping schemes for n-body problems. *International Journal for Numerical Methods in Engineering* **49** (2000), 599–638.

[15] *Betsch, P.; Steinmann, P.*: Conservation properties of a time FE method. Part II: Time-stepping schemes for non-linear elastodynamics. *International Journal for Numerical Methods in Engineering* **50** (2001), 1931–1955.

[16] *Biot, M. A.*: General theory of three-dimensional consolidation. *Journal of Applied Physics* **12** (1941), 155–164.

[17] *Bishop, A. W.*: The effective stress principle. *Teknisk Ukeblad* **39** (1959), 859–863.

[18] *Blome, P.*: *Ein Mehrphasen-Stoffmodell für Böden mit Übergang auf Interface-Gesetze.* Dissertation, Bericht Nr. II-10 aus dem Institut für Mechanik (Bauwesen), Universität Stuttgart 2003.

[19] *de Boer, R.*: *Vektor- und Tensorrechnung für Ingenieure.* Springer-Verlag, Berlin 1982.

[20] *de Boer, R.*: *Theory of Porous Media.* Springer-Verlag, Berlin 2000.

[21] *de Boer, R.; Ehlers, W.*: *Theorie der Mehrkomponentenkontinua mit Anwendung auf bodenmechanische Probleme.* Forschungsberichte aus dem Fachbereich Bauwesen, Heft 40, Universität-GH-Essen 1986.

[22] *de Boer, R.; Ehlers, W.; Kowalski, S.; Plischka, J.*: *Porous Media – a Survey of Different Approaches.* Forschungsberichte aus dem Fachbereich Bauwesen, Heft 54, Universität-GH-Essen 1991.

[23] *Borri, M.; Bottasso, C.*: A general framework for interpreting time finite element formulations. *Computational Mechanics* **13** (1993), 133–142.

[24] *de Borst, R.*: Numerical modelling of bifurcation and localisation in cohesive-frictional materials. *Pure and Applied Geophysics* **137** (1991), 368–390.

[25] *de Borst, R.*: Simulation of strain localization: A reappraisal of the Cosserat continuum. *Engineering Computations* **8** (1991), 317–332.

[26] *de Borst, R.*: A generalisation of J_2-flow theory for polar continua. *Computer Methods in Applied Mechanics and Engineering* **103** (1993), 347–362.

[27] *de Borst, R.; Mühlhaus, H.-B.*: Computational strategies for gradient continuum models with a view to localization of deformation. In *Bićanic, N.; Owen, D. J. R.; Marović, P.; Jović, V.; Mihanović, A.*, editors, *Nonlinear Engineering Computations.* Pineridge Press, Swansea 1991, pp. 239–260.

[28] *de Borst, R.; Mühlhaus, H.-B.*: Gradient-dependent plasticity: Formulation and algorithmic aspects. *International Journal for Numerical Methods in Engineering* **35** (1992), 521–539.

[29] *de Borst, R.; Mühlhaus, H.-B.; Pamin, J.; Sluys, L. J.*: Computational modelling of localisation of deformation. In *Owen, D. J. R.; Oñate, E.; Hinton, E.*, editors, *Computational Plasticity – Fundamentals and Applications.* Pineridge Press, Swansea 1992, pp. 483–508.

[30] *de Borst, R.; Pamin, J.*: Some novel developments in finite element procedures for gradient-dependent plasticity. *International Journal for Numerical Methods in Engineering* **39** (1996), 2477–2505.

[31] *Bowen, R. M.*: Theory of mixtures. In *Eringen, A. C.*, editor, *Continuum Physics*, Vol. III. Academic Press, New York 1976, pp. 1–127.

[32] *Bowen, R. M.*: Incompressible porous media models by use of the theory of mixtures. *International Journal of Engineering Sciences* **18** (1980), 1129–1148.

[33] *Bowen, R. M.*: Compressible porous media models by use of the theory of mixtures. *International Journal of Engineering Sciences* **20** (1982), 697–735.

[34] *Braess, D.*: *Finite Elemente.* Springer-Verlag, Berlin 1997.

[35] *Brezzi, F.; Fortin, M.*: *Mixed and Hybrid Finite Element Methods.* Springer-Verlag, New York 1991.

[36] *Brinkgreve, R. B. J.*: *Geomaterial models and numerical analysis of softening.* Ph. D. thesis, CIP-Gegevens Koniglijke Bibliotheek, Den Haag 1994.

[37] *Brooks, R. N.; Corey, A. T.*: Properties of porous media affecting fluid flow. *ASCE: Journal of the Irrigation and Draining Division* **92** (1966), 61–88.

[38] *Cosserat, E.; Cosserat, F.*: *Théorie des corps déformables.* A. Hermann et fils, Paris 1909. (Theory of Deformable Bodies, NASA TT F-11 561, 1968).

[39] *Danilov, A.*: *Numerical Treatment of Dynamics in Porous Media.* Master Thesis, Report No. 04-II-5 from the Institute of Applied Mechanics (CE), University of Stuttgart 2004.

[40] *Davis, R. O.; Selvadurai, A. P. S.*: *Plasticity and Geomechanics.* Cambridge University Press, Cambridge 2002.

[41] *Dias da Silva, V.*: A simple model for viscous regularization of elasto-plastic constitutive laws with softening. *Communications in Numerical Methods in Engineering* **20** (2004), 547–568.

[42] *Diebels, S.*: *Mikropolare Zweiphasenmodelle: Formulierung auf der Basis der Theorie Poröser Medien.* Habilitation, Bericht Nr. II-4 aus dem Institut für Mechanik (Bauwesen), Universität Stuttgart 2000.

[43] *Diebels, S.; Ehlers, W.*: On fundamental concepts of multiphase micropolar materials. *Technische Mechanik* **16** (1996), 77–88.

[44] *Diebels, S.; Ellsiepen, P.; Ehlers, W.*: A two-phase model for viscoplastic geomaterials. In *Besdo, D.; Bogacz, R.*, editors, *Dynamics of Continua.* Shaker-Verlag 1998, pp. 103–112. Proceedings of the International Conference of Dynamics of Continua, Bad Honnef 1997.

[45] *Diebels, S.; Ellsiepen, P.; Ehlers, W.*: Error-controlled *Runge-Kutta* time integration of a viscoplastic hybrid two-phase model. *Technische Mechanik* **19** (1999), 19–27.

[46] *Diepolder, W.*: *Das Cosserat-Kontinuum als Strukturmodell für plastische Korndrehungen*. Dissertation, Fakultät für Maschinenwesen, Technische Universität München 1992.

[47] *Dietsche, A.; Steinmann, P.; Willam, K.*: Micropolar elastoplasticity and its role in localisation. *International Journal of Plasticity* **9** (1993), 813–831.

[48] *Ehlers, W.*: *Poröse Medien – ein kontinuumsmechanisches Modell auf der Basis der Mischungstheorie*. Habilitation, Forschungsberichte aus dem Fachbereich Bauwesen, Heft 47, Universität-GH-Essen 1989.

[49] *Ehlers, W.*: Constitutive equations for granular materials in geomechanical context. In *Hutter, K.*, editor, *Continuum Mechanics in Environmental Sciences and Geophysics*, CISM Courses and Lectures No. 337. Springer-Verlag, Wien 1993, pp. 313–402.

[50] *Ehlers, W.*: A single-surface yield function for geomaterials. *Archive of Applied Mechanics* **65** (1995), 246–259.

[51] *Ehlers, W.*: Grundlegende Konzepte in der Theorie Poröser Medien. *Technische Mechanik* **16** (1996), 63–76.

[52] *Ehlers, W.*: *Vector and tensor calculus: an introduction*. Lecture notes, Institute of Applied Mechanics (CE), University of Stuttgart 2000. `http://www.mechbau.uni-stuttgart.de/ls2/lehre/uebungen/index.php`.

[53] *Ehlers, W.*: Foundations of multiphasic and porous materials. In *Ehlers, W.; Bluhm, J.*, editors, *Porous Media: Theory, Experiments and Numerical Applications*. Springer-Verlag, Berlin 2002, pp. 3–86.

[54] *Ehlers, W.; Ammann, M.*: A time finite element method based on the generalized variational calculus. *Proceedings in Applied Mathematics and Mechanics (PAMM)* **2** (2003), 220–221.

[55] *Ehlers, W.; Ammann, M.; Diebels, S.*: *h*-Adaptive FE methods applied to single- and multiphase problems. *International Journal for Numerical Methods in Engineering* **54** (2002), 219–239.

[56] *Ehlers, W.; Diebels, S.; Mahnkopf, D.; Ellsiepen, P.*: *Theoretische und numerische Studien zur Lösung von Rand- und Anfangswertproblemen in der Theorie Poröser Medien*. DFG-Bericht, Bericht aus dem Institut für Mechanik (Bauwesen), Nr. 96-II-1, Universität Stuttgart 1996.

[57] *Ehlers, W.; Droste, A.*: A continuum model for highly porous aluminium foam. *Technische Mechanik* **19** (1999), 341–350.

[58] *Ehlers, W.; Ellsiepen, P.:* PANDAS: Ein FE-System zur Simulation von Sonder-problemen der Bodenmechanik. In *Wriggers, P.; Meißner, U.; Stein, E.; Wunder-lich, W.*, editors, *Finite Elemente in der Baupraxis: Modellierung, Berechnung und Konstruktion.* Ernst & Sohn, Berlin 1998, pp. 391–400. Beiträge zur Tagung FEM '98 an der TU Darmstadt am 5. und 6. März 1998.

[59] *Ehlers, W.; Ellsiepen, P.:* Theoretical and numerical methods in environmental continuum mechanics based on the Theory of Porous Media. In *Schrefler, B. A.*, ed-itor, *Environmental Geomechanics*, CISM Courses and Lectures No. 417. Springer-Verlag, Wien 2001, pp. 1–81.

[60] *Ehlers, W.; Ellsiepen, P.; Ammann, M.:* Time- and space-adaptive methods applied to localization phenomena in empty and saturated micropolar and standard porous materials. *International Journal for Numerical Methods in Engineering* **52** (2001), 503–526.

[61] *Ehlers, W.; Ellsiepen, P.; Blome, P.; Mahnkopf, D.; Markert, B.: Theoretische und numerische Studien zur Lösung von Rand- und Anfangswertproblemen in der The-orie Poröser Medien.* Abschlußbericht zum DFG-Forschungsvorhaben Eh 107/6-2, Bericht aus dem Institut für Mechanik (Bauwesen), Nr. 99-II-1, Universität Stuttgart 1999.

[62] *Ehlers, W.; Graf, T.; Ammann, M.:* Deformation and localization analysis in par-tially saturated soil. *Computer Methods in Applied Mechanics and Engineering* **193** (2004), 2885–2910.

[63] *Ehlers, W.; Markert, B.:* A linear viscoelastic biphasic model for soft tissues based on the Theory of Porous Media. *ASME Journal of Biomechanical Engineering* **123** (2001), 418–424.

[64] *Ehlers, W.; Volk, W.:* On theoretical and numerical methods in the theory of porous media based on polar and non-polar elasto-plastic solid materials. *International Journal of Solids and Structures* **35** (1998), 4597–4617.

[65] *Eipper, G.: Theorie und Numerik finiter elastischer Deformationen in fluidgesättig-ten porösen Medien.* Dissertation, Bericht Nr. II-1 aus dem Institut für Mechanik (Bauwesen), Universität Stuttgart 1998.

[66] *Ellsiepen, P.: Zeit- und ortsadaptive Verfahren angewandt auf Mehrphasenprob-leme poröser Medien.* Dissertation, Bericht Nr. II-3 aus dem Institut für Mechanik (Bauwesen), Universität Stuttgart 1999.

[67] *Engelen, R. A. B.; Geers, M. G. D.; Baaijens, F. P. T.:* Nonlocal implicit gradient-enhanced elasto-plasticity for the modelling of softening behaviour. *International Journal of Plasticity* **19** (2003), 403–433.

[68] *Eriksson, K.; Estep, D.; Hansbo, P.; Johnson, C.: Computational Differential Equa-tions.* Cambridge University Press, Cambridge 1996.

[69] *Eringen, A. C.*: On non-local plasticity. *International Journal of Engineering Sciences* **19** (1981), 1461–1474.

[70] *Eringen, A. C.; Edelen, D. G. B.*: On non-local elasticity. *International Journal of Engineering Sciences* **10** (1972), 233–248.

[71] *Eringen, A. C.; Kafadar, C. B.*: Polar field theories. In *Eringen, A. C.*, editor, *Continuum Physics*, Vol. VI. Academic Press, New York 1976, pp. 1–73.

[72] *van de Felde, E. F.*: *Concurrent Scientific Computing.* Springer-Verlag, New York 1993.

[73] *Finsterle, S.*: *Inverse Modellierung zur Bestimmung hydrogeologischer Parameter eines Zweiphasensystems.* Dissertation, Technischer Bericht der Versuchsanstalt für Wasserbau, Hydrologie und Graziologie der Eidgenössischen Technischen Hochschule Zürich 1993.

[74] *Flynn, M. J.*: Some computer organisations and their effectiveness. *IEEE Transactions on Computers* **21** (1972), 948–960.

[75] *Fried, I.*: Finite element analysis of time-dependent phenomena. *AIAA Journal* **7** (1969), 1170–1173.

[76] *Geist, A.; Beguelin, A.; Dongarra, J.; Jiang, W.; Manchek, R.; Sunderam, V.*: *PVM Parallel Virtual Machine, A User's Guide and Tutorial for Networked Parallel Computing.* MIT Press, Cambridge 1994.

[77] *van Genuchten, M. T.*: A closed-form equation for predicting the hydraulic conductivity of unsaturated soils. *Soil Science Society of America Journal* **44** (1980), 892–898.

[78] *Ghadiani, S.*: *A multiphasic continuum mechanical model for design investigation of an effusion-cooled rocket thrust chamber.* Dissertation, Institut für Mechanik (Bauwesen), Universität Stuttgart 2005.

[79] *Godfrey, M. D.; Hendry, D. F.*: The computer as von Neumann planned it. *IEEE Annals of the History of Computing* **15** (1993), 11–21.

[80] *Günther, W.*: Zur Statik und Kinematik des Cosseratschen Kontinuums. *Abhandlungen der Braunschweigischen Wissenschaftlichen Gesellschaft* **10** (1958), 195–213.

[81] *Hadamard, J.*: *Lectures on the Cauchy Problem in Linear Partial Differential Equations.* Dover Publications, Yale University Press, New York 1923.

[82] *Hairer, E.; Nørsett, S.; Wanner, G.*: *Solving Ordinary Differential Equations, Vol. 1: Nonstiff Problems.* Springer-Verlag, Berlin 1987.

[83] *Hairer, E.; Wanner, G.*: *Solving Ordinary Differential Equations, Vol. 2: Stiff and Differential-Algebraic Problems.* Springer-Verlag, Berlin 1991.

[84] *Hartmann, S.; Lührs, G.; Haupt, P.*: An efficient stress algorithm with applications in viscoplasticity and plasticity. *International Journal for Numerical Methods in Engineering* **40** (1997), 991–1013.

[85] *Hassanizadeh, S. M.; Gray, W. G.*: General conservation equations for multi-phase systems: 1. Averaging procedure. *Advances in Water Resources* **2** (1979), 131–144.

[86] *Heinrich, G.; Desoyer, K.*: Hydromechanische Grundlagen für die Behandlung von stationären und instationären Grundwasserströmungen. *Ingenieur-Archiv* **23** (1955), 182–185.

[87] *Heinrich, G.; Desoyer, K.*: Hydromechanische Grundlagen für die Behandlung von stationären und instationären Grundwasserströmungen, II. Mitteilung. *Ingenieur-Archiv* **24** (1956), 81–84.

[88] *Heinrich, G.; Desoyer, K.*: Theorie dreidimensionaler Setzungsvorgänge in Tonschichten. *Ingenieur-Archiv* **30** (1961), 225–253.

[89] *Helmig, R.*: *Multiphase Flow and Transport Processes in the Subsurface.* Springer-Verlag, Berlin 1997.

[90] *Hinkelmann, R.*: *Hochleistungsrechnen in der Umweltströmungsmechanik.* Vorlesungsskript, Institut für Wasserbau, Lehrstuhl für Hydromechanik und Hydrosystemmodellierung, Universität Stuttgart 2002.

[91] *Hinkelmann, R.*: *Efficient Numerical Methods and Information-Processing Techniques in Environment Water.* Habilitation, Mitteilungsheft Nr. 117 aus dem Institut für Wasserbau, Universität Stuttgart 2003.

[92] *Hughes, T. J. R.*: *The Finite Element Method.* Prentice-Hall, London 1987.

[93] *Hughes, T. J. R.; Hulbert, G. M.*: Space-time finite element methods for elastodynamics: Formulations and error estimates. *Computer Methods in Applied Mechanics and Engineering* **66** (1988), 339–363.

[94] *Hulbert, G. M.; Hughes, T. J. R.*: Space-time finite element methods for second-order hyperbolic equations. *Computer Methods in Applied Mechanics and Engineering* **84** (1990), 327–348.

[95] *Jirásek, M.*: Objective modeling of strain localization. *Revue Française de Génie Civil* **6** (2002), 1119–1132.

[96] *Kreienmeyer, M.*: *Kopplung von Rand- und Finite-Element-Methoden für ebene Elastoplastizität mit Implementierung auf Parallelrechnern.* Dissertation, Forschungs- und Seminarberichte aus dem Bereich der Mechanik der Universität Hannover, Bericht-Nr. F 96/5, Universität Hannover 1996.

[97] *Kröner, E.*: Elasticity theory of materials with long range cohesive forces. *International Journal of Solids and Structures* **3** (1967), 731–742.

[98] *Kumar, V.; Grama, A.; Gupta, A.; Karypis, G.*: *Introduction to Parallel Computing.* Benjamin Cummings, Redwood City 2003.

[99] *Lade, P. V.; Duncan, J. M.*: Cubical triaxial tests on cohesionless soil. *ASCE: Journal of Soil Mechanics and Foundations Division* **99** (1973), 793–812.

[100] *Langtangen, H. P.; Tveito, A.*, editors: *Advanced Topics in Computational Partial Differential Equations*, Vol. 33 of *Lecture Notes in Computational Science and Engineering.* Springer-Verlag, Berlin 2003.

[101] *Lasry, D.; Belytschko, T.*: Localization limiters in transient problems. *International Journal of Solids and Structures* **24** (1988), 581–597.

[102] *Louis, A. K.*: *Inverse und schlecht gestellte Probleme.* Teubner, Stuttgart 1989.

[103] *Mahnkopf, D.*: *Lokalisierung fluidgesättigter poröser Festkörper bei finiten elasto-plastischen Deformationen.* Dissertation, Bericht Nr. II-5 aus dem Institut für Mechanik (Bauwesen), Universität Stuttgart 2000.

[104] *Markert, B.*: *Porous media viscoelasticity with application to polymeric foams.* Dissertation, Institut für Mechanik (Bauwesen), Universität Stuttgart 2005.

[105] *Miehe, C.; Schröder, J.; Schotte, J.*: Computational homogenization analysis in finite plasticity. Simulation of texture development in polycrystalline materials. *Computer Methods in Applied Mechanics and Engineering* **171** (1999), 387–418.

[106] *Mindlin, R. D.*: Second gradient of strain and surface tension in linear elasticity. *International Journal of Solids and Structures* **1** (1965), 417–438.

[107] *Moore, G. E.*: Cramming more components onto integrated circuits. *Electronics* **38** (1965), 114–117. http://www.intel.com/research/silicon/mooreslaw.htm.

[108] *Morozov, V. A.*: *Methods for solving incorrectly posed problems.* Springer-Verlag, New York 1984.

[109] *MPI.* http://www-unix.mcs.anl.gov/mpi/.

[110] *Mühlhaus, H.-B.; Aifantis, E. C.*: A variational principle for gradient plasticity. *International Journal of Solids and Structures* **28** (1991), 845–857.

[111] *Mühlhaus, H.-B.; Vardoulakis, I.*: The thickness of shear bands in granular materials. *Géotechnique* **37** (1987), 271–283.

[112] *Müllerschön, H.*: *Spannungs-Verzerrungsverhalten granularer Materialien am Beispiel von Berliner Sand.* Dissertation, Bericht Nr. II-6 aus dem Institut für Mechanik (Bauwesen), Universität Stuttgart 2000.

[113] *Needleman, A.*: Material rate dependence and mesh sensitivity in localization problems. *Computer Methods in Applied Mechanics and Engineering* **67** (1988), 69–85.

[114] *von Neumann, J.:* First Draft of a Report on the EDVAC. Moore School of Electrical Engineering, University of Pennsylvania 1945.

[115] *Oden, J. T.:* A general theory of finite elements II. Applications. *International Journal for Numerical Methods in Engineering* **1** (1969), 247–259.

[116] *Oden, J. T.; Reddy, J. N.: An Introduction to the Mathematical Theory of Finite Elements.* John Wiley & Sons, New York 1976.

[117] PANDAS: A coupled FEM solver. `http://www.get-pandas.com`.

[118] *Perzyna, P.:* Fundamental problems in viscoplasticity. *Advances in Applied Mechanics* **9** (1966), 243–377.

[119] *Pijaudier-Cabot, G.; Bažant, Z. P.:* Nonlocal damage theory. *ASCE: Journal of Engineering Mechanics* **113** (1987), 1512–1533.

[120] *di Prisco, C.; Imposimato, S.:* Time dependent mechanical behaviour of loose sands. *Mechanics of Cohesive-Frictional Materials* **1** (1996), 45–73.

[121] *di Prisco, C.; Imposimato, S.; Aifantis, E. C.:* A visco-plastic constitutive model for granular soils modified according to non-local and gradient approaches. *International Journal for Numerical and Analytical Methods in Geomechanics* **26** (2002), 121–138.

[122] *Schaefer, H.:* Das Cosserat-Kontinuum. *Zeitschrift für Angewandte Mathematik und Mechanik (ZAMM)* **47** (1967), 485–498.

[123] *Schanz, T.: Zur Modellierung des mechanischen Verhaltens von Reibungsmaterialien.* Habilitation, Mitteilung 45 des Instituts für Geotechnik, Universität Stuttgart 1998.

[124] *Schöberl, J.:* NETGEN – an advancing front 2d/3d-mesh generator based on abstract rules. *Computing and Visualization in Science* **1** (1997), 40–52.

[125] *Schöberl, J.; Gerstmayr, H.; Gaisbauer, R.:* NETGEN – automatic mesh generator. `http://www.hpfem.jku.at/netgen/`.

[126] *Schröder, J.: Homogenisierungsmethoden der nichtlinearen Kontinuumsmechanik unter Beachtung von Stabilitätsproblemen.* Habilitation, Bericht Nr. I-7 aus dem Institut für Mechanik (Bauwesen), Universität Stuttgart 2000.

[127] *Schwarz, H. R.: Methode der finiten Elemente.* Teubner, Stuttgart 1991.

[128] *Shewchuk, J. R.: Triangle: A Two-Dimensional Quality Mesh Generator and Delaunay Triangulator.* School of Computer Science, Carnegie Mellon University, Pittsburgh, Pensilvania 1996. `http://www.cs.cmu.edu/~quake/triangle.html`.

[129] *Simo, J. C.; Taylor, R. L.:* Consistent tangent operators for rate-independent elastoplasticity. *Computer Methods in Applied Mechanics and Engineering* **48** (1985), 101–118.

[130] *Skempton, A. W.*: Significance of Terzaghi's concept of effective stress (Terzaghi's discovery of effective stress). In *Bjerrum, L.; Casagrande, A.; Peck, R. B.; Skempton, A. W.*, editors, *From Theory to Practice in Soil Mechanics.* John Wiley & Sons, New York 1960, pp. 42–53.

[131] *Steeb, H.; Diebels, S.; Ehlers, W.*: *Galerkin*-type space-time finite elements for volumetric coupled problems. *Proceedings in Applied Mathematics and Mechanics (PAMM)* **2** (2003), 264–265.

[132] *Steinmann, P.*: A micropolar theory of finite deformation and finite rotation multiplicative elasto-plasticity. *International Journal of Solids and Structures* **31** (1994), 1063–1084.

[133] *Steinmann, P.; Willam, K.*: Localization within the framework of micropolar elastoplasticity. In *Brüller, O.; Mannl, V.; Najar, J.*, editors, *Advances in Continuum Mechanics.* Springer-Verlag, Berlin 1991, pp. 296–313.

[134] *Strang, G.; Fix, G. J.*: *An Analysis of the Finite Element Method.* Prentice-Hall, Englewood Cliffs, New York 1973.

[135] *Strehmel, K.; Weiner, R.*: *Numerik gewöhnlicher Differentialgleichungen.* Teubner, Stuttgart 1995.

[136] *Strömberg, L.; Ristinmaa, M.*: FE-formulation of a nonlocal plasticity theory. *Computer Methods in Applied Mechanics and Engineering* **136** (1996), 127–144.

[137] *Stroud, A. H.*: *Approximate Calculation of Multiple Integrals.* Prentice-Hall, New Jersey 1971.

[138] *Tejchman, J.; Wu, W.*: Numerical study of patterning of shear bands in a Cosserat continuum. *Acta Mechanica* **99** (1993), 61–74.

[139] *Terzaghi, K.*: *Erdbaumechanik auf bodenphysikalischer Grundlage.* Franz Deuticke, Leipzig 1925.

[140] *Törnig, W.; Spellucci, P.*: *Numerische Mathematik für Ingenieure und Physiker – Numerische Methoden der Analysis*, Vol. 2. Springer-Verlag, Berlin 1990.

[141] *Truesdell, C.*: The origins of rational thermodynamics. In *Truesdell, C.*, editor, *Rational Thermodynamics.* Springer-Verlag, New York, 2nd ed. 1984, pp. 1–57.

[142] *Truesdell, C.*: Thermodynamics of diffusion. In *Truesdell, C.*, editor, *Rational Thermodynamics.* Springer-Verlag, New York, 2nd ed. 1984, pp. 219–236.

[143] *Truesdell, C.; Toupin, R. A.*: The classical field theories. In *Flügge, S.*, editor, *Handbuch der Physik*, Vol. III/1. Springer-Verlag, Berlin 1960, pp. 226–902.

[144] *Volk, W.*: *Untersuchung des Lokalisierungsverhaltens mikropolarer poröser Medien mit Hilfe der Cosserat-Theorie.* Dissertation, Bericht Nr. II-2 aus dem Institut für Mechanik (Bauwesen), Universität Stuttgart 1999.

[145] *Walker, D. W.; Dongarra, J. J.*: MPI: a standard message passing interface. *Super-computer* **12** (1996), 56–68.

[146] *Wang, W. M.; Sluys, L. J.; de Borst, R.*: Interaction between material length scale and imperfection size for localisation phenomena in viscoplastic media. *European Journal of Mechanics A/Solids* **15** (1996), 447–464.

[147] *Wieners, C.*: M++. `http://www.mathematik.uni-karlsruhe.de/~wieners/`.

[148] *Wieners, C.*: Efficient elasto-plastic simulation. In *Sändig, A. M.; Schiehlen, W.; Wendland, W. L.*, editors, *Multifield Problems – State of the Art.* Springer-Verlag, Berlin 2000, pp. 209–216.

[149] *Wieners, C.*: Taylor-Hood elements in 3D. In *Wendland, W. L.; Efendiev, M.*, editors, *Analysis and Simulation of Multifield Problems.* Springer-Verlag, Berlin 2003, pp. 189–196.

[150] *Wieners, C.*: Distributed Point Objects. A New Concept for Parallel Finite Elements. `http://www.mathematik.uni-karlsruhe.de/~wieners/Forschung/Publikation.html`, Karlsruhe 2003.

[151] *Wieners, C.; Ammann, M.; Diebels, S.; Ehlers, W.*: Parallel 3-d simulations for porous media models in soil mechanics. *Computational Mechanics* **29** (2002), 73–87.

[152] *Wieners, C.; Ammann, M.; Ehlers, W.*: Distributed Point Objects: A new concept for parallel finite elements applied to a geomechanical problem. *Future Generation Computer Systems,* in press 2005.

[153] *Wieners, C.; Ammann, M.; Ehlers, W.; Graf, T.*: Parallel Krylov methods and the application to 3-d simulations of a triphasic porous media model in soil mechanics. *Computational Mechanics,* in press 2005.

[154] *Wood, W. L.*: *Practical time-stepping schemes.* Clarendon Press, Oxford 1990.

[155] *Wriggers, P.*: *Konsistente Linearisierung in der Kontinuumsmechanik und ihre Anwendung auf die Finite-Elemente-Methode.* Dissertation, Forschungs- und Seminarberichte aus dem Bereich der Mechanik der Universität Hannover, Bericht-Nr. F 88/4, Universität Hannover 1988.

[156] *Zienkiewicz, O. C.; Taylor, R. L.*: *The Finite Element Method: The Basis*, Vol. 1. Butterworth-Heinemann, London 2000.

[157] *Zienkiewicz, O. C.; Taylor, R. L.*: *The Finite Element Method: Solid Mechanics*, Vol. 2. Butterworth-Heinemann, London 2000.

[158] *Zimmermann, D.*: *Ein implizites Gradientenmodell zur Beschreibung nicht-lokaler finiter Plastizität formuliert in logarithmischen Verzerrungen: Konstitutiver Ansatz und numerische Implementation.* Diplomarbeit, Bericht Nr. 03-I-2 aus dem Institut für Mechanik (Bauwesen), Universität Stuttgart 2003.

Curriculum Vitae

Name:	Martin Ammann
Date of birth:	11th June 1972
Place of birth:	Ellwangen/Jagst, Germany
Nationality:	German
Marital Status:	Unmarried
Education:	09/1978 – 07/1982
	Elementary School: Abtsgmünd
	09/1982 – 07/1983
	Secondary School: Realschule Abtsgmünd
	08/1983 – 05/1992
	Secondary School: Kopernikus-Gymnasium
	Aalen-Wasseralfingen
Community Service:	08/1992 – 10/1993
	Community Service at "Deutsches Rotes Kreuz", Aalen
Studies:	10/1993 – 10/1998
	Studies in Civil Engineering at the University of Stuttgart
Professional Occupation:	11/1998 – 03/2005
	Assistant Lecturer at the Institute of Applied Mechanics
	(Civil Engineering) at the University of Stuttgart
	since 04/2005
	Computational Engineer at DaimlerChrysler AG, Stuttgart

Bisher in dieser Reihe erschienen:

II-1   G. EIPPER: Theorie und Numerik finiter elastischer Deformationen in fluidgesättigten porösen Festkörpern, Juni 1998.

II-2   W. VOLK: Untersuchung des Lokalisierungsverhaltens mikropolarer poröser Medien mit Hilfe der *Cosserat*-Theorie, Mai 1999.

II-3   P. ELLSIEPEN: Zeit- und ortsadaptive Verfahren angewandt auf Mehrphasenprobleme poröser Medien, Juli 1999.

II-4   S. DIEBELS: Mikropolare Zweiphasenmodelle: Formulierung auf der Basis der Theorie Poröser Medien, März 2000.

II-5   D. MAHNKOPF: Lokalisierung fluidgesättigter poröser Festkörper bei finiten elastoplastischen Deformationen, März 2000.

II-6   H. MÜLLERSCHÖN: Spannungs-Verformungsverhalten granularer Materialien am Beispiel von Berliner Sand, August 2000.

II-7   S. DIEBELS (Hrsg.): Zur Beschreibung komplexen Materialverhaltens: Beiträge anläßlich des 50. Geburtstages von Herrn Prof. Dr.-Ing. Wolfgang Ehlers, August 2001.

II-8   J. WIDJAJAKUSUMA: Quantitative Prediction of Effective Material Parameters of Heterogeneous Materials, Juni 2002.

II-9   A. DROSTE: Beschreibung und Anwendung eines elastisch-plastischen Materialmodells mit Schädigung für hochporöse Metallschäume, Oktober 2002.

II-10   P. BLOME: Ein Mehrphasen-Stoffmodell für Böden mit Übergang auf Interface-Gesetze, Oktober 2003.

II-11   M. AMMANN: Parallel Finite Element Simulations of Localization Phenomena in Porous Media, April 2005.